Defining the role of rabies virus glycoprotein trafficking in virus neurotropism and pathogenesis

Ibrahim Al-Masoud

Submitted in accordance with the requirements for the degree of Doctor of Philosophy

The University of Leeds

Faculty of Biological Sciences

School of Molecular and Cellular Biology

November 2020

The candidate confirms that the work submitted is his own and that appropriate credit has been given where reference has been made to the work of others.

Acknowledgements

I thank my supervisor, Dr Jamel Mankouri for his guidance and support throughout the course of this research. I also thank my co-supervisor Dr John Barr, lab group, colleagues, friends, the department faculty and staff for making my time in Leeds enjoyable. Thanks to Kuwaiti Government for funding this project. Finally, thanks to my family for their encouragements and to my wife for her hours of patience, respect and love.

“There are no incurable diseases – only the lack of will. There are no worthless herbs – only the lack of knowledge.” – Avicenna.

Abstract

More than 90% of fatal rabies cases are caused by rabies virus, the prototypical neurotropic virus. Rabies virus glycoprotein (RABV-G) is the only protein expressed at the surface of rabies virions and it is solely responsible for neuroinvasiveness and extracellular virion transport. Whilst the role of RABV-G in virus entry has been extensively studied, the cellular roles of RABV-G during infection, including its trafficking within infected cells and host protein binding partners that contribute to virus pathogenesis remain less well-characterised.

In this thesis, the trafficking phenotypes of RABV-G were assessed through comparison of RABV-G proteins from pathogenic vs attenuated virus strains (Chapter 3). It is shown that when expressed in cells of the central nervous system, the pathogenic RABV-G from strain CVS-11 more rapidly internalises from the cell surface compared to RABV-G from the attenuated SAD-B19 strain that shows slower rates of internalisation and higher cell surface expression. Alanine scanning was used to identify regions responsible for this altered trafficking phenotype which identified Y497 and several C-terminal residues in RABV-G that govern this rapid internalisation. This may be of particular interest as the internalisation of RABV-G from the cell surface of RABV infected cells imparts the virus with ‘stealth’ from the host immune defences. This infers the discovery of key residues in RABV-G that govern virus pathogenicity.

In Chapter 4, through BioID interactomic screening of the proteins proximate to the cytoplasmic tail of CVS-G and SAD-G, functional protein clusters were identified in actomyosin regulation, clathrin-mediated endocytosis, cilium assembly and Golgi-ER transport that were uniquely proximate to CVS-G and not SAD-G. Key hits were then validated revealing targetable host factors that contribute to virus pathogenesis. Two key targets, non-muscle myosin IIA and its regulator Rho-kinase (ROCK) enzyme were found to have a remarkable effect on CVS-G-induced filopodia where treatment with Blebbistatin or Y-27632 retracted almost 50% or 58% of CVS-G-induced filopodia, respectively. This provided evidence of the selective inhibition of a pathogenic CVS-G process that may represent a novel antiviral target.

In Chapter 5, the last two residues of the CVS-G and SAD-G transmembrane domain were investigated through site-directed mutagenesis, revealing a double palmitoylation event at C_{460} and C_{461} in SAD-G, as opposed to a single palmitoylation event that occurs at C_{461} in CVS-G. Mutagenesis of these residues revealed a functional contribution of palmitoylated cysteines to the lipid raft association of both proteins that correlated with their internalisation from the cell surface. These findings reveal a new mechanism of virus coat protein internalisation through palmitoylation of residues at the interface of transmembrane and cytoplasmic domains.

Overall, this project illuminates our understanding of RABV-G and its role in dictating the pathogenicity of specific RABV strains.

Table of Contents

List of Tables

List of Figures

Abbreviations

AAK1	AP2-associated kinase 1
APC	Antigen-presenting cell
BioID	Proximity-dependent biotin identification
BirA*	Modified biotin ligase
CavME	Caveolae mediated endocytosis
CME	Clathrin mediated endocytosis
CNS	Central nervous system
CVS	Rabies Challenge Virus Standard strain 11 (CVS-11)
DLC	Dynein light chain
DMEM	Dulbecco’s modified Eagle’s medium
DOG	Rabies canine street isolate (Azerbaijan)
EBLV	European bat lyssavirus I
ECM	Extracellular matrix
EE	Early endosome
EIAV	Equine infectious anaemia virus
EIPA	Ethylisopropylamiloride
Env	Viral envelope protein
ER	Endoplasmic reticulum
F-actin	Fibrous actin
G	Rabies glycoprotein
GAPDH	Glyceraldehyde 3-phosphate dehydrogenase
HCV	Hepatitis C virus
HDCV	Human tissue culture-based diploid cell vaccine
HIV	Human immunodeficiency virus

HPV	Human papillomavirus
Hrs	Hours
HSV	Herpes simplex virus
ic	Intracerebral injection
IFN	Interferon
IGF-I	Insulin-like growth factor I
im	Intramuscular injection
L	Rabies RNA-dependent RNA polymerase
LE	Late endosome
M	Rabies matrix protein
mGluR2	Metabotropic glutamate receptor subtype 2
MβCD	Methyl beta cyclodextrin
N	Rabies nucleoprotein
nAChR	Nicotinic acetylcholine receptor
NAD	Nicotinamide adenine dinucleotide
NCAM	Neuronal cell adhesion molecule
NGF	Nerve growth factor
NiV	Nipah virus
NMJ	Neuromuscular junction
P	Rabies phosphoprotein
$p75^{NTR}$	p75 neurotrophin receptor
PBS	Phosphate-buffered saline
PEP	Post-exposure prophylaxis
PFA	Paraformaldehyde
PIV	Parainfluenza virus

PM	Plasma membrane
RABV	Rabies lyssavirus
RE	Restriction enzyme
RNP	Ribonucleoprotein
ROCK	Rho-kinase
RSV	Respiratory syncytial virus
RT	Room temperature
SAD	Rabies Street Alabama Dufferin strain B19 (SAD-B19)
SARS-CoV	Severe acute respiratory syndrome coronavirus
SDS-PAGE	Sodium dodecyl sulphate-polyacrylamide gel electrophoresis
SEM	Standard error of the mean
SHBRV	Silver-haired bat rabies virus strain 18 (SHBRV-18)
SIV	Simian immunodeficiency virus
Tf	Transferrin
TGN	Trans Golgi network
TMT	Tandem mass tagging
VNAs	Virus neutralising antibodies
VSV	Vesicular stomatitis virus
WHO	World Health Organisation

Chapter 1 | Introduction

1.1 Rabies disease

1.1.1 Rabies background

Rabies lyssavirus (RABV) causes the fatal neurological disorder *rabies* which is an ancient dog-associated disease that has afflicted humanity for the last 4,000 years (Tarantola, 2017). Historical interrogation suggests that the current form of rabies evolved in the fifteenth century in southern Europe (Baer, 2007), spreading during the European age of exploration to the Americas and to the rest of the world.

Rabies is caused by lyssaviruses, a family of 12 closely related viruses that cause a frenzy-like neurotropic disease (Warrell and Warrell, 2004). The two unique symptoms of rabies are hydrophobia and Negri body formations in the central nervous system (CNS) (Viets, 1926). Hydrophobia is the fear of water where the virus-infected host displays a bizarre fear of hydration. In humans, this translates into difficulty in swallowing and drinking, thought to prevent dilution of the saliva to facilitate virus spread. This ‘mad disease’ pushed humanity in ancient times to kill and burn suspected rabies victims to prevent the disease spread (Tarantola, 2017). In addition, rabies-causing viruses remain viable in dead hosts until their complete dehydration, taking up to three days in tropical climates, up to a month in cool temperatures, and years in very cold temperatures (McElhinney et al., 2014). This ensures long-term survival of this pathogen by hungry scavengers.

1.1.2 Rabies symptoms

Following RABV exposure, the incubation period lasts for ~30-90 days (Leung et al., 2007). During this time the virus spreads slowly from the wound site to nearby tissues and the patient feels tingling and pain at the wound site. Wounding at the head or neck significantly decrease this incubation period (Lafon, 2008). When RABV invades CNS through the neuromuscular junction, various prodromal symptoms appear for 2-10 days where effective Post-Exposure Prophylaxis (PEP) treatment becomes increasingly ineffective. These prodromal symptoms are non-specific and they include influenza-like symptoms, paraesthesia, hyperesthesia, pain and numbness at the virus entry site (Leung et al., 2007).

Following this stage, ~80% of patients display acute neurological signs such as hydrophobia, aerophobia, inspiratory spasms and fluctuating consciousness, clinically classified as furious rabies. Patients survive on average for 5.7 days that can be extended for up to a month following intensive care support (Hemachudha et al., 2013). A minority of patients display milder paralytic rabies, the symptoms of which include limb weakness, motor neuron disturbance and dizziness before consciousness is lost (Mitrabhakdi et al., 2005). Paralytic rabies patients survive an average of ~11 days (Hemachudha et al., 2013). RABV eventually causes death through neuronal dysfunction by overwhelming the body's CNS, leading to cardiac arrest and/or lung failure (Fu and Jackson, 2005).

1.1.3 Epidemiology

Warm-blooded mammals are the natural reservoirs of this zoonotic virus which spreads between animals and to humans via bites and scratches. Contrary to popular belief, cross-species transmission typically results in dead-end infections (Fisher et al., 2018) and zombie human-to-human spread does not occur. Rabies infection is contact-dependent and rarely spreads through other means, though airborne transmission in humid bat caves (Constantine, 1967) and transmission in poorly-regulated rabies-handling labs have been documented (Winkler et al., 1973; Davis et al., 2015). On rare occasions, RABV infection via organ transplantation of a rabies-infected donor has been documented (Bronnert et al., 2007).

Most human rabies cases are caused by rabid dogs (~ 90%) followed by rabid bats (5%), accidental lab exposure (4%) and other animals (1%) (Leung et al., 2007). In terms of fatalities, almost all (~99.9%) are caused by rabid dogs (Meslin, 2008) due to the prevalence of wild dog populations in rabies-endemic regions around the globe. These regions are usually rural, poor and lack the necessary medical and transportation infrastructure to deliver quality PEP (Hampson et al., 2008). Rabies PEP biologics (antibodies and vaccines) require cold-chain transportation conditions and storage to maintain their stability and efficacy, although a thermotolerant vaccine was recently developed (Lankester et al., 2016). Poor accessibility to hospitals leads to improper PEP administration, patients missing PEP follow-ups and a minority

resorting to alternative medicine. These factors alone contribute to up to a third of rabies-related deaths annually (Wilde, 2007). In addition, PEP supplies and administration are disrupted in regions of conflict. As an exemplar, the number of rabies associated fatalities increased by 500% in Yemen after the 2011 conflict (Al-Shamahy et al., 2013). The availability of alternative therapies can offset these inherent drawbacks of current PEP regimens.

Recent statistics by the World Health Organisation (WHO) estimate that 60,000-70,000 human deaths per year are caused by rabies infections (World Health Organization, 2018) which is more than heat-related deaths (55,000) and half of the number of deaths from hepatitis (135,000) (Roth et al., 2018). The WHO is currently campaigning a United Against Rabies programme with the aim of eradicating rabies in natural reservoirs by 2030 (Minghui et al., 2018). These statistics and current global campaigns highlight the significance of this neurotropic viral disease.

1.1.4 Prevention and treatment strategies

To prevent rabies infection, the only viable treatment option[1] is prompt wound cleansing followed by PEP administration (Schnell et al., 2010; Kuzmin et al., 2014). This preventative medical treatment is routinely administered to all potential rabies exposure sites as rabies cannot be reliably diagnosed immediately after exposure (Hemachudha et al., 2013), leading to 80-90% of PEP administration to presumed positive cases that are then confirmed to be negative (Wilde, 2007) costing time, resources and failing to treat those that actually require rabies treatment.

Following the onset of symptoms, PEP treatment is ineffective as rabies reaches the immune-privileged region of the CNS where it preferentially replicates (Schnell et al., 2010). Rabies PEP procedures involve the injection of inactivated rabies vaccine and anti-rabies virus neutralising antibodies

[1] The Milwaukee protocol (Willoughby et al., 2005) worked once against a patient showing late-stage symptoms of rabies. It is the process of inducing medical coma, followed by ketamine and amantadine administration while managing cerebral vasospasm to attempt to stop rabies from killing its human host and allow the immune system to fight it. So far this treatment protocol was never successfully reproduced (Zeiler and Jackson, 2015; Wilde and Hemachudha, 2015) and it is not worth consideration as a rabies treatment option as the most likely scenario is that a milder strain of bat rabies infected the Milwaukee girl and she recovered due to the attenuated nature of that strain.

(VNAs) over the course of 5 to 6 weeks and boosts are re-administered after 6-12 months (Baer and Fishbein, 1987). The current PEP procedure was optimised from Pasteur's primitive nerve-tissue vaccine (Pasteur et al., 1884) after the development of a human tissue culture-based diploid cell vaccine (HDCV) (Koprowski et al., 1976). This inactivated HDCV vaccine is safe, effective and reliable with very few recorded failures, making it WHO's gold standard PEP against rabies infection (Hicks et al., 2012; World Health Organization, 2018). Unfortunately, rabies VNAs are expensive to produce and HDCV production is difficult to scale-up, leading to shortages of supply and making this second generation PEP not available to 95-98% of patients requiring rabies treatment (Bourhy et al., 2009). This led to countries in Africa, South America and Asia with limited access to tissue culture facilities to use Pasteur's first-generation methods that are based on animal injection with rabies and subsequent virus purification and inactivation from their nervous tissue, resulting in vaccines with low immunogenicity that cause severe side effects. These nervous tissue-based vaccines are not recommended by the WHO (Warrell and Warrell, 1995; World Health Organization, 2018).

Monoclonal VNAs are well-characterised and are easier to produce in large quantities than serum derived polyclonal VNAs. VNA production is the major rate-limiting step of large-scale PEP production, with efforts made to overcome this issue through the production and characterisation of a broad-range monoclonal antibody (RVC20) which co-crystalised with RABV-G showing binding to conserved antigenic sites I and II (Hellert et al., 2020). It was also shown that polymorphisms at the most variable positions (190, 194 and 231 of RABV-G ectodomain) did not significantly affect RVC20 neutralisation, highlighting RVC20 as potential gold standard rabies monoclonal VNA.

Third generation molecular PEP vaccines are currently in testing and are under development. Included in these is a genetically engineered RABV strain LEP that has two copies of its glycoprotein (RABV-G) reverse-engineered into the virus, creating LEP_{GG}. After inactivated vaccine testing of LEP versus LEP_{GG}, LEP_{GG} provided higher virus neutralisation titres than LEP and induced longer immunity against rabies in mice and dogs (Tao et al., 2011).

This double-glycoprotein experiment was repeated in another strain, CVS-11, creating CVS-11_{GG}. It was reported that CVS-11_{GG} produced larger virions with 1.4-fold higher RABV-G expression. These recombinant viruses also required ~80% lower doses to induce the same levels of virus neutralisation (Xue et al., 2014).

A further development was the generation of a super-attenuated vaccine that does not lead to rabies even after intracranial inoculation (direct injection into the brain). This super-vaccine is based on the modification of the already-attenuated[2] strain SAD-B19 via disrupting two charged residues in the extracellular domain of RABV-G; R_{333} and N_{194} (Faber et al., 2005). These two residues regulate the cell-to-cell spread of RABV (Dietzschold et al., 2008). When substituted with non-charged amino acids, a stable live-attenuated strain was generated leading to immunity in mice without the need for inactivation. This super-vaccine was further reverse-engineered to include three RABV-G copies to elicit higher virus neutralisation (Faber et al., 2009). This vaccine seemed viable to administration as a live vaccine, providing a logistical advantage of a single immunisation event to induce strong innate and adaptive immune responses, capable of clearing RABV from the host, as opposed to the gold standard inactivated vaccines that require several shots over several weeks to be effective. However, this super-vaccine is only effective when administered live (ineffective when inactivated), requires careful handling conditions, and is ineffective following the onset of symptoms (Li et al., 2012). In addition, live RABV vaccines retain residual pathogenicity in immune-immature suckling mice (Tuffereau et al., 1989) and can become pathogenic upon mutation. Its safety for human use is therefore not guaranteed. For this reason, only attenuated vaccines are approved for human use (Wirblich and Schnell, 2011).

RABV live vaccines have been successfully used to eradicate RABV from European carnivore reservoirs such as dogs, foxes and wolves (Rupprecht et al., 2005). Large scale oral vaccination programmes were initiated in Switzerland in 1978 using bait inoculated with live RABV strain SAD-B19 that

[2] Discussed in the next section (1.2).

confers immunity to the animal that eats it (Steck et al., 1978). Edible baits were initially developed as severed chicken heads containing plastic sachets of 1.8 ml of virus-containing serum (Steck et al., 1978). Baits were then refined into square fish meal blocks encapsulating paraffin sachets containing 1.5 ml of virus-containing serum in addition to 150 mg tetracycline as a biomarker (Müller et al., 2015). Millions of air-dropped edible vaccines virtually eliminated RABV from Western and Central Europe (Servat et al., 2020). However, bats still harbour RABV and eliminating RABV and RABV-like lyssaviruses from bats and non-carnivores remains unfeasible (Fisher et al., 2018). Documented spillover events from bats to dogs in Chile (De Mattos et al., 2000), skunks in Arizona, USA (Leslie et al., 2006) and cats in France (Dacheux et al., 2009) have occurred, highlighting the challenges of oral vaccination. Further surveillance and eradication programs are required to control rabies in wild animals and bats.

PEP inactivated vaccines require complementation with anti-rabies antibodies for effective rabies treatment. Vaccines and antibodies also have the inherent limitation of unreliable protection against non-RABV lyssaviruses (Nel, 2001) and new and emerging strains have arisen as the ectodomain of RABV-G is prone to mutations (Hoffmann et al., 2002). In general, treatment strategies against RABV infection revolve around RABV-G, highlighting the importance of this coat protein.

1.2 RABV classification

RABV belongs to the lyssavirus genus, of the rhabdovirus family of the mononegavirus order of non-segmented negative sense RNA viruses. The mononegaviruses order was initially created in 1991 to group three virus families (and their prototypical viruses): filoviruses (Ebola), paramyxoviruses (respiratory syncytial virus (RSV)) and rhabdoviruses (RABV) (Pringle, 1991). All three families share common traits, including the 3'-core proteins-G-L-5' genome organisation and helical RNPs (Amarasinghe et al., 2018). The Rhabdovirus family includes RABV of the lyssavirus genus and VSV of the vesiculovirus genus. Both viruses share the bullet-shaped structure. One major difference between VSV and RABV is the presence of a relatively long pseudogene sequence (ψ) between RABV-G and RABV-L in RABV (see

Figure 1.2) which is absent in VSV and other Rhabdoviruses (Walker et al., 2011). This sequence was shown to contribute to the neuroinvasiveness of RABV-G (Faber et al., 2004), inferred to attenuate RABV-L expression (Finke et al., 2000), and stabilise RABV-G RNA interactions with host proteins (Ravkov et al., 1995). Even though deleting this region was originally shown to have no effect on RABV neuroinvasiveness (Ceccaldi et al., 1998), it was shown to contribute to RABV pathogenesis through a yet uncharacterised regulatory role (Faber et al., 2004). This Lyssavirus-only ψ sequence requires further characterisation to better understand its role in RABV pathogenesis.

The Lyssavirus genus also differs from other rhabdovirus viruses in terms of neurotropism and disease fatality. In essence, all lyssaviruses are 'rabies viruses' as they cause rabies; namely progressive fatal encephalitis. The prototypical strain rabies lyssavirus (abbreviated here as RABV) differs from all other lyssaviruses in its association with mostly terrestrial canine rabies (Figure 1.1).

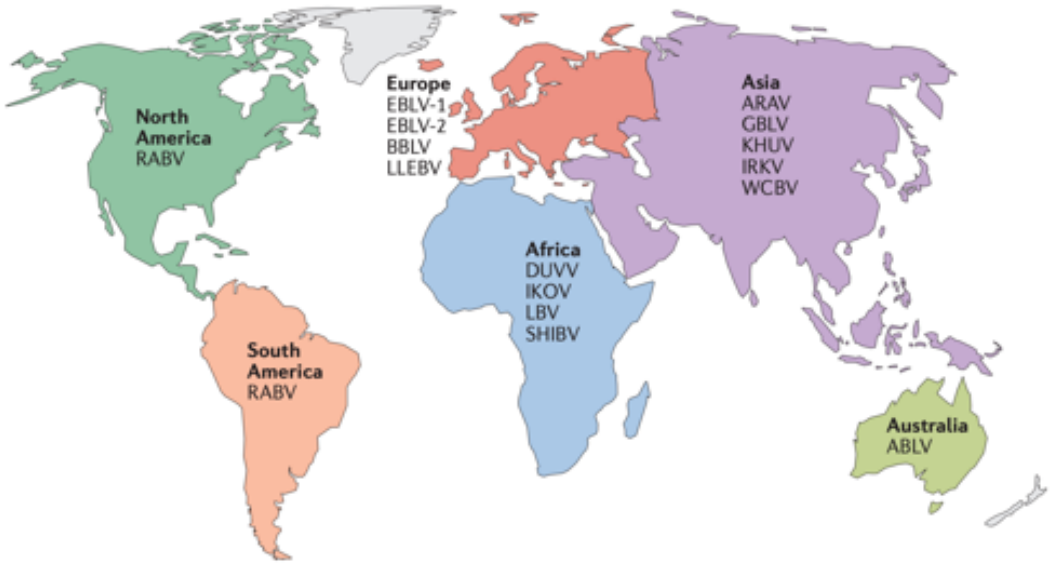

Figure 1.1 Continental distribution of lyssaviruses. Lyssaviruses circulate all continents except for Antarctica. In the Americas, RABV is the dominant lyssavirus whereas in Europe, Asia, Africa and Australia other lyssaviruses are the dominant circulating strains. Europe is considered free from RABV due to vaccination efforts of terrestrial animals. RABV was never reported in Australia or New Zealand. Abbreviations are expanded in Table 1.1. (adapted from Fisher et al. 2018).

Lyssaviruses are genetically similar to each other, but are relatively distant from related rhabdoviruses. The phylogenetic demarcation between lyssaviruses is based on expert opinion of the International Committee on Taxonomy of Viruses (ICTV). Non-RABV lyssaviruses are mostly bat associated (14 out of 16 lyssaviruses) and they are not RABV as they are not canine-associated (Rupprecht et al., 2017). Lyssaviruses are further divided into three phylogroups based on the sequence of the RABV-G ectodomain and VNA sensitivity (Table 1.1).

Table 1.1 Lyssaviruses and rabies-related viruses (Fisher et al., 2018).

Phylogroups	Species name	Abbreviation
Phylogroup I	Rabies lyssavirus	RABV
	European bat lyssaviruses I	EBLV-I
	European bat lyssaviruses II	EBLV-II
	Australian bat lyssavirus	ABLV
	Aravan lyssavirus	ARAV
	Bokeloh bat lyssavirus	BBLV
	Duvenhage lyssavirus	DUVV
	Irkut lyssavirus	IRKV
	Khujand lyssavirus	KHUV
Phylogroup II	Mokola lyssavirus	MOKV
	Lagos bat lyssavirus	LBV
	Shimoni bat lyssavirus	SHIBV
Unclassified	West Caucasian bat lyssavirus	WCBV
	Lleida bat lyssavirus	LLEBV
	Ikoma lyssavirus	IKOV
	Gannoruwa bat lyssavirus	GBLV

In total, 16 strains have been classified to-date (Fisher et al., 2018). This phylogroup division means that any strain from phylogroup I can be neutralised by VNA generated towards other phylogroup I strains, but not from e.g. phylogroup II (Badrane et al., 2001). This division is continuously changing and updated with emerging strains.

1.4.1 RABV strains

Traditional classification and current medical classification divides RABV into either furious or paralytic, based on the clinical manifestation of rabies disease in infected humans and dogs (Warrell, 1976). Generally, clinical rabies is observed with a 2:1 ratio of furious:paralytic cases (Hemachudha et al., 2013). Genetics-based attempts to characterise the strains noted no significant difference between furious and paralytic rabies, although several RABV-G point mutations occur in non-ectodomain regions. These include T447A and R471Q in one furious isolate (HM65G), though no conserved variations are observed and it was concluded that the route of infection and infectious load dictates whether furious or paralytic rabies develops (Hemachudha et al., 2003).

Whilst RABV is naturally found in terrestrial animals and bats, it has been successfully cultivated for decades in rabbits and mice, even though these represent non-natural reservoirs of RABV (Lafon, 2008). Infected rabbits were the basis of the first Pasteur virus strain (Pasteur et al., 1884) that still exists today, as several variant strains have been adapted to replicate in mice and a range of neuronal and non-neuronal cell lines. These RABV strains are slightly unnatural and ‘fixed’ as they are serially passaged in the same animal or cell line to obtain constant characteristics such as onset of symptoms, incubation period and virulence (Wu et al., 2011). Cell culture adapted strains replicate faster in cell culture and are easier to genetically manipulate. Fixed strains were used to provide answers to most of the mechanistic questions in the RABV lifecycle, but their adaptation to unnatural hosts and cancerous cell lines raise concerns. This is in contrast to wild type strains that are directly isolated from naturally infected hosts and humans (Faber et al., 2004), representing the source of most of our descriptive understanding of RABV pathogenesis.

Almost all wild type strains are pathogenic and fixed strains are either:

- Pathogenic
- Attenuated (through intramuscular injection (im))
- Highly attenuated (through both im and intracerebral injection (ic))

These fixed strains are mostly derived from one of three RABV source strains (Wu et al., 2011): Pasteur virus strain (1882 in Paris, France); SAD virus strain (1935 in Alabama, USA); and Flury virus strain (1939 in Georgia, USA). All three originated from rabid dogs, though few studies reported rabid cow origin of Pasteur virus strain (Sacramento et al., 1992). As discussed, the Pasteur virus strain was the first RABV strain isolated but it does not exist today in its original sequence. Several variants of this strain now exist such as the North American CVS-11 and Pitman-Moore strains, South American Pasteur virus strain and the Japanese Nishigahara strain (Lafon, 2008). CVS-11 (CVS) is arguably the most well-characterised fixed RABV strain as it is the challenge virus standard strain used worldwide to assess RABV vaccine efficiency in mice, and was the first strain studied to define RABV viral epitopes (Dietzschold et al., 1983). It is derived from adaptation in mouse brains followed by brief incubation in BHK-21 cells (Sacramento et al., 1992). CVS has been further characterised into two variants, the neuroblastoma-adapted variant CVS-N2c and the slightly apathogenic fibroblast-adapted CVS-B2c (Morimoto et al., 2000). VNA escape mutants were identified through the generation of CVS-F3 (also named RV-194-2) and the attenuated strain AvO1, with the common R333Q point mutation (Lafon, 2008).

Pitman-Moore was derived from the Pasteur virus following its passage in human diploid cells, which was then adapted to replicate in BHK-21 cells (Wiktor et al., 1964). The South American variant of the Pasteur virus is commonly referred to as ‘Pasteur virus (PV)’ and was derived after passaging in rabbit brains and adapted in foetal bovine kidney cells (Atanasiu et al., 1974). Nishigahara and its apathogenic variant RC-HL are also derived from the Pasteur virus and have been adapted in rabbit brains and hamster lung cells, respectively (Ito et al., 2001). The Flury strain was passaged in chick embryos to develop two variants: LEP-Flury (low egg passage) that was passaged 40-50 times and the attenuated HEP-Flury (high egg passage) that was passaged 180 times or more, until this strain naturally developed an R333Q mutation in RABV-G to become apathogenic (Fox et al., 1957).

SAD (Street Alabama Dufferin) that originated from a rabid dog was adapted in mice then passaged 25 times in hamster kidney cells, followed by 10

passages in chick embryos. The original SAD strain does no longer exist and common variants include ERA (Evelyn Rokitnicki-Abelseth) which was passaged 40 times in porcine kidney cells, followed by passage in BHK cells. Another common variant SAD-B19 (herein referred to as SAD) was selected following BHK passage after displaying low residual pathogenicity and thermostability (Sacramento et al., 1992). European variants are ERA strain adapted in BHK cells to create SAD Bern (Switzerland), SAG1 and SAG2 (France), Vnukovo-32 (Russia) and the Chinese strain SRV9 (Geue et al., 2008). SHBRV-18 (silver-haired bat rabies virus, strain 18) differs from all other fixed strains due to its bat origin and was adapted in neuroblastoma cells (Lafon, 2008).

1.2.2 Genetics of RABV strains

The aforementioned strains were isolated from rabid dogs. SHBRV-18 is more genetically distant from other RABV strains, with genome alignments revealing an association closer to EBLV-I than RABV (Figure 1.2). Both SHBRV-18 and EBLV-I (that is not classified as RABV) originated from bats and differs to those circulating in carnivores. Most sequence variation occurs in the C-terminal domain if RABV-G and in the intergenomic Ψ region between G and L (Figure 1.2). There is 0% sequence homology between EBLV-I and RABV at a segment of this intergenomic Ψ region due to genetic deletions in EBLV-I and most other non-RABV viruses (Ravkov et al., 1995).

Most fixed RABV strains are developed as vaccine strains, with RABV-G the key mediator of attenuation. Conserved regions of pathogenic and attenuated RABV-G sequences have been compared to identify the regions that dictate attenuation, with limited success (Section 1.4). Without the identification of a robust attenuation sequence, no live rabies vaccine for humans can be approved.

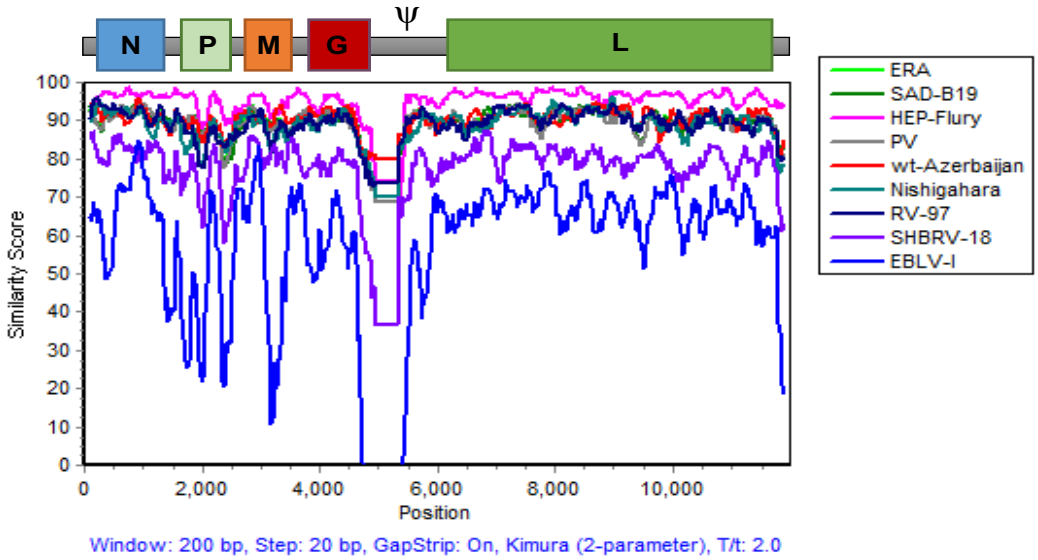

Figure 1.2 Whole-genome similarity plot of CVS-11 and RABV strains. Eight strains of RABV and ELBV are compared to CVS-11 through Simplot, window size of 200 base pairs and a step size of 20 base pairs. As shown, most sequence variations occur within the G cytoplasmic domain and the G-L intergenomic region (Ψ).

1.2.3 Pathogenic CVS and attenuated SAD

CVS was the first characterised fixed RABV strain, commonly used as the challenge virus in vaccine development (Dietzschold et al., 1983). SAD is the attenuated strain mostly used to eradicate canine RABV from Europe (Servat et al., 2020). Both strains originated from rabid dogs and CVS was passaged mostly in live mouse brains and it is highly neurotropic, displaying a mostly neuron-only infection pattern compared to SAD that has been passaged mostly in non-neuronal cells and displays non-selective diffusion in the infected brain (Yan et al., 2002). When used as a neurotracing tool, SAD travels throughout the CNS slowly, inducing apoptosis along its infection route (Wickersham et al., 2007). In contrast, CVS travels quickly through neurons, inducing apoptosis and cell death only during the later stages of infection (Reardon et al., 2016).

An important question in the RABV literature is why SAD and related RABV strains are attenuated. In 2000, Morimoto and colleagues engineered a hybrid strain SAD with its G protein replaced with CVS-G, creating SAD-G_{CVS}. This

hybrid strain was pathogenic, implicating RABV-G as the key mediator of RABV pathogenesis (Morimoto et al., 2000). When RABV-G sequences of both strains were compared, most amino acid differences are observed in the transmembrane and cytoplasmic tail regions (Figure 1.3).

```
CVS-11      MVPQVLLFVP LLGFSLCFGK FPIYTIPDKL GPWSPIDIHH LSCPNNLVVE
SAD B19     ....A..... ..V.P..... .......... .......... ..........
CVS-11      DEGCTNLSEF SYMELKVGYI SAIKVNGFTC TGVVTEAETY TNFVGYVTTT
SAD B19     ........G. .......... L......... .......... ..........
CVS-11      FKRKHFRPTP DACRAAYNWK MAGDPRYEES LHNPYPDYHW LRTVRTTKES
SAD B19     .......... .......... .......... ........R. ....K.....
CVS-11      LIIISPSVTD LDPYDKSLHS RVFPGGKCSG ITVSSTYCST NHDYTIWMPE
SAD B19     .V......A. .....R.... ....S..... VA........ ..........
CVS-11      NPRPRTPCDI FTNSRGKRAS KGNKTCGFVD ERGLYKSLKG ACRLKLCGVL
SAD B19     ...LGMS... .......... ..SE...... .......... ..K.......
CVS-11      GLRLMDGTWV AMQTSDETKW CPPDQLVNLH DFRSDEIEHL VVEELVKKRE
SAD B19     .......... S....N.... ....K..... .......... ......R...
CVS-11      ECLDALESIM TTKSVSFRRL SHLRKLVPGF GKAYTIFNKT LMEADAHYKS
SAD B19     .......... .......... .......... .......... ..........
CVS-11      VRTWNEIIPS KGCLKVGGRC HPHVNGVFFN GIILGPDGHV LIPEMQSSLL
SAD B19     .......L.. ....R..... .......... ........N. ..........
CVS-11      QQHMELLKSS VIPLMHPLAD PSTVFKEGDE AEDFVEVHLP DVYKQISGVD
SAD B19     .......E.. ....V..... ......D... .......... ..HN.V....
CVS-11      LGLPNWGKYV LMTAGAMIGL VLIFSLMTWC RRANRPESKQ RSFGGTGRNV
SAD B19     .......... .LS...LTA. M..IF...C. ..V..S.PT. HNLR....E.
CVS-11      SVTSQSGKVI PSWESYKSGG EIRL
SAD B19     ...P....I. S....H.... .T..
```

Figure 1.3 Primary amino acid sequence comparison between CVS and SAD glycoproteins. The signal sequence is highlighted in red, transmembrane sequence in light grey and the cytoplasmic tail in dark grey. Both glycoproteins are 524 amino acids long that mature into 505 amino acid protein after N-terminal signal peptide cleavage. There is an overall 89% sequence identity and most variations are in the transmembrane and intracellular domains.

1.3 RABV genetics and lifecycle

Similar to other Rhabdoviruses, RABV forms a ~200 nm by ~80 nm rigid bullet-like virion (Figure 1.4) and this bullet-like shape is regulated by the matrix protein (RABV-M) (Ge et al., 2010). The virion is enveloped with a host-derived membrane that is studded with RABV-G trimers (Whitt et al., 1991). As with other Rhabdoviruses, RABV has a single non-segmented negative-sense RNA genome of ~12 kb length that is encapsulated by the nucleoprotein (RABV-N) to form the genetic core of the ribonucleocapsid (RNP) (Albertini et al., 2006). The RNPs are helical and are complexed to the phosphoprotein (RABV-P) and the RNA-dependent RNA polymerase (RABV-L) as mammalian cells cannot naturally transcribe negative sense RNA (Harmon et al., 1985). The helical RNP protects the RNA genome from RNases and

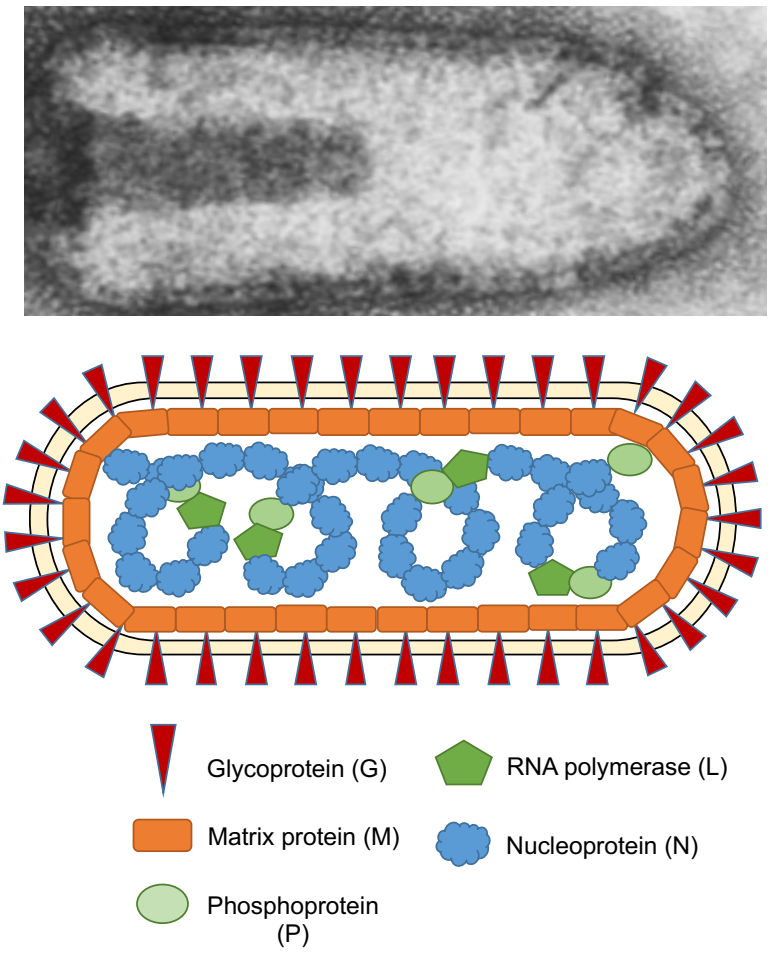

Figure 1.4 Rabies virus under an electron microscope and its constitutive proteins. RABV is bullet-shaped (above) as seen by Dr Sean Whelan's electron microscope (image taken with permission). Rabies has just five proteins: a coat glycoprotein (G), a bridging matrix protein (M), an RNA polymerase (L), a helper phosphoprotein (P) and a genome-protecting nucleoprotein (N).

facilitates viral transcription and replication (Figure 1.4). RABV-P forms homotrimers when phosphorylated (Chenik et al., 1998) with known functions including protection from host innate immune responses through its binding to phosphorylated-STAT1, binding RABV-N to prevent its non-specific binding to non-genomic RNA, formation of the non-catalytic subunit of the RNA polymerase and linking RABV-L with the RNPs (Fisher et al., 2018).

Between the RNP and the RABV-G-studded virion membrane is RABV-M that bridges the two complexes via binding the cytoplasmic tail of RABV-G and grooves between N-RNA helical protrusions of the RNP complexes (Graham et al., 2008; Riedel et al., 2019). The RABV-G trimers or ‘spikes’ as observed through electron microscopy (Gaudin et al., 1992) protrude outside the virion membrane and facilitate the binding and transport of RABV.

Despite encoding just five proteins (Figure 1.5) RABV can infect almost all warm-blooded mammals, is neurotropic, and causes a fatal neurological disease. Most RABV infections start when a rabid animal infects a susceptible host through bites or scratches at peripheral muscles and surrounding tissue, where RABV replicates slowly until its budding virions reach innervating motor or sensory neurons (Leung et al., 2007). Despite its replication at the wound site, RABV cannot be detected immediately after exposure and this has been attributed to its immune-evasion capability (Fisher et al., 2018). RABV then travels through the neuromuscular junction (8 mm/day, Gluska et al., 2014) in a retrograde axonal fashion towards the CNS. Once inside the CNS, RABV displays a strict synaptic, neuron-to-neuron-only spread and does not infect surrounding astrocytes or microglia (Davis et al., 2015) providing stealth (Schnell et al., 2010). RABV virions then travel through a reverse anterograde pathway from the CNS to other host organs including the salivary glands and hair follicles. RABV also reaches the heart and adrenal glands, eventually killing the host through respiratory and/or cardiac failure (Davis et al., 2015).

1.3.1 Host entry receptors

RABV spreads through contact between infected saliva and broken skin. From the wound site, RABV virions migrate through the extracellular matrix (ECM) towards susceptible cells through the interaction of RABV-G with one of several cell surface receptors. One of the first identified entry receptors was

nicotinic acetylcholine receptor (nAChR) (Lentz et al., 1982). nAChR α1 subunit is expressed in muscle cells (Fertuck and Salpeter, 1974) and it is enriched at postsynaptic membranes at the muscle end of the neuromuscular junction (NMJ) (Burrage et al., 1985). Following entry and replication, RABV virions bud off through NMJ synapses to motor neurons, establishing their second stage of retrograde neuronal spread. The binding of RABV-G to nAChR is well-defined. Specifically, the neurotoxin-like region of the RABV-G ectodomain (amino acid positions 190-203) binds to nAChR α1 at positions 173-204 (Lentz et al., 1987). Despite the validation of this interaction *in vitro* (Gastka et al., 1996) and in primary neuronal cells (Castellanos et al., 1997), the role of nAChR in RABV infection post-entry is not well understood. Since NMJs represent the main entry site for the CNS (as opposed to the blood brain barrier) and nAChRs are enriched at the muscle end of NMJ synapses, it is reasoned that nAChR enriches RABV virion-budding at the muscle end of the NMJ (Lewis et al., 2000).

Another major entry receptor is neuronal cell adhesion molecule (NCAM) or CD56. This glycophosphatidylinositol (GPI)-anchored glycoprotein is ubiquitously present on astrocytes, neurons and non-myelinating Schwann cells. It is a cell adhesion factor that is involved in regulating developmental processes (neurite outgrown, cell migration and synaptic plasticity) and in the maintenance of synaptic function at NMJs following injury (Paratcha et al., 2003). In addition to its adhesive regulatory role, it also acts as a signaling receptor for glial-derived neurotrophic factor. Researchers investigated its role in RABV infection and after infecting both NCAM positive and NCAM negative cells *in vitro*, NCAM-negative cells were less susceptible to RABV infection (Thoulouze et al., 1998). It was also observed that blocking NCAM with specific antibodies and/or heparin reduced the susceptibility of cells to infection. The same authors assessed this role *in vivo* in NCAM deficient mice and observed similarly slower rates of RABV infection. It was also reported that following RABV infection, NCAM deficient mice survive RABV infection for 4 days longer than wild type mice (Thoulouze et al., 1998). They concluded that NCAM is a key determinant of RABV pathogenesis, but it is not completely required to mediate RABV infection and spread. It remains unclear whether NCAM deficiency or the physiological changes in NMJs limit RABV

infection, as NCAM-knockout mice display smaller NMJs and slower rates of synaptic recovery.

A third entry factor is p75 neurotrophin receptor ($p75^{NTR}$) also named low-affinity receptor for nerve growth factor (NGF). This protein is a member of the tumour necrosis factor receptor superfamily and it is mainly involved in neuronal survival, cell death, synaptic transmission and axonal elongation. It has been linked to many neurodegenerative diseases, including epilepsy, Alzheimer's disease and axotomy (Dechant and Barde, 2002). Initial evidence of its association with RABV was in 2002 when Langevin and colleagues showed that $p75^{NTR}$ interacts with the soluble form of RABV-G, confirmed through co-immunoprecipitation experiments. CRD1 is a subunit of $p75^{NTR}$ and binds with high affinity (Kd ~ 30 pM) to trimeric RABV-G (Langevin and Tuffereau, 2002) further supporting a role of $p75^{NTR}$ during RABV infection. However, in *vivo* evidence that supports the claim that $p75^{NTR}$ is RABV entry receptor is lacking, as mice lacking $p75^{NTR}$ develop severe CNS abnormalities. Lee et al. created knockout mice for $p75NTR^{exon\ III}$ which still express the CRD1 subunit that binds with high affinity to RABV-G. In these studies however, no significant difference in RABV infection between $p75NTR^{exon\ III}$ knockout and wild type mice were observed (Lee et al., 1992).

Bu's group performed global siRNA knockdowns to screen the entry of an attenuated RABV strain ERA, mutated to encode green fluorescent protein (GFP) in HEK293T cells. This virus is mostly apathogenic and after targeting 21,585 human mRNAs, metabotropic glutamate receptor subtype 2 (mGluR2) was identified as an entry receptor (Wang et al., 2018). They validated their findings using anti-mGluR2 antibodies to block RABV infection *in vitro*. They further showed that the soluble ectodomain of mGluR2 neutralises RABV infection *in vivo*. Another target of the screen was AP2-associated kinase 1 (AAK1), a serine threonine kinase that phosphorylates and regulates AP2M1. Using anti-AAK1 antibodies, they showed that when AP2M1 phosphorylation was abrogated, mice challenged with RABV had prolonged survival times (Wang et al., 2019). Their third identified target was integrin β1, the overexpression of which correlated with higher infection rates (Shuai et al., 2019). As soluble integrin β1 neutralizes RABV infection and integrin β1

interacts with nAChR, this provided further insight into the mechanisms of RABV attachment and entry.

1.3.2 Lipid rafts and RABV entry

Lipid based components of the plasma membrane (PM) have been reported to interact with RABV-G and are involved in RABV attachment and entry. Lipid raft localised gangliosides, phospholipids and/or glycolipids have been shown to play a role in RABV infection of fibroblasts (Wunner et al., 1984) where neuraminidase treatment decreased RABV infection, with overexpression of the gangliosides GT1b and GQ1b restoring infection in neuraminidase-treated cells (Superti et al., 1986). Gangliosides are overexpressed in neuronal tissues (Ledeen and Wu, 2018) which may explain the neurotropism of pathogenic RABV.

Many of the identified host entry receptors localise at lipid rafts. The major RABV entry receptor nAChR forms large clusters in lipid raft domains in the CNS (Brusés et al., 2001) and the GPI-anchored NCAM is present in lipid raft microdomains. Variants of NCAM-140 and -180 associate with lipid rafts through palmitoylation (Maness, 2003). $P75^{NTR}$ was found to interact with rafts associated with caveolin (Huang et al., 1999) further highlighting the importance of these microdomains during RABV pathogenesis.

Pharmaceutical perturbation of lipid rafts has produced conflicting results on RABV infection. On one hand, the caveolae mediated endocytosis inhibitors (CavME) nystatin and filipin had minimal effect on virus entry (Table 1.2), whilst cholesterol depletion by methyl beta cyclodextrin (MβCD) led to 95% inhibition of RABV strain SAD-B19 (SRV_9 variant) in epithelial Vero cells (Xu et al., 2015) and 40% entry inhibition of RABV strain CVS-11 in neuronal N2a cells (Gao et al., 2019). Others rather unexpectedly showed that MβCD treatment quadrupled the infection rate of CVS-11 and doubled the levels of RABV adsorption to infected cells (Hotta et al., 2009). These data are summarised in Table 1.2.

1.3.3 Entry and internalisation

RABV internalisation is mediated by endocytosis, as endocytic restrictive temperatures of 4°C inhibit more than 98% of RABV entry (Xu et al., 2015). As with other Rhabdoviruses, RABV-G is a key mediator of RABV endocytosis and subsequent low pH-dependent fusion (Gaudin, 2000; Roche and Gaudin, 2004). Following interaction between RABV-G and host attachment factors, RABV virions internalise through adsorptive endocytosis (Superti et al., 1984). The clustering of RABV-bound entry receptors activates downstream intracellular processes where early electron microscopy studies showed that RABV internalises through coated pits in chicken embryo cells (Superti et al., 1984) and primary hippocampal neurons (Lewis and Lentz, 1998).

It was then revealed that RABV internalises primarily through clathrin mediated endocytosis (CME) in non-neuronal cells (Piccinotti et al., 2013; Xu et al., 2015) and in primary neuronal tissues (Piccinotti and Whelan, 2016). Rhabdoviruses such as vesicular stomatitis virus (VSV) and Australian bat lyssavirus internalise in a similar manner (Sun et al., 2005; Weir et al., 2014). The requirement for pH-dependent fusion was also validated during RABV entry though using the endosome acidification inhibitors bafilomycin and NH_4Cl that inhibited more than 80% of RABV entry in a range of cell lines (Piccinotti et al., 2013; Piccinotti and Whelan, 2016; Gao et al., 2019). CME was validated as an RABV entry route through the disruption of dynamin and clathrin sequestering drugs such as hypertonic sucrose and chlorpromazine, where more than 80% of RABV entry was inhibited (Table 1.2). Non-clathrin based endocytic processes were also investigated. Macropinocytosis inhibitor EIPA had no significant effect on RABV entry in epithelial cells (Piccinotti et al., 2013) but interestingly led to a 50% reduction in RABV entry in neuronal cells (Piccinotti and Whelan, 2016). These data (summarised in Table 1.2) suggest that RABV entry into epithelial cells is almost exclusively CME-dependent as opposed to RABV entry into neuronal cells that appears to use a multitude of endocytic routes. Further studies are required to fully characterize these differences in RABV-susceptible cells.

Table 1.2 Selected range of drugs used to assess RABV entry and internalisation

Drug	Conc.	Effect	RABV entry	RABV strain	Cell line	Source
4°C	-	Endocytosis inhibition	98% inhibition	SRV_9	Vero cells	Xu et al., 2015
Dynasore	100 μM	Dynamin inhibitor	80% inhibition	rVSV SAD-G	BS-C-1 (kidney epithelial cells)	Piccinotti et al., 2013
	10 μM		90% inhibition	SRV_9	Vero cells	Xu et al., 2015
	150 μM		95% inhibition	rVSV CVS-G	DRG primary neurons	Piccinotti and Whelan 2016
	100 μM		60% inhibition	CVS-11	N2a	Gao et al., 2019
EIPA	25 μM	Macropinocytosis inhibitor	No effect	rVSV SAD-G	BS-C-1	Piccinotti et al., 2013
			50% inhibition	rVSV CVS-G	DRG primary neurons	Piccinotti and Whelan 2016
Bafilomycin	0.1 μM	Endosome acidification inhibitor	99% inhibition	rVSV SAD-G	BS-C-1	Piccinotti et al., 2013
	1 μM		87% inhibition	rVSV CVS-G	DRG primary neurons	Piccinotti and Whelan 2016
	40 nM		70% inhibition	CVS-11	N2a	Gao et al., 2019
NH_4Cl	10 mM	Endosome acidification inhibitor	98% inhibition	CVS-11	BHK-21	Hatta et al., 2009
	20 mM		60% inhibition		N2a	Gao et al., 2019
Latrunculin B	1 μM	Actin polymerisation inhibitor	62% inhibition	rVSV SAD-G	BS-C-1	Piccinotti et al., 2013
Cytochalasin B	20 μM	Actin polymerisation inhibitor	97% inhibition	SRV_9	Vero cells	Xu et al., 2015
Sucrose	200 mM (hypertonic conc.)	Dissociates clathrin vesicles from PM (CME inhibitor)	99% inhibition	SRV_9	Vero cells	Xu et al., 2015

Chlorpromazine	10 μg/mL	Blocking assembly of clathrin-coated pits (CME inhibitor)	95% inhibition	SRV_9	Vero cells	Xu et al., 2015
	70 μM		40% inhibition	CVS-11	N2a	Gao et al., 2019
MβCD	10 mM	Cholesterol depletion	95% inhibition	SRV_9	Vero cells	Xu et al., 2015
			200% cell-surface adsorption	CVS-11	BHK-21	Hatta et al., 2009
	5 mM		40% inhibition		N2a	Gao et al., 2019
Nystatin	100 μM	CavME inhibitor	25% inhibition	SRV_9	Vero cells	Xu et al., 2015
	200 μg/mL		No effect	CVS-11	N2a	Gao et al., 2019
Filipin	10 μg/mL	CavME inhibitor	2% inhibition	SRV_9	Vero cells	Xu et al., 2015
Nocodazole	60 μM	Microtubule polymerisation inhibitor	80% inhibition of intracellular movement	SRV_9	Vero cells	Xu et al., 2015
	20 μM		Increased virus titles 8 folds	CVS-11	N2a	Zan et al., 2017
Taxol	10 μM	Microtubule depolymerisation inhibitor	90% reduction of virus titres	CVS-11	N2a	Zan et al., 2017

1.3.4 Intracellular trafficking

Upon cell penetration, RABV movement is actin dependent, since treatment with the actin-polymerising drugs latrunculin B and cytochalasin B could inhibit RABV entry (Piccinotti et al., 2013). Following membrane attachment, AP-2 and actin-regulated proteins are recruited (Guo et al., 2019) and RABV virions move rapidly into Rab5/EEA1 positive early endosomes (Semerdjieva et al., 2008) within 10 minutes of endocytosis (Albertini et al., 2012).

In epithelial cells, early endosomes carrying RABV travel along microtubules directly to the microtubule-associated retrograde motor dynein. This microtubule movement was validated through pharmaceutical treatment with the microtubule polymerisation inhibitor nocodazole, where more than 80% of intracellular movement was inhibited (Xu et al., 2015). Colchicine and vincristine, also microtubule inhibitors, showed similar inhibitory effects *in vivo* (Tsiang, 1979; Ceccaldi et al., 1989).

In neurons, RABV has been shown to hijack synaptic vesicle recycling pathways (De Camilli and Takei, 1996; Lewis and Lentz, 1998). The entry receptor $p75^{NTR}$ is predominantly present at presynaptic locations of the CNS (Lafon, 2005) and upon NGF binding, its internalisation switches from CME-independent to CME dependent endocytosis (Deinhardt et al., 2007). Live cell imaging showed that RABV hijacks this fast NGF CME dependent endocytosis, enhancing its rate of transport upon entry (Gluska et al., 2014) with a higher velocity and fewer stops en route. $p75^{NTR}$ is not essential for RABV pathogenesis as Tuffereau and colleagues showed no significant differences in the *in vivo* mortality rates of neuronal infection and specificity of infection between wild type mice and mice lacking $p75^{NTR}$ (Tuffereau et al., 2007), adding to the multi-faceted nature of RABV infection. It is generally thought that other neuronal entry receptors such as NCAM or other unidentified receptors facilitate RABV entry and axonal retrograde trafficking in a similar manner (Gluska et al., 2014; Guo et al., 2019).

Following internalisation and trafficking towards EEs, the mildly acidic endosomal environment triggers conformational changes in RABV-G that facilitate fusion of the viral and endosomal membranes, resulting in virus uncoating and RNP release (Gaudin et al., 1993). Details of these RABV-G conformational changes are discussed in section 1.4.

1.3.5 Transcription and replication

Much of our understanding of RABV transcription and replication is based on the related model Rhabdovirus, VSV (Albertini et al., 2011) due to its non-pathogenic nature in humans and lower biosafety handling requirement. RABV differs from VSV by having a slower rate of transcription and replication, releasing progeny virions at 24 h post-infection as opposed to the release of

VSV virions after just 4 h (Hummeler et al., 1967). It is also significantly less cytotoxic; VSV leads to cell death within 12 h while RABV causes no cell cytotoxicity for several days to weeks (Matsumoto, 1974; Marcus and Sekellick, 1975) thought to be a key feature of RABV pathogenesis (Schnell et al., 2010).

Following RABV-G-mediated fusion and release, the helical and condensed RNP core expands and unwinds, revealing the RNA genome. Then, RABV-L together with the helper RABV-P transcribe the RNA genome from the 3' leader sequence, which is well-conserved between Rhabdoviruses and acts as the genomic transcription initiation signal (Figure 1.5). This is followed by sequential transcription of the five structural proteins. Transcription stops when the polymerase complex reaches the 5' trailer sequence that contains the genomic termination signal (Schnell et al., 2010).

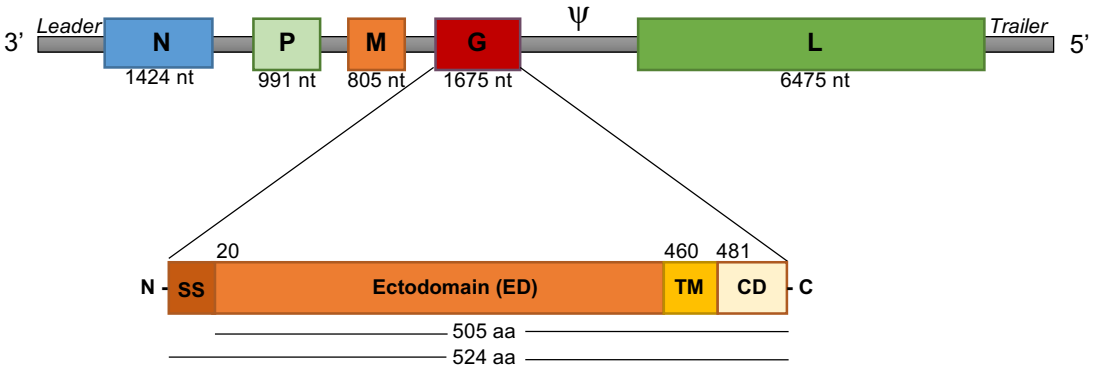

Figure 1.5 RABV genome organisation and RABV-G. RABV has a 12 kb genome encoding just five structural proteins. The genome is organised as 3'-N-P-M-G-L-5' with a gradient transcription rate. N has the highest expression levels and L has the lowest expression levels. The 3' leader sequence contains the genomic transcription initiation signal and 5' trailer sequence contains the genomic transcription termination signal. N is 450 amino acids long nucleoprotein that enwraps the fragile RNA genome. P is a 297 amino acids long phosphoprotein that functions as the helper protein that stabilises RNP and prevents antiviral response. M is a 202 amino acids long matrix protein that regulates RABV structure. G is a 524 amino acids glycoprotein that is cleaved to become a 504 amino acids protein to function as the envelope protein of RABV. L is a 2127 RNA-directed RNA polymerase that catalyses the transcription of RABV mRNAs.

In total, six mRNA transcripts are transcribed including a 58-nt 3′ leader sequence and mRNA encoding the five structural proteins. The leader sequence is rich in U and A nucleotides, making transcription relatively simple due to the lower hydrogen bonding between U-A pairs. This mRNA sequence is uniquely unpolyadenylated and uncapped binding almost exclusively to RABV-N, which itself has 10 times higher affinity to the leader sequence than any other viral mRNA (Yang et al., 1999) to facilitate its function of encapsulating RABV-N and regulating the switch between transcription and replication (Schnell et al., 2010). The five structural proteins are all polyadenylated and capped, making them virtually identical to mammalian mRNAs, aiding the subversion of host pathogen recognition.

The region between RABV genes, the intergenomic region, contains the initiation (promotor) and termination sequences for each mRNA. Termination sequences are conserved and contain a polyadenylation sequence of guanosine followed by seven uridine residues (Barr et al., 2002). Disrupting this multi-uridine polyadenylation sequence results in non-functional polycistronic viral mRNA transcripts (Barr et al., 1997). RABV viral mRNAs are monocistronic as the transcription stop-start model suggests that RABV-L transcribes RABV genes after reading the upstream intergenomic promoter sequence and stops transcription after reaching the downstream terminator sequence (Albertini et al., 2011). After reaching the downstream gene promotor sequence, a transcription-restarting mechanism is on occasion initiated, contributing to a relatively unique transcription phenomenon, namely a sequential transcription gradient.

This sequential transcription follows a high-to-low gradient: N has the highest expression levels and L has the lowest expression levels due to the restrictive initiation and termination transcription signals between genes within the intergenomic regions. The intergenomic initiation and termination transcription signals are longer than those of the VSV transcription signals and are thus weaker (lower rate of transcripts/time) due to the RNA polymerase RABV-L requiring a longer walking distance. This in turn attenuates downstream gene transcription after each initiation/termination transcription of the five proteins (Albertini et al., 2011). This initiation/termination transcriptional attenuation

was validated by genetic substitution of the N/P intergenomic region with the three other intergenomic regions (see Figure 1.5). P/M substitution results in 22% transcriptional reduction, M/G substitution results in 19% transcriptional reduction and G/L substitution results in 81% transcriptional reduction (Finke et al., 2000). This explains why RABV-L has low expression levels as when the G/L intergenomic region is replaced with N/P intergenomic region, RABV-L gene expression increases five-fold, resulting in a significant increase of RABV transcription and replication, ultimately leading to cell death, with a phenotype similar the relatively apathogenic VSV. It is thus inferred that the transcriptional regulation of RABV is mostly encoded within its intergenomic regions and this is a major reason behind its relatively slow rates of infection.

The matrix protein M also regulates transcription (Finke and Conzelmann, 2005). Mutating a single amino acid residue R58G in RABV-M leads to 15-fold higher transcription rates than wild-type RABV, leading to cytopathic effects *in vitro* (Finke and Conzelmann, 2003). Biotechnology applications and vaccine-development programs have used RABV ΔM viruses as a replication-deficient potent vaccine (Cenna et al., 2009). RABV ΔG is used extensively as a single-cycle neurotrancing tool (Wickersham et al., 2010), RABV ΔP is used as live vaccine (Cenna et al., 2008) and RABV ΔL allowed the identification of residues responsible for efficient polymerase complex (RABV-L + RABV-P) activity (Nakagawa et al., 2017) and a long term non-toxic RABV tool for neurotracing (Chatterjee et al., 2018).

RABV-M also supports the switch from transcription to replication (Finke et al., 2003). This switching is postulated to occur when sufficient RABV-N proteins are synthesised and are present around the genome. Full length anti-genomes are transcribed instead of the several short functional mRNAs (Schnell et al., 2010). These nascent anti-genomes are immediately encapsulated with RABV-N and are used as template for progeny viral genomes that are also encapsulated by RABV-N (Albertini et al., 2011). RABV-N by itself has no selective binding of RABV RNA and binds to any nearby RNA. The presence of RABV-P and its binding to RABV-N regulates its interaction with viral RNA by promoting its selective binding to RABV genomes and antigenomes (Liu et al., 2004). This was further validated by

showing that RABV can incorporate foreign genes into its genome, such as HIV structural proteins, with a functional genetic capacity of 150% or 16 kb (McGettigan et al., 2003). This cloning capacity is a rare feature of viruses as McGettigan and colleagues showed that cloning RABV-G into HIV significantly lowered its replication rate. Rhabdoviruses such as RABV and VSV possess this rare cloning capacity (McKenna et al., 2003) which has been subsequently exploited in several biotechnology gene delivery applications.

Over time, RABV transcription and replication concentrates RABV proteins in inclusion bodies commonly known as Negri bodies (Negri, 1903). These cytoplasmic inclusion bodies are a unique diagnostic feature of RABV and related Lyssaviruses. Once formed, most RABV transcription and replication occurs within Negri bodies (Albertini et al., 2011). RNPs (RABV-N, RABV-P, RABV-L and RNA genome) are sufficient to form Negri body-like inclusions without the need for RABV-M or RABV-G (Finke et al., 2004). Up to one or two Negri body inclusions form per cell and contain Hsp70 and ubiquitinylated proteins (Lahaye et al., 2009). Negri body formation has been shown to be dependent on the innate immune response receptor, toll-like receptor 3 (TLR3) where mice lacking TLR3 show no Negri body inclusions and higher survival rates than wild type mice (Ménager et al., 2009).

1.3.6 Budding and release

Newly synthesised RNPs that have encapsulated genomic RNA are transported to the cell membrane through a yet unknown mechanism to associate with RABV-M and RABV-G. Once at the cell surface, the RNPs are engulfed by a lipid bilayer derived from the host cell plasma membrane during the budding process. Both RABV-M and RABV-G are membrane associated and RABV-M is localised beneath the PM to form a bridge between the RNPs and RABV-G (Albertini et al., 2011), forming the complete bullet-shaped RABV virion that buds from infected cells.

RABV-M is essential for RABV budding as RABV with a deleted M is localised at the PM and its virus titres are reduced by 500,000-fold (Mebatsion et al., 1999), making it almost non-infectious. This is in contrast to RABV-G where its deletion results in a 30-fold reduction of budding (Mebatsion et al., 1996).

Although RABV with deleted RABV-G still buds, it cannot spread *in vitro* (Mebatsion et al., 1996) or *in vivo* (Etessami et al., 2000). After the release of infectious virions, RABV spreads to nearby cells and preferentially infects neurons (Murphy, 1977). Arguably, the spreading capacity of RABV is the major determinant of RABV pathogenesis, a process solely mediated by RABV-G.

1.4 Rabies virus glycoprotein

Of the five RABV proteins, RABV-G is the most important in RABV pathogenesis and has several unique properties. It is a ~60 kDa transmembrane-embedded, ER synthesised, Golgi processed, acylated and palmitoylated protein. RABV-G is not present within RNPs and is independent of the RABV transcription and replication machinery (Morimoto et al., 2000). It is a multifunctional protein that exists as homotrimers (Gaudin et al., 1992) on virion surfaces.

This envelope protein is first transcribed in the cytoplasm by RABV-L as a capped and polyadenylated mRNA. Then, RABV-G mRNA migrates to the endoplasmic reticulum (ER) where it is co-translationally translated as a 524 amino acid precursor protein. As a type I transmembrane protein, it mimics the secretory pathway of host transmembrane proteins destined for the PM. The N terminal signal sequence of RABV-G is cleaved, leaving a functional form of 505 amino acids (Anilionis et al., 1982). Once localised at the PM (Figure 1.6), RABV-G aids RABV budding and release.

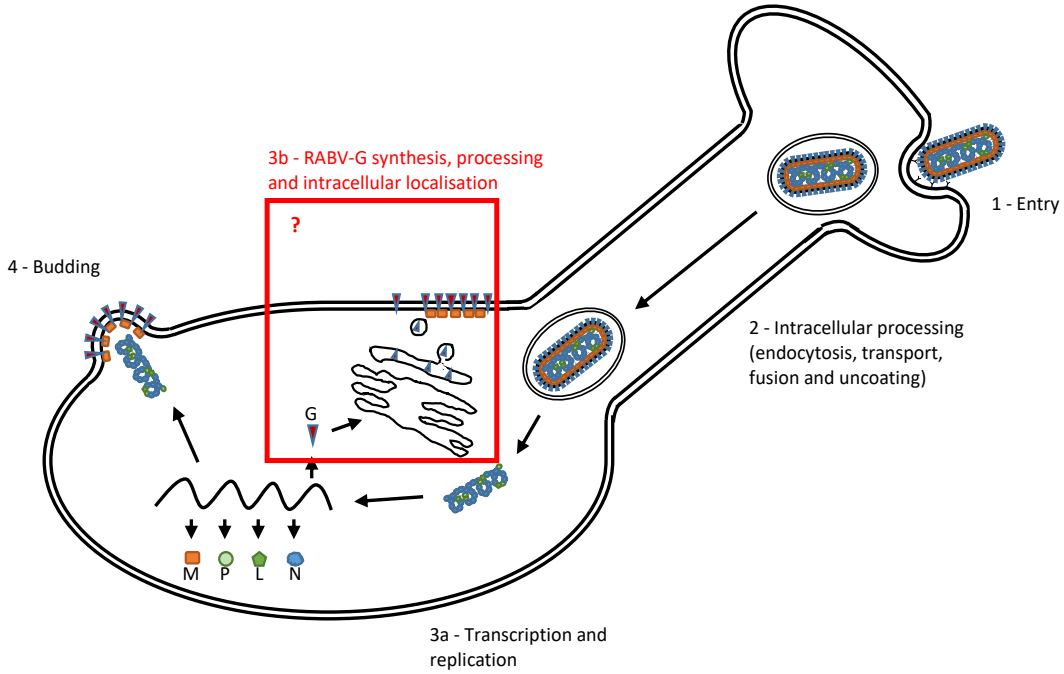

Figure 1.6 RABV lifecycle and intracellular RABV-G. RABV virions attach to and bind entry receptors. This is followed by fast retrograde transport towards the cytoplasm where pH changes lead to fusion between RABV-G and endosomal membranes. This is followed by uncoating and release of virion content where transcription occurs in the cytoplasm through the RABV-encoded RNA polymerase RABV-L. When RABV-G is transcribed, it is trafficked to Golgi apparatus and eventually the PM. RNPs associate with RABV-M to traffic towards PM regions rich with RABV-G where budding occurs and new RABV virions are released from intact infected cells.

As it is a transmembrane protein, RABV-G contains three distinct domains: (1) an ectodomain; (2) transmembrane domain; and (3) cytoplasmic domain. The ectodomain's folding environment is shared between the ER lumen and the extracellular environment. This 'modular' folding hypothesis is supported by work showing that chimeric glycoproteins with exchanged domains from other viruses are successfully expressed and transported to the PM (Gaudin et al., 1999).

1.4.1 RABV-G Ectodomain

The ectodomain is the largest portion of G, being 440 amino acids in length (459 with the signal sequence) or 87% of RABV-G (Figure 1.4). The ectodomain contains three major antigenic sites at positions (I) 231, (II) 34-42 and 198-200 and (III) 330-338. Most anti-RABV-G VNAs and non-neutralising antibodies recognise one or more of these sites (Lafon et al., 1983; Marissen

et al., 2005). The site of nAChR binding is 175-203 (Lentz, 1990) which overlaps with antigenic site II (Benmansour et al., 1991). Residues 330 and 333 are lysine/arginine rich and govern the interaction of RABV-G with $p75^{NTR}$ (Tuffereau et al., 1998) within antigenic site III.

Reverse genetic studies in RABV (Schnell et al., 1994) have led to the extensive characterisation of R_{333} in RABV-G (Seif et al., 1985). Seif and colleagues showed that whilst K_{330}, D_{336} and I_{338} of antigenic site III are targeted by VNAs, only mutations at R_{333} altered the pathogenicity of RABV. This phenotype was further exploited to create apathogenic SAD and ERA strains that are apathogenic after peripheral intramuscular injection (im), and pathogenic after intracranial injection (ic) (Tuffereau et al., 1989). However, R333Q mutations are unstable with reversions common following serial passage in newborn mice (Tao et al., 2010). Compensatory mutations are also common in R333Q mutant viruses, with an N194K mutation commonly observed (Faber et al., 2005).

Other residues directly involved in pathogenesis are D_{255} (Luo, Zhang, Lyu, et al., 2020) and G_{349} (Luo, Zhang, Wu, et al., 2020). Mutation of both residues were investigated by Guo and colleagues in the Chinese pig strain GD-SH-01 where D255G caused GD-SH-01 to become apathogenic following ic administration, with G349Q showed similar results (Luo, Zhang, Wu, et al., 2020).

RABV-G dictates neurotropism, highlighted by the peripheral infection of equine infectious anaemia virus (EIAV) pseudotyped with RABV-G that invades the CNS, whilst EIAV pseudotyped with VSV-G has no CNS invasion capacity (Mazarakis et al., 2001). Intracranial infection of RABV ΔG fails to spread beyond the inoculation site (Etessami et al., 2000). It has also been shown that the non-neuroinvasive strain SN-10 became neuroinvasive when its G is replaced with Gs from neuroinvasive and pathogenic strains CVS-N2c or SHBRV-18 (Morimoto et al., 2000). Similarly, the attenuated strain SAD-B19 (non-pathogenic after peripheral infection) becomes pathogenic when its G is replaced with G from the highly pathogenic strain CVS, even though mice infected with the recombinant virus died four days later than mice infected with

wild type CVS (Finke and Conzelmann, 2005). These studies indicate that RABV-G is the dominant determinant of RABV neuroinvasiveness.

The neuroinvasiveness of RABV-G has been linked to 11 residues within the nAChR-binding region (175-203) (Hueffer et al., 2017) that are mostly homologous to HIV GP120, cobratoxin and bungarotoxin (McLane et al., 1991):

RABV-G	CDIFTNSRGKR (189-199)
HIV gpl20	CDAFCSIRGKR (164-174)
Cobratoxin	FNISTSIRGKV (30-40)
Bungarotoxin	CDAFCSSRGKV (30-40)
k-Bungarotoxin	CDKFCSIRGPV (30-40)

Bungarotoxin and other neurotoxins are strong inhibitors of nAChR (Dutertre et al., 2017). Caspian cobratoxin also reduces up to 80% of CVS infection *in vitro* (Farzad et al., 2020). Injection of just the 175-203 region of RABV-G as a peptide into mice makes them hyperactive, a signature behavioural change following rabies infection that has been linked to nAChR binding (Hueffer et al., 2017).

RABV-G is structurally influenced by an acidic pH that leads to its transition into a fusion competent form (Roche and Gaudin, 2002) This pH-dependent structural rearrangement is reversible and RABV-G structurally shifts towards its native state upon egress from the Golgi apparatus during its synthesis (Gaudin et al., 1995). Two hydrophobic fusion loops exist at positions 73-79 and 117-125 that become exposed under low pH conditions. The first crystal structure of the RABV-G ectodomain was solved upon the replacement of these fusion loops with GGSGG linker sequences (Figure 1.7) as without these linker replacements, the soluble RABV-G ectodomain forms aggregates that could not be crystallised (Yang et al., 2020).

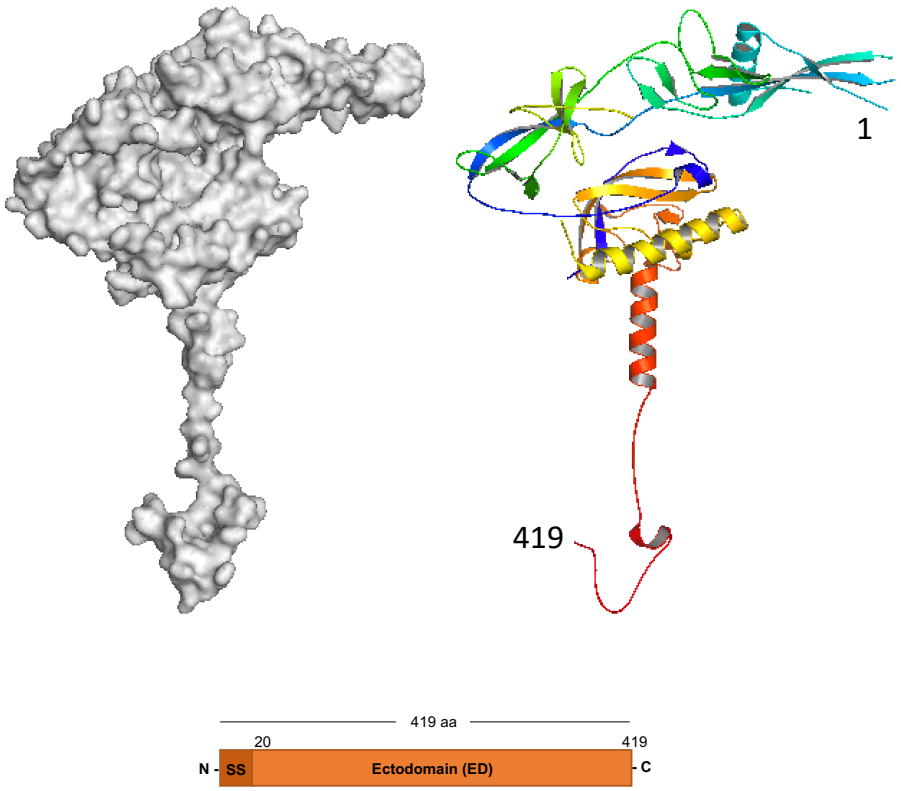

Figure 1.7 RABV-G crystal structure at pH 8.0. This structure was solved from the first 419 amino acids representing the ectodomain. Hydrophobic fusion loops at positions 73-79 and 117-125 are replaced with GGSGG inker sequences. RABV-G is monomeric in solution and trimeric at plasma membranes (PDB: 6LGX).

The ectodomain also governs the trimeric nature of RABV-G in the virion. Yang et al. structurally validated the putative 7 disulphide bridges of the 14 ectodomain cysteines (Gaudin, 1997) and demonstrated through gel filtration experiments that RABV-G is monomeric in solution. Previous electron microscopy studies showed that RABV-G forms trimers on surfaces (Gaudin et al., 1992) and to resolve these two observations, the authors crosslinked RABV-G at the cell surface and detected it as trimers using surface plasmon resonance (SPR). The related rhabdovirus VSV-G readily associates as homotrimers in low pH conditions (Baquero et al., 2017) with Yang et al. failing to observe the formation of RABV-G trimers in low pH conditions, although weak trimerisation did occur at pH 5.5 (Yang et al., 2020).

RABV-G is N-glycosylated at multiple sites with this common form of protein modification including the attachment of a mannose core to the amide nitrogen of asparagine (Asn) within the Asn-X-Ser/Thr motif (Vigerust and Shepherd, 2007). This protein modification occurs in the ER and after trafficking to the

Golgi, are trimmed into varying oligosaccharide structures that are essential for correct, RABV-G protein folding (Vigerust and Shepherd, 2007). For this reason, RABV-G cannot fold correctly in prokaryotic cells (Yelverton et al., 1983; McGarvey et al., 1995). RABV-G is N-glycosylated at N_{37} and N_{319} (Badrane and Tordo, 2001) and many tissue culture-adapted strains have additional glycosylation events at N_{158}, N_{204} or $N_{247,}$ predicted to influence glycoprotein stability (Yamada et al., 2012; Yamada et al., 2014).

1.4.2 RABV-G transmembrane domain

RABV-G contains a stretch of 22 hydrophobic amino acids from K_{439} (Y in some strains) to R_{462} (Anilionis et al., 1981) that form a single transmembrane domain. This was confirmed in studies showing that truncated RABV-G expressing only the first 439 residues (plus N terminal signal sequence) is soluble, monomeric and folds in a different conformation than native RABV-G (Maillard and Gaudin, 2002). Upon replacement of the transmembrane region with the pseudorabies glycoprotein transmembrane domain, the recombinant glycoprotein becomes trimeric and shares the antigenicity of RABV-G. It is worth noting that pseudorabies is a herpesvirus that is not related RABV and its envelope glycoprotein is not trimeric. This study suggests that the existence of a hydrophobic transmembrane domain is important for RABV-G trimerisation.

1.4.3 RABV-G cytoplasmic domain

The tail region of RABV-G is 44 amino acids long with the main functionality of binding to RABV-M (Schnell et al., 2010) to regulate virus assembly and budding (Mebatsion et al., 1999). Accordingly, deletion of the cytoplasmic tail reduces RABV budding by 6-fold (Mebatsion et al., 1996). Residue specificity of the cytoplasmic tail is essential for RABV-G pathogenesis, in contrast to VSV-G that retains its bovine pathogenicity with any sequence in the cytoplasmic domain (Schnell et al., 1998).

The C-termini of cell surface proteins typically contain motifs that dictate their trafficking (Bonifacino and Glick, 2004). Surprisingly, no sorting signals have been identified in the cytoplasmic domain of RABV-G, though it was shown that the introduction of a lysosomal targeting motif (GYEVM) to this region

shifted RABV-G expression from the PM and ER to the PM and lysosomes (Starodubova et al., 2017), indicating that native RABV-G does not enter a conventional lysosomal associated pathway.

Prehaud and colleagues showed that most RABV strains possess a C-terminal $ETRL_{COOH}$ motif that binds to PDZ containing proteins including MAST2 and PTPN4 (Préhaud et al., 2010). PTPN4 is an anti-apoptotic protein that is postulated to be targeted by RABV-G to maintain the survival of infected cells (Caillet-Saguy et al., 2016). The same group identified a E502Q point mutation in the ERA strain that does not bind PTPN4 and this loss of binding seems to enhance pathogenicity through the induction of extensive neurite outgrowth in RABV infected cells (Seo et al., 2017). These studies highlight the potential contribution of the RABV-G cytoplasmic tail to neurite outgrowth and pathogenicity.

The C-terminal tail region of RABV-G has also been linked to the surface levels of RABV-G. When SAD-G had its cytoplasmic domain replaced with that of SHBRV-G, the chimeric glycoprotein SAD-G_{SHBRVT} showed lower surface levels than SAD-G but higher surface levels than SHBRV-G (Morimoto et al., 2000), indicating that secretion efficiency or PM localisation of RABV-G is partially dependent on the RABV-G cytoplasmic domain.

1.4.4 Pathogenic contribution of RABV-G

Studies have created a range of RABV hybrids with gene replacement of RABV-G and/or RABV-M to determine RABV-G and -M binding and the involvement of each gene with virus pathogenicity (Table A1). Almost all gene-replacement studies concluded that RABV-G is the major determinant of pathogenicity, with other RABV genes showing a minor contribution to RABV pathogenesis. The first gene-replacement study was conducted six years after the RABV reverse genetics system was introduced (Schnell et al., 1994). The authors replaced SAD-G with CVS-G or the bat strain SHBRV-G. They observed that following CVS replacement, SAD-G_{CVS} becomes pathogenic after im injection whereas SHBRV-18 gene replacement does not make SAD pathogenic after im injection (Morimoto et al., 2000; Finke and Conzelmann, 2005).

Following the study by Morimoto et al., Ito and colleagues replicated this gene replacement study in Japanese strains by replacing the glycoprotein from the highly attenuated strain RC-HL's glycoprotein with that of pathogenic strain Nishigahara's glycoprotein, creating RC-HL-G_{NISHI} that is as pathogenic as Nishigahara in four out of five mice infected (Ito, Takayama, et al., 2001). They inoculated mice through the ic route as RC-HL is apathogenic through im or ic route of inoculation (in contrast, SAD is apathogenic through im and pathogenic through ic). They have also noted that RC-HL-G_{NISHI} chimera had a delayed onset of pathogenesis.

The apathogenic phenotype of SAD-G_{SHBRV} chimera is puzzling as it should, in theory, become pathogenic like SAD-G_{CVS} and RC-HL-G_{NISHI} chimeras. This was further investigated by Faber and colleagues (2004) where they replaced almost all genes of SAD with the corresponding genes from SHVRV-18 (Table A1). They found that RABV pathogenicity is shared between RABV genes and it is not confined in RABV-G, when they compared SAD to SHBRV-18. They observed that upon replacement of all SAD genes (except RABV-L and Ψ) with SHBRV-18 genes, 60% of SHBRV-18's pathogenicity was restored. Addition of Ψ from SHBRV-18 made the hybrid strain 90% pathogenic which is remarkable in the sense that this non-coding region influences 30% of the pathogenicity of RABV. Nevertheless, this effect was not replicable when comparing SAD to CVS or RC-HL to Nishigahara as almost 100% of RABV's pathogenicity was confined within their pathogenic RABV-G sequences.

Another group investigated the SAD-G_{SHBRV} hybrid at higher viral loads and observed that RABV-G contributes to 20% of pathogenicity (Pulmanausahakul et al., 2008). SAD-M_{SHBRV} was apathogenic and SAD-MG_{SHBRV} led to 40% of im infected mice to become fatally infected with RABV (Table A1). The 2008 study argued that RABV-M enhances pathogenicity though it does not confer pathogenicity alone. Enhanced RABV-G binding to RABV-M when they are from the same strain may explain this observation.

LEP-Flurry and its apathogenic variant HEP-Flurry have also been compared through gene substitutions, replacing the glutamine 333 found naturally in HEP with its pathogenic variant arginine (HEP-G_{Q333R}) made the virus hybrid pathogenic through ic but not through im even though HEP-Flurry is

pathogenic through both the ic and im routes of infection (Table A1). This is an interesting observation as it paints a picture of RABV pathogenesis, with partial pathogenic restoration making RABV pathogenic through ic and complete pathogenic restoration making RABV pathogenic through both ic and peripheral im routes of infection. Lastly, Marsten et al. (2013) replaced the SAD glycoprotein with EBLV 1 and 2 and saw both hybrids became apathogenic, almost replicating the pathogenic adaptation of SHBRV-18. It can therefore be assumed that genetic replacement between carnivore adapted RABV and bat adapted RABV does not restore the complete phenotype of RABV.

1.5 RABV host interactions

As with all virus infections, pathogenesis is dictated by the ability of viral proteins to modulate host cell processes to promote a cellular environment favourable for their survival. RABV is unusual in its ability to avoid immune detection until it is well established in the CNS, a time when it is too late to save the infected victim. Attenuated RABV strains are exposed to immune detection and induce VNA in infected hosts, leading to their clearance. RABV causes infected cells to develop filopodia-like projections in non-neuronal cells (Xu et al., 2015) and neurites in neurons (Préhaud et al., 2010; Seo et al., 2017), contributing to its immune-avoidance mechanism by forcing direct cell-to-cell spread. To develop antiviral therapies against RABV, it is essential to understand the host proteins that are directly or indirectly required for virus pathogenesis.

Several studies have attempted to characterise RABV pathogenesis through comparison of the host cell responses to pathogenic vs. attenuated RABV. Mice infected with the attenuated strain CVS-B2c display extensive inflammation throughout the CNS whereas mice infected with pathogenic strain SHBRV-18 display little to no inflammation (Wang et al., 2005). Microarray analysis revealed that CVS-B2c induces the upregulation of alpha/beta interferon (IFN-α/β) signalling and TLR signalling, all of which are absent in SHBRV-18 infected mice. Primary neurons infected with a pathogenic strain (CVS-N2c) have intact neuronal bodies but degenerated neurites (neuronal projections i.e. axons and dendrites) whilst neurons

infected with an attenuated strain (SAD-derived SN-10) display the opposite phenotype, causing apoptosis in neurons and intact neurites (Li et al., 2005). CVS-N2c-infected neurons show no recognisable axons or dendrites and show reduced expression of two neuronal markers MAP2 and NF-200. These are not downregulated in SN-10-infected neurons. Neurite degeneration in response to RABV has been shown to be related to F-actin depolymerisation (Song et al., 2013) and SARM1 activation (Sundaramoorthy et al., 2020). SARM1 (Sterile Alpha and TIR Motif-containing 1) is an inducer of axon degeneration through its ability to target NAD (nicotinamide adenine dinucleotide) and is activated when physical axonal damage occurs. CVS-N2c infection activates SARM1 and when NAD levels in axons fall below a certain threshold, a suicide signalling cascade is triggered (Essuman et al., 2017) causing neurite degeneration.

The neuronal proteomes of dogs infected with furious or paralytic rabies show differences in the expression of proteins involved in intracellular trafficking, cytoskeleton proteins, heat shock proteins and immune regulators (Thanomsridetchai et al., 2011). Notable differences include the upregulation of apoptosis-inducing annexin A2 and the downregulation of the motor protein myosin heavy chain 2 in paralytic rabies. RABV virions contain several scavenged proteins from infected host cells that represent potential interacting partners of RABV proteins. The most abundant protein identified in RABV virions (CVS strain) is CD9 (Y. Zhang et al., 2020) a cell adhesion protein involved in cell-to-cell fusion (Charrin et al., 2013). Dynein light chain (DLC8) was also shown to be abundant in RABV virions and it is known to interact with RABV-P (Raux et al., 2000). RABV virions of the attenuated strain SAD-derived SRV_9 shared ~ 25% of the proteins identified for CVS (Tu et al., 2015) but cell line differences between the studies (mouse neuronal-like cells (N2a)) vs (baby hamster kidney cells (BHK-21)) make direct comparisons of these datasets challenging. Few conserved proteins have been identified, including cofilin-1, subsequently shown to be required for efficient RABV budding (Zan et al., 2016).

Dhingra and colleagues compared the proteomes of mouse synaptic tissues infected with SHBRV-18 or CVS-B2c, identifying major changes in the

proteins that govern ion homeostasis (Dhingra et al., 2007). As expected, they also observed an upregulation of several innate immunity and apoptotic proteins following CVS-B2c infection that would lead to inflammation in the CNS. Wang and colleagues looked at the proteomes of a mouse neuronal-like cell line (N2a) and observed the upregulation of cytoskeleton proteins, signal transduction and metabolic proteins following pathogenic infection with wild type strain BD06 or CVS. An upregulation of splicing factors and stress proteins following SAD-derived SRV_9 infection was also observed (Wang et al., 2011). A similar study compared proteomes of N2a cells infected with CVS or Pasteur virus (PV) strain. Approximately 30% of PV-infected mice survived whereas CVS-infected mice almost all died (Majer et al., 1977). Upon analysis of the proteomic datasets, the authors observed changes in cytoskeletal, trafficking and stress-related proteins in both CVS and PV infected cells' proteomes, with CVS proteomes showing ~30% higher association with cytoskeletal proteins than the PV proteomes (Zandi et al., 2013).

1.5.1 RABV-G host interactions

RABV-G is solely responsible for the transport and neuroinvasiveness of RABV. Yin and colleagues produced a Flag-tagged RABV-G fusion to directly compare interactomes of CVS-G to SAD-G in primary neuronal cells, identifying 89 hits for CVS-G and 26 hits for SAD-G. Both G proteins shared 23 hits (Yin et al., 2020). Most of these interacting partners were proteins involved in intracellular trafficking (vesicle transport), followed by neuronal-specific proteins for CVS-G and actin-binding proteins for SAD-G. The authors further validated CVS-G as binding to a neuronal SNARE protein, SNAP25 and validated its effect on CVS by siRNA knockdown, finding that it might have a role in RABV budding and release.

1.6 Potential antiviral treatment

Rabies causes a high number of fatalities as current PEP treatment are either unavailable (Bourhy et al., 2009) or unaffordable (Chulasugandha et al., 2006) to most regions with endemic rabies. PEP treatment is not effective after the onset of clinical symptoms (Fooks et al., 2014). In addition, RABV PEP is not

100% effective against emerging phylogroup II lyssaviruses such as MOKV and Lagos bat viruses (Du Pont et al., 2019). These limitations can be potentially alleviated if effective RABV antiviral therapies are developed. Antivirals in general are shelf-stable and their production is easily scaled up, potentially replacing anti-RABV antibodies in PEP or current PEP treatment altogether.

One of the earliest rabies antivirals tested were the microtubule polymerisation inhibitors colchicine and vinblastine. These drugs prevent the transport of RABV if administered within 6-8 hrs of infection to mice (Bijlenga and Heaney, 1978). Once RABV passes through neuronal axons, fatal infection could not be prevented by this class of drugs. Approximately half of the mice treated with vinblastine at 0 hrs eventually develop fatal rabies one week later than untreated mice, indicating that colchicine and vinblastine interfere with RABV transport but do not effectively prevent RABV infection.

RABV entry is dynamin dependent (Table 1.2) and can be prevented by the dynamin inhibitor dynasore (Piccinotti and Whelan, 2016). After high-throughput screening, Wu and colleagues observed that a similar dynamin inhibitor 1-adamanthyl 5-bromo-2-methoxybenzyl amine (AMBA) protected ~50% of RABV challenged mice from fatal infection (Wu et al., 2017). Synthetic optimisation to improve efficacy was suggested but greater affinity for dynamin coincided with increased cytotoxicity as dynamin is an essential, ubiquitous cellular protein (Du Pont et al., 2019).

The multi-target tyrosine kinase inhibitor sorafenib curbs angiogenesis in cancer patients and it was repurposed to treat a variety of viruses as a broad-range antiviral, including Hepatitis C virus (HCV), chikungunya virus and enterovirus with varying efficacy (Gao et al., 2014; Descamps et al., 2015; Lundberg et al., 2018). When administered with IFN-β, sorafenib reduced RABV titres significantly (Marosi et al., 2019). Sorafenib is associated with several gastrointestinal complications in cancer patients (Rimola et al., 2018) as so is not deemed a preferable antiviral option.

Favipiravir is a direct acting nucleoside inhibitor that is currently licensed for influenza treatment in Japan (Goldhill et al., 2018) and is currently being repurposed for SARS-CoV-2 therapy (Cai et al., 2020). When used against

RABV *in vitro*, it decreased titres by 3-4 orders of magnitude. However, *in vivo* results showed that ~50% of the mice died and the other half developed limb paralysis, indicating viral circulation within the nervous system (Yamada et al., 2016). When combined with interferon therapy, favipiravir was less effective than ribavirin, sorafenib and infliximab, indicating that favipiravir is not an optimal antiviral agent against RABV (Marosi et al., 2019).

Emetine is a protein synthesis inhibitor that selectively inhibits RABV retrograde axonal transport (MacGibeny et al., 2018). The authors showed that other similar protein synthesis inhibitors cycloheximide or puromycin had no effect on RABV transport, indicating that this inhibition is not related to protein synthesis. They also showed that Rab5- or Rab7-positive vesicles in axons were not affected by emetine, suggesting it does not cause a global inhibition of axonal transport. The authors concluded that emetine acts directly on RABV to prevent motor recruitment to the abnormally large RABV-containing endosomes. Gluska and colleagues (2014) previously showed RABV retrograde movement is faster than NGF-positive vesicles and RABV hijacks this pathway for retrograde axonal transport (See 1.3.4).

Ranpirnase has antitumor and antiviral activity through its ability to inhibit ribonucleases. Smith and colleagues (2020) recently showed that ranpirnase inhibits RABV cell-to-cell spread and RABV release *in vitro*. *In vivo* however, ranpirnase had no effect on RABV spread from intramuscular infection routes (Smith et al., 2020). It appears that many antivirals effectively inhibit RABV *in vitro* but show at-most a partial effect *in vivo,* despite their efficacy against a range of viruses *in vivo.* A better understanding of RABV pathogenesis is paramount to effective antiviral therapy development.

1.7 Aims and Objectives

Pathogenic RABV can avoid immune detection whilst attenuated RABV is rapidly detected and cleared from infected hosts. As a key dictator of virus pathogenesis, this thesis compared RABV-G proteins from pathogenic and attenuated RABV strains to identify key host factors and cellular behaviours

that may contribute to the altered pathogenesis between these strains. RABV-G was selected as it is the key regulator of RABV pathogenesis.

Chapter 3 investigated if differences in the cellular localisation of RABV-G exists between pathogenic and attenuated RABV-G proteins. It was found that pathogenic RABV-G from CVS is primarily localised within intracellular puncta whereas attenuated RABV-G from SAD is primarily localised at the PM. These differences were subsequently found to be related to the internalisation rates of both proteins; CVS-G undergoes rapid endocytosis from the cell surface which is significantly slower for SAD-G. It was further shown that several residues in the cytoplasmic tail of CVS-G regulate this internalisation behaviour. This is the first identification of the internalisation of the RABV-G protein and implicates this cellular behaviour as a key phenotypic difference between CVS and SAD strains.

Chapter 4 involved the utilisation of the BioID system to screen differences in RABV-G host interactions between CVS-G and SAD-G. Several functional protein clusters were identified in actomyosin regulation, clathrin-mediated endocytosis, cilium assembly and Golgi-ER transport that were uniquely proximate to CVS-G and not SAD-G. Promising hits were validated to show that myosin IIA and its regulator Rho-kinase (ROCK) were involved in G-mediated filopodia outgrowth. CVS-G mediated filopodia could be selectively inhibited with the ROCK inhibitor Y-27632. BioID screening also revealed several potential host binding partners that selectively interact with CVS-G but not SAD-G, revealing a more detailed picture of CVS-G intracellular trafficking.

Chapter 5 investigated differences in the palmitoylation of CVS-G and SAD-G using site-directed mutagenesis. It was found that SAD-G has a dual palmitoylation event at C_{460} and C_{461} whereas CVS-G had single palmitoylation event at C_{461}. The phenotypic consequences of this altered palmitoylation were also investigated, revealing a critical contribution of palmitoylation to lipid raft association and cell surface expression.

Overall, this thesis expands on current understanding of RABV-G intracellular trafficking, the role of RABV-G during RABV lifecycle, and critical residues that differ between CVS-G and SAD-G that dictate their interaction with cells.

Chapter 2 | Materials and Methods

2.1 Chemicals

Unless otherwise stated, chemicals were obtained from Sigma-Aldrich (Sigma), Antibodies were obtained from Abcam, restriction enzymes were obtained from New England Biolabs (NEB) and miscellaneous reagents were obtained from ThermoFisher. Deionised water (dH_2O) was filtered through an ELGA PURELAB ultra machine and sterilisation was performed through autoclaving (121°C, 30 min, 15 psi) or filtration through 0.22 µm filters (Millipore). Key chemicals and reagents are shown in Tables 2.1 and A2.

Table 2.1 Key chemicals and reagents.

Reagent type (species)	Designation	Source	Identifier	Additional information
Strain (*Escherichia coli*)	NEB5α	NEB	Cat. #: C2987	
Strain (*Escherichia coli*)	dam^-/dcm^-	NEB	Cat. #: C2925	For methylated restriction sites
Enzyme	NotI-HF	NEB	Cat. #: R3189S	
Enzyme	EcoRI-HF	NEB	Cat. #: R3101S	
Enzyme	NheI-HF	NEB	Cat. #: R3131S	
Enzyme	XbaI	NEB	Cat. #: R0145S	Dam methylated
Enzyme	AfeI	NEB	Cat. #: R0652S	
Enzyme	BspEI	NEB	Cat. #: R0540S	
Recombinant DNA reagent	CVS-G-pCAGGS	This project	Accession #: ABV24348.1	Codon optimised

Recombinant DNA reagent	SAD-G-pCAGGS	This project	Accession #: P16288.1	Codon optimised
Recombinant DNA reagent	DOG-G-pCAGGS	Gift from Stefan Finke	Accession #: CUI02214.1	
Recombinant DNA reagent	EBLV-G-pCAGGS	Gift from Stefan Finke	Accession #: SMD54588.1	
Recombinant DNA reagent	CVS_{SADT}-pCAGGS	Gift from Stefan Finke	657 Finke lab	
Recombinant DNA reagent	$EBLV_{SADT}$-pCAGGS	Gift from Stefan Finke	660 Finke lab	
Recombinant DNA reagent	pcDNA3.1-empty	Gift from Joseph Ward	https://www.addgene.org/vector-database/2093/	
Recombinant DNA reagent	CVS-G-pcDNA3.1	This project		
Recombinant DNA reagent	SAD-G-pcDNA3.1	This project		
Recombinant DNA reagent	pcDNA3.1 mycBioID	Gift from Alex Coleman	https://www.addgene.org/35700/).	N terminal BirA* fusion site
Recombinant DNA reagent	pcDNA3.1 mycBioID-R118G	Gift from Alex Coleman		Inactive mutant
Recombinant DNA reagent	MCS-13X-linker-BioID2-HA	Roux lab	https://www.addgene.org/80899/	C terminal BirA* fusion site with glycine linker
Recombinant DNA reagent	mycBioID2-13X Linker-MCS	This project	https://www.addgene.org/92308/	N terminal BirA* fusion site with glycine linker
Cell line (*Homo sapiens*)	SVG-A	ATCC	Cat. #: CRL-8621	Large cytoplasm

Cell line (*Homo sapiens*)	HEK293T	ATCC	Cat. #: CRL-3216	High exogenous protein expression
Cell line (*Homo sapiens*)	SH-SY5Y	ECACC	Cat. #: 94030304	Neuroblast
Reagent (Cell culture)	Lipofectamine 2000	Thermo Fisher	Cat. #: 11668030	
Chemical compound, drug	PitStop2	Abcam	Cat. #: ab120687	DMSO, 30 μM working conc.
Chemical compound, drug	MβCD	Sigma	Cat. #: C4555	dH2O, 2 mM working conc.
Chemical compound, drug	EIPA	Sigma	Cat. #: A3085	DMSO, 25 μM working conc.
Antibody	Mouse anti-RABV-G (E559)	Gift from Stefan Finke		IF: 1:100
Antibody	Rabbit anti-RABV-G (P160)	Gift from Stefan Finke		WB: 1:250
Antibody	Mouse anti-GAPDH	Santa Cruz Biotechnology	Cat. #: sc-32233	WB: 1:2000
Antibody	Mouse anti-GAP43	Santa Cruz Biotechnology	Cat. #: sc-17790	IF: 1:200 WB: 1:500
Antibody	Rabbit anti-HA	Abcam	Cat. #: ab137838	IF: 1:200 WB: 1:2000
Antibody	Streptavidin-HRP	Thermo Fisher	Cat. #: N100	WB: 1:20000
Antibody	Streptavidin-594	Thermo Fisher	Cat. #: S11227	IF: 1:500
Antibody	Rabbit anti-Myosin IIA	Sigma	Cat. #: M8064	IF: 1:100 WB: 1:500
Antibody	Rabbit anti-ROCK1	Cambridge Bioscience	Cat. #: A300-457A	WB: 1:500

Antibody	Rabbit anti-COPA	GeneTex	Cat. #: GTX45827	WB: 1:200
Antibody	Rabbit anti-HSP90	Cell Signalling Technology	Cat. #: 4874S	WB: 1:200
Antibody	Mouse anti-β-actin	Abcam	Cat. #: ab3280	WB: 1:2000
Antibody	Rabbit anti-β-tubulin	Cell Signalling Technology	Cat. #: 2128S	IF: 1:100 WB: 1:500
Antibody	Rabbit anti-EEA1	Cell Signalling Technology	Cat. #: 2411S	IF: 1:200
Antibody	Rabbit anti-CD63	Cell Signalling Technology	Cat. #: 55051S	IF: 1:200
Antibody	Rabbit anti-Calnexin	Cell Signalling Technology	Cat. #: 2679S	IF: 1:250
Antibody	Rabbit anti-GM130	Cell Signalling Technology	Cat. #: 12480S	IF: 1:250
Antibody	Rabbit anti mouse HRP	Sigma	Cat. #: A9044	WB: 1:2000
Antibody	Goat anti rabbit HRP	Sigma	Cat. #: A0545	WB: 1:5000
Antibody	Alexa-Fluor chicken anti mouse 488	Thermo Fisher	Cat. #: A-21200	IF: 1:500
Antibody	Alexa-Fluor goat anti rabbit 594	Thermo Fisher	Cat. #: A-11012	IF: 1:500
Reagent (BioID)	Dynabeads MyOne	Thermo Fisher	Cat. #: 65001	300 µl per 4 x 10^7 cells

	Streptavidin C1			
Kit (Biochemistry)	CAPTUREome S-Palmitoylated protein kit	Badrilla (Leeds)	Cat. #: K010-311	
Kit (Biochemistry)	FOCUS Signal Proteins	G-Biosciences	Cat. #: 786-250	For isolation of lipid rafts proteins

2.2 Plasmid DNA preparation

2.2.1 Bacteria growth and storage

Escherichia coli NEB5α (DH5α variant) was used as the host for plasmid DNA amplification and dam^-/dcm^- was used to process methylated restriction sites. *E. coli* were grown on either semi-solid LB agar (1.5% agar) or in liquid LB (Luri-Bertani medium: 1% w/v tryptone, 0.5% w/v yeast extract, 1% w/v NaCl) overnight (o/n) in a 37°C shaking incubator. Antibiotics ampicillin (100 µg/µl) or kanamycin (50 µg/µl) were added for selection. Semisolids were stored at 4°C for 3-4 weeks. For long-term storage, glycerol (20%) was added to o/n liquid LB and stored at -80°C.

2.2.2 Generation of competent *E. coli* cells

Competent cells were prepared according to the Banerjee lab protocol (UCLA). Briefly, single colonies were grown o/n in LB. Liquid cultures were then diluted 1:100 in LB and flasks were maintained at 37°C in a shaking incubator until optical density measured at 600 nm (OD_{600}) reaches 0.6. Cells were harvested by centrifugation at 3000 x g for 10 min at 4°C. All subsequent steps were performed at 4°C. Cell pellets were resuspended in 0.1 M $MgCl_2$ for 5 min, centrifuged, and resuspended in 0.05 M $CaCl_2$ for 20 min and centrifuged again. Cell pellets were subsequently resuspended in 0.1 M $CaCl_2$ with 15% w/v glycerol and stored immediately at -80°C.

2.2.3 Transformation

The heat shock method was employed for bacterial transformation (Hanahan, 1983). Plasmid DNA (1 µg) was added to 25-50 µl of competent NEB5α cells and incubated on ice for 30 min. Cells were subjected to 42^{o}C heat pulse for 45 s followed by the addition of 950 µl of SOC media (NEB) and incubation at 37^{o}C for 1 h with shaking. Cultures (100 µl) were then spread onto LB agar containing selection media. For low copy number plasmids, liquid cultures were centrifuged for 1 min at 1000 x g and harvested cells were resuspended in 10% of liquid culture and spread onto LB agar.

2.2.4 Plasmid DNA isolation

Single colonies were picked and used to inoculate o/n LB cultures with antibiotic selection. Liquid cultures of 1.5 ml volume were used to obtain 5 µg plasmid DNA (QuickLyse, Qiagen), 7 ml liquid cultures to obtain 25 µg plasmid DNA (Miniprep, Qiagen) and 50 ml liquid cultures to obtain 250 µg of tissue culture grade plasmid DNA (Pronobis et al., 2016). For low copy number plasmids, 250 ml liquid cultures were used to isolate 10 µg plasmid DNA (Maxiprep, Qiagen). DNA concentrations were determined using a Nanodrop spectrometer (ND-ONE-W, Thermo Fisher).

2.3 Plasmid DNA manipulation

2.3.1 Site-directed mutagenesis

Up to 4 adjacent nucleotides were mutated through Q5 Site-Directed Mutagenesis (NEB). Briefly, 1 X Q5 master mix was mixed with 10 ng of plasmid DNA, 0.5 µM forward primer and 0.5 µM reverse primer. Sample mixtures were subject to polymerase chain reaction (PCR) in a thermocycler (Veriti, Thermo Fisher). Thermocycler conditions are outlined in Table 2.2. PCR products were KLD digested for 5 min at room temperature (RT) and transformed into competent cells as described in 2.2.3.

Table 2.2 Thermocycler conditions.

Step	Temperature	Time
Initial denaturation	98°C	30 s
25 cycles	98°C 54-70°C* 72°C	10 s 30 s 30 s / kb (~ 3-4 min)
Final extension	72°C	2 min
Hold	10°C	o/n

* Annealing temperature is 5°C less than predicted Ta for PCR primer pairs (NEBasechanger.neb.com).

2.3.2 Restriction digestion and ligation

Plasmid DNA (1 µg) was digested with single compatible restriction enzymes (RE) to ensure correct length and insertion. Double RE digestion of ~2 µg plasmid DNA was employed for insert and backbone generation. Restriction with high fidelity enzymes (Table 2.1) were incubated at 37°C for 15 min prior to loading onto agarose gels with 1X gel loading dye (NEB). Ligation with T4 ligase (NEB) was performed at a ratio of 3:1 (60-20 ng) insert:backbone and incubated at RT for 30 min prior to transformation into competent cells.

2.3.3 Agarose gel electrophoresis and gel extraction

PCR products or restricted plasmid DNA were separated by agarose gel electrophoresis. Gels consisted of 1% agarose (w/v) in TAE buffer (40 mM Tris, 20 mM acetic acid, 1 mM EDTA) to which SYBR safe (Thermo Fisher) was added. Electrophoresis was performed at 80 V for 1 h in fresh TAE buffer. Gel extractions were performed using a scalpel, and DNA was isolated using Gel Extraction Kits (Qiagen). Gels were imaged using an InGenius3 gel documentation system (Syngene Bioimaging, UK). Sanger sequencing validation was outsourced to Genewiz UK that also provided vector-specific or custom sequencing primers.

2.4 DNA construct generation

2.4.1 Vector backbones

CVS-G and SAD-G constructs in pMA-T were synthesised by GeneArt (codon optimised CVS-G, SAD-G) with engineered EcoRI and NotI insertion sites. Constructs were then cloned into pCAGGS for mammalian expression (Table 2.1). For site directed mutagenesis, constructs were cloned into pcDNA3.1 and re-cloned back into pCAGGS, as pCAGGS with RABV-G constructs are unsuitable for Q5 site directed mutagenesis.

2.4.2 Generation of CVS-G and SAD-G mutants

CVS-G mutants were generated by first isolating CVS-G from pCAGGS through EcoRI and NheI restriction. A compatible pcDNA3.1 backbone was generated through EcoRI and XbaI digestion. CVS-G was then ligated into pcDNA3.1 as NheI and XbaI cut compatible sites. Several point mutations in CVS-G-pcDNA3.1 were generated in house as outlined in Table 2.3. Cutting with NheI and XbaI at the same site generates a scar, this scar was replaced with NheI cut site through site directed mutagenesis. Then, these mutants were subcloned back into pCAGGS through EcoRI and NheI.

Table 2.3 Oligonucleotides used to generate CVS-G mutants.

Mutation site	Sequence (5'-3')
pcDNA3.1 3' scar -> NheI	F– CAGACTGTAAGCTAGCGGGCC R– GTCTCACCCCCACTCTTGTGTG
W460C	F– TAATGACATGCTGCAGAAGAGC R– GGGAAAATATCAACACCAG
C461A	F– AATGACATGGGCCAGAAGAGCC R– AGGGAAAATATCAACACC
P467A	F– AGAGCCAATCGAGCAGAATCGAAACAA R– TCTGCACCATGTCATTAGGGAAAATATCAACA
S469A	F– AATCGACCAGAAGCGAAACAACGCAGTTTT R– GGCTCTTCTGCACCATGTCATTAGGGAAAA

K470A	F– GACCAGAATCGGCACAACGCAGTTTTGGA R– GATTGGCTCTTCTGCACCATGTCATTAGGGA
R472A	F– GAATCGAAACAAGCCAGTTTTGGAGGGA R– TGGTCGATTGGCTCTTCTGCACC
S473A	F– AATCGAAACAACGCGCTTTTGGAGGGACA R– CTGGTCGATTGGCTCTTCTGCACCA
F474A	F– AAACAACGCAGTGCTGGAGGGACAG R– CGATTCTGGTCGATTGGCTCTTCTG
G475A	F– CAACGCAGTTTTGCAGGGACAGGGG R– TTTCGATTCTGGTCGATTGGCTCTTCTGCACC
S485A	F– TGTCAGTCACTGCCCAAAGCGGAAA R– CATTCCCCCCTGTCCCTCCAAAAC
P492A	F– CAAAGCGGAAAAGTCATAGCTTCATGGGAATCATATAAGA R– GGAAGTGACTGACACATTCCCCCC
Y497A	F– TTCATGGGAATCAGCTAAGAGTGGAGGTGA R– GGTATGACTTTTCCGCTTTGGGAAGTG
I503A	F– ATAAGAGTGGAGGTGAGAGACTGTAACTC R– ATGATTCCCATGAAGGTATGACTTTTCCGCTTTGGGAAGT

Table 2.4 Oligonucleotides used to generate SAD-G mutants.

Mutation site	**Sequence (5'-3')**
pcDNA3.1 3' scar -> NheI	F– CAGACTGTAAGCTAGCGGGCC R– GTCTCACCCCCACTCTTGTGTG
C460W	F– CTGATGACATGGTGTAGAAGAGTC R– GAAAATTATCAACATCAAGGCAGTCAG
C460A	F– CTGATGACAGCTTGTAGAAGAGTC R– GAAAATTATCAACATCAAGGCAGTCAG
C461A	F– CTGATGACATGTGCTAGAAGAGTC R– GAAAATTATCAACATCAAGGCAGTCAG
C460A/461A	F– CTGATGACAGCTGCTAGAAGAGTC R– GAAAATTATCAACATCAAGGCAGTCAG

2.4.3 Generation of BioID constructs

MycBioID (Roux et al., 2012) and the inactive mutant mycBioID-R118G were a kind gift from Prof Adrian Whitehouse (University of Leeds). CVS-G and SAD-G were ligated into both constructs through EcoRI and NotI restricted sites, generating BioID-RABV-G constructs in which the BioID was upstream of the RABV-G coding sequence. upstream AfeI and downstream BspEI sites were inserted into CVS-G and SAD-G permitting their subcloning into 13X-linker-BioID2-HA (Kim et al., 2016). For double digestions with AfeI and BspEI, AfeI was initially added in CutSmart buffer (NEB) for 30 min followed by the addition of BspEI in 100 mM NaCl to mimic a 3.1 buffer (NEB) that BspEI requires to become enzymatically active. Deletion primers were then designed to ensure the constructs were in-frame and to delete the stop-codon in BioID2 (Table 2.5). A start codon was then inserted upstream of the 13X-linker-BioID2-HA through site directed mutagenesis (Table 2.5). RABV-G-BioID2 constructs (reverse) were subcloned into pcDNA3.1 through EcoRI and XhoI. The N terminal constructs were designed as 5'-myc-SP-BioID2-RABV-G-3' to avoid RABV-G signal sequence cleavage.

Table 2.5 Oligonucleotides used in BioID construct generation.

Mutation site	Sequence (5'-3')
CVS-G 5' NotI site to AfeI	F– AGAAGCTCGAAGCGCTGCGCCACCATG R– CTGCGCTTCTCAGGGAGA
SAD-G 5' NotI site to AfeI	F– AGAAGCTCGAAGCGCTGCGCCACCATG R– CTGCGCTTCTCAGGGAGA
CVS-G 3' EcoRI site to BspEI	F– TCTGAGCTAGTCCGGACACCACACTGGACTAGTG R– GTCTGATCTCTCCGCCGC
SAD-G 3' EcoRI site to BspEI	F– TCTGAGCTAGTCCGGACACCACACTGGACTAGTGG R– GTCTTGTCTCTCCGCCGC
Deletion of region between BioID2 and CVS-G	F– GGTGGAGGCGGGTCTGGA R– GAGTCTGATCTCTCCGCCGC
Deletion of region between BioID2 and SAD-G	F– GGTGGAGGCGGGTCTGGA R– GAGTCTTGTCTCTCCGCCGC

Add 5' ATG to 13X-linker-BioID2-HA	F– GGGATGGGTGGAGGCGGGTCTGGA R– GGATCCGAATTCCGAAAAAAGATGGG

2.5 Cell culture

2.5.1 Cell line maintenance

Human cell lines SVG-A (foetal astrocytes), HEK293T (embryonic kidney cells) and SH-SY5Y (bone marrow derived neuroblasts) were obtained from the European Collection of Cell Cultures (ECACC) or American Type Culture Collection (ATCC) (Table 2.1). Cells were maintained in Dulbecco's Modified Eagle Media (DMEM) supplemented with 10% Foetal Calf Serum (FBS) in a humidified incubator (Sanyo, USA) at 37°C with 5% CO_2. Media was supplemented with 100 U/ml penicillin and 100 µg/ml streptomycin (1% pen/strep). Cell culture reagents were obtained from Gibco. Cells were passaged every 2-3 days using trypsin-EDTA. All cell culture work was performed in a BSL2 biological safety cabinet (Esco).

2.5.2 Neuronal cell differentiation

SH-SY5Y cells were differentiated into 70% neuronal-like cells and 30% epithelial-like cells, as described by Dwane et al. (2013). Briefly, SH-SY5Y were seeded onto 10 µg/ml laminin for 24 h to support differentiation followed by transfection. After 4 hours post transfection, the cell media was replaced with serum-free DMEM supplemented with 50 nM insulin growth factor (IGF-I). After 3 days, cells were fixed or harvested and differentiation was validated through GAP43 neuronal marker detection via immunofluorescence or western blotting, respectively.

2.5.3 Transient transfection

Transfections were performed using lipofectamine 2000 (Thermo Fisher) following the manufacturer's instructions. Briefly, cells were seeded into 12 wells at a density of 1 x 10^5 cells/ml and incubated o/n. The next day, 1 µg of plasmid DNA was mixed with 3 µl of lipofectamine (1:3 ratio) in 50 µl Opti-MEM at RT for 5 min and added dropwise to the cells. Media was replaced

with antibiotic-free DMEM prior to the addition of the transfection mix. After 4 h, transfection mixes were removed from the cells and fresh media was added. Experiments were performed 24 h post-transfection.

2.6 Biochemical assays

2.6.1 Cell lysis

Cells were lysed in either triton-based lysis buffer (25 mM glycerol phosphate, 20 mM tris, 150 mM NaCl, 1 mM EDTA, 1% triton, 10% glycerol, 50 mM NaF, 5 mM $Na_4O_7P_2$, pH 7.4) or SDS-based BioID lysis buffer (50 mM tris, 500 mM NaCl, 0.4% SDS, 1 mM DTT, pH 7.4 (Kim et al., 2016)). Buffers were supplemented with a protease inhibitor cocktail (Thermo Fisher). Cells were lysed for 15 min at 4°C with gentle rocking. Cell lysates were harvested using a sterile cell scraper and clarified by centrifugation at 17,000 x g for 10 min. Clarified supernatants were collected and total protein concentrations were determined through bicinchoninic assay (BCA, Thermo Fisher).

2.6.2 SDS-PAGE electrophoresis

Normalised protein samples were mixed with Laemmli SDS-loading buffer (4x, Bio-Rad, supplemented with β-mercaptoethanol), boiled for 10 min at 95°C, and centrifuged for 5 min at 17,000 x g. Samples were loaded onto 5% stacking/12% resolving discontinuous acrylamide SDS gels (Table 2.6) and resolved through SDS-PAGE (SDS-polyacrylamide gel electrophoresis) at 200 V for 60 min in SDS-PAGE running buffer (Table 2.6).

Table 2.6 SDS-PAGE buffer recipes (sufficient for 2 gels).

12% Resolving Gel	**5% Stacking Gel**	**SDS-PAGE Running Buffer (pH range 7.0-9.0)**
3.75 ml tris-HCl (1.5 M, pH 8.8)	0.25 ml tris-HCl (1 M, pH 6.8)	25 mM tris
4.93 ml dH_2O	3.00 ml dH_2O	250 mM glycine
6.00 ml 30% acrylamide	0.66 ml 30% acrylamide	0.1% (w/v) SDS

0.15 ml 10% SDS	0.04 ml 10% SDS	
0.15 ml 10% APS[1]	0.04 ml 10% APS	
0.024 ml TEMED[2]	0.02 ml TEMED	
Total = 15 ml	Total = 4 ml	

1 Ammonium persulfate.

2 Tetramethylethylenediamine.

2.6.3 Western blotting

Lysates resolved by SDS-PAGE were transferred onto polyvinylidene difluoride (PVDF) membranes using a semi-dry transfer system (Trans-blot Turbo, Bio-Rad) in Tris-based transfer buffer (25 mM tris, 88.5 mM glycine, 20% (v/v) methanol) at 25 V for 30 min. Membranes were then blocked for 1 h in 10% milk in TBS-T (25 mM tris, 137 mM NaCl, 0.1% (v/v) Tween-20, pH 7.5) with gentle rocking. Target proteins were labelled with primary antibodies in 5% milk o/n at 4^{o}C (Table 2.1). Unbound antibodies were removed after 3 x 5 min washes in TBS-T. Membranes were then incubated with the corresponding horseradish peroxide (HRP)-conjugated secondary antibodies in 5% milk/TBS-T for 1 h at RT with gentle rocking. Membranes were washed 4 x 5 min times with TBS-T and target proteins were detected through chemiluminescence (ECL, Thermo Fisher). Gels were imaged through an x-ray developer (Xograph Healthcare, UK).

2.7 Immunofluorescence staining

2.7.1 Steady state immunofluorescence

SVG-A cells were seeded onto sterilised poly-L-lysine (Sigma) coated coverslips in 12 well plates (1 x 10^5 cells per well) and allowed 24 h to adhere. After transfection, cells were fixed with 4% PFA for 10 min at 4°C and permeablised with ice-cold 1:1 methanol:acetone solution for 10 min. Cells were blocked in 1% bovine serum albumin (BSA) in PBS for 15 min and labelled with primary anti-RABV-G in 1% BSA for 1 h, followed by 3 x PBS washes. Cells were then stained with the corresponding fluorescent Alexa-

Fluor 488 nm conjugated antibody (Table 2.1) for a further 1 h and washed 4 times in PBS. For co-labelling experiments, cells were labelled with a second primary antibody and corresponding fluorescent Alexa-Fluor secondary antibodies as described. Cells were then washed in PBS and mounted using ProLong Gold anti-fade reagent with DAPI (Thermo Fisher) onto glass slides.

2.7.2 Internalisation assays

To label cell surface RABV-G, live cells were labelled with anti-RABV-G and its corresponding fluorescent Alexa-Fluor secondary in DMEM for 90 min. Cells were then washed in PBS, fixed in 4% PFA for 10 min at 4°C and imaged through IncuCyte Zoom plate reader to validate labelling. The number of fluorescent cells or mean fluorescence intensity (GCU, green calibration units) were quantified using IncuCyte analysis software.

2.7.3 Surface stripping of antibody-glycoprotein complexes

To remove antibody labelled complexes, cells were live labelled for 90 min as described in 2.7.2 and fixed in 4% PFA for 10 min. Antibody-labelled complexes were then stripped with acidic glycine buffer (pH 2, 0.2M glycine and 0.15M NaCl) for 2 min. To ensure specific cell surface labelling in the absence of endocytosis, antibodies were added to cells in ice-cold labelling media at 4°C for 30 min prior to fixation.

2.7.4 Filopodia measurements

To measure filopodia projections, cells were co-live labelled with anti-RABV-G, corresponding fluorescent Alexa-Fluor secondary and phallodidin-680 in DMEM for 90 min. Cells were then washed in PBS and fixed in 4% PFA for 10 min. Filopodia projections were quantified per-cell and lengths were measured through Fiji.

2.7.5 Image acquisition and analysis

Cells were imaged on an inverted laser scanning microscope (Zeiss LSM-700) with an oil-immersion 40x objective lens. The Fiji platform was used for image analysis. For co-localisation studies, five Z-stacks were analysed using the coloc 2 colocalisation analysis tool by highlighting single regions of interest.

Internalisation was quantified through assessment of intracellular puncta per-cell from 50 cell images or by highlighting the intracellular region (excluding the plasma membrane) and dividing its fluorescence value by the total fluorescence of the cell images.

2.8 BioID proximity labelling

2.8.1 Biotinylation assays

HEK293T cells were seeded onto poly-L-lysine-coated 10 cm dishes at a density of 2.2 x 10^6. Cells were transfected for 4 h and cell media was replaced with serum-free DMEM supplemented with 50 µM biotin (Sigma). After 16 h, cells were washed twice in PBS and lysed in SDS-based BioID buffer (50 mM tris, 500 mM NaCl, 0.4% SDS, 1 mM DTT, pH 7.4) supplemented with protease inhibitor cocktail (2.6.1).

2.8.2 Dynabeads pulldowns

Lysates from four confluent 10 cm dishes were pooled (4 x 10^7) and mechanically disrupted 10 times by passage through 25 G needles, followed by two-cycles of sonication (30 s each cycle, Grant Ultrasonic). Triton was added to a 2% final concentration and equal volumes of 50 mM tris pH 7.4 were added prior to clearing the lysates through centrifugation at 16,000 x g for 10 min. Of the cleared lysates, 10% of the sample was stored as input material and the rest was mixed with 300 µl of Dynabeads (MyOne Streptavidin C1, Thermo Fisher) overnight at 4^{o}C on a rotating wheel. Dynabeads were equilibrated for 10 min in the same lysis buffer diluted 1:1 in 50 mM Tris prior to use. Beads were collected on a magnetic stand and washed with four different wash buffers for 8 min each: wash buffer 1 (2% SDS); wash buffer 2 (50 mM HEPES, 1 mM EDTA, 500 mM NaCl, 1% triton, 0.1% Na-deoxycholate, pH 7.4); wash buffer 3 (10 mM tris, 250 mM LiCl, 1 mM EDTA, 0.5% NP-40, 0.5% Na-deoxycholate, pH 8); and wash buffer 4 (50 mM tris). Beads destined for mass spectrometry analysis were stored in 30 µl of wash buffer 4. Beads that were subject to input analysis were eluted

through a biotin-based elution buffer (10 mM tris, 2% SDS, 5% β-mercaptoethanol, 2 mM biotin, pH 7.4).

2.8.3 Mass spectrometry and data analysis

Successful BioID labelling was validated through western blotting and immunofluorescence. Samples were then sent on dry ice to the Bristol Proteomics Facility (Kate Heesom, University of Bristol, UK) for TMT mass spectrometry analysis. At Bristol, samples were digested with trypsin, fractionated by high pH reverse-phase (RP) chromatography prior to analysis through nano-liquid chromatography-tandem mass spectrometry (LC-MS/MS). Raw data were analysed using Proteome Discoverer software and searched against UniProt human database using a SEQUEST algorithm. Data was filtered to satisfy a false discovery rate (FDR) of 1%. For analysis, highly enriched proteins with comparatively 2.00-fold higher expression in CVS-G-BioID were selected. Proteomics analysis was repeated three times prior to network analysis.

2.8.4 Network analysis

STRING network analysis tool (https://string-db.org/) was used to identify protein-protein association networks. High confidence interaction scores (0.7 or higher) were highlighted by thick lines and medium confidence interaction scores (0.4-0.7) were highlighted by thin lines to maximise the strength of data support. REACTOME algorithms were then applied to classify five functional association networks. STRING network was also analysed through GO enrichment analysis and KEGG pathway analysis to independently identify additional functional association networks. Only terms with high confidence (p-value < 0.005) were considered.

2.9 Palmitoylated protein isolation

HEK293T cells were seeded onto poly-L-lysine-coated 10 cm dishes at a density of 2.2 x 10^6 prior to transfection the following day. Cell media was replaced 4 h post-transfection. At 24 h post transfection, cells were washed twice with PBS and scrapped in SDS-based lysis buffer supplemented with

Thiol blocking reagent (CAPTUREome S-Palmitoylated Protein kit, Badrilla Ltd, Leeds Innovation Centre, UK) and incubated at 40°C for 4 h in a shaking heat block (Eppendorf thermomixer C). Proteins were then mixed with 3 x ice-cold acetone and precipitated at -20°C for 20 min. Sample mixtures were centrifuged at 16,000 g for 5 min and the pellets were stored. Pellets were subsequently washed 5 times with ice-cold 70% acetone, air dried, and re-dissolved in binding-buffer at 40°C for 1 h in a shaking heat block. Once the solution was cleared (complete protein dissolution), sample mixtures were centrifuged at 16,000 x g for 1 min and 10% of the supernatants mixed with Laemmli Buffer as input material. The remainder of the sample was mixed with Thioester Cleavage Reagent and CAPTUREome Capture Resin at RT on a rotating wheel for 2.5 h. The sample-resin mixture was centrifuged for 1 min at 16,000 x g and pellets were washed 5 times with binding-buffer prior to the elution of resin-captured proteins through the addition of Laemmli Buffer and boiling at 95°C for 10 min. Samples were then resolved by SDS-PAGE and RABV-G was detected through western blotting.

2.10 Lipid raft protein isolation

HEK293T cells were seeded onto poly-L-lysine-coated 10 cm dishes at a density of 2.2 x 10^6 and transfected as described. Twenty-four hours post-transfection, cells were washed twice in PBS and harvested in Extraction Buffer I (FOCUS Signal Protein Extraction Kit, G-Biosciences) supplemented with protease inhibitor cocktail (2.6.1). Samples were then mechanically disrupted (2.8.2) and added to an equal volume of pre-chilled Extraction Buffer II. Sample mixtures were then incubated at 4°C on a rotating wheel for 20 min then left on ice for 10 min prior to centrifugation at 16,000 g for 15 min. Pellets were then re-suspended in FPS Buffer supplemented with Laemmli Buffer and protease inhibitor cocktail (2.6.1). Samples were mixed on a rotating wheel for 20 min and then left at RT for 15 min prior to centrifugation at 16,000 g for 10 min. Cleared supernatants were then resolved by SDS-PAGE and RABV-G was detected through western blotting.

Chapter 3 | Glycoproteins of pathogenic and attenuated rabies virus strains show differential trafficking profiles in cultured cell lines

3.1 Introduction

Rabies virus glycoprotein (RABV-G) is the major protein implicated in RABV pathogenesis (Dietzschold et al., 2008) as it regulates neuroinvasiveness (Guo et al., 2019), virus spread (Davis et al., 2015) and immune avoidance (Li et al., 2019). When RABV is chemically inactivated, hosts infected with these attenuated RABV strains develop VNAs primarily against RABV-G (Perrin et al., 1985) where lasting immunity against RABV occurs. Without this inactivation, RABV has one of the highest infection-to-mortality ratios of any viral pathogen (Fooks et al., 2014). The gold standard treatment for RABV is PEP which is expensive (~ £100) (Chulasugandha et al., 2006), challenging to produce (Bourhy et al., 2009) and cannot be transported or stored in remote rural areas in poor regions where up to 60,000 annual RABV fatalities occur (Fisher et al., 2018). As many RABV cases remain unreported, it is estimated that the virus results in 1.74 million lost DALYs (disability adjusted life years) each year (Knobel et al., 2005).

Following RABV-G attachment to host entry receptors, RABV internalises via CME in an actin and dynamin dependent manner (Piccinotti et al., 2013; Gao et al., 2019). After endocytosis, endosomal acidification triggers RABV-G fusion with host endosomal membranes where virus uncoating occurs and the RNP is released into the cytoplasm, where progeny RABV proteins are synthesised (Schnell et al., 2010). RABV-G is synthesised in the rough ER, modified in the Golgi apparatus, and trafficked to the PM where virus budding occurs (Guo et al., 2019). The later stages of RABV-G trafficking are not well understood (see Chapter 1, Figure 1.6).

Live attenuated RABV strains such as SAD-B19 (SAD) were created in the 1970s to eradicate RABV from animal reservoirs (Sacramento et al., 1992). SAD-B19-laced baits eradicated most canine RABV in Europe, though bat RABV remains in circulation (Servat et al., 2020). SAD infections are rapidly cleared from infected hosts but the potential for pathogenic reversion remains (Faber et al., 2005; Tao et al., 2010), which prevents their usage as live vaccines for humans. Similar to inactivated RABV, SAD-infected hosts develop VNAs primarily against RABV-G (Perrin et al., 1985) and this VNA-development is abolished when SAD is engineered to express CVS-G instead

of its own G protein (Morimoto et al., 2000; Finke and Conzelmann, 2005). By studying RABV-G trafficking, Li and colleagues (2019) showed that pathogenic RABV strains limit their levels of RABV-G expression to avoid immune surveillance. In contrast, attenuated strains express RABV-G to high levels and are more readily detected by host defences. Pathogenic strains that express a dual copy of RABV-G lead to increased VNAs against RABV (Cenna et al., 2008) and the loss of specific motifs within pathogenic RABV-G prevent its presentation to antigen-presenting cells (Yang et al., 2015). Work on chimeric viruses expanded this observation and showed that when exchanging RABV-G from attenuated RABV with RABV-G from pathogenic RABV, reduced RABV-G PM expression was observed (Morimoto et al., 2000).

These studies suggest sequence-encoded, intrinsic trafficking differences between pathogenic RABV-G and attenuated RABV-G that have to-date remained uncharacterised. The aim of this chapter was to investigate the trafficking profile of pathogenic and attenuated RABV-G proteins. Both pathogenic CVS-G and attenuated SAD-G were transfected into mammalian cell lines in which phenotypic differences in intracellular trafficking were observed. These differences were confirmed and characterised and their potential implications in RABV pathogenesis discussed.

3.2 Localisation assessment of RABV-G

3.2.1 Puncta are composed of RABV-G proteins

Limited information is available regarding the post-synthesis trafficking of RABV-G. To observe RABV-G localisation at steady state, SVG-A cells were transfected with CVS-G or SAD-G, fixed, permeabilised, and labelled with monoclonal E559 anti RABV-G antibodies. When visualised by confocal microscopy, clear differences in the localisation patterns of CVS-G and SAD-G were observed (Figure 3.1A). CVS-G localised to intracellular puncta (white arrowhead) that concentrated within the perinuclear region of cells. CVS-G was also observed at the plasma membrane (PM) where RABV budding and immune detection may occur *in vivo*. This is in contrast with SAD-G that was

mostly present at the PM with no noticeable distinct staining pattern in the perinuclear region of cells.

To investigate whether these differences were related to the levels of RABV-G expression, cells transfected with CVS-G or SAD-G were lysed and proteins were resolved by SDS-PAGE. Western blot analysis against RABV-G showed similar total expression levels between CVS-G and SAD-G (Figure 3.1B), indicating that differences in localisation were not related to the levels of RABV-G expressed. A size shift between CVS-G and SAD-G was observed on the blots, due to known differences in their glycosylation patterns (Yin et

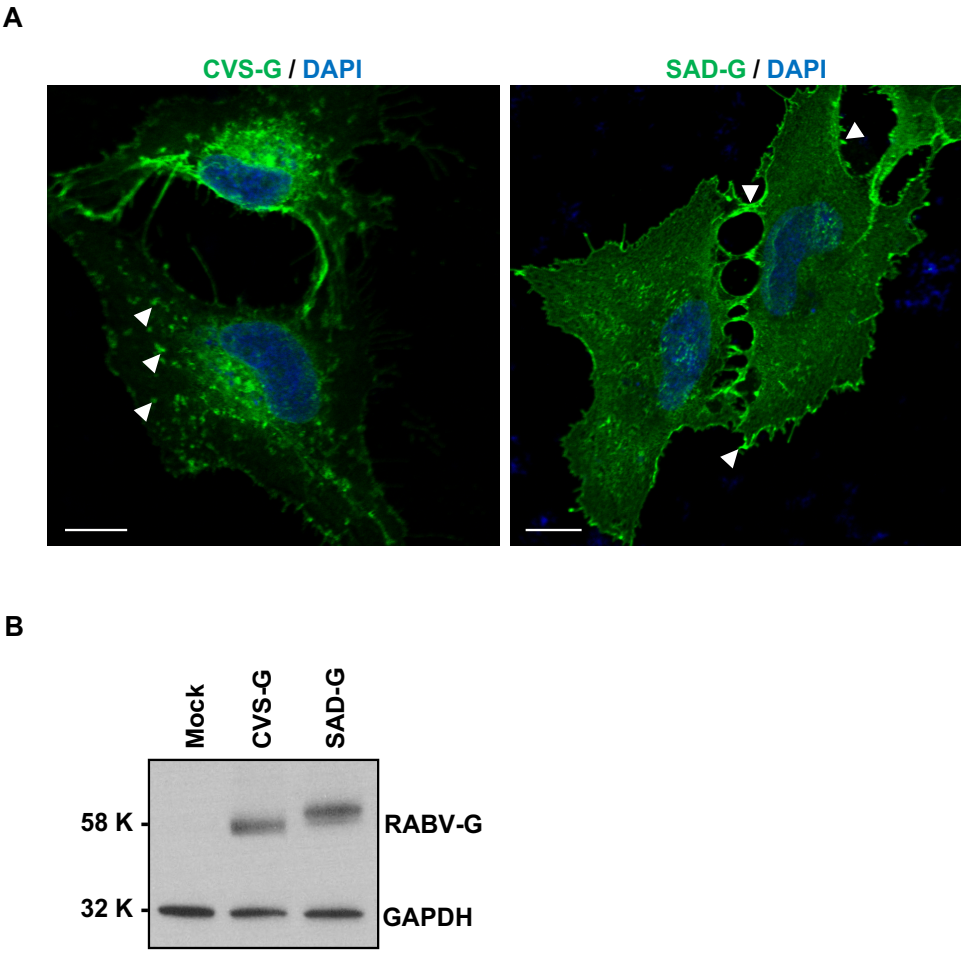

Figure 3.1 Expression profiles of CVS-G and SAD-G. (A) Human SVG-A cells were transfected with CVS-G or SAD-G, fixed, permeabilised and labelled with E559 anti-RABV-G (1:100) alongside fluorescent Alexa-Fluor secondary antibodies (1:500). Representative cell images (>100 cells) show that CVS-G is mostly localised as intracellular puncta (white arrowhead) whereas SAD-G is mostly localised at PM (white arrowhead) are shown. Cells were imaged on a confocal microscope, scale bar = 10 µm. **(B)** Western blot analysis of RABV-G and GAPDH suggests that both glycoproteins are expressed to similar levels. Differences in band size correlates with differing glycosylation profiles (n = 3).

al., 2020). The housekeeping protein GAPDH was probed to confirm equal gel-loading.

3.2.2 Live surface labelling reveals higher rates of CVS-G internalisation

As both RABV-G variants are localised at the PM, it was hypothesised that they could be stained in live unpermeabilised cells to investigate whether the observed differences in trafficking profiles were related to their internalisation from the PM. In the experiments that followed, live CVS-G or SAD-G expressing cells were antibody labelled for 90 min at 37°C, prior to fixation and imaging in unpermeabilised cells. CVS-G expressing cells showed numerous intracellular cytoplasmic puncta (white arrowheads) in addition to PM expression, whereas SAD-G labelled proteins were mostly limited to the PM (Figure 3.2A-B). Upon quantification, CVS-G had on average ~75 visible internalised puncta per cell, compared to ~20 internalised puncta for SAD-G under identical labelling conditions (Figure 3.2C). To further validate these differences, Fiji analysis was used to quantify the levels of intracellular fluorescence versus whole-cell fluorescence. It was found that CVS-G showed mostly intracellular expression whereas SAD-G has mostly PM expression (Figure 3.2C). These data suggest that differences in the internalisation rate of CVS-G vs. SAD-G exist, with CVS-G showing higher levels of- or faster internalisation rates.

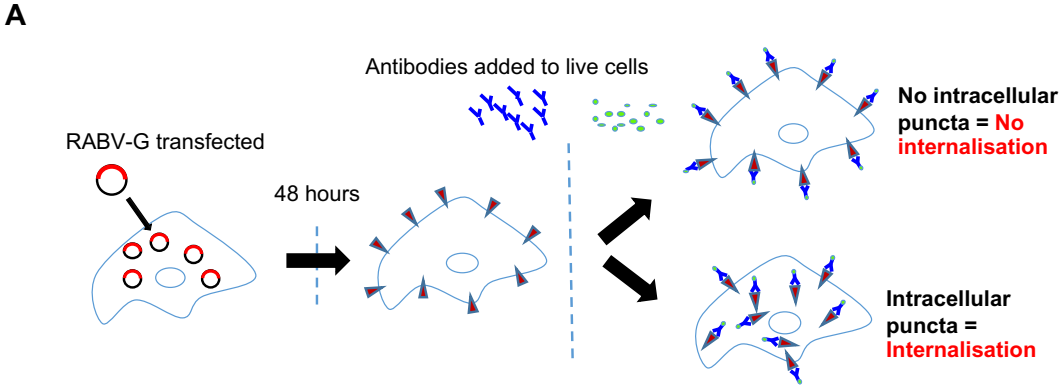

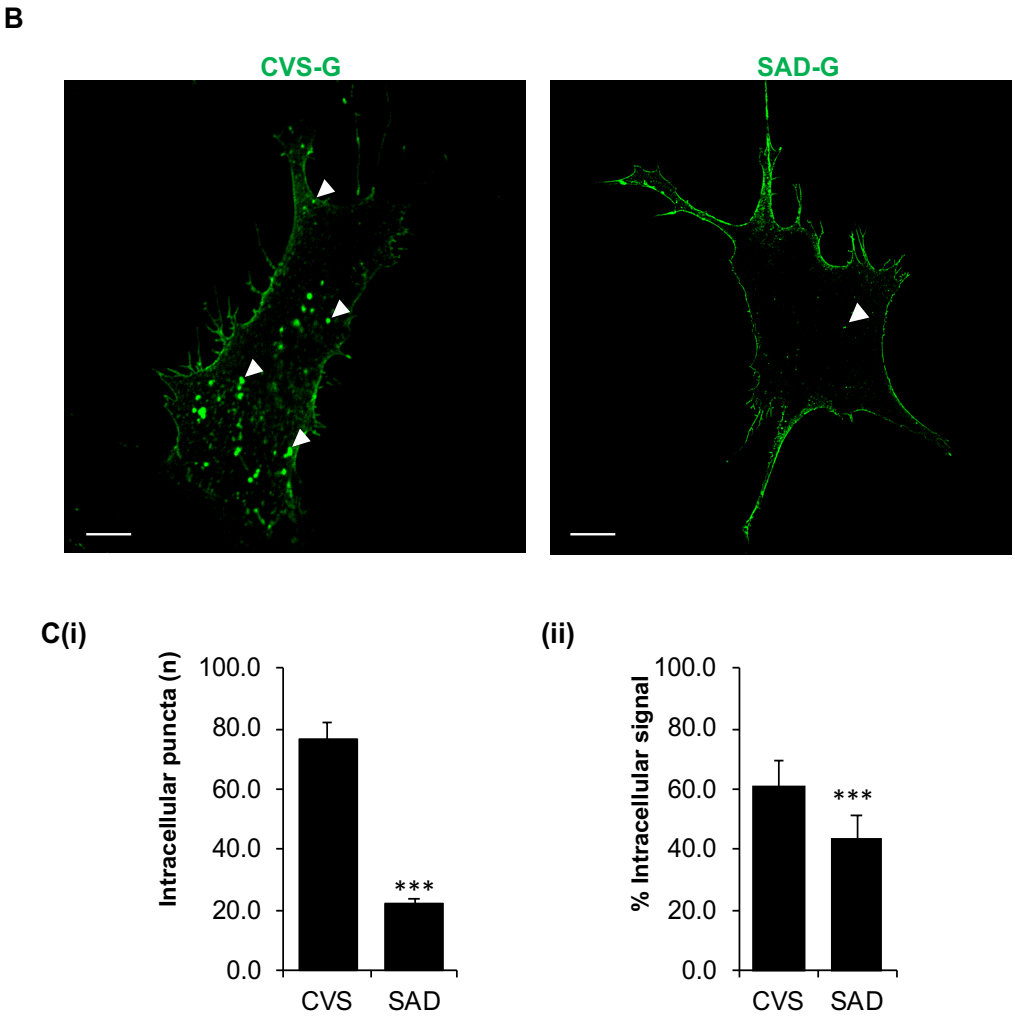

Figure 3.2 Live labelling reveals differences in internalisation rate of CVS-G versus SAD-G. (A) Schematic protocol of the internalisation assay. After 48 hours, cells transfected with CVS-G or SAD-G were live-labelled with anti RABV-G antibodies and fluorescent Alexa-Fluor antibodies in unpermeabilised cells. If intracellular puncta are visible, surface labelled RABV-G has undergone internalisation. **(B)** Representative images visualised under a confocal microscope are shown with numerous internalised puncta for CVS-G (white arrowhead) and few internalised puncta for SAD-G (white arrowhead) observed, scale bar = 10 µm. **(C)** Quantification of intracellular puncta was performed **(i)** manually counting the number of intracellular puncta or **(ii)** using Fiji to quantify intracellular fluorescence of RABV-G-expressing cells and comparing their levels total fluorescence. Quantifications are the average of 50 different cell images and suggest that significant differences between CVS-G and SAD-G internalisation exist. Error bars indicate mean ± SEM. ***significant difference between the two conditions ($P < 0.0005$).

3.2.3 Cold surface-labelling confirms internalising puncta are RABV-G proteins

To confirm that the internalising puncta are RABV-G proteins, live RABV-G expressing cells were labelled at 4°C (a non-endocytic permissive temperature) without permeabilisation. The results showed that under these conditions, both CVS-G and SAD-G were exclusively stained at the PM, with

no intracellular puncta observed (Figure 3.3A). Automated quantitative analysis using the IncuCyte plate reader also showed higher levels of PM staining for SAD-G compared to CVS-G, though these differences were not significant (Figure 3.3B). These results confirm that the intracellular puncta observed for CVS-G represent internalising RABV-G proteins.

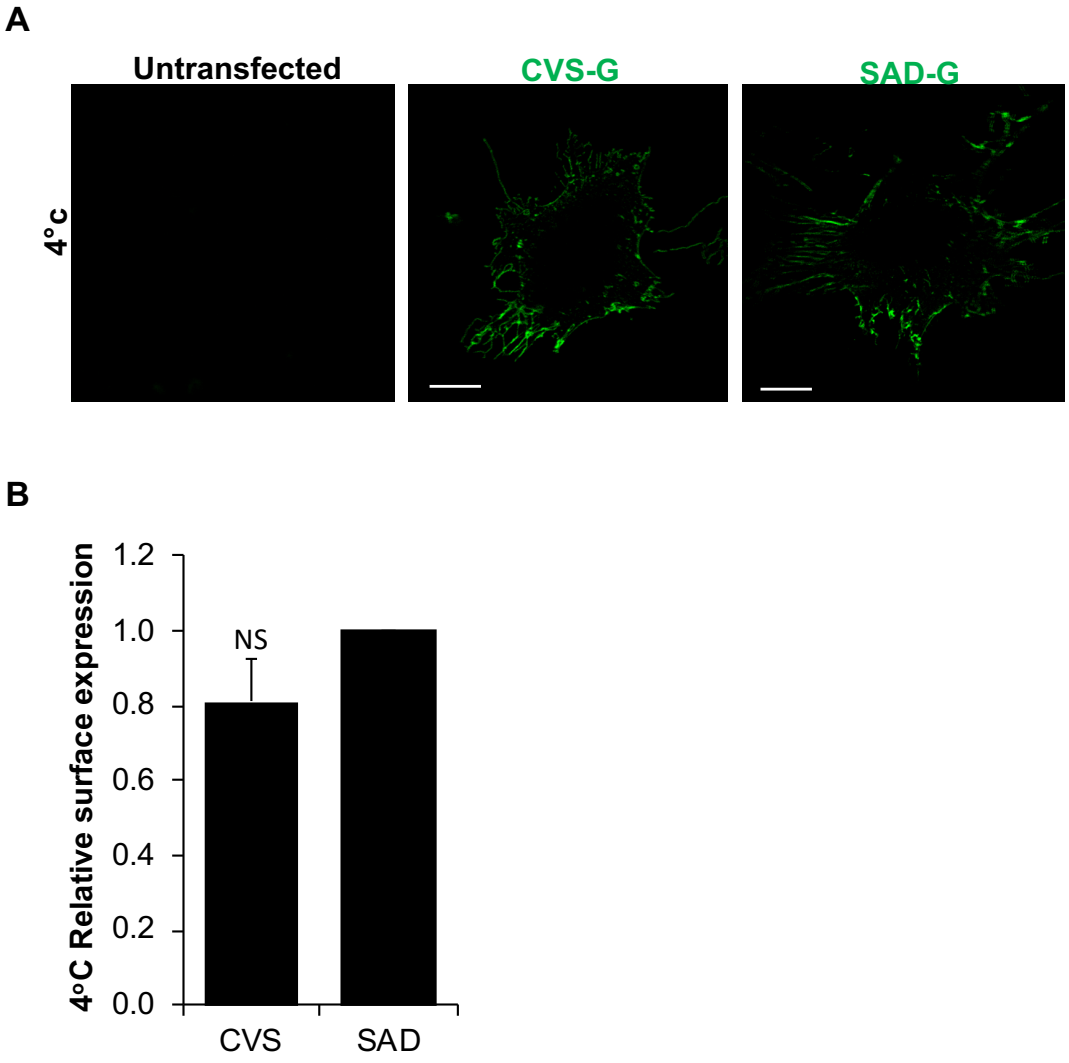

Figure 3.3 Cold surface-labelling suggests that internalised puncta are RABV-G proteins. (A) Cells transfected with CVS-G or SAD-G were live-labelled at 4°C for 2 hours with anti RABV-G antibodies and fluorescent Alexa-Fluor antibodies. Both CVS-G and SAD-G show PM expression without visible intracellular puncta. **(B)** Automated IncuCyte plate reader quantification showed higher SAD-G expression at the PM. Error bars indicate mean ± SEM.

3.2.4 Surface acid stripping confirms the intracellular nature of the internalising puncta

The data obtained so far suggest that both CVS-G and SAD-G are localised at the PM and that CVS-G internalises more readily from the PM than SAD-G. To rule out the possibility that the intracellular internalising puncta observed for CVS-G are cell membrane associated sub-cisternae, RABV-G expressing cells were labelled at either 4°C or 37°C for 90 min and exposed to a glycine-based acid stripping buffer (pH 2, 0.15M NaCl, 0.2M glycine) for 2 min to strip away cell surface RABV-G-antibody complexes. At the restrictive temperature of 4°C, all the RABV-G-antibody signal could be removed by acid stripping, whereas at the endocytic permissive temperature of 37°C, differences between CVS-G and SAD-G puncta were observed (Figure 3.4A-B). CVS-G again displayed an abundance of intracellular puncta, whilst SAD-G had minimal numbers of intracellular puncta visible, again indicating that SAD-G is mostly expressed at the PM. IncuCyte analysis was used to quantify the average green count of pre- versus post- acid treatment, showing approximately 25% of the CVS-G signal being internalised and protected from acid-strip, compared to only 10% of the SAD-G signal (Figure 3.4C). This observation confirmed higher internalisation levels for CVS-G and suggested that the internalising puncta were intracellular RABV-G proteins that had internalised from the PM.

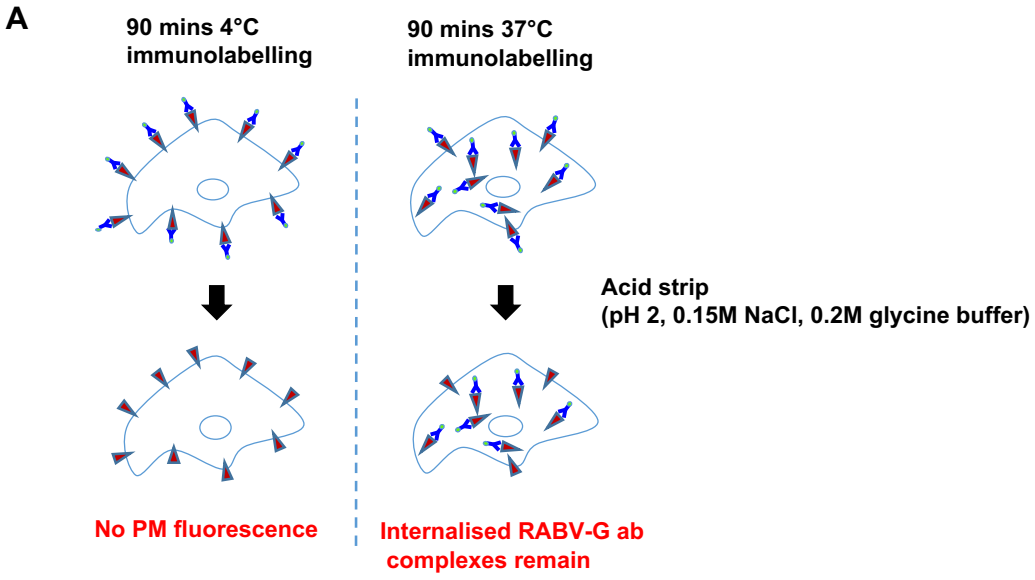

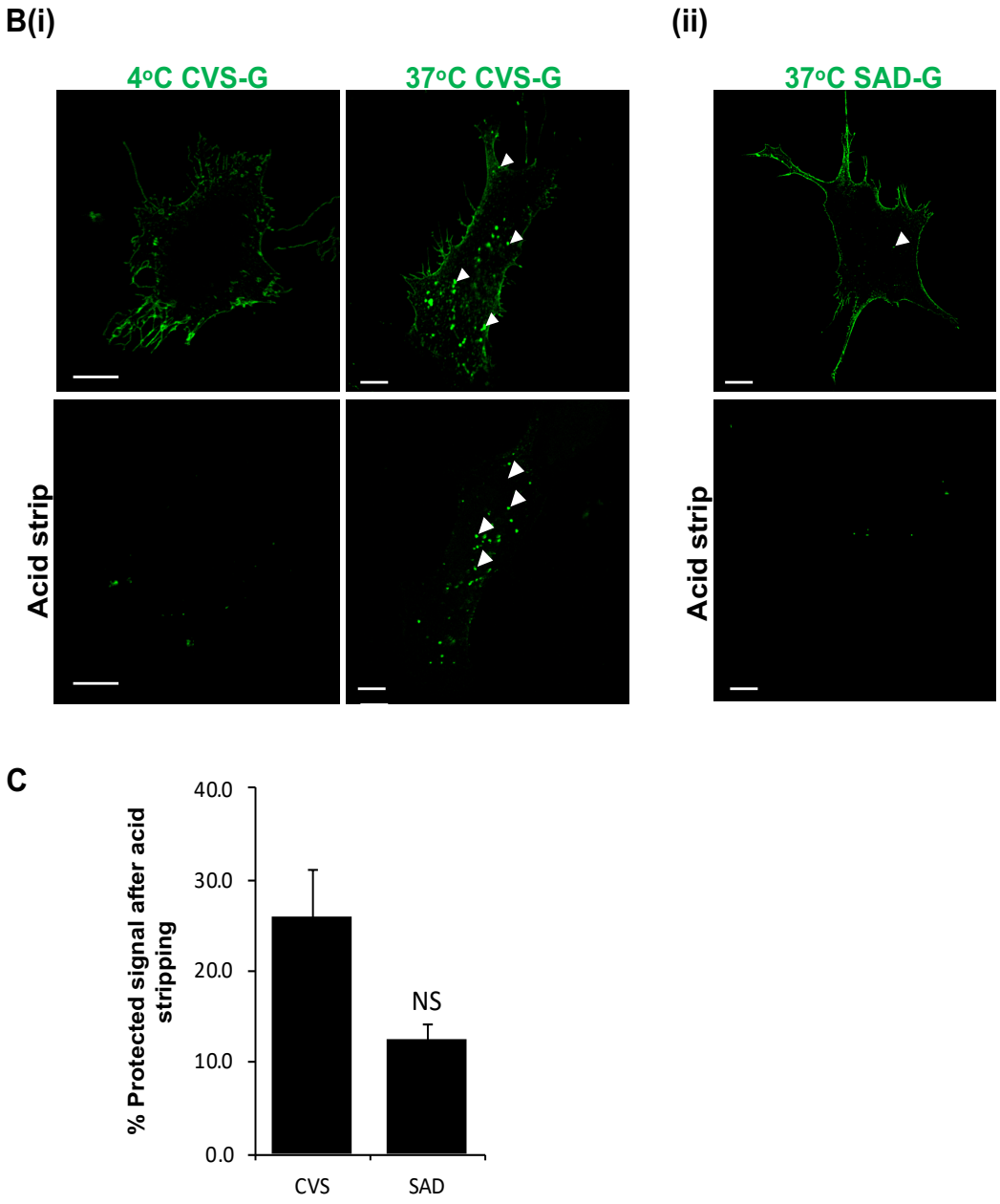

Figure 3.4 Surface acid stripping confirms internalised RABV-G puncta are not PM associated. (A) Schematic protocol of the acid stripping assay. After 48 hours, cells transfected with CVS-G or SAD-G were surface live-labelled with anti RABV-G antibodies and fluorescent Alexa-Fluor antibodies. Cells were then subjected to an acidic glycine buffer for 2 min to strip away RABV-G-antibody complexes at the PM. At 4°C, the fluorescence signal was lost, whilst at 37°C, intracellular puncta were visible, indicating RABV-G proteins were internalising. **(B)** Representative images show many internalised puncta for acid-stripped CVS-G (white arrowheads) and almost no internalised puncta for acid-stripped SAD-G. Scale bar = 10 µm. **(C)** IncuCyte analysis was used to compare pre- and post-acid treated cells, revealing higher protected signal for CVS-G (n =3). Error bars indicate mean ± SEM.

3.2.5 Internalisation time course suggests CVS-G internalises more rapidly than SAD-G

To further probe differences in the internalisation of CVS-G and SAD-G, the numbers of internalising puncta were compared at different time points post-labelling. In the assays that followed, RABV-G expressing cells were labelled with anti RABV-G at 4°C then rapidly warmed to 37°C in a water bath, prior to fixation in ice-cold PFA at the indicated time points (Figure 3.5A). The greatest difference between CVS-G and SAD-G internalisation rates were observed after 90 min of warming. Over-time, the accumulation of intracellular puncta could be observed as early as 10 min, and were consistently higher for CVS-G compared to SAD-G from 15 to 240 min, highlighting that the surface removal of these proteins was more rapid for CVS-G than SAD-G (Figure 3.5B). This rapid accumulation likely point towards a clathrin dependent route of surface removal (Jovic et al., 2010). Given this information, the trafficking pathways taken by the PM resident RABV-G proteins were next assessed.

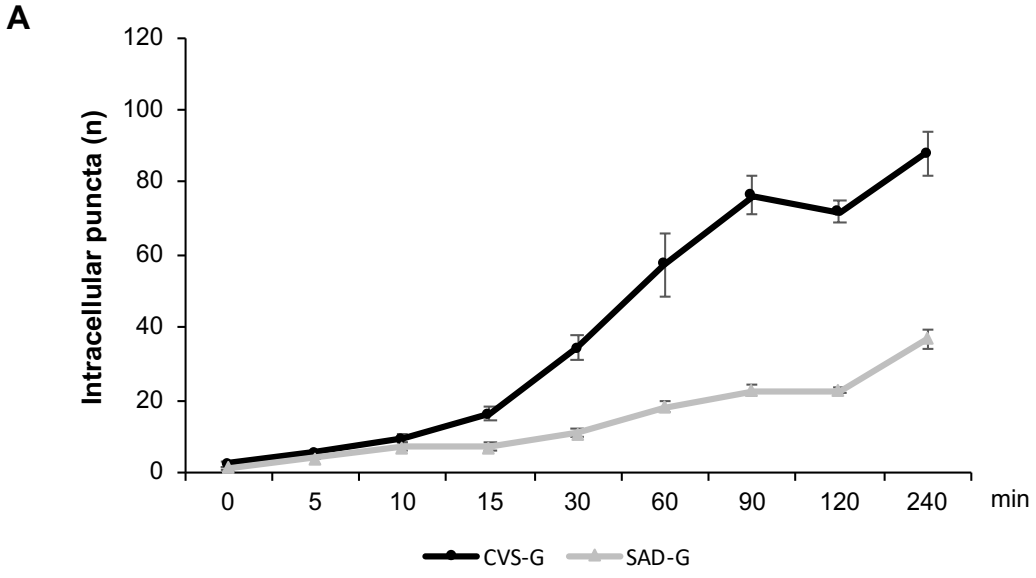

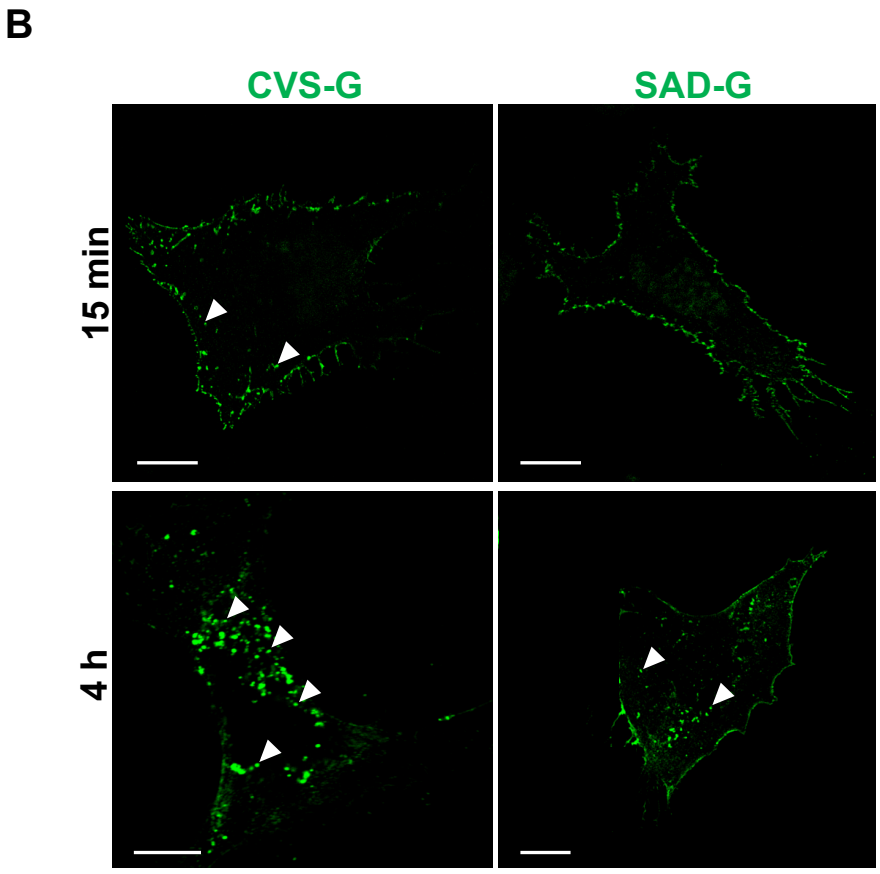

Figure 3.5 Labelling time course shows internalisation differences between CVS-G and SAD-G from 15 min post-internalisation. (A) RABV-G expressing cells were live labelled from 0 to 4 h and after each time point (average of 25 cell images) cells were fixed, imaged, and subjected to quantitative analysis by counting the number of internalised puncta at each timepoint. **(B)** Representative images from 15 min and 4 h labelling show that CVS-G begins to internalise from 15 min (white arrowhead) and at 4 h of labelling, PM-labelled RABV-G further accumulates in the cytoplasm (white arrowhead), indicating that internalisation is a continuous process. Scale bar = 10 µm.

3.3 Intracellular trafficking profile of RABV-G

3.3.1 RABV-G internalises into early endosomes

To confirm whether RABV-G proteins internalise to early endosomes (EEs), RABV-G expressing cells were fixed, permeabilised, and colabelled with both RABV-G and EEA1, a marker of early endosomes. Representative images show colocalised CVS-G and EEA1 puncta (white arrowhead) whereas fewer SAD-G puncta colocalised with EEA1 (white arrowhead) (Figure 3.6A). The Coloc 2 tool of Fiji was used to measure colocalisation in five z-stack images. The results show that ~50% of the cytoplasmic CVS-G puncta colocalised with EEA1 compared to only ~20% for SAD-G (Figure 3.6B). These data indicate

that at steady state, CVS-G is significantly present at EEs to higher levels than SAD-G.

A

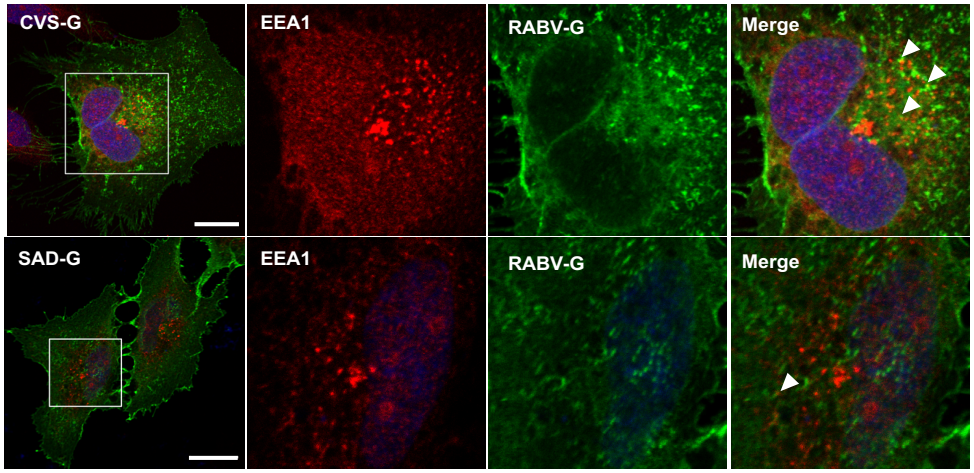

B

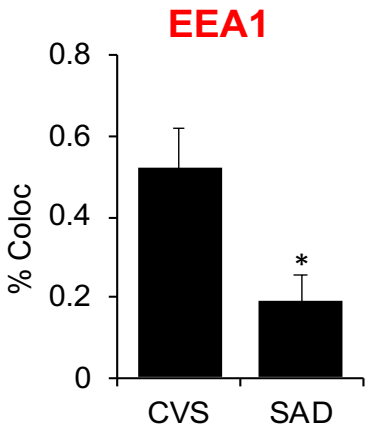

Figure 3.6 RABV-G internalises into early endosomes. (A) Cells transfected with CVS-G or SAD-G were fixed, permeabilised and labelled with RABV-G and fluorescent Alexa-Fluor antibodies. Cells were then steady-state co-labelled with EEA1 (1:200) and Alexa-fluor 594 (1:500). CVS-G puncta could be seen to colocalise with EEA1 (white arrowhead) to higher levels than SAD-G (white arrowhead), scale bar = 10 μm. **(B)** Quantitative analysis of five z-stacks performed using the Coloc 2 tool of Fiji. CVS-G was found to significantly colocalise with EEA1. Error bars indicate mean ± SEM. *significant difference between CVS-G and SAD-G ($P < 0.05$).

3.3.2 CVS-G partially traffics to lysosomes

The route of internalised RABV-G post-EEs was next investigated. Under the same treatment conditions, cells were labelled with CD63, a marker of late endosomes (LEs). The data showed that both CVS-G and SAD-G did not significantly co-localise with CD63 positive endosomes (Figure 3.7A-C). To label lysosomes, cells were labelled with RABV-G and Magic Red. Following co-labelling, a small number of CVS-G puncta colocalised with magic-Red positive lysosomes (Figure 3.7B), indicating that some of the internalising RABV-G puncta traffic to lysosomes, but most puncta either subvert or rapidly bypass the late endosomal system.

A

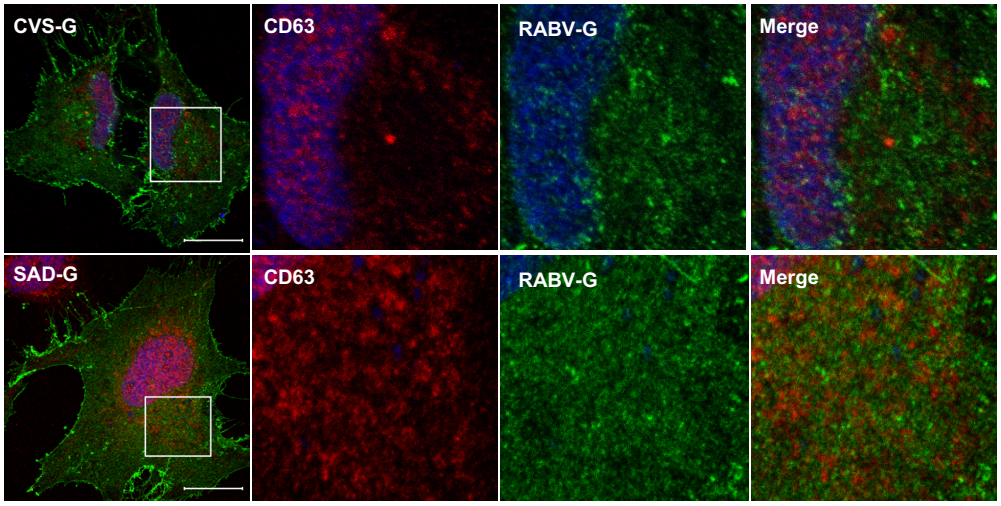

B

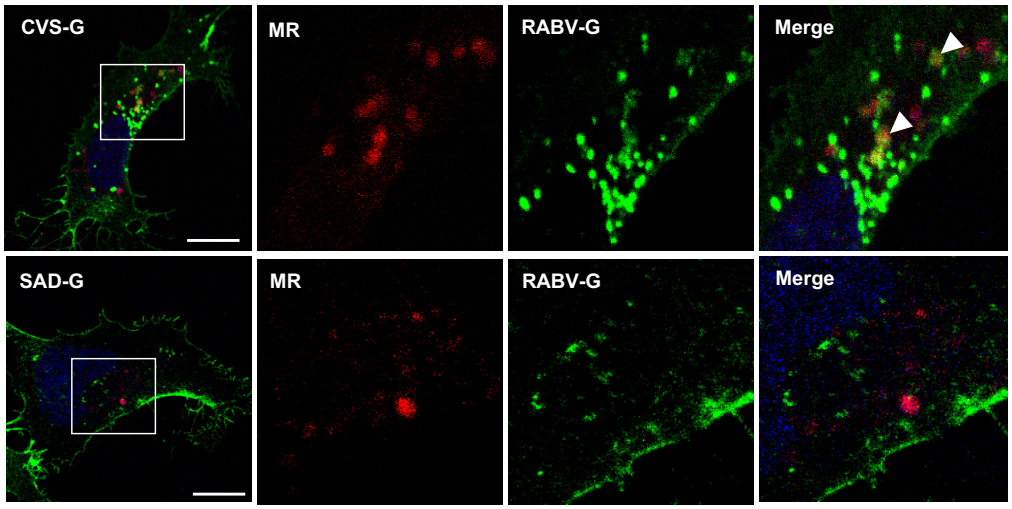

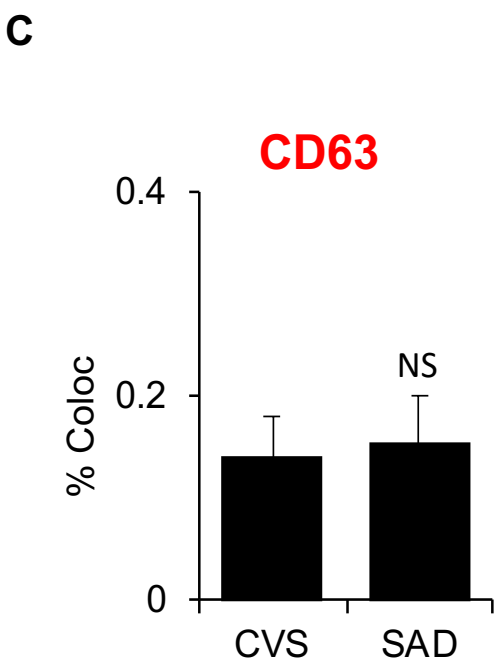

Figure 3.7 RABV-G partially traffics to lysosomes. (A) RABV-G expressing cells were colabelled with RABV-G and CD63 (1:200), no significant colocalisation was observed. **(B)** Live cells were colabelled with RABV-G and Magic Red (1:250), a marker of lysosomes. Few CVS-G puncta were colocalised with Magic Red (white arrowhead) whereas no visible SAD-G puncta were seen colocalising with Magic Red, indicating that RABV-G eventually traffics to lysosomes at perhaps high expression levels, scale bar = 10 µm. **(C)** Quantitative analysis of five cell image z-stacks show that both CVS-G and SAD-G only minimally colocalise with CD63. Error bars indicate mean ± SEM.

3.3.3 Live colabelling with EGF confirms lysosomal trafficking

To further confirm the route of CVS-G and SAD-G entry, cells were treated with labelled epidermal growth factor (EGF) during RABV-G antibody labelling at endocytic temperatures. EGF typically binds to cell surface expressed EGFR and then traffics via a clathrin dependent route into EEs, LEs and lysosomes (Dykes et al., 2017). After colabelling live RABV-G-expressing cells for 2 hours, approximately 40% colocalisation was observed between internalising CVS-G and EGF puncta compared to ~20% between SAD-G and EGF puncta (Figure 3.8). At this timepoint and labelling conditions, these results indicate that CVS-G and SAD-G take different routes of cell entry – a faster EE and lysosome route for CVS-G compared to alternative slower route for SAD-G.

A

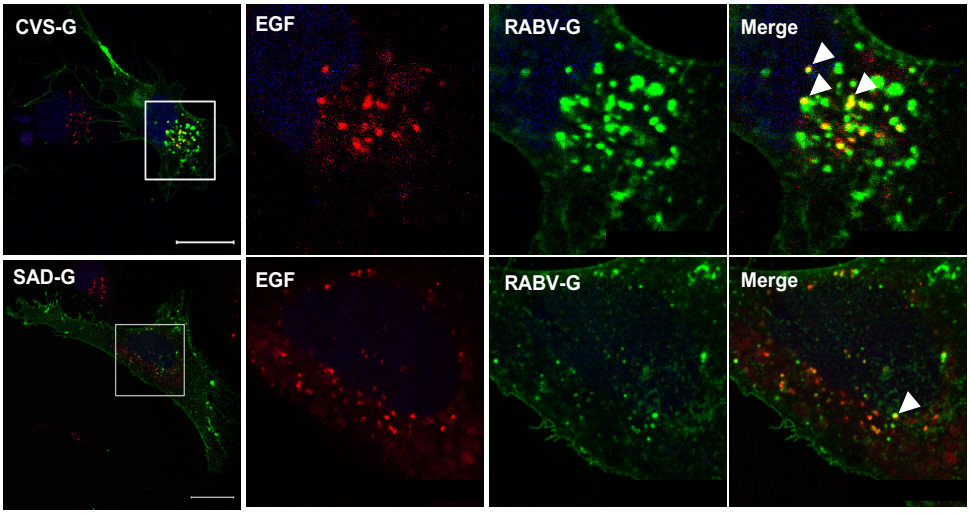

B

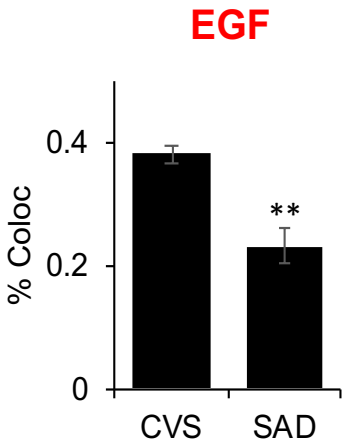

Figure 3.8 EGF co-labelling confirms RABV-G trafficking to EEs and lysosomes. (A) RABV-G expressing cells were colabelled with RABV-G and EGF-594 (1:250). CVS-G puncta colocalised with EGF (white arrowheads) to significantly higher levels than SAD-G (white arrowheads). Scale bar = 10 µm. **(B)** Quantitative analysis of five z-stacks showing that ~40% of internalising CVS-G puncta colocalised with internalising EGF vs. ~ 25% for SAD-G following 2 h of live, surface labelling. Error bars indicate mean ± SEM. **significant difference between two conditions ($P < 0.005$).

3.3.4 Live co-labelling with Tf shows higher rates of SAD-G trafficking through recycling endosomes

The trafficking profile of SAD-G suggests that it internalises into EEs then traffics towards an intracellular region close to the PM (see Figure 3.5B). To further assess the nature of these SAD-G puncta, cells were live labelled with Texas-Red-Transferrin (Tf), a characterised marker of recycling endosomes

following its binding to TfR and subsequent internalisation (Mayle et al., 2012). Colocalisation analysis revealed that despite the higher numbers of internalised puncta for CVS-G, significantly fewer co-localised with Tf compared to SAD-G (Figure 3.9A). This higher association of SAD-G with Tf (Figure 3.9A white arrowhead) may be suggestive of its movement into REs, on route to its recycling back to the PM. This may explain the high surface expression of SAD-G observed, and the reduced presence of intracellular SAD-G compared to CVS-G.

A

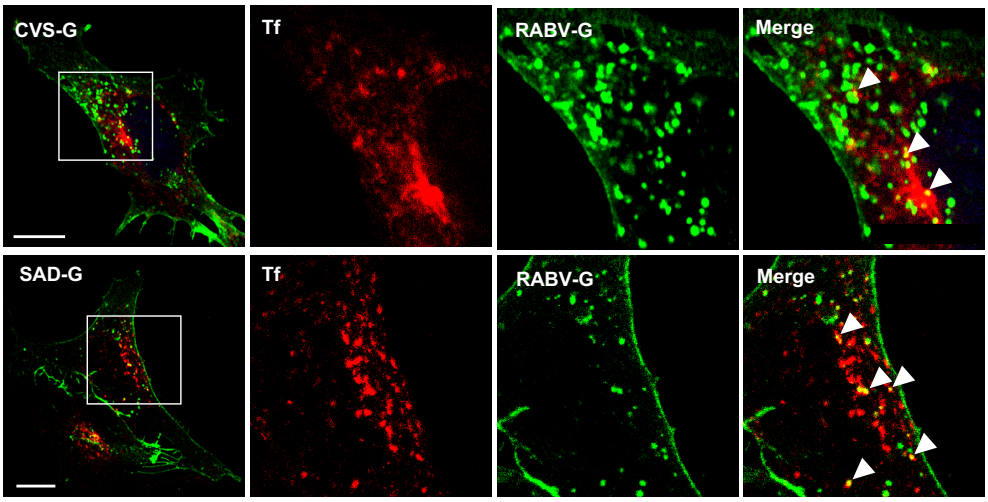

B

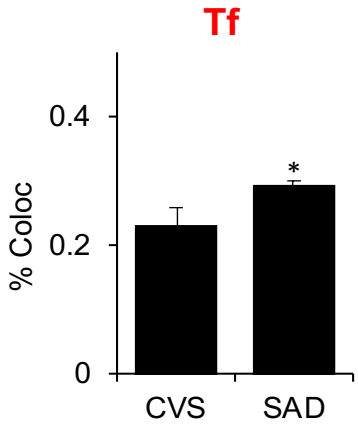

Figure 3.9 Tf co-labelling suggests that SAD-G traffics towards recycling endosomes. (A) RABV-G expressing cells were colabelled live with RABV-G and Tf-Texas-Red (1:250). Both CVS-G and SAD-G colocalised with Tf (white arrowhead) though these levels were higher for SAD-G, suggesting that a higher percentage of internalising SAD-G puncta traffic through REs, scale bar = 10 µm. **(B)** Quantitative analysis of z-stacks. Error bars indicate mean ± SEM. *significant difference between CVS-G and SAD-G ($P < 0.05$).

3.3.5 Drug treatments suggest that CVS-G internalises via both clathrin and cholesterol mediated routes

The endocytic route through which RABV-G internalises was next assessed. Cells were pre-treated with characterised inhibitors of clathrin, caveoale, and micropinocytosis uptake pathways and RABV-G antibodies were added to live cells in the presence of each drug for 90 min prior to fixation and imaging (Figure 3.10). Upon quantification, PitStop2 (CME inhibitor) significantly inhibited more than ~70% of CVS-G internalisation, confirming it as a major route of CVS-G endocytosis. Of interest, the low levels of SAD-G that did internalise, were similarly inhibited by PitStop2 (Figure 3.10B-C). Internalisation was next investigated in the presence of methyl-β-cyclodextrin (MβCD), a cholesterol-sequestering drug that inhibits cholesterol dependent endocytosis. CVS-G internalisation was again significantly inhibited by MβCD whilst SAD-G internalisation was unaffected, suggesting that CVS-G internalised through both CME and cholesterol dependent routes, whilst SAD-G internalised through CME alone (Figure 3.10B-C). Ethylisopropylamiloride (EIPA), a macropinocytosis inhibitor, caused no observable effect on the internalisation of either G protein, suggesting that neither CVS-G nor SAD-G internalise via micropinocytosis (Figure 3.10B-C).

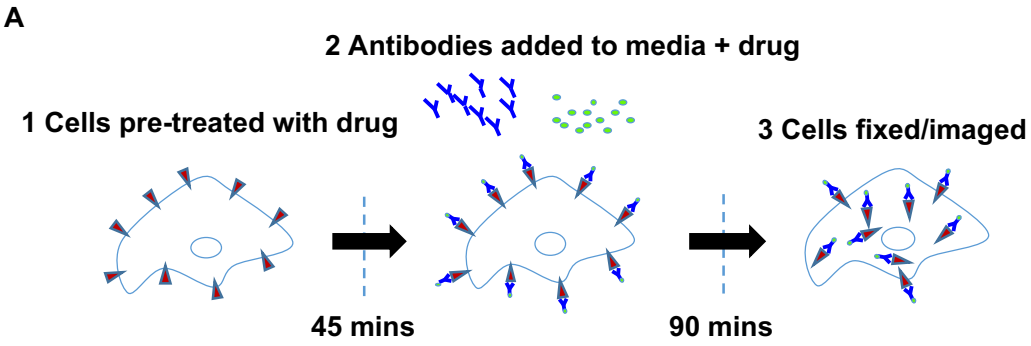
A
2 Antibodies added to media + drug
1 Cells pre-treated with drug
3 Cells fixed/imaged
45 mins
90 mins

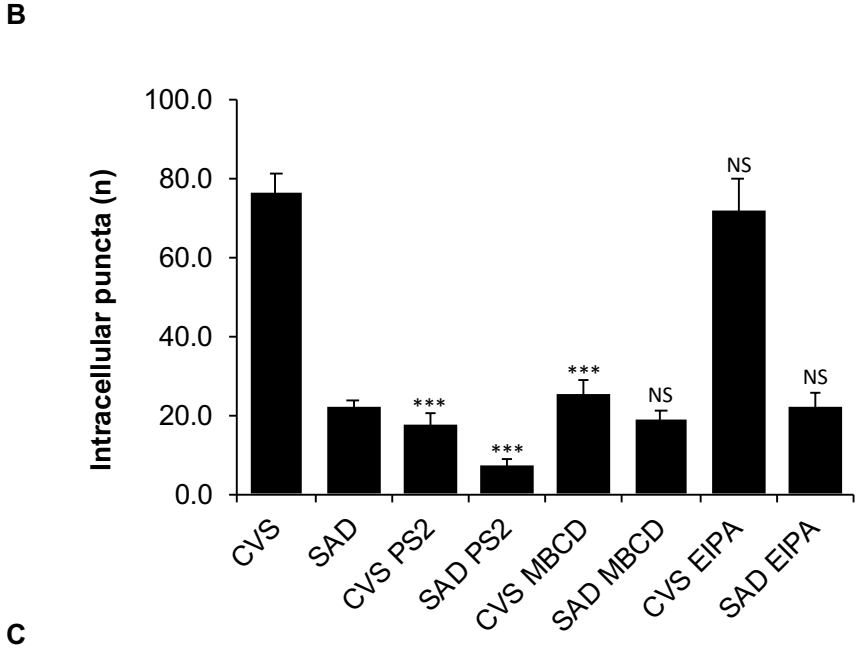
B
Intracellular puncta (n)
100.0
80.0
60.0
40.0
20.0
0.0
***
***
***
NS
NS
CVS
SAD
CVS PS2
SAD PS2
CVS MBCD
SAD MBCD
CVS EIPA
SAD EIPA

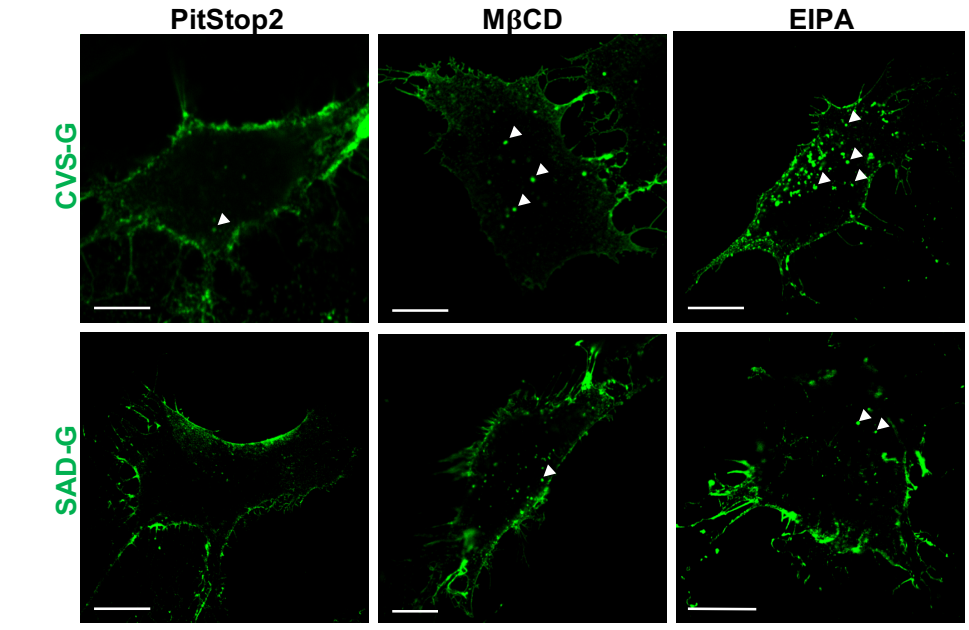
C
PitStop2
MβCD
EIPA
CVS-G
SAD-G

Figure 3.10 RABV-G internalisation is mostly through CME. (A) RABV-G expressing cells are pre-treated with the drug for 45 min followed by 90 min treatment with antibodies + drugs. Then cells are fixed and imaged. **(B)** Quantifications of average number of intracellular puncta suggest that both RABV-Gs are affected by the CME inhibitor PitStop2 (30 μM) and only CVS-G is affected by the cholesterol sequestering drug MβCD (2 mM) and no RABV-G is affected by the micropinocytosis inhibitor EIPA (25 μM). This suggests that Both RABV-Gs are internalising through CME and only CVS-G simultaneously use cholesterol-based entry that could be lipid rafts-mediated. Error bars indicate mean ± SEM. ***significant difference between two conditions ($P < 0.0005$). **(C)** Representative images of each treatment. Internalised puncta are shown with white arrowheads. Scale bar = 10 μm.

3.4 RABV-G internalisation regulation and validation

3.4.1 Internalisation difference is observed in other cell lines

Given these data, it was next validated that the differences in internalisation of CVS-G and SAD-G were not a result of a cell line artefact. To investigate this, HEK293T and SH-SY5Y cells were transfected and labelled live for 90 min. Upon analysis, comparable internalisation profiles were observed, namely CVS-G showed a high number of internalised puncta indicative of its greater levels of internalisation than SAD-G, that was mainly cell surface associated (Figure 3.11A). Acid stripping assays in SH-SY5Y cells also showed protection of the intracellular CVS-G puncta and almost a complete loss of the SAD-G signal, again signifying lower levels of internalisation (Figure 3.11B). These results suggest that the differences in internalisation rates between CVS-G and SAD-G are not cell line dependent, and represent an altered trafficking behaviour between these two proteins.

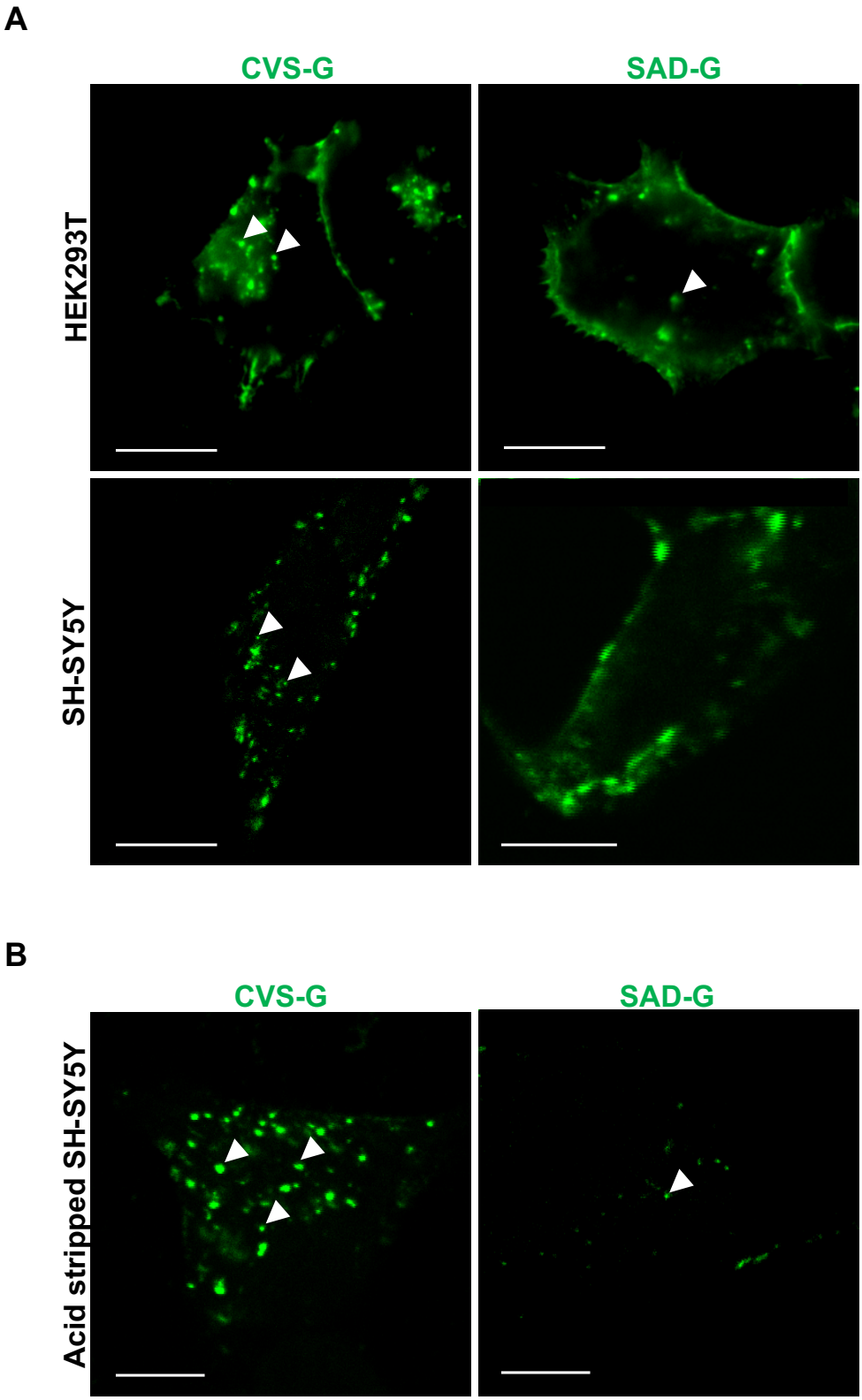

Figure 3.11 Internalisation in other cell lines. (A) CVS-G or SAD-G were transfected into HEK293T or SH-SY5Y cells and CVS-G was observed to internalise more readily than SAD-G in both cell lines, confirming previous observations. Scale bar = 10 μm. **(B)** Surface acid stripping of RABV-G-antibody complexes in SH-SY5Y confirms CVS-G puncta protection.

3.4.2 CVS-G internalisation occurs in more physiological neuronal models

To further confirm that the internalisation of CVS-G takes place in more physiological models of RABV infection, SH-SY5Y cells were differentiated into neuronal-like cells using the protocol described by Dwane et al., 2013. Briefly, cells were adhered to the substratum through the addition of laminin and treated with IGF-I for 4 days. Differentiated cells typically shrink in size and develop long neurite projections (Figure 3.12A white arrowheads). Differentiation was confirmed through GAP43 probing through both immunofluorescence and western blots as previously described (Figure 3.12B). Differentiated neurons were then transfected with CVS-G and live antibody labelled as described. As previously observed, CVS-G could be observed at the plasma membrane and accumulated in intracellular puncta in the neuronal cell body and in axon-like projections. In contrast, SAD-G expressing neurons showed mostly surface expression with limited intracellular localisation that are suggestive of internalisation (Figure 3.12C). This suggests that both RABV-G variants are expressed at the surface of more physiological neuronal models and that CVS-G internalises and accumulates in neuronal cell bodies.

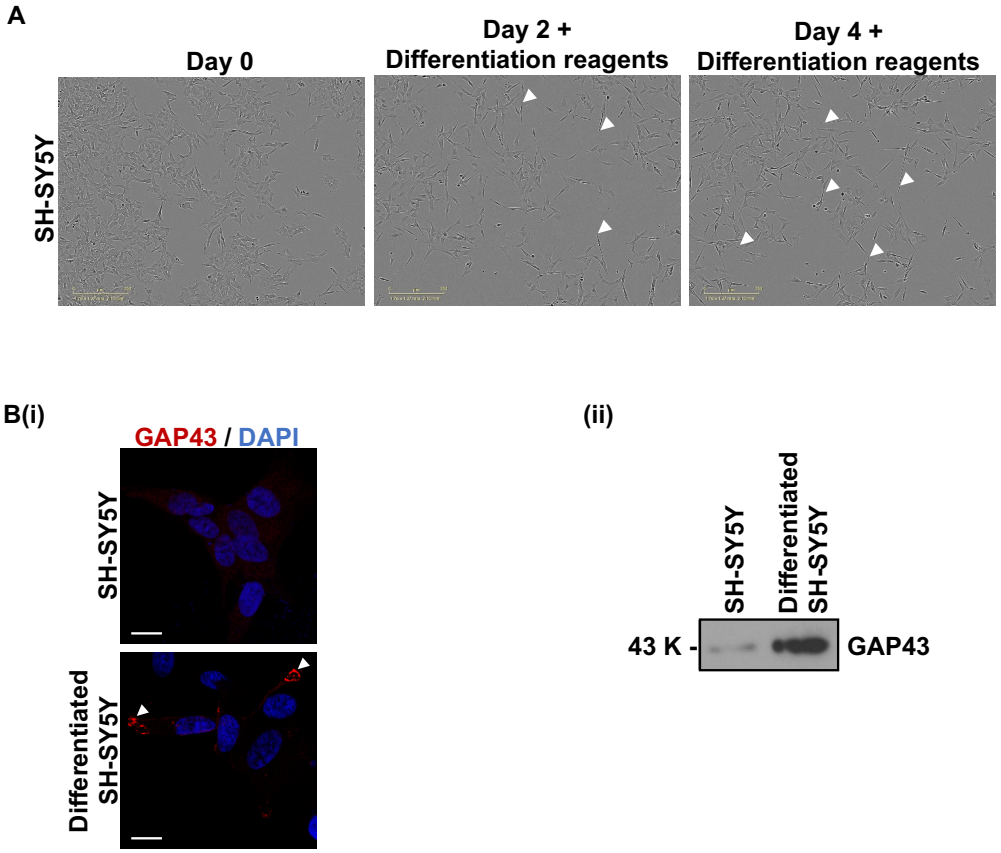

C

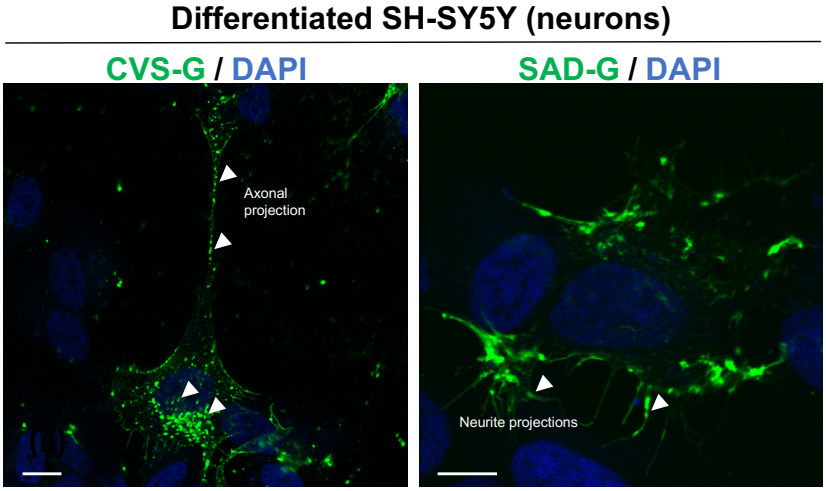

Figure 3.12 CVS-G undergoes internalisation in neurons. (A) SH-SY5Y cells were differentiated by plating on laminin and supplementation with IGF-I for 4 days. Differentiated cells shrink and extend long projections. **(B)** Differentiation was confirmed by probing GAP43 in **(i)** IF images (1:200) and **(ii)** western blots (1:1000). **(C)** Representative images of live labelled CVS-G transfected neurons show preferential accumulation in the soma of the neuron's cell body and at an extended axon-like projection (white arrowhead). SAD-G expressing neurons show mostly localisation at the PM (white arrowhead) with minimal internalisation, scale bar = 10 μm.

3.4.3 Trafficking and internalisation of other RABV-G variants

So far, pathogenic CVS-G had been shown to rapidly internalise from the PM, whilst attenuated SAD-G showed mostly PM localisation with low levels of internalisation. To investigate if this internalisation event is a feature of pathogenic RABV-G proteins, other pathogenic RABV-G variants were investigated. DOG-G is derived from a circulating virus isolate from Azerbaijan that shows a diffuse expression at steady state with the presence of some intracellular puncta (Figure 3.13A white circle). EBLV-G is European bat lyssavirus 1 and shows both PM and diffuse expression in cells (Figure 3.13A). When these RABV-G variants were live labelled from the PM, both showed rapid internalisation, with DOG-G in particular showing almost a complete loss of PM expression, and a large number of intracellular puncta (Figure 3.13B). Taken together, these data suggest that rapid internalisation from the PM is a trait of pathogenic RABV-G proteins.

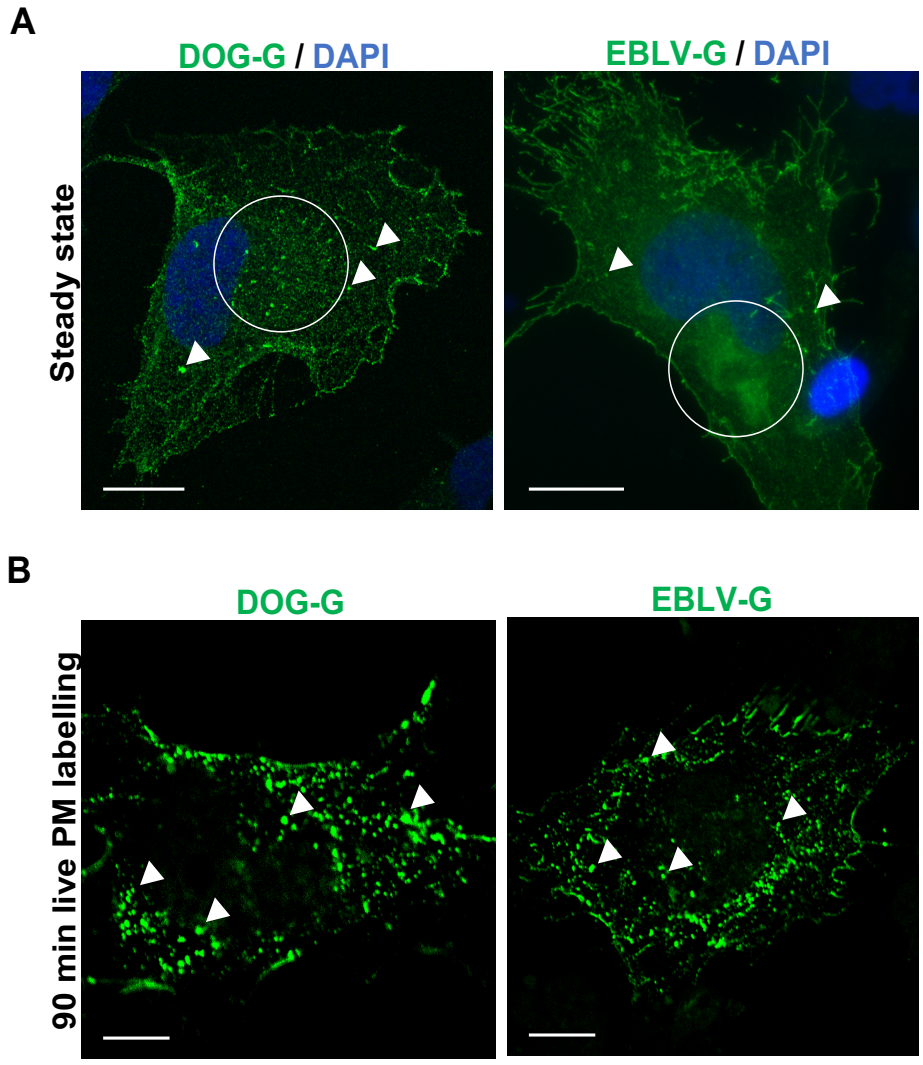

Figure 3.13 Steady state and internalisation of DOG-G and EBLV-G. (A) Fixed and permeabilised cells were labelled and DOG-G showed dispersed expression with some perinuclear accumulation (white circle). EBLV-G showed dispersed expression and PM expression with significant perinuclear localisation (puncta highlighted with white arrowhead). **(B)** Live labelling for 90 min showed that both RABV-G variants internalise quickly from PM and DOG-G show almost no surface expression, despite labelling from the cell surface. Scale bar = 10 µm.

3.4.4 Internalisation is partially dictated by the RABV-G C-terminus

The regions responsible for the internalisation of pathogenic RABV-G proteins were next investigated. To achieve this, CVS-G and EBLV-G were engineered to express the cytoplasmic tail of SAD-G, creating $CVSG_{SADT}$ and $EBLVG_{SADT}$ chimeric proteins (Figure 3.14A). Quantitative analysis of live-labelled cells for 90 min that expressed these chimeric proteins showed $CVSG_{SADT}$ having ~50% reduction in CVS-G internalisation behaviour, whilst $EBLVG_{SADT}$ reverted to an almost exclusive SAD-G-like phenotype with low levels of

internalisation, evidenced by the low numbers of intracellular puncta (Figure 3.14B-E). Whilst the more pronounced effect in EBLVG$_{SADT}$ is unknown, these data strongly suggest that the C-terminal tail of RABV-G is the key dictator of internalisation in both CVS-G and EBLV pathogenic proteins.

A

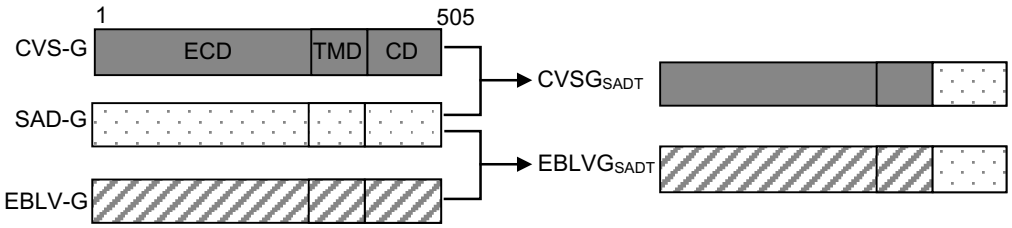

B

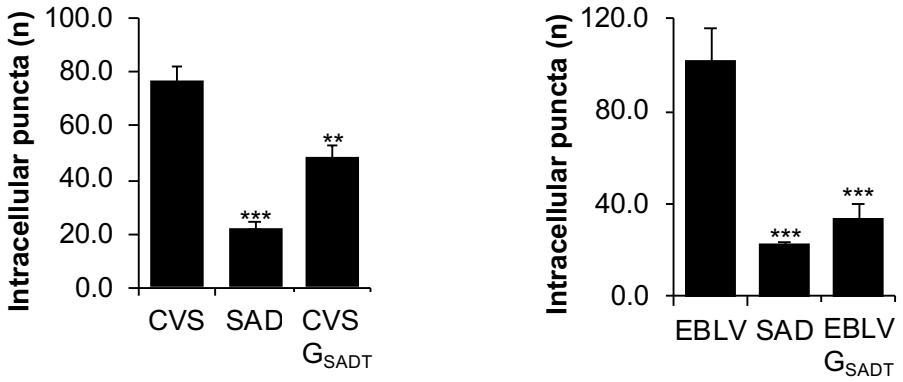

C

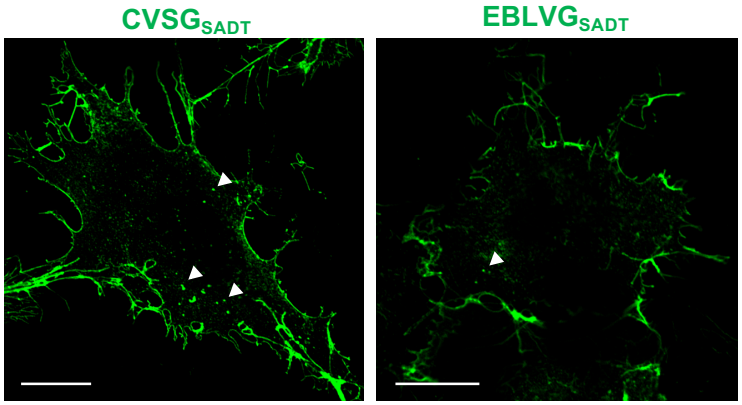

Figure 3.14 RABV-G C-terminus regulates internalisation. (A) Schematics of how $CVSG_{SADT}$ and $EBLVG_{SADT}$ chimeric RABV-G proteins were created. **(B)** Quantitative analysis of 90 min live labelled cells expressing $CVSG_{SADT}$ show approximately half the rate of internalisation of CVS-G. $EBLVG_{SADT}$ had almost complete reversion to SAD-G internalisation. Each condition is an average of 25 cell images. Error bars indicate mean ± SEM. ** or ***significant difference between two conditions ($P < 0.005$ or 0.0005). (**C)** Live Representative images show attenuated internalisation for both $CVSG_{SADT}$ and $EBLVG_{SADT}$ with $EBLVG_{SADT}$ showing SAD-G-like low rate of internalisation. Internalising puncta highlighted with white arrowhead, scale bar = 10 μm.

3.4.5 Several residues in the C terminus influence the internalisation of CVS-G

Given the apparent regulation of internalisation from within the RABV-G cytoplasmic tail, it was logical to investigate the specific residue(s) involved. To achieve this, a total of 11 residues in CVS-G at locations that differed to SAD-G but were retained in DOG-G which similarly undergoes rapid internalisation were investigated (Figure 3.15A). The expression and internalisation rates of each mutant were investigated following 90 min live labelling through quantification of the number of internalising puncta. The results showed that four mutations (S469A, F474A, G475A and Y497A) led to a decrease in the number of internalising CVS-G puncta, whilst surprisingly, P492A significantly increased the number of internalising puncta, as compared to WT CVS-G (Figure 3.15B). These observations suggest that internalisation is regulated by several residues, whilst P492A likely disrupts the stability of CVS-G at the PM leading to its rapid surface removal (Shakin-Eshleman et al., 1992; Yamada et al., 2013). Interestingly, all apathogenic live vaccine strains originating from the SAD strain possess a H_{497} instead of Y_{497} (Figure 3.15C), the point mutation which led to the most pronounced inhibition of CVS-G endocytosis. These results suggest that P_{492} is essential for CVS-G PM expression and that Y_{497} is a major residue implicated in CVS-G internalisation.

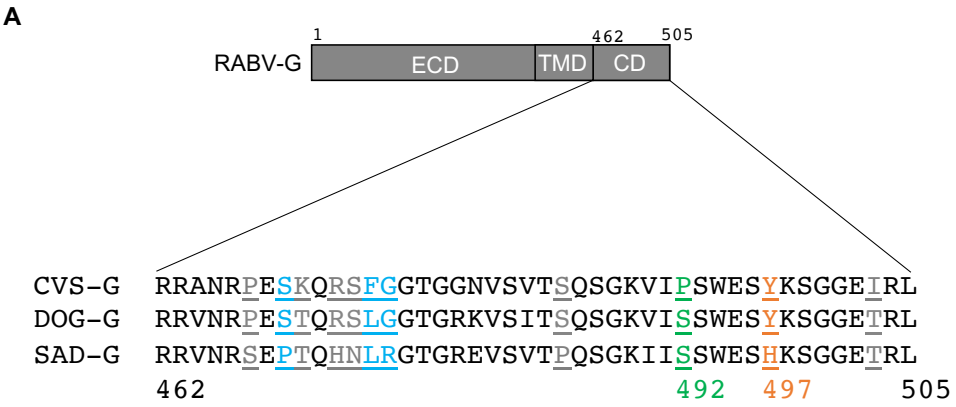

B(i)

Table 2 | Cytoplasmic tail alanine scanning mutants of CVS-G

Mutant	Effect
P467A	No effect
S469A	Decreased internalization
K470A	No effect
R472A	No effect
S473A	No effect
F474A	Decreased internalization
G475A	Decreased internalization
S485A	No effect
P492A	Enhanced internalization
Y497A	Significantly decreased internalization
I503A	No effect

(ii)

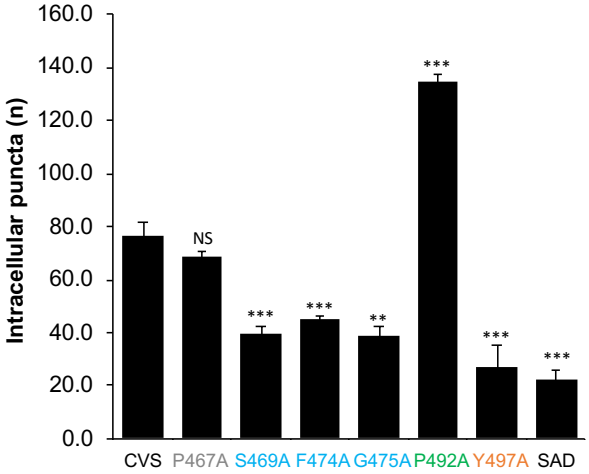

C

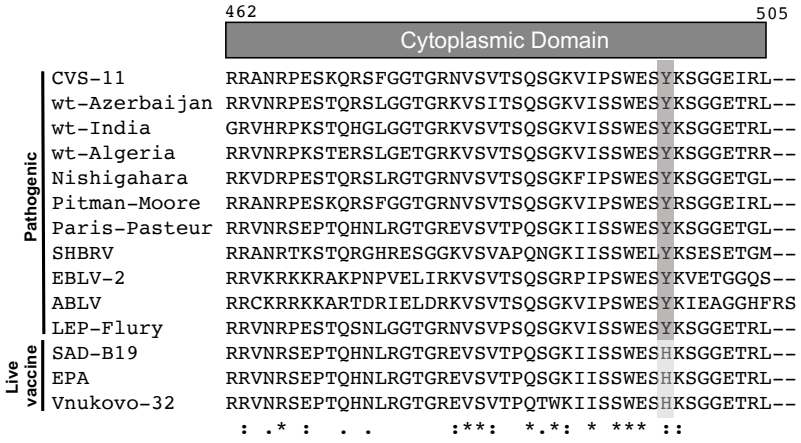

Figure 3.15 Alanine scanning reveals residues involved in internalisation regulation. **(A)** Schematics of the 11 residues mutated in CVS-G to alanine. These residues differ in SAD-G and are conserved in DOG-G, a wild type pathogenic strain. **(B)** Quantitative analysis of 90 min live labelled cells expressing the 11 mutants show that S_{469}, F_{474}, G_{475} and Y_{497} decrease the rate of internalisation when mutated to alanine and P492A increases the rate of internalisation through most likely a disruption of PM retention. Each condition is an average of 25 cell images. Error bars indicate mean ± SEM. ** or ***significant difference between two conditions ($P < 0.005$ or 0.0005). (**C**) SAD-derived live attenuated strains all possess a conserved Y497H mutation. This loss of tyrosine might be why these attenuated strains are PM localised.

3.5 Discussion

Data presented in this chapter show that when mammalian cell lines are transfected with RABV-G from CVS or SAD, CVS-G is rapidly internalised from the PM which effectively limits its levels of surface exposure, whilst SAD-G undergoes low levels of endocytosis, leading to higher PM expression. This observation was validated through labelling at non-endocytic permissive temperatures and surface acid stripping that showed protected internalised puncta for CVS-G. It was further shown that internalising CVS-G puncta traffic through EEs to lysosomes. Fewer internalising SAD-G puncta traffic through EEs then follow lysosome route, with most accumulating at REs following 2 h of live surface labelling.

The internalisation behaviour was conserved in different cell lines and other pathogenic strains internalised in a similar manner to CVS-G. The domains of CVS-G that mediate this rapid internalisation event were then investigated by creating RABV-G chimeric proteins, and through alanine scanning the cytoplasmic tail to reveal several residues contribute to internalisation. Y_{497} had the strongest effect on CVS-G internalisation and is conserved between all pathogenic strains. Live-attenuated strains derived from SAD all possess a conserved H_{497} at this position. This loss of the tyrosine in the RABV-G cytoplasmic tail may explain why SAD-G and perhaps other attenuated strains undergo low levels of endocytosis and are primarily surface-localised. This surface localisation may explain SAD attenuation through the exposure of the SAD-G in infected cells to antigen-presenting cells (APC), leading to its recognition and ultimately clearance of the virus (Yang et al., 2015; Li et al., 2019). The *in vitro* data suggest that *in vivo* validation should be performed to ascertain if the attenuation of internalisation is directly related to RABV pathogenicity. This can be achieved through reverse genetic approaches through the mutation of these residues in fully infectious virus systems and assessment of the pathogenicity of these mutant strains. At the time of writing, the Y_{497} mutation has been introduced into the fully infectious clone of CVS-G, and its *in vivo* assessment is under investigation in the laboratory of collaborator Prof Stefan Finke.

3.5.1 CVS-G internalisation

Following RABV entry, RNPs are released into the cytoplasm and transcription occurs through RABV-encoded RABV-L. Following the transcription of RABV-G, this virus coat protein is transported to the rough ER where it is translated as a membrane-embedded protein. RABV-G is then trafficked to the PM via the Golgi apparatus where it remains until virus assembly is complete (See 1.4). The data in this chapter show that CVS-G then undergoes internalisation via CME and non-clathrin routes, as drug treatment with PitStop2 and MβCD inhibited the accumulation of intracellular/internalising CVS-G puncta.

The internalisation of virus envelope proteins expressed at the cell surface is commonly observed with a variety of viruses (Bu et al., 2004; Vogt et al., 2005; Favoreel et al., 2006). The biological relevance of this internalisation is not well understood. Retroviruses such as human and simian immunodeficiency viruses (HIV and SIV, respectively) internalise gp41 envelope proteins to avoid antibody detection (von Bredow et al., 2015). Nipah virus (NiV) fusion protein internalisation is essential for cathepsin L activation (Vogt et al., 2005). Parainfluenza virus 5 (PIV-5) HN glycoprotein internalisation is directly related to virus fitness (Robach and Lamb, 2010). Many groups have linked this downregulation of viral antigen surface expression to reduced recognition of infected cells by the immune system (Marsh and Pelchen-Matthews, 2000; Van de Walle et al., 2003; Bu et al., 2004; Favoreel et al., 2006). RABV-G surface expression levels have similarly been linked to immune detection (Yang et al., 2015; Li et al., 2019) and this thesis is the first to link this internalisation/ reduced surface expression to pathogenic variants of RABV-G, as attenuated RABV-G variants (SAD-G) do not efficiently internalise and mostly remain surface exposed.

Virus envelope internalisation is spontaneous but can be induced by antibody interaction with envelope proteins expressed at the cell surface, followed by internalisation of antibody-antigen complexes in the cell. The latter is observed with RSV (Leemans et al., 2017), pseudorabies herpesvirus (Ficinska et al., 2005), and varicella zoster herpesvirus (Shiraki et al., 2011). Of note however, distinct phenotypic differences in the internalisation of CVS-G and SAD-G

were observed here that would not occur if antibody labelling induced the internalisation of all PM RABV-G proteins. In addition, differences in steady state trafficking of both proteins in fixed cells was clearly observed between CVS-G and SAD-G (Figure 3.1) in which the majority of SAD-G was cell surface expressed, supporting the theory that pathogenic CVS-G rapidly internalises.

3.5.2 SAD-G internalisation

The slow internalisation rate of attenuated RABV strains was indirectly reported 35 years ago. Dietzschold and colleagues (1985) reported that when anti-RABV-G antibodies were added to ERA infected cells for 45 min, the ERA strain was prevented from infecting nearby cells whereas CVS was unaffected, indicating low CVS-G exposure to extracellular antibodies. This phenotype may be related to the rapid endocytosis observed for pathogenic CVS-G that correlates with low PM expression levels. This rapid endocytosis is absent in attenuated SAD-G/ERA-G that remains PM expressed and exposed to extracellular antibodies. SAD-G and ERA-G share ~99.4% sequence identity so it is likely that the two glycoproteins are phenotypically identical. CVS-G and SAD-G share 87.2% sequence identity.

The data presented in this Chapter also suggest that SAD-G traffics in a distinct manner to CVS-G. The low levels of internalising SAD-G proteins colocalised with EEs and REs over-time after co-labelling in fixed cells. Studies by Pierre and colleagues compared ERA-G surface labelling to steady state labelling. They observed that when live labelled, ERA-G traffics from EEs to LEs and lysosomes, whilst steady-state labelled ERA-G trafficked from EEs to REs (St. Pierre et al., 2011). They deduced that antibody-binding to ERA-G causes this glycoprotein to shift from recycling endosomes to degradative endosomes. Live-labelled SAD-G also accumulated intracellularly over time (Figure 3.5) and when colabelled with a lysosome marker, a small proportion of SAD-G showed evidence of lysosomal trafficking (Figure 3.7B). Given that SAD-G internalised at a lower rate, it may follow a similar trafficking pattern if investigated over a longer time period. Importantly in this study, CVS-G showed more rapid surface removal than SAD-G, which may represent a key feature of pathogenic RABV-G proteins.

3.5.3 Regulation of internalisation

The production of RABV-G chimeric proteins showed that the internalisation of CVS-G could be reduced ~50% upon replacement of its cytoplasmic tail with SAD-G, whilst EBLV-G internalisation was almost completely reduced to the levels of SAD-G by the SAD-G tail (Figure 3.14). Upon alanine scanning of CVS-G at residues in the cytoplasmic tail that differed to SAD-G, Y_{497} had the most pronounced effect on internalisation. Of interest, this is the only tyrosine residue in the cytoplasmic tail of RABV-G (Figure 3.15C). Tyrosine residues in cytoplasmic tails have long been associated with endocytic motifs (Ochsenbauer et al., 2000; Favoreel et al., 2002; Ilinskaya et al., 2010) and this study was the first to investigate the single tyrosine residue Y_{497} in the internalisation of RABV-G. It is likely that this residue has been missed in this context as it does not conform to consensus YXXΦ motif where X is any residue and Φ is a residue with a bulky side chain. Most RABV-G variants do however possess a conserved WXXYXXGG sequence that conforms to the previously described unconventional internalisation motif YXXGL (Royle et al., 2002) or may represent a flipped YXXΦ sequence as W is an amino acid with a bulky side chain upstream of the tyrosine residue. However, the additional contribution of identified upstream residues such as S_{469} and F_{474} in the internalisation event hints at a more complex motif that warrants further investigation.

All known SAD-derived live attenuated strains possess H_{497} instead of Y_{497}. Both SAD-B19 and ERA were derived from the original pathogenic SAD strain through passaging in different sets of cell lines (Conzelmann et al., 1990) and the occurrence of this conserved mutation between these attenuated strains hints at a role for H_{497} that does not perturb efficient replication in cell culture. RABV preferentially and naturally replicates in neuronal cells so this attenuation of SAD-B19 and similar strains likely occurred either through natural selection or due to the redundant role of immune evasion through cell surface downregulation that would occur in cell culture. This is in contrast to CVS that is mostly maintained in live mouse brains with an immune clearance pressure that means the Y_{497} and its role in rapid internalisation provides an

evolutionary advantage. Further *in vivo* validation will reveal the relevance of Y_{497} to virus internalisation, spread and pathogenesis.

Chapter 4 | Investigating the host cell proteins differentially targeted by pathogenic CVS-G and attenuated SAD-G

4.1 Introduction

Viruses are obligate parasites that exploit host cell processes to establish a cellular environment that favours their survival and propagation. RABV has a close to 100% infection: fatality rate, the highest of any known infectious disease (Fooks et al., 2014). This fatal disease can be circumvented with PEP biologics that introduce anti-RABV-G antibodies (World Health Organization, 2018), often lacking in those that suffer fatal RABV infections (Hemachudha et al., 1988; De Souza and Madhusudana, 2014). RABV strains attenuated through cell culture, including the SAD strain, raise a robust anti-RABV-G antibody response and are rapidly cleared from their hosts (Fooks et al., 2019). In Chapter 3, key trafficking differences were reported between the RABV-G proteins of the non-pathogenic SAD strain and the pathogenic CVS strain that may contribute to the differences observed in their disease outcome, given the known involvement of RABV-G in virus pathogenesis.

Understanding the contribution of RABV-G to the RABV lifecycle is key to the development of new targets for antiviral intervention, currently lacking in RABV research (Du Pont et al., 2019). Colchicine and vinblastine have been shown to prevent RABV intracellular transport through their ability to disrupt microtubules *in vitro*, but ~50% of mice treated with vinblastine succumb to RABV infection (Bijlenga and Heaney, 1978). Dynasore and AMBA inhibit RABV through their inhibition of dynamin-dependent virus-entry, but AMBA-treated mice failed to show protection to RABV *in vivo* (Wu et al., 2017). Favipiravir, an inhibitor of a number of viral RNA-dependent RNA polymerases, partially inhibits RABV spread *in vivo* (Yamada et al., 2016), whilst emetine can inhibit the neuronal transport of RABV in primary neuronal cells by preventing motor recruitment to RABV-containing endosomes (Gluska et al., 2014; MacGibeny et al., 2018). To-date however, a single drug with robust and verified anti-RABV efficacy has not been identified.

A better understanding of the host proteins that govern specific stages of the RABV lifecycle are paramount to the development of effective host-directed antiviral drugs. Early *in vivo* studies showed a marked difference in the host cell proteomes of cells infected with pathogenic or attenuated RABV strains. Attenuated RABV causes inflammation throughout the CNS and nerve cell

damage within the brain, both of which are absent in the brains of those infected with pathogenic RABV strains *in vivo* (Li et al., 2005; Wang et al., 2005). Several *in vitro* proteomics studies also showed marked changes in the expression of cytoskeleton proteins and those governing cell stress responses following RABV infection (Dhingra et al., 2007; Wang et al., 2011; Thanomsridetchai et al., 2011; Zandi et al., 2013). The proteomic profiling of RABV virions also revealed several scavenged trafficking proteins within RABV virions including DLC8, cofilin-1, Cdc42, RhoA and casein kinase (Tu et al., 2015; Y. Zhang et al., 2020). In this regard, Yin and colleagues (2020) compared the host interactomes of Flag-tagged CVS versus SAD and identified SNAP25, VDAC1, and the motor protein MYH10 as host cell proteins solely recruited by pathogenic CVS-G during virus infection.

In 2012, Roux and colleagues (2012) developed a proximity dependent biotin identification (BioID) system to permit the identification of weak, transient, and membrane-embedded protein binding-partners of a tagged target (Schubert et al., 2017). The proximity dependent biotin identification (BioID) was further refined through the utilisation of the smallest known biotin ligase from *Aquifex aeolicus* to decrease the size of the biotin ligase and introduce a flexible linker sequence that can increase the resolution of proximal proteins (Kim et al., 2016). Using the BioID system, novel virus-host interactions have been identified for HIV (Kueck et al., 2015; Staubus et al., 2019), Epstein-Barr virus (Holthusen et al., 2015; Rider et al., 2018), Zika virus (Coyaud et al., 2018) and coronavirus proteins (V'kovski et al., 2019). Importantly, the system has not to-date been utilised for the comparison of viral proteins from pathogenic and attenuated virus strains.

In this chapter, the host proteins that may contribute to the pathogenicity of RABV were investigated through the fusion of the BioID BirA* enzyme to both CVS-G and SAD-G. A list of proteins within a proximal distance to both proteins were then identified by mass spectrometry and compared. Several differential protein partners between CVS-G and SAD-G were subsequently identified and validated. A specific focus on non-muscle myosin IIA (MYH9), known to mediate filopodia outgrowth in RABV infection, was then performed.

4.2 RABV-G BioID generation

4.2.1 Experimental design

Proximity-based interactomics involves the fusion of a modified biotin ligase (BirA*) to N- or C- termini of a bait protein. For successful fusion of BirA* to the bait, the target protein must be validated to ensure its native trafficking is maintained. When exogenous biotin is added to cells exogenously expressing the BirA*-bait construct, BirA* biotinylates exposed lysines within a proximity of ~10 nm, tagging cellular partners that interact with, or come in close contact to the bait protein (Figure 4.1). Biotinylated proteins can then be isolated on Streptavidin-conjugated beads and identified via Tandem mass tagging (TMT) mass spectrometry analysis. Following the identification of the interactomes, major “hits” must be validated. This chapter describes experiments in which BirA* was successfully fused to the C-termini of both CVS-G and SAD-G, and the interactomes of these proteins compared to reveal those that differ between pathogenic and attenuated RABV-G proteins.

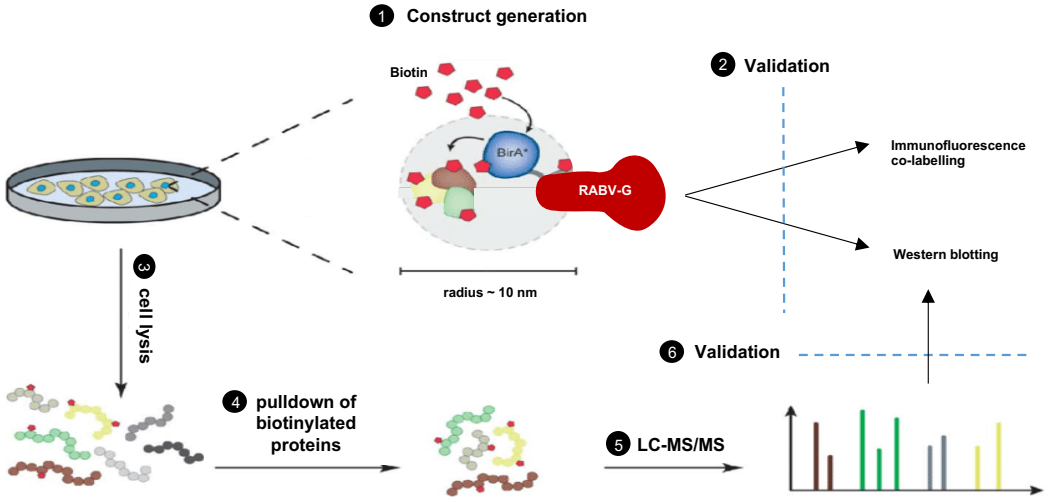

Figure 4.1 Schematic of the BioID protocol. (1) BirA* constructs were designed and generated; **(2)** biotinylation and normal protein trafficking were then validated through western blotting and immunofluorescence. Cells expressing the Bio-fusions were lysed **(3)** and **(4)** immunoprecipitations were performed using streptavidin-dynabeads. Biotinylated proteins were then sent for **(5)** TMT LC-MS/MS analysis. Resulting interactome datasets were **(6)** validated through immunofluorescence and western blotting.

4.2.2 Generation of BirA* fusion constructs

Codon optimised CVS-G and SAD-G were commercially synthesised by GeneArt (Invitrogen technologies). The Roux lab recently developed a smaller and more efficient version of BirA* containing a HA tag, and a glycine-based linker sequence to overcome the potential steric hindrance of BirA* fusions, which can improve the coverage of proteins proximate to the BirA* enzyme (Kim et al., 2016). CVS-G and SAD-G were cloned upstream or downstream of BirA* followed by the deletion of the respective interfering stop codons to produce BirA*-RABV-G fusions.

The two sets of constructs (Figure 4.2A) were generated to probe cytosolic (C-terminal constructs) or luminal trafficking regulators (N terminal constructs), as shown in Figure 4.2B. However, and of note, RABV-G is subject to cleavage at an N-terminal signal peptide (SP) sequence (Anilionis et al., 1982). BirA*-RABV-G fusions were therefore ligated downstream of the RABV-G N-terminal signal peptide. Through this design, it was hypothesised that the SP cleavage will guide the BirA*-RABV-G complex into the natural trafficking pathway of RABV-G.

A

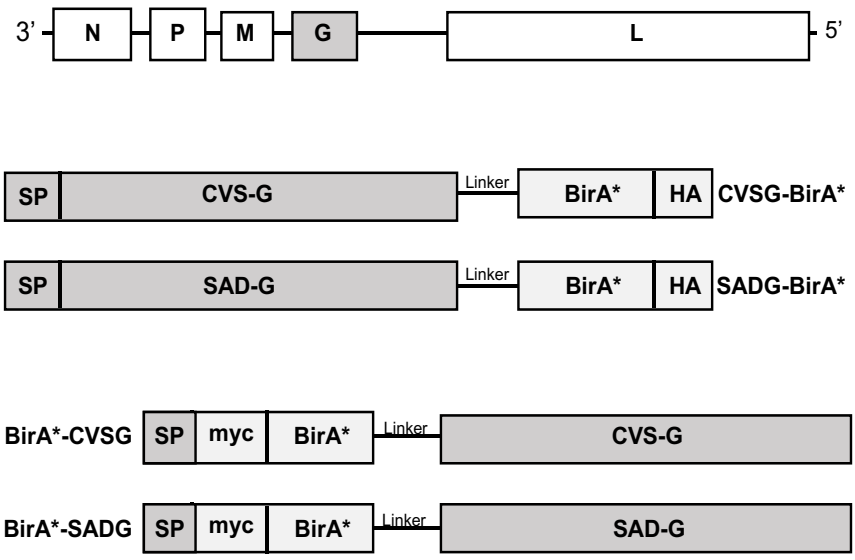

B

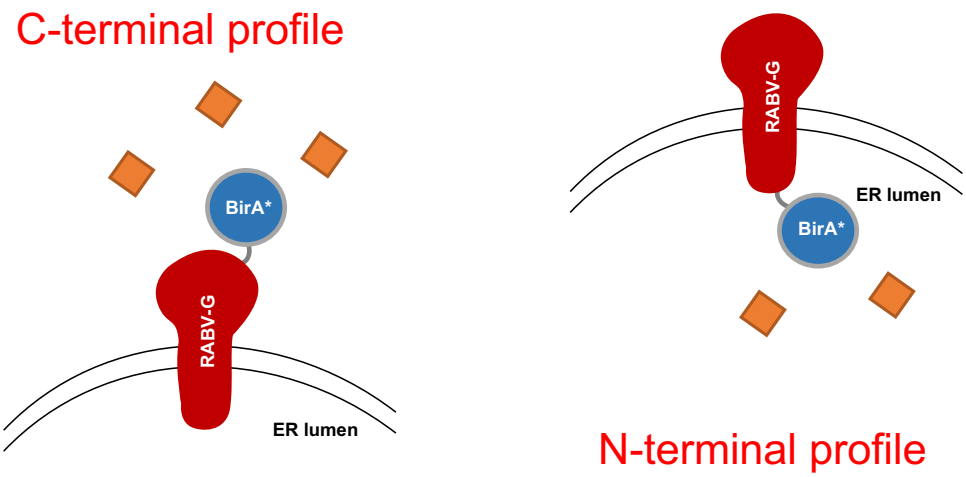

Figure 4.2 Generation of BirA* fusions. (A) RABV-G from CVS or SAD strains was synthesised and subcloned into the indicated BioID plasmids. RABVG-BirA* C-term constructs were generated through AfeI and BspEI restriction digest and the subsequent deletion of RABV-G stop codon. BirA*-RABVG N-term constructs were synthesised with SP upstream of BirA* construct, creating SP-BirA*-RABV-G. **(B)** Schematic of the BirA* fusions and the relative location of the BirA* tag.

4.3 BioID construct validation

4.3.1 Immunofluorescence biotinylation validation

The BioID system is dependent on the ability of BirA* to selectively biotinylate proteins in close proximity to the fused bait protein, in this instance CVS-G or SAD-G (Roux et al., 2012). To assess the selective biotinylation of proximate proteins, SVG-A cells were transfected with BirA* control, or C terminal or N terminal BioID fusion constructs. At 4 h post-transfection, the transfection media was replaced with serum-free DMEM supplemented with 50 µM biotin for BirA* activation (Roux et al., 2012). After 16 h, cells were fixed, permeabilised and labelled with E559 anti RABV-G antibodies and Streptavidin-549. When visualised, BirA* extensively biotinylated intracellular proteins compared to mock transfected cells that showed only background levels of biotinylation (Figure 4.3A), likely to include carboxylases and other endogenous biotin substrates (Roux et al., 2012; Tytgat et al., 2015).

Upon analysis of the BioID-RABV-G fusions, only cells expressing RABV-G showed visible levels of biotinylation (Figure 4.3Ai-ii), indicating that RABV-G BirA* fusions correctly biotinylate proximate proteins. In cells transfected with RABV-G-BirA* C-terminal constructs, high levels of biotinylated proteins were observed throughout the cells (white arrowheads) with almost no evidence of the biotinylation of nuclear proteins (Figure 4.3B). This contrasted that observed for both the CVS-G and SAD-G BirA* N-term constructs in which low levels of biotinylation were observed.

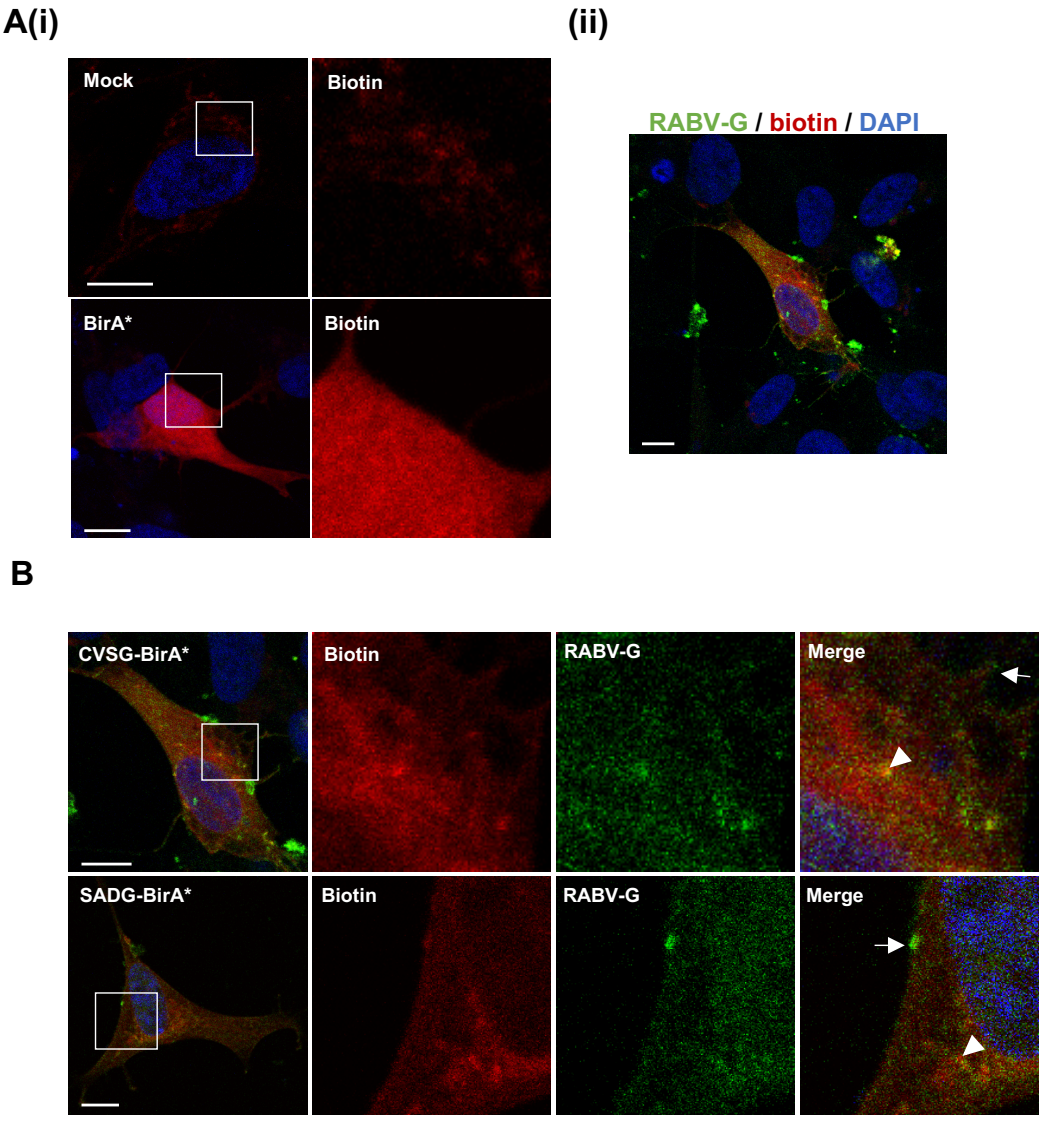

C

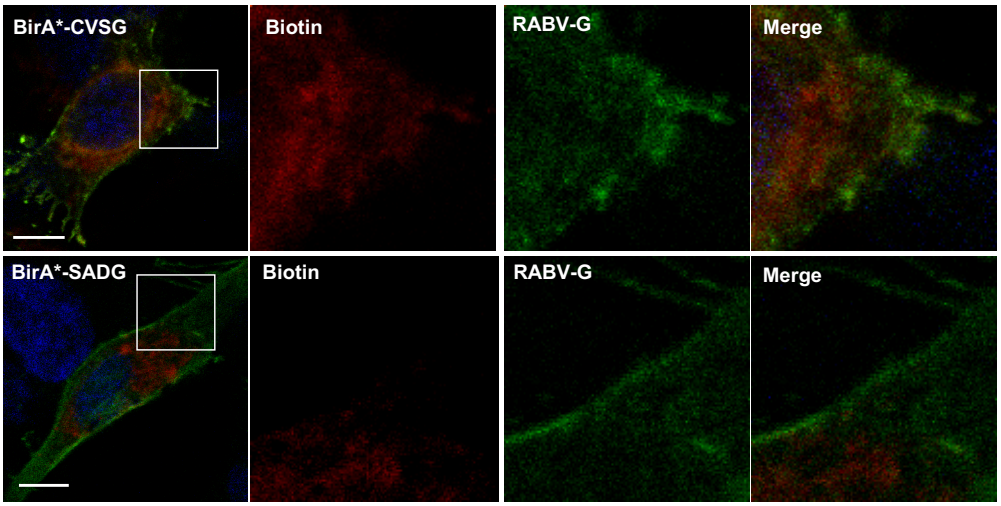

Figure 4.3 Immunofluorescent validation of the BirA* RABV fusions. (A) Cells transfected with **(i)** BirA* show extensive intracellular biotinylation of cellular proteins compared to mock transfected cells. **(ii)** Example of a RABV-G BioID cell showing extensive biotinylation of cellular proteins compared to the surrounding untransfected cells. **(B)** CVS-G and SAD-G BirA* C-term expressing cells show high levels of intracellular biotinylation (white arrowheads) compared to **(C)** low levels of biotinylation observed in cells expressing the BirA*-CVS-G and SAD-G N-term constructs. The **(B)** CVS-G image is a zoomed image of **A(ii)**. Scale bar = 10 µm.

4.3.2 Western blot validation of the RABV-G BirA* constructs

Next, biochemical validations of the BirA* constructs were performed. In the experiments that followed, HEK239T cells were transfected with BirA*, RABV-G-BirA* C-term constructs or BirA*-RABV-G N-term constructs and incubated in either serum free DMEM (-) or serum free DMEM supplemented with 50 µM biotin (+) for 16 h. Cells were then lysed in SDS-based BioID buffer and proteins were resolved by SDS-PAGE. Proteins were transferred onto PVDF membranes and probed with streptavidin-HRP (1:10,000) for 40 min to assess the levels of biotinylated proteins in the sample. The data showed that BirA* control cells showed an abundance of biotinylated proteins in response to the addition of biotin, compared to cells lacking biotin supplementation (Figure 4.4). CVSG-BirA* and SADG-BirA* C-term constructs showed similar levels of biotinylated proteins compared to the low levels observed in cells lacking biotin supplementation (Figure 4.4). Consistent with the immunofluorescence data, both the N-terminal BirA* fusions showed lower levels of biotinylated proteins in response to biotin supplementation (Figure 4.4.). The

housekeeping protein GAPDH was probed to confirm equal gel loading. These results indicate that C-terminally BirA* tagged RABV-G constructs can effectively biotinylate proximal proteins near the RABV-G cytoplasmic tail, in contrast to the N-terminally BirA* tagged constructs that fail to effectively biotinylate host proteins. CVSG-BirA* and SADG-BirA* C-term constructs were therefore selected for further characterisation.

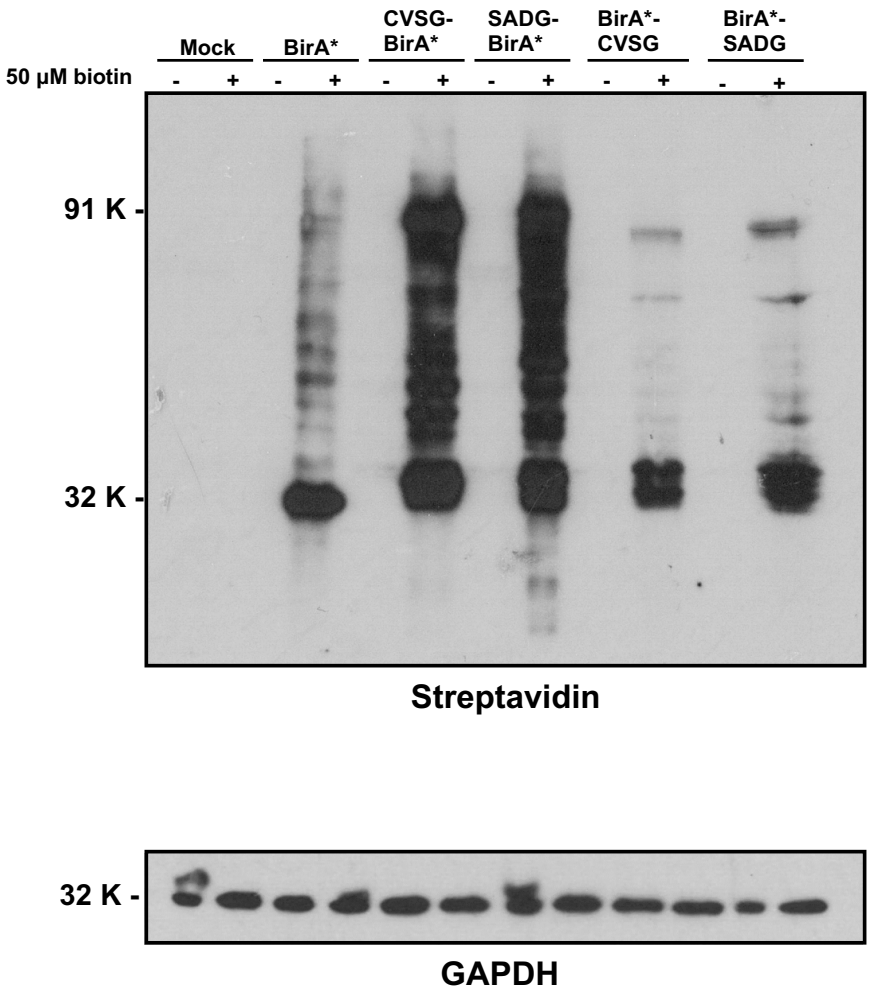

Figure 4.4 Western blot validation of the BirA* RABV-G constructs. HEK293T cells were transfected, lysed and probed with streptavidin-HRP to label biotinylated proteins. Western blot analysis suggested robust BirA*-mediated biotinylation in response to 50 µM biotin supplementation. BirA* fused to the C-terminal of both CVS-G and SAD-G showed high numbers of biotinylated proteins whilst BirA* fused to the N-terminus of RABV-G showed only low levels of biotinylation. GAPDH was probed as a loading control. Results are representative of three independent blots.

4.3.3 IncuCyte based validation of RABV-G BirA* constructs

To further confirm the activity of CVSG-BirA* and SADG-BirA* C-term expressing cells, transfected cells were biotin treated, fixed, labelled with anti-biotin-594, and imaged using an IncuCyte plate reader. Analysis of the red fluorescence count per well showed high levels of biotinylation for both CVSG-BirA* and SAD-BirA* (Figure 4.5) further confirming their activity.

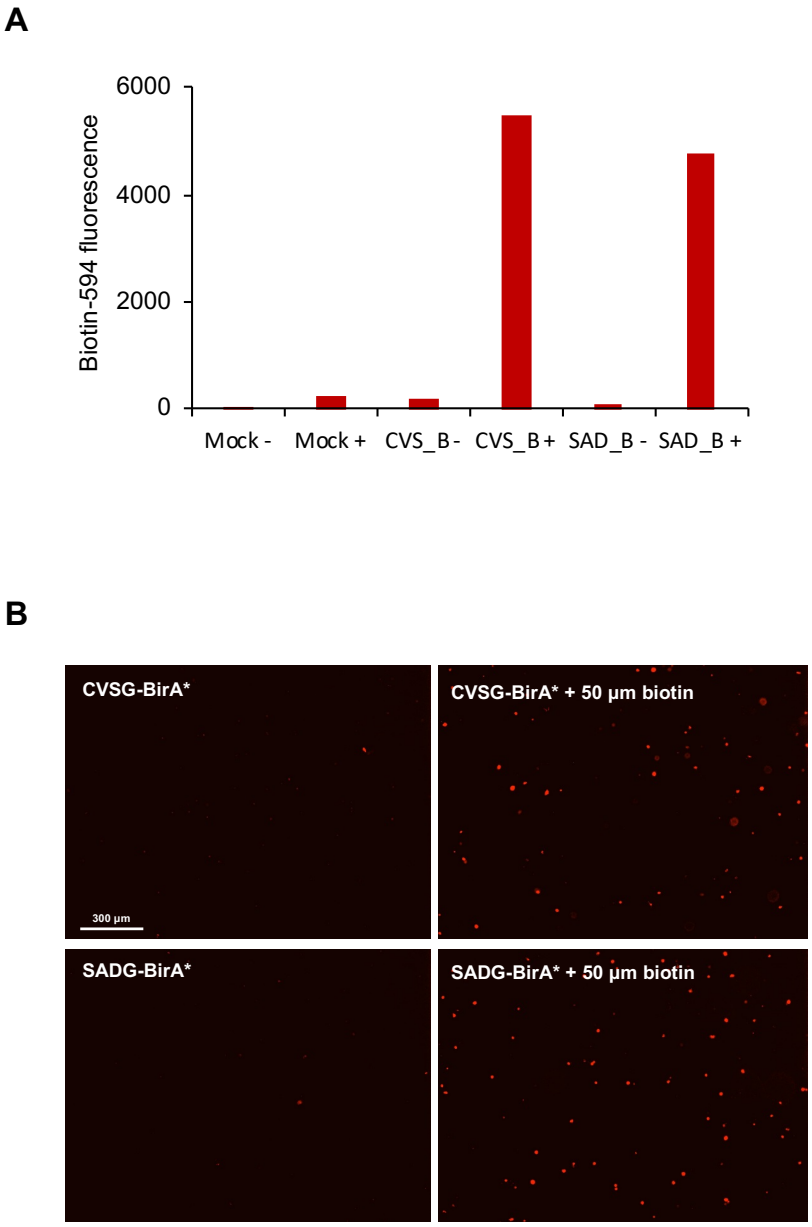

Figure 4.5 IncuCyte based validation of protein biotinylation by the BirA*-RABV-G fusions. HEK293T cells were transfected with the indicated BioID constructs, biotin treated, fixed, and labelled with anti-biotin-594. Cells were imaged through IncuCyte analysis to assay the levels of biotinylated proteins. **(A)** Automated fluorescence red counts and **(B)** widefield images in response to 50 µM biotin supplementation.

4.3.4 Validation of the RABV-G BirA* constructs

Following the validation of biotinylation, both CVSG-BirA* and SADG-BirA* C-term constructs were investigated to ensure they retained the characteristics of each native RABV-G protein. To achieve this, HEK293T cells were transfected with BirA*, CVSG-BirA* or SADG-BirA* C-term constructs, lysed, and proteins were resolved by SDS-PAGE to ensure they produced tagged-RABV-G proteins of the expected size. Western blot analysis following anti-HA labelling of the HA-tagged BirA* enzyme showed that both RABVG-BirA* constructs expressed a ~91 kDa fusion which conformed to the predicted size of the RABVG-BirA* fusion, with a lower band of ~27 kDa observed for BirA* alone (Figure 4.6A). Of note, both RABVG-BirA* constructs showed the presence of smaller bands ranging from ~27 kDa to ~38 kDa that likely correspond to RABVG-BirA* degradation products. Immunofluorescence labelling of BirA*-transfected cells with anti-HA antibodies showed diffuse expression throughout the cells, whilst both RABVG-BirA* constructs showed a more localised intracellular expression profile (Figure 4.6B). Co-labelling with anti-RABV-G antibodies showed almost complete co-localisation between the HA-tagged BirA* and RABV-G in cells, confirming that the RABVG-BirA* fusions remained in-tact following their exogenous expression (Figure 4.6B). Taken together, these results suggest that the RABVG-BirA* proteins were intact, active, and applicable to further studies of the identity of proteins located proximally to each RABV-G variant.

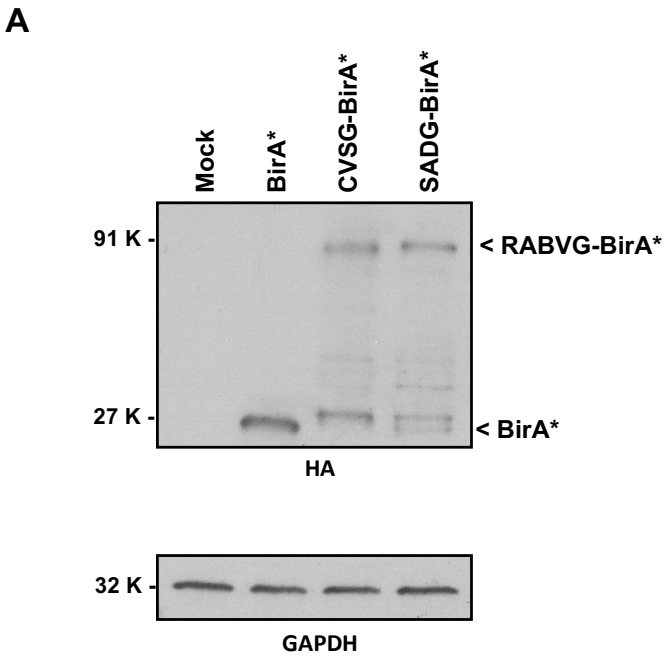

B

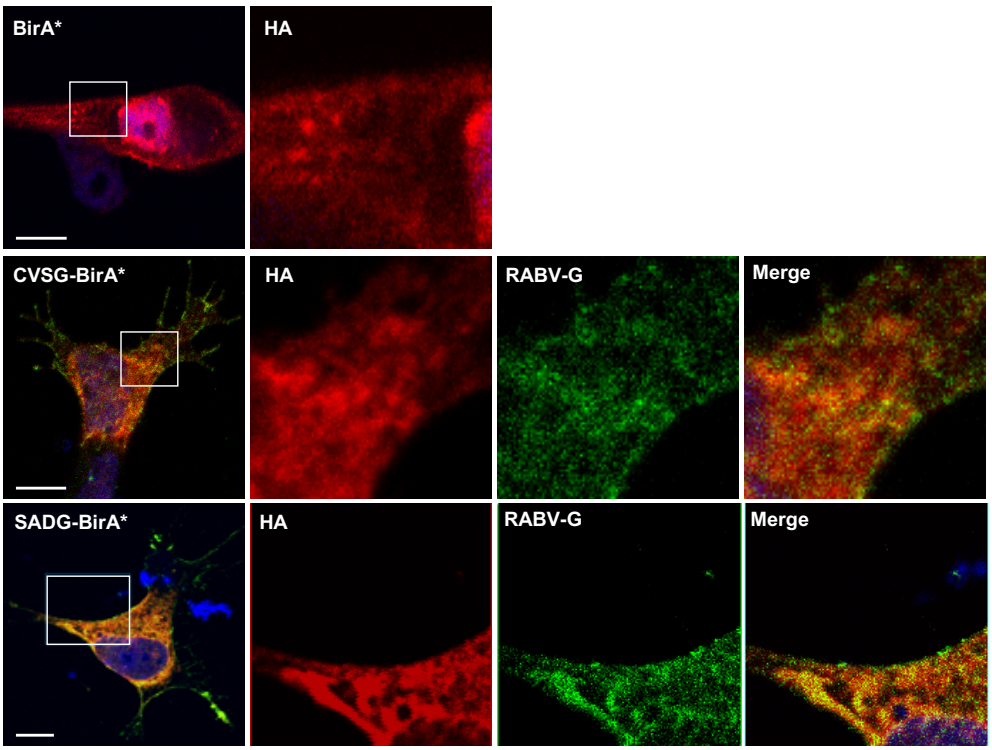

Figure 4.6 Validation of the trafficking of BirA* fusions. (A) Western blot analysis following anti-HA (1:2000) labelling shows that BirA* is expressed as a ~27 kDa protein, whilst RABVG-BirA* constructs show a band of ~ 91 kDa, consistent with the fusion of BirA* to the ~58 kDa RABV-G protein. Of note, both RABVG-BirA* lanes showed low levels of degradation products from ~27 kDa to ~38 kDa. GAPDH (1:2000) was probed as a loading control. **(B)** Immunofluorescence labelling of BirA* expressing cells with anti-HA antibodies (1:200) showed a diffused intracellular distribution. In contrast, RABVG-BirA* constructs showed a predominantly intracellular distribution and co-localised following labelling with anti-RABV-G and Anti-HA antibodies, suggesting that the majority of RABVG-BirA* constructs were expressed as full-length fusions. Scale bar = 10 μm. Images are representative of 25 cells.

4.3.5 RABVG-BirA* fusions show a comparable trafficking profile to RABV-G

The correct trafficking profile of the RABVG-BirA* fusions were next confirmed through immunofluorescence analysis. To achieve this, SVG-A cells were transfected with CVS-G, CVSG-BirA*, SAD-G, or SADG-BirA* and either live-labelled for 90 min to confirm correct PM expression and internalisation, or permeablised, fixed, and subsequently labelled to confirm a comparable steady-state distribution to the wild type proteins. Live labelled CVS-G and CVSG-BirA* expressing cells showed cell surface labelling and intracellular internalised RABV-G puncta (white arrowheads), whilst SAD-G and SADG-

BirA* showed a predominantly cell surface localisation with only limited levels of intracellular expression (Figure 4.7). Steady state assessments also revealed a characteristic perinuclear localisation for both CVS-G and CVSG-BirA* (white arrowheads), whilst SAD-G and SADG-BirA* showed a predominantly PM expression with limited intracellular staining (white arrowheads, Figure 4.7). As both these trafficking profiles matched those for native CVS-G and SAD-G (see Figure 3.1), this confirmed that RABVG-BirA* fusions retain their anticipated folding and trafficking patterns, validating them for further analyses.

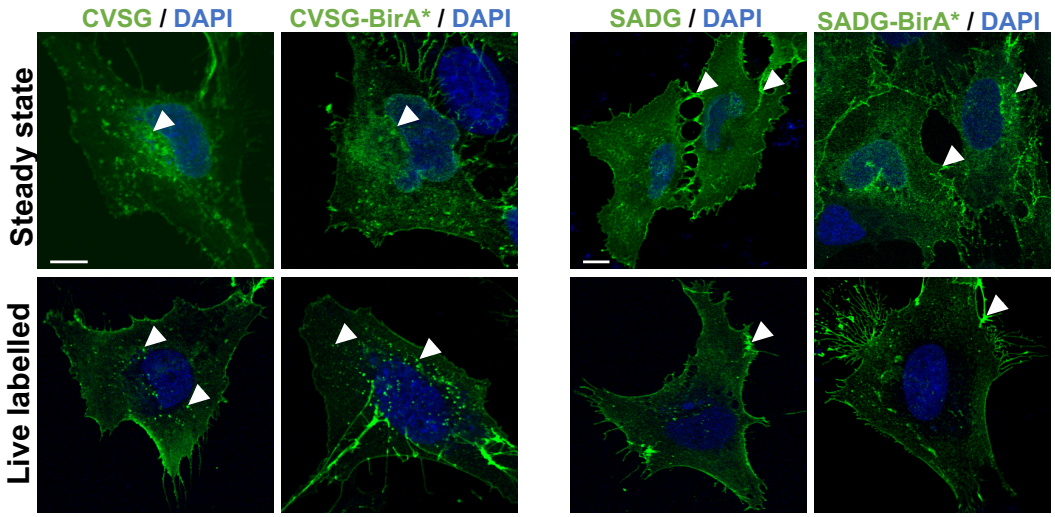

Figure 4.7 RABV-G trafficking is unaffected by BirA* fusions. SVG-A cells expressing RABV-G or RABV-G-BirA* from CVS or SAD were either live labelled for 90 min or fixed, permeabilised and labelled to reveal internalisation from the PM or steady state trafficking, respectively. All analysed cells showed a similar trafficking phenotype between the native proteins and their BirA* fusions (white arrowheads). Images are representative of 25 cells. Scale bar = 10 μm. Nuclei were stained with DAPI.

4.4 BioID assays

4.4.1 Streptavidin pulldowns

Following validation of the RABV-G BirA* fusions, analysis of their proximal proteins were next performed. To achieve this, each construct was transfected into HEK293T cells (~4 x 10^7 cells total) and treated with biotin as described (see Figure 4.4). The next day, cells were lysed in BioID buffer and mixed with streptavidin Dynabeads overnight at 4°C. From the lysates, 10% was stored

as input material. Beads were then collected, washed, and stored in 50 mM Tris buffer for TMT analysis. Input and pulldown samples (IP) were then assessed by western blotting with streptavidin-HRP and anti-RABV-G antibodies to ensure successful biotinylation and comparable levels of CVS-G and SAD-G expression, respectively (Figure 4.8). Analysis of the blots confirmed the successful pull-down of the biotinylated proteins by the streptavidin-conjugated beads and the comparable levels of GAPDH expression in each sample. Verified samples were then sent to the University of Bristol Proteomics Facility for TMT mass spectrometry analysis (n=3 for each construct).

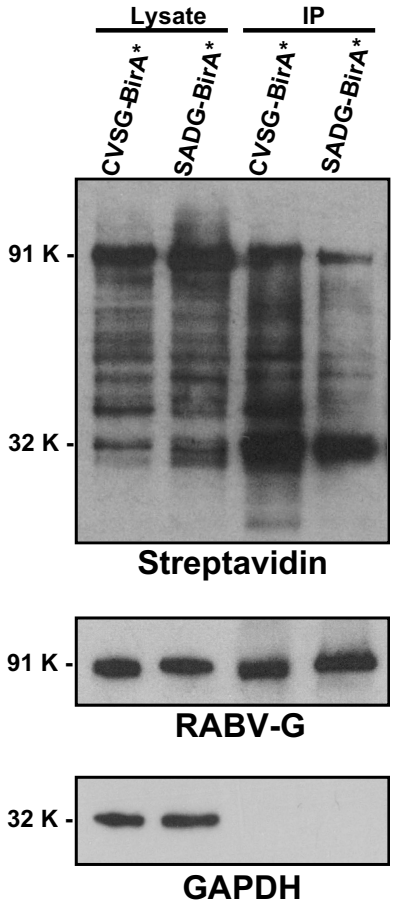

Figure 4.8 Streptavidin pulldowns. Lysates from large scale transfections of CVSG-BirA* or SADG-BirA* were incubated overnight with 300 µl of streptavidin-conjugated Dynabeads. Biotinylated proteins were then isolated through magnetic pulldowns (see Methods section 2.8). Input and pulldown (IP) lysates were probed with streptavidin-HRP revealing numerous biotinylated proteins. Probing with anti-RABV-G antibodies showed similar levels of RABV-G expression across the samples (n = 3) validating the samples for further mass spectrometry analysis.

4.4.2 BioID analysis

Three biological replicates of the proteins proximal to CVSG-BirA* or SADG-BirA* were analysed through TMT LC tandem-mass spectrometry (LC-MS/MS) by Dr Kate Heesom (University of Bristol). The resulting raw datasets produced 4611 hits with the majority of proteins showing higher levels of proximity to CVSG-BirA*. Protein hits were next ranked through SEQUEST, an algorithm that compares identified peptides to theoretical peptides with higher values correlating to a higher probability of a hit being a true binding partners. Hits with high scores (75 or higher) were included, revealing a total of 837 potential proximal proteins for CVS-G and SAD-G (Table A3).

The proteins identified represent either transient binders, proteins in close proximity to the RABV-G constructs, or specific interactors. To specifically focus on proteins that may dictate the differential pathogenicity between CVS and SAD strains, all proteins that showed comparable levels of proximity to CVS-G and SAD-G, calculated as a CVS-G/SAD-G ratio close to 1, were eliminated from the analysis. This permitted a specific focus on those proteins of differing proximity to CVS-G *vs.* SAD-G and also allowed the removal of any false positive hits associated with non-specific BirA* biotinylation that would be expected to be present for both RABV-G fusions. Following these analyses, the list of potential proteins that differed between CVS-G and SAD-G were narrowed down to 120 hits. STRING protein interaction networks were constructed from these proteins using Reactome algorithms to reveal four functional clusters namely: (1) Proteins involved in actin-myosin filaments; (2) CME; (3) Cilium assembly; and (4) ER-to Golgi transport (Figure 4.9A). These clusters represent 38 high-confidence proximal protein partners to CVS-G (Table 4.1) with the top three hits being dynein 1, non-muscle myosin IIA and clathrin 1.

The Actin-myosin (actomyosin) filament cluster included all non-muscle myosin II variants IIA, IIB and IIC, encoded by *MYH9, MYH10* and *MYH14* respectively. This was consistent with previous studies showing that Myosin IIB is a binding partner of Flag-tagged CVS-G (Yin et al., 2020). Rho-associated protein kinase activators of myosin ROCK1 and ROCK2 were also identified as proximal to CVS-G BirA* in addition to cofilin-1, a previously

identified binding partner of CVS-G (Zan et al., 2016). Taken together, this cluster revealed the potential association of CVS-G with alterations in the actin-based cytoskeleton, a known feature of pathogenic RABV infections.

The CME cluster included clathrin 1 and four of its adaptor proteins: AP2 α1, AP2 α2, AP2 β1 and AP2 μ. Transferrin receptor and dynamin 2 were also present in the cluster. These adaptor proteins are associated with YXXΦ-based endocytosis, a motif present in CVS-G and absent in SAD-G as described in Chapter 3. Targeting clathrin with PitStop2 could also inhibit RABV-G internalisation (Figure 3.11). These BioID analysis therefore revealed key clathrin-adapters that are likely to be responsible for the rapid internalisation of CVS-G from the PM.

The cilium assembly cluster included t-complex subunits (CCT3, CCT4, and CCT8) and microtubule-associated proteins including CKAP5, CLASP1 and PLK1. Of these, CLASP1 mediates the attachment of microtubules to actomyosin filaments (Meiring et al., 2020), whilst PLK1 promotes tumorigenesis through the disruption of cell cycle progression (Malumbres and Barbacid, 2007). Dynein 1 and 2 function as microtubule motors for vesicles transport (Reck-Peterson et al., 2018). Exocyst complex component 4 binds to myosin IIA and it is involved in the docking of exocytic vesicles with fusion sites on the PM (Nihalani et al., 2019). These proteins would be expected to contribute to RABV-G trafficking towards the PM.

The ER-Golgi transport cluster included kinesins that are responsible for vesicular transport towards the PM, including KIF5B, KIF23 and KIF2C (Mallik et al., 2013). Several coatomer proteins were also identified including COPA, COPB1, COPG1, COPG2 and ARCN1 along with their associated proteins USO1, SEC23IP and SEC24C, known to regulate Golgi to ER shuttling (Brandizzi and Barlowe, 2013). This cluster suggests that CVS-G may traffic between the Golgi apparatus and the ER.

GO biological process analysis of the identified proteins confirmed the potential role of CVS-G in cytoskeleton organisation, microtubule-based processes, Golgi vesicle transport, actin filament-based processes, the regulation of exocytosis, the development of neuronal projections, and cilium assembly (Figure 4.9B). KEGG pathway analysis also revealed the regulation

of the actin cytoskeleton, tight junctions, endocytosis, calcium reabsorption, Salmonella infection, Huntington's disease, and synaptic vesicle recycling (Figure 4.9B). The ability of RABV-G to hijack these pathways may shed new insight into the neuronal pathways perturbed during fatal RABV infections.

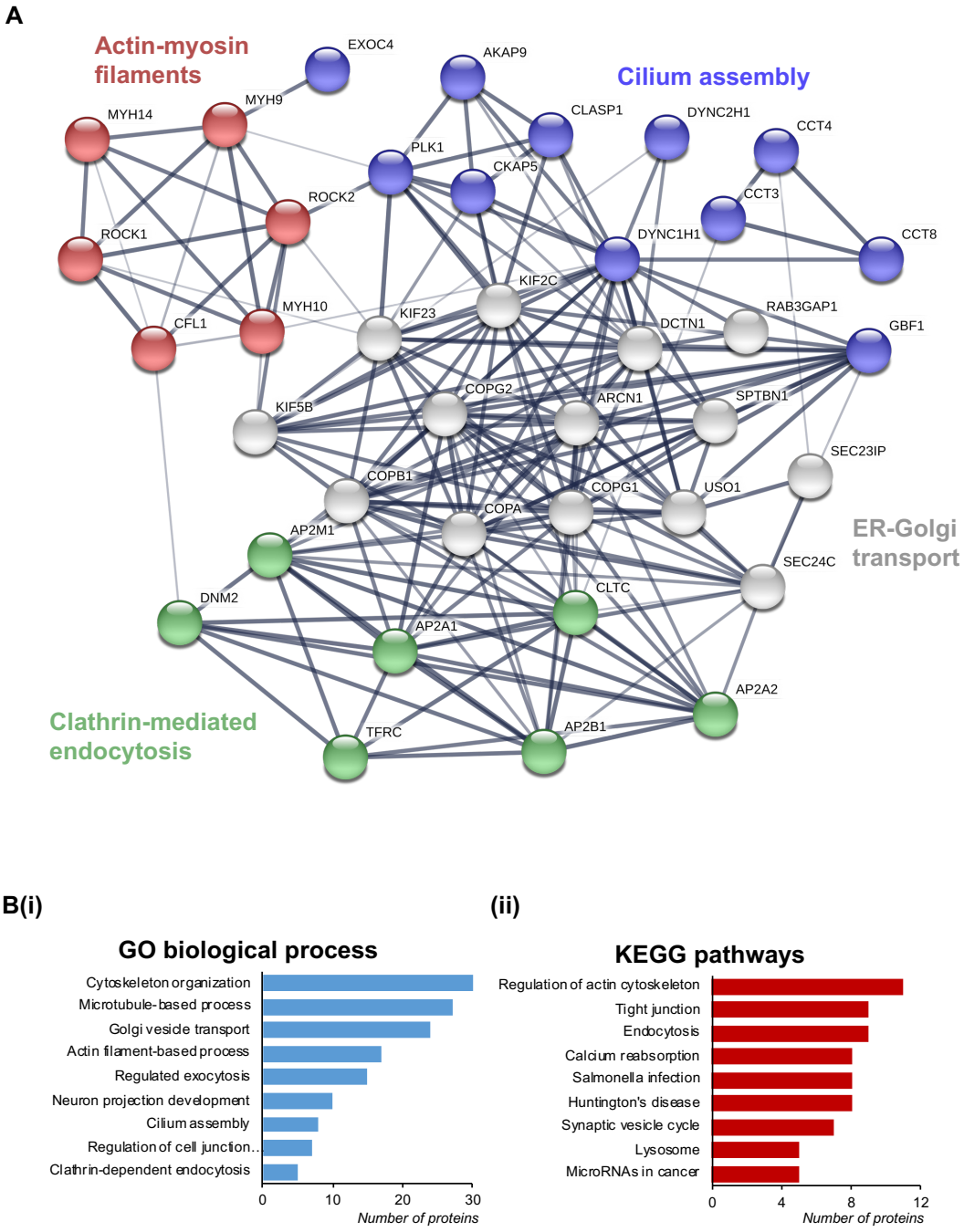

Figure 4.9 BioID network analysis. (A) Raw data were processed to 38 functional hits. STRING protein interaction network analysis were performed using the reactome algorithm, revealing four key protein clusters as potential targets for CVS-G. These clusters were actin-myosin filaments, CME, cilium assembly and ER-Golgi transport. **(B)** GO biological analysis **(i)** revealed cytoskeletal organization, microtubule-based processes and Golgi vesicles as associated with CVS-G. **(ii)** KEGG pathway analysis revealed an association with the regulation of the actin cytoskeleton, tight junctions, endocytosis, calcium reabsorption, Salmonella infection, Huntington's disease and synaptic vesicle recycling.

Table 4.1 Selected top 38 proteins enriched in the CVS-G BirA* pull-downs.

Accession	Gene	Description	Reactome pathway	Coverage (%)	Unique peptide	CVS Ab	SAD Ab	Ab ratio CVS/SAD	Sequest Score
Q14204	DYNC1H1	Cytoplasmic dynein 1 heavy chain 1	Cilium assembly	49.4	227	20108	7198.1	2.794	1174.2
A0A024R1N1	MYH9	Myosin heavy chain 9 (non-muscle myosin IIA)	Actin-myosin filaments	56.8	100	8376	3506.7	2.389	755.87
A0A087WVQ6	CLTC	Clathrin heavy chain 1	Clathrin-mediated endocytosis	52.9	63	8566	3079.5	2.782	676.92
P35580	MYH10	Myosin heavy chain 10 (non-muscle myosin IIB)	Actin-myosin filaments	52.5	89	5321	2156.3	2.468	619.76
Q14008	CKAP5	Cytoskeleton-associated protein 5	Cilium assembly	43.9	91	5199	1947.9	2.669	384.23
P53621	COPA	Coatomer subunit alpha	ER-Golgi transport	64.1	64	4343	1382.4	3.142	366.23
P53618	COPB1	Coatomer subunit beta	ER-Golgi transport	48.3	42	4497	1841.8	2.441	266.45
P50990	CCT8	T-complex protein 1 subunit theta	Cilium assembly	70.1	38	2494	1328.3	1.877	251.61
P50991	CCT4	T-complex protein 1 subunit delta	Cilium assembly	63.3	33	3454	1427.2	2.42	243.51
Q59H77	CCT3	T-complex protein 1 subunit gamma	Cilium assembly	64.5	38	3225	1464.3	2.203	242.43
B0I1S0	DYNC2H1	Cytoplasmic dynein 2 heavy chain 1	Cilium assembly	16.8	71	3072	1035	2.968	212.19
E7EX90	DCTN1	Dynactin subunit 1	ER-Golgi transport	44.7	43	1451	612.1	2.37	200.49
A0A140VJE8	AP2B1	AP complex subunit beta	Clathrin-mediated endocytosis	37.2	18	1615	592.6	2.724	173.46
P33176	KIF5B	Kinesin-1 heavy chain	ER-Golgi transport	44.4	38	960.1	554.4	1.732	152.34
P50570	DNM2	Dynamin-2	Clathrin-mediated endocytosis	46.3	21	1915	679.4	2.819	144.71
Q7Z406	MYH14	Myosin-14	Actin-myosin filaments	18.8	21	387.2	189.8	2.04	138.9
Q92538	GBF1	Golgi-specific brefeldin A resistance factor 1	Cilium assembly	23.5	34	1692	698.1	2.424	136.65
O95782	AP2A1	AP-2 complex subunit alpha-1	Clathrin-mediated endocytosis	36.3	20	1469	507.2	2.895	136.22
Q9Y678	COPG1	Coatomer subunit gamma-1	ER-Golgi transport	38.6	27	1610	642	2.507	130.17
O94973	AP2A2	AP-2 complex subunit alpha-2	Clathrin-mediated endocytosis	36.0	14	782.1	303.7	2.575	125.84
A0A2P9DU05	ROCK2	Rho-associated protein kinase 2	Actin-myosin filaments	29.5	34	1239	497.5	2.49	122.06
Q9UBF2	COPG2	Coatomer subunit gamma-2	ER-Golgi transport	30.1	19	1160	436.9	2.655	122.04
D9ZGF8	ROCK1	Rho-associated protein kinase 1	Actin-myosin filaments	28.8	32	615.3	288.2	2.135	117.42
A0A087WUZ3	SPTBN1	Spectrin beta chain	ER-Golgi transport	18.9	33	865.6	698.4	1.239	114.65
Q7Z460	CLASP1	CLIP-associating protein 1	Cilium assembly	25.5	4	936.9	403.9	2.319	112.49
B0YIW6	ARCN1	Archain 1	ER-Golgi transport	46.9	29	1290	961.4	1.342	112.47
E9PK25	CFL1	Cofilin-1	Actin-myosin filaments	67.6	14	2072	1098.5	1.886	111.74
Q02241	KIF23	Kinesin-like protein KIF23	ER-Golgi transport	35.1	30	1407	734.1	1.917	106.34
O60763	USO1	General vesicular transport factor p115	ER-Golgi transport	28.6	25	950.7	541.5	1.756	106.13
Q6NX51	EXOC4	Exocyst complex component 4	Cilium assembly	30.3	26	1034	424.3	2.436	100.69
A0A140VKF1	KIF2C	Kinesin-like protein KIF2C	ER-Golgi transport	37.8	22	749.5	322.4	2.325	92.15
P02786	TFRC	Transferrin receptor protein 1	Clathrin-mediated endocytosis	36.3	24	543	256.8	2.114	90.45
B2R841	PLK1	Serine/threonine-protein kinase PLK1	Cilium assembly	44.6	23	1227	393.6	3.117	90.32
E9PFW3	AP2M1	AP-2 complex subunit mu	Clathrin-mediated endocytosis	50.7	23	780.9	440.5	1.773	86.73
A0A0A0MRF6	AKAP9	A-kinase anchor protein 9	Cilium assembly	8.3	27	567.1	387.1	1.465	84.6
B9A6J2	RAB3GAP1	RAB3 GTPase activating protein subunit 1	ER-Golgi transport	31.3	24	576.6	281.4	2.049	81.8
P53992	SEC24C	Protein transport protein Sec24C	ER-Golgi transport	25.0	21	795.4	217.3	3.661	81.72
Q9Y6Y8	SEC23IP	SEC23-interacting protein	ER-Golgi transport	27.3	23	884.4	348.7	2.536	79.91

4.5 Validation of the BioID datasets

4.5.1 Western blot validation

The BioID datasets revealed a total of 120 proteins that were proximal to CVS-G and SAD-G, of which 85 were associated to higher levels with CVS-G, compared to 16 that were more strongly associated with SAD-G (Figure 4.10A). For confirmation of the datasets, selected hits were validated through western blot analysis. In the experiments that followed, input lysates from those analysed by TMT mass spectrometry were probed for the expression of myosin IIA, COPA, HSP90, β-tubulin and β-actin. The resulting blots showed lower levels of myosin IIA and COPA in the input lanes of the CVSG-BirA* samples, but higher expression of all probed proteins in the streptavidin-isolated (IP) pulldown of proteins proximal to CVSG-BirA*, compared to mock-transfected and SADG-BirA* lanes (Figure 4.10B). Comparative quantification analysis of blots showed comparable fold-enrichment to the interactome datasets for myosin IIA, COPA and HSP90, whilst β-tubulin showed 2-fold higher expression following western blot analysis, with β-actin showing 6-fold higher levels (Figure 4.10B). It was reasoned that the reduced expression of myosin IIA and COPA in the input lanes may be a result of their expressional regulation by CVS-G BirA*. All other analysed proteins showed uniform expression across the input samples (Figure 4.10B) and validated the mass spectrometry based interactomes of CVS-G.

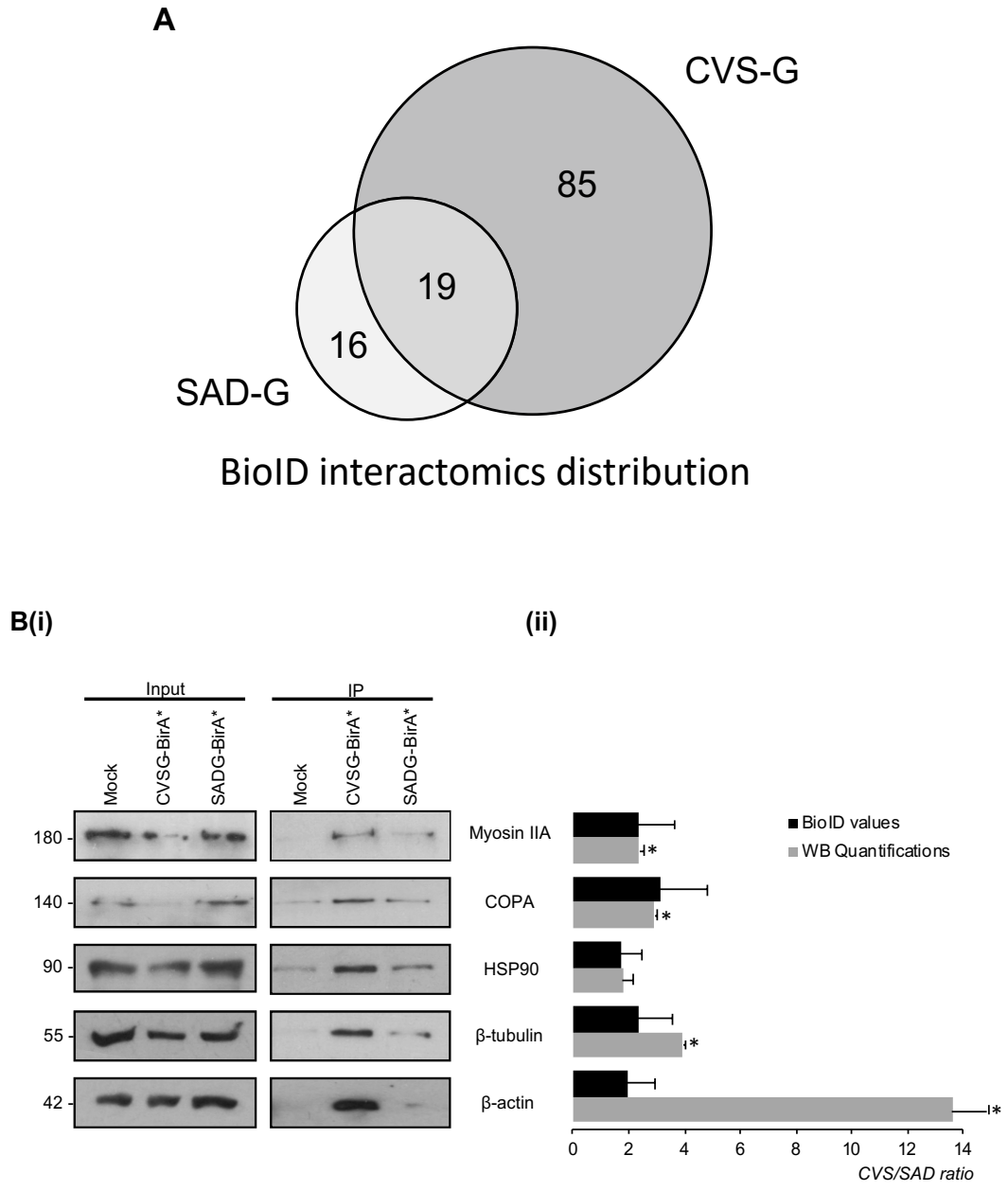

Figure 4.10 BioID interactome validations. (A) Significant proximal proteins totalled 120 for both CVSG-BirA* and SADG-BirA*, of which 85 showed significantly higher binding to CVSG-BirA*. **(B)** Western blot validation and quantitative comparison of the BioID data. **(i)** Western blot analysis of input and streptavidin-isolated (IP) proteins. Western blots showed higher CVSG-BirA* binding to all probed proteins. IP expression was quantitatively compared **(ii)** to the corresponding interactome values and western blot CVSG-BirA*/SADG-BirA* ratios. Both tubulin and actin showed higher expression in the western blots. Error bars indicate mean ± SEM. *significant difference between BioID values and WB quantifications ($P < 0.05$).

4.5.2 Golgi-ER trafficking of CVS-G but not SAD-G

The BioID screen suggested an enrichment of CVS-G with proteins that regulate cargo trafficking from the Golgi to ER (Table 4.1). To confirm these data, SVG-A cells were transfected with untagged CVS-G or SAD-G, permeablised, and co-labelled with anti-RABV-G antibodies and either calnexin or COPA as markers of the ER, or Golgi to ER trafficking respectively (Müller-Taubenberger et al., 2001). Representative images showed ~70% colocalisation between CVS-G and calnexin within perinuclear regions of the cells (white arrowheads), compared to the ~30% colocalisation observed for SAD-G (Figure 4.11A). CVS-G also showed numerous puncta that colocalised with COPA, whilst the SAD-G staining pattern appeared completely distinct from the COPA positive regions (Figure 4.11B).

To further validate these data, the localisation of CVS-G and SAD-G at the Golgi apparatus was investigated. Transfected cells were labelled with the well-characterised Golgi marker GM130 or Trans-Golgi marker 46 (TGN46). The results showed that CVS-G colocalised with both markers (white arrowheads) to high levels, compared to the minimal overlap observed between SAD-G and this compartment (Figure 4.11C-D). Upon quantification, CVS-G showed ~50% colocalisation with GM130 compared to SAD-G that showed ~10% colocalisation (Figure 4.11E). Taken together, these results validate the enrichment of the ER-Golgi trafficking components observed in the CVS-G BirA* samples, and confirm that CVS-G is more highly associated with the ER-Golgi apparatus than SAD-G.

B

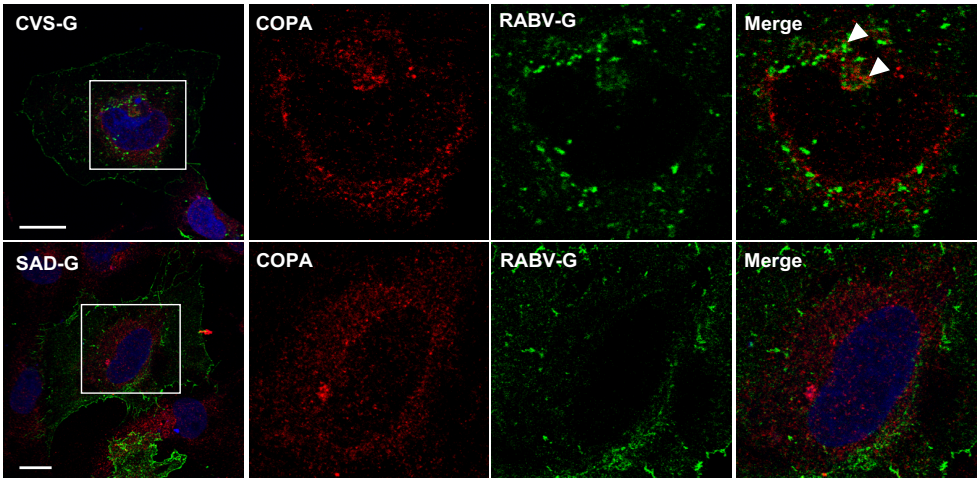
CVS-G
COPA
RABV-G
Merge
SAD-G
COPA
RABV-G
Merge

C

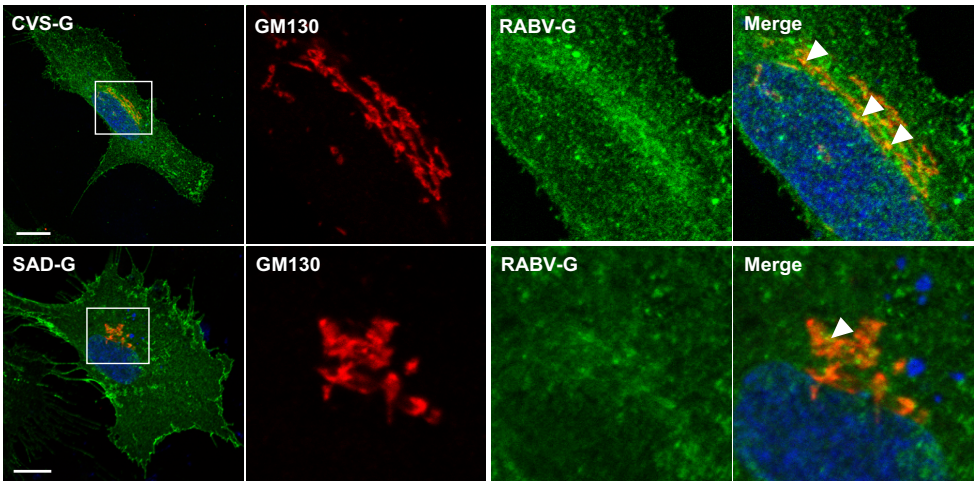
CVS-G
GM130
RABV-G
Merge
SAD-G
GM130
RABV-G
Merge

D

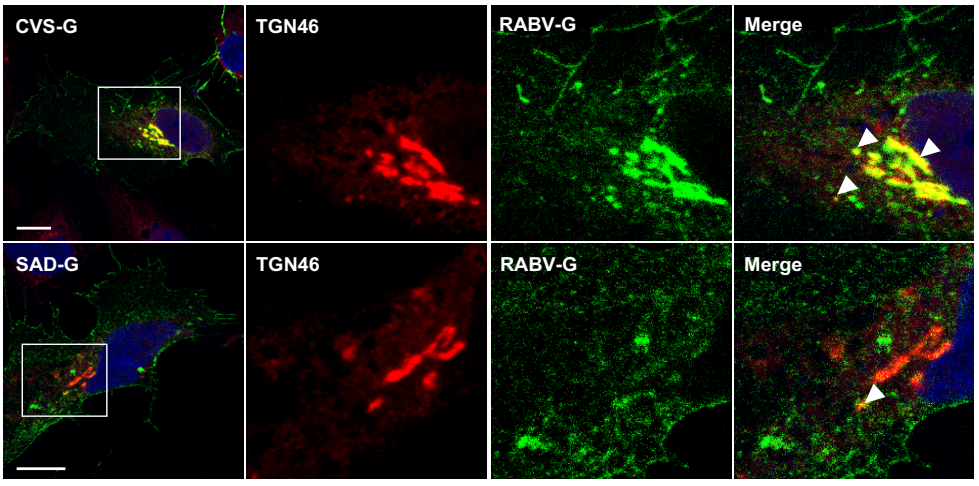
CVS-G
TGN46
RABV-G
Merge
SAD-G
TGN46
RABV-G
Merge

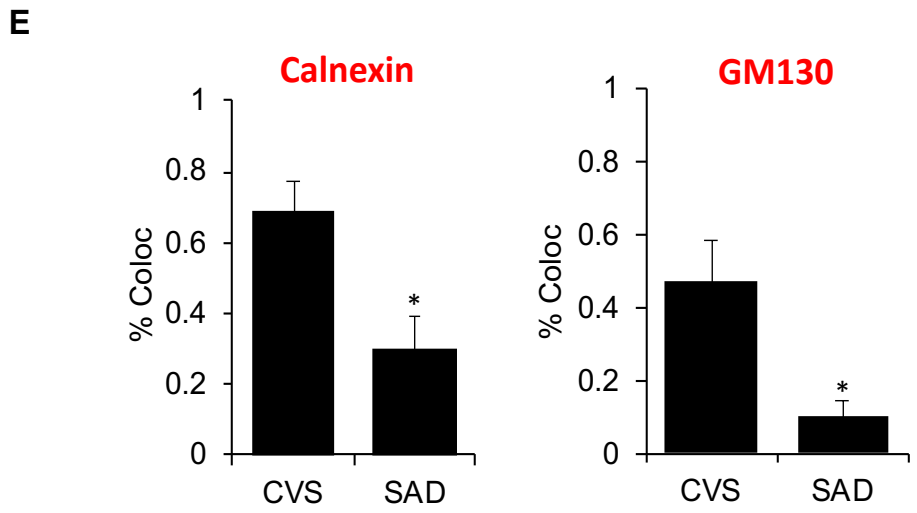

Figure 4.11 CVS-G but not SAD-G traffics through Golgi-ER compartments. (A) Cells transfected with CVS-G or SAD-G were fixed, permeabilised and labelled with anti-RABV-G and Alexa Fluor 488. Cells were then co-colabelled with anti-calnexin (1:200) or **(B)** anti-COPA (1:200), **(C)** anti-GM130 (1:200) or **(D)** anti-TGN46 (1:200) and their corresponding Alexa Fluor 594 antibodies. CVS-G puncta significantly colocalised with all four markers (white arrowheads) whilst SAD-G showed minimal colocalisation. Images are representative of 20 cells. Scale bar = 10 µm. **(E)** Quantitative analysis of five z-stacks performed using the Fiji Coloc 2 tool. CVS-G colocalised to significantly higher levels with calnexin and GM130, compared to SAD-G. Error bars indicate mean ± SEM. *significant difference between CVS-G and SAD-G ($P < 0.05$).

4.5.3 Cytoskeletal association of CVS-G

Network analysis of the proteins proximal to CVS-G suggested that the organisation of the cytoskeletal system is a major target for CVS-G over SAD-G (Figure 4.9B). Previous proteomic analysis of cells infected with pathogenic and attenuated RABV strains also implicated several cytoskeletal proteins as key mediators of RABV pathogenesis, though a role for RABV-G in these processes was not assigned (Dhingra et al., 2007; Wang et al., 2011; Zandi et al., 2013). To confirm an association of this organelle, cells transfected with untagged CVS-G or SAD-G were labelled with antibodies targeting the microtubule marker β-tubulin or myosin IIA (*MYH9*), selected as top hits from the CVS-G datasets (Table 4.1). The results revealed higher levels of CVS-G colocalisation with both β-tubulin and myosin IIA (white arrowheads) compared to SAD-G, in agreement with the datasets (Figure 4.12A-B). In addition, the perinuclear actin microfilaments and microtubules appeared to extend into the cytoplasm to a greater degree in SAD-G cells, compared to

their more peripheral distribution in CVS-G expressing cells, suggestive of rearrangement of these cytoskeletal components.

The actin cytoskeleton mediates cell expansion and is implicated in a range of cellular responses. For further confirmation of the association of CVS-G with cytoskeletal components and/or reorganisation, the average sizes of 20 cells expressing CVS-G and SAD-G were compared. The data showed that CVS-G expressing cells were ~20% smaller than SAD-G expressing or mock-transfected cells (Figure 4.12C). These results further implicate CVS-G in the active reorganisation of the cytoskeleton.

A

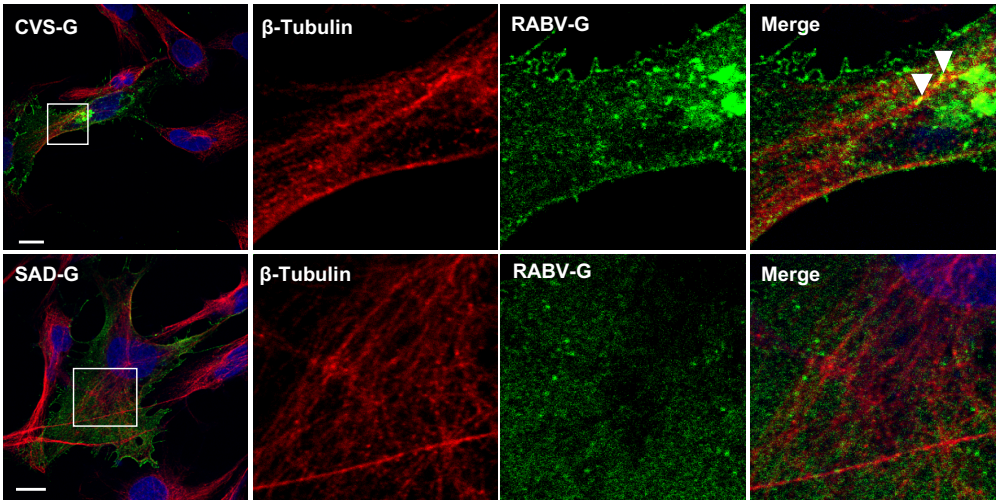

B

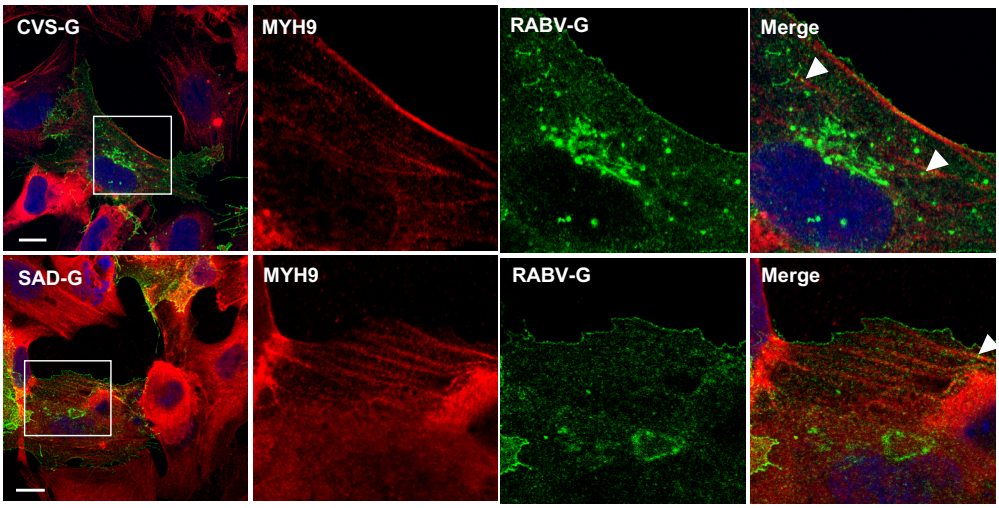

C

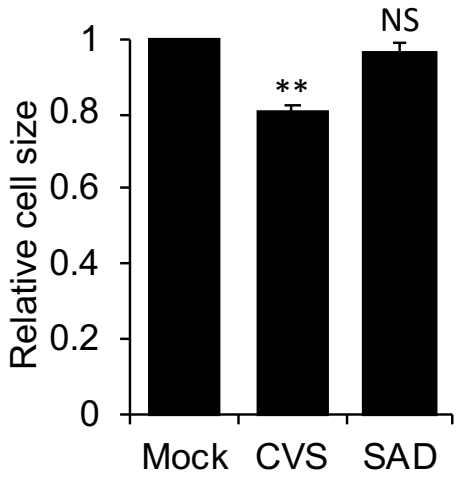

Figure 4.12 CVS-G influences the cellular cytoskeleton. (A) SVG-A cells transfected with CVS-G or SAD-G were fixed, permeabilised and labelled with RABV-G and Alexa Fluor 488. Cells were then co-colabelled with β-tubulin (1:100) or **(B)** MYH9 (1:100) and their corresponding Alexa Fluor 594 secondary antibodies. CVS-G puncta significantly colocalised with β-tubulin and myosin IIA (white arrowhead) whilst SAD-G showed minimal colocalisation with these markers (white arrowheads). Scale bar = 10 μm. **(C)** Quantitative analysis of 20 cell lengths performed using ImageJ. Mock transfected SVG-A cells had a cell length of approximately ~46 μm which was comparable to SAD-G expressing cells. CVS-G expressing cells had an average cell length of ~38 μm which was ~20% lower than either mock or SAD-G expressing cells. Error bars indicate mean ± SEM. **significant difference between mock and CVS-G ($P < 0.005$).

4.6 RABV-G expression induces filopodia outgrowth

Filopodia are thin cytoplasmic projections that contain actin filaments cross-linked into bundles by actin-binding proteins (Alieva et al., 2019). Although the major functions of filopodia are the formation of adhesions between a substratum and cells, in neurons, they guide axons and dendrites to their correct targets in response to cellular cues (Kim et al., 2002). Emerging data also highlights their role in virus entry, virus spread from cell-to-cell, and the clinical pathology associated with virus-associated disease (Schelhaas et al., 2008; Nikolic et al., 2011; Schudt et al., 2013; Xu et al., 2015; Chang et al., 2016). These observations have led to an intense research interest into the key determinants of filopodia induction during virus infection.

RABV infection with CVS-G or SRV_9 (SAD-G) was recently shown to induce filipodia and neurite outgrowth, but the cellular and viral mechanisms responsible for this induction were not investigated in detail (Xu et al., 2015; Seo et al., 2017). Filopodia are dynamic structures composed of F-actin bundles, the initiation and elongation of which are regulated by the assembly of actin filaments and their subsequent cross-linking (Doherty and McMahon, 2008; Alieva et al., 2019; Zhang et al., 2020). An interesting feature of both CVS-G and SAD-G expressing cells was their distribution to elongated filopodia like-projections observed in surface-labelled transfected cells (see Figure 3.1). Given the association of CVSG BirA* with a range of actin-binding proteins, the features of these projections were next investigated in further detail.

Somewhat surprisingly, when CVS-G and SAD-G cells were stained with phalloidin (an F-actin marker), distinctive filopodia like projections containing the RABV-G proteins were observed in regions of the cell devoid of F-actin staining (Figure 4.13A-B). This filopodia outgrowth was RABV-G specific and was also observed for DOG-G and EBLV-G (both pathogenic RABV strains), but absent in VSV-G expressing cells (Figure 4.13C). In previous studies, a dramatic decrease in F-actin staining was observed during the late stages of RABV infection (Song et al., 2013). These effects were hypothesised to be related to the influence of RABV-N on actin-binding proteins, including synapsin I, but no role of RABV-G during these processes was described (Ceccaldi et al., 1997). The protein showing the highest proximal score to CVS-G following BioID analysis was myosin IIA, a protein that localises to the base of cell edges to induce filopodia outgrowth (Alieva et al., 2019). Co-immunofluorescence analysis confirmed the partial co-localisation of myosin IIA with CVS-G at the base of the cell surface (Figure 4.12B), suggesting a potential role in the formation of these RABV-G specific protrusions.

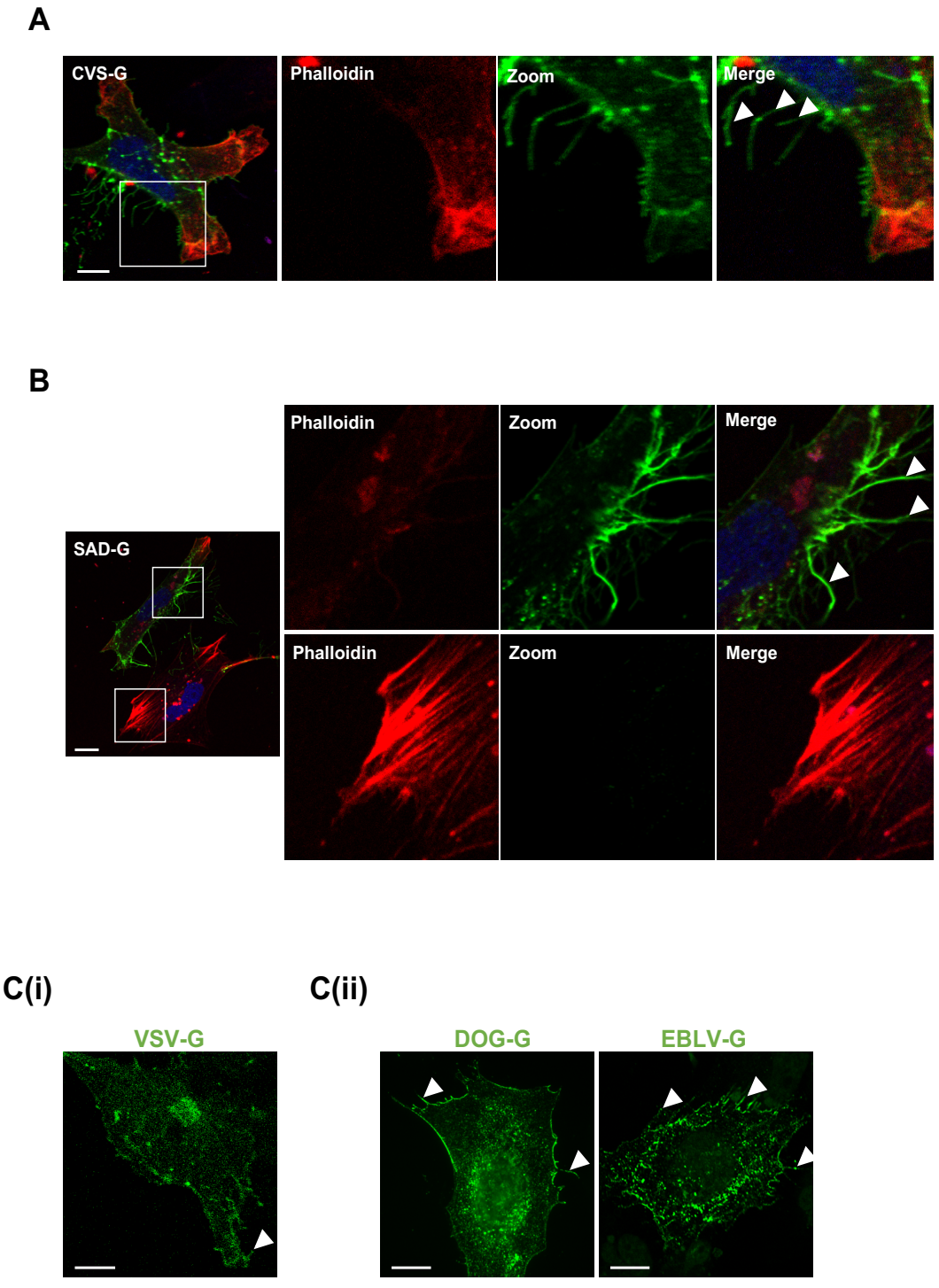

Figure 4.13 RABV-G expression induces filopodia outgrowth. (A) CVS-G transfected cells were live labelled with CVS-G and phalloidin-680. CVS-G- filopodia projections with no F-actin staining (white arrowheads) were observed, with F-actin localising to regions of the cell devoid of CVS-G. **(B)** SAD-G expressing cells show a similar distribution of SAD-G in filopodia and F-actin in distant regions. Mock transfected cells show high levels of polarised F-actin expression. **(C)(i)** VSV-G expressing cells showed no filopodia outgrowth. **(ii)** Other RABV-G variants DOG-G and EBLV-G induce filopodia outgrowth, scale bar = 10 μm.

4.6.1 Inhibition of myosin II or ROCK disrupts RABV-G-induced filopodia

BioID analysis revealed three myosin II variants and ROCK1 and ROCK2 as proteins proximal to CVS-G at higher levels than SAD-G (Figure 4.9A). ROCK phosphorylates and activates myosin II, with its downregulation correlating with the retraction of filopodia outgrowth (Alieva et al., 2019). The role of these proteins in CVS-G mediated filopodia formation were therefore investigated. In the experiments that followed, CVS-G and SAD-G expressing cells were treated with blebbistatin (an inhibitor of the motor activity of myosin II) or Y-27632 (a ROCK inhibitor), and the number of filopodia projections per-cell were quantitated as previously described (Alieva et al., 2019). The results showed similar levels of filopodia upon comparison of CVS-G to SAD-G cells (Figure 4.14; ~19 per cell for CVS-G *vs.* ~23 per cell for SAD-G). Interestingly, blebbistatin treatment led to a ~50% reduction in the number of filopodia in both CVS-G and SAD-G expressing cells, but the filopodia that remained were significantly elongated compared to undrugged cells (Figure 4.14). In contrast, CVS-G expressing cells treated with Y-27632 showed an almost complete loss of filopodia-like projections (Figure 4.14B-Ci; ~58% decrease in numbers), compared to SAD-G expressing cells that retained numerous short-filopodia-like projections when treated with Y-27632 (Figure 4.14B-C (i); ~138% increase in numbers). These results suggest that CVS-G and SAD-G induce filopodia outgrowth by distinct mechanisms, in which CVS-G but not SAD-G expressing cells show almost complete filopodia retraction following ROCK inhibition, consistent with requirement for both myosin II and ROCK activity for CVS-G induced filopodia outgrowth. Importantly, these data were further confirmed in SH-SY5Y neuroblasts (Dwane et al., 2013), in which the expression of CVS-G or SAD-G induced the development of short neurites (Figure 4.14D), and consistent with the SVG-A data, the number and length of the neurites decreased in both CVS-G and SAD-G cells (Figure 4.14E) upon treatment with blebbistatin, whilst Y-27632 led to retraction of the neurites in CVS-G expressing but not SAD-G expressing cells (Figure 4.14F). These results confirmed the role of myosin II and ROCK activity in the formation of CVS-G induced filopodia and neurites in neuroblasts.

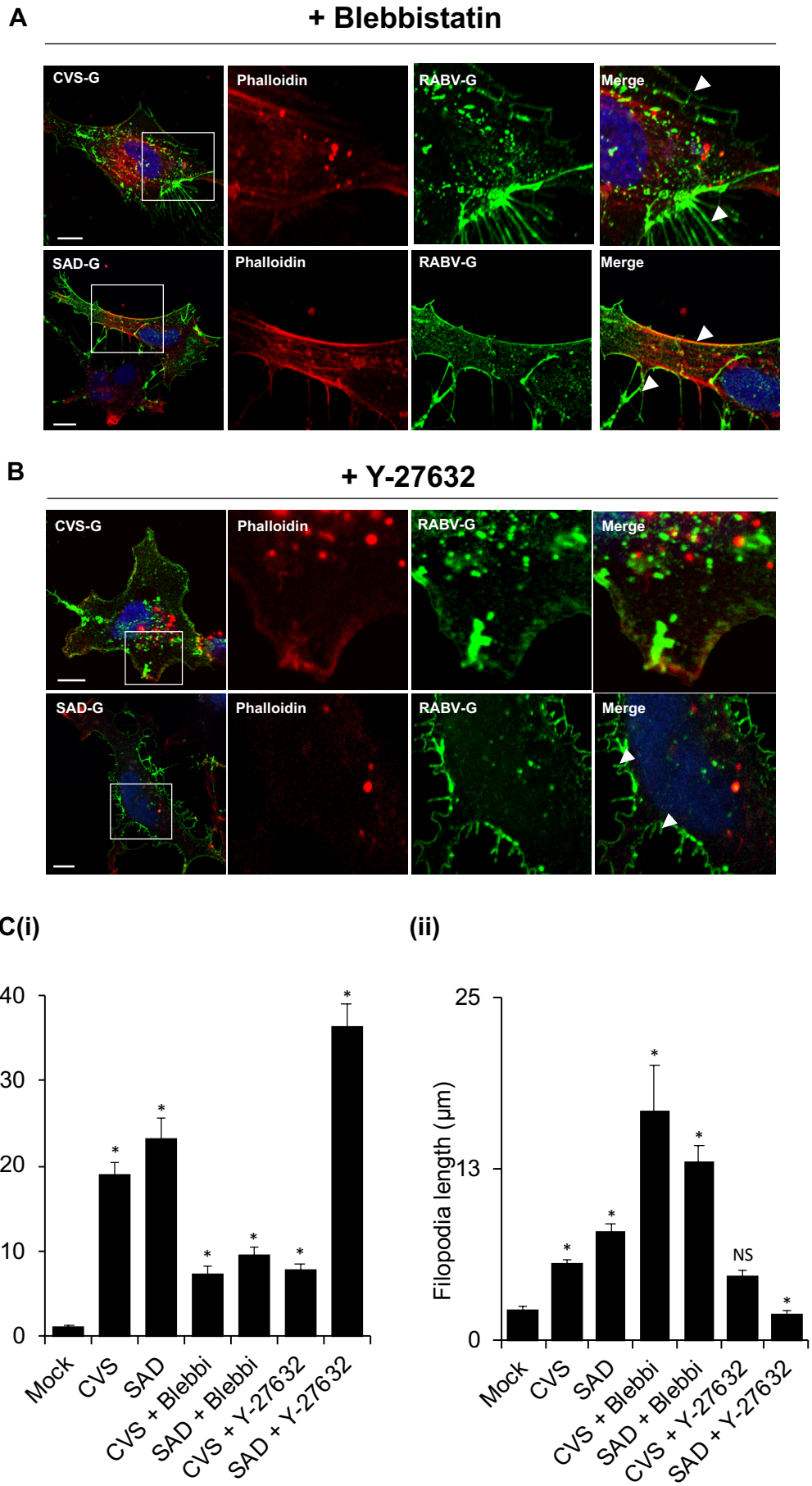
A
+ Blebbistatin
CVS-G
Phalloidin
RABV-G
Merge
SAD-G
Phalloidin
RABV-G
Merge
B
+ Y-27632
CVS-G
Phalloidin
RABV-G
Merge
SAD-G
Phalloidin
RABV-G
Merge
C(i)
Filopodia per cell
40
30
20
10
0
Mock
CVS
SAD
CVS + Blebbi
SAD + Blebbi
CVS + Y-27632
SAD + Y-27632
(ii)
Filopodia length (µm)
25
13
0
NS
Mock
CVS
SAD
CVS + Blebbi
SAD + Blebbi
CVS + Y-27632
SAD + Y-27632

D

SH-SY5Y

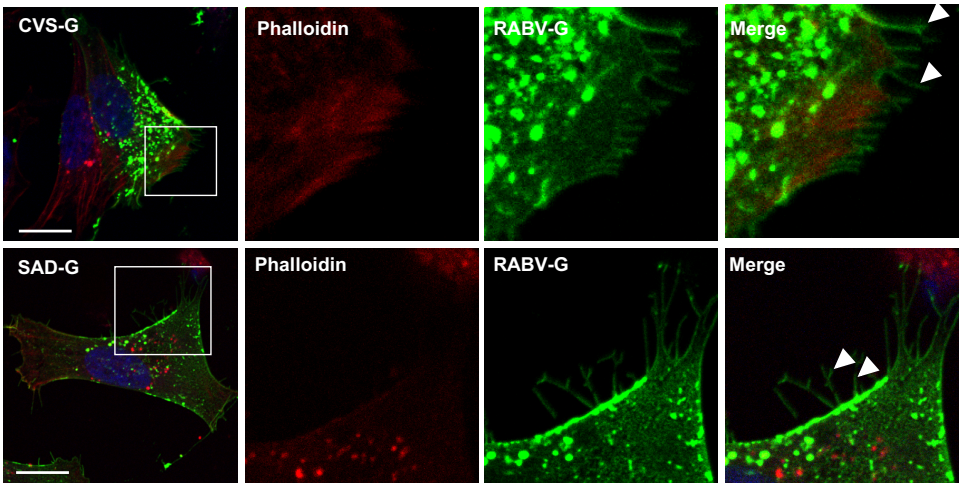

E

SH-SY5Y + Blebbistatin

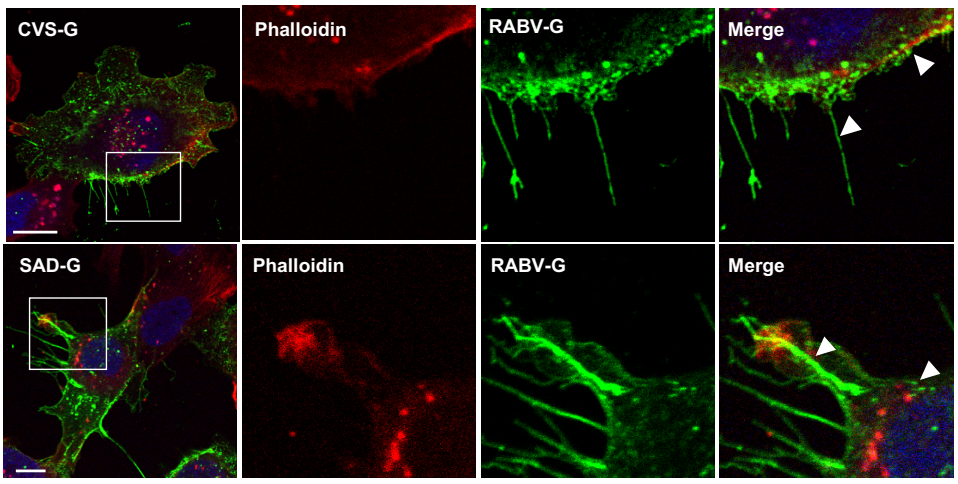

F

SH-SY5Y + Y-27632

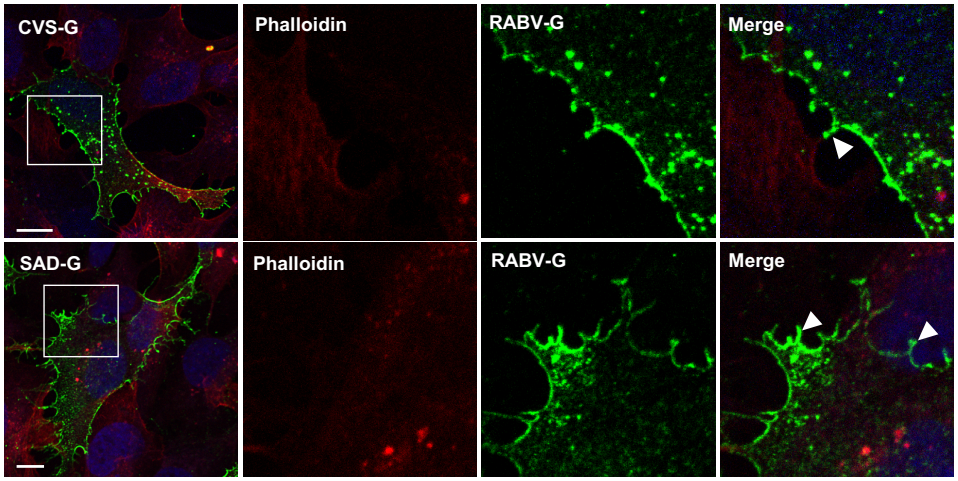

Figure 4.14 Myosin II and ROCK inhibition prevent CVS-G induced filopodia formation. (A) CVS-G or SAD-G expressing SVG-A cells were pre-treated for 45 min with 50 μM S-nitro-blebbistatin (myosin II ATPase inhibitor) then live labelled with anti-RABV-G and phalloidin-680 for 90 min. The filopodia projections appeared to retract from the cell edges except for small regions where filopodia projections appeared elongated in response to drug treatment. **(B)** CVS-G cells treated with 30 μM Y-27632 (ROCK inhibitor) showed almost a complete loss of filopodia, whilst SAD-G cells maintained their filopodia following drug treatment, Scale bar = 10 μm. **(C)** Quantitative analysis of **(i)** filopodia projection numbers and **(ii)** length in μm (n = 40) in response to blebbistatin treatment. Error bars indicate mean ± SEM. *significant difference between mock, CVS-G and SAD-G ($P < 0.05$). **(D)** SH-SY5Y cells also develop neurite-like projections upon CVS-G or SAD-G expression. Drug treatment with **(E)** Blebbistatin decreased the number of filopodia projections but led to elongation of the remaining filopodia. **(F)** Y-27632 treatment retracts filopodia for CVS-G but not SAD-G. Cell images are representative of 20 cells.

4.7 Discussion

In this Chapter, BioID fusions of CVS-G and SAD-G were constructed to probe the host-interacting partners that differ between the pathogenic and attenuated forms of these proteins. A BioID screen was then performed through profiling the range of cellular proteins within a ~10 nm distance to CVS-G and SAD-G. Several host candidates were identified with greater proximity to CVS-G than SAD-G, which were subsequently validated through a range of biochemical and immunofluorescent assays. The key findings were that CVS-G altered the cellular cytoskeleton and showed higher levels of ER-Golgi vesicle transport compared to SAD-G. Finally, it was shown that myosin II and ROCK inhibition interfere with CVS-G mediated filopodia production, through a mechanism distinct to SAD-G. The BioID screen therefore enhances our understanding of the host cell proteins targeted by the pathogenic forms of RABV-G, and reveals several new host cell processes that may be differentially regulated by pathogenic and attenuated RABV strains.

4.7.1 Ligation of BirA* to RABV-G

Of the BioID constructs generated, only the C-terminal ligation of BirA* to RABV-G bait (RABVG-BirA*) produced a panel of functionally biotinylated proximate proteins. Previous virus BioID screening analyses revealed host interactomes to HIV's Gag protein (Ritchie et al., 2015), envelope protein (Staubus et al., 2019), Epstein-Barr virus's latent membrane protein 1 (Rider

et al., 2018), influenza A virus's PA-X protein (Gaucherand et al., 2019), human cytomegalovirus pUL103 protein (Ortiz et al., 2016) and murine coronavirus virions (V'kovski et al., 2019) where new viral targets were identified including FLNA, HDLBP, GBF1, Arf1, and Sec61. High throughput BioID approaches were also produced through the fusion of BirA* to all constituent proteins of Zika virus (Coyaud et al., 2018) and SARS-CoV-2 (St-Germain et al., 2020; Laurent et al., 2020). These analyses revealed several respective cellular targets for both proteins, including RAB23, SNX19, RAB7A, VAPB and TMEM111. This study was the first to utilise the BioID system to compare the same proteins from pathogenic and attenuated strains of the same virus, namely CVS-G and SAD-G.

4.7.2 Intracellular trafficking of RABV-G

Previous analysis of the host proteome in response to RABV infection revealed a range of proteins with altered expression, including those involved in cytoskeleton regulation, intracellular trafficking, stress responses and virus spread from cell-to-cell, including VIM, PRX, LGALS1, SNAP and TRIM9 (Dhingra et al., 2007; Wang et al., 2011; Thanomsridetchai et al., 2011; Zandi et al., 2013). Similar candidate proteins were revealed through analysis of the RABV-G datasets, suggesting that RABV-G may mediate these interactions observed in fully infectious RABV systems (Figure 4.9). The purpose of this chapter was however to model how specific proteins that are proximal to CVS-G but not SAD-G may contribute to specific roles of pathogenic RABV-G during the virus lifecycle. Endogenous transfections of CVS-G and SAD-G into cells were used to model their role following RABV infection by pathogenic and attenuated strains, respectively. Trafficking differences exist between CVS-G and SAD-G (reported in Chapter 3) in which CVS-G traffics to the PM and rapidly internalises, whilst SAD-G traffics to- and is primarily retained at the PM with only low levels of internalisation observed (Chapter 3). From the BioID analysis of CVS-G *vs*. SAD-G, several host targets potentially responsible for these differences were identified, including those involved in clathrin-mediated endocytosis, including Clathrin 1, AP2 α1, AP2 α2, AP2 β1 and AP2 μ that would be expected to govern rapid removal of cargo from the PM. These proteins provide further detail on the transport of CVS-G following

its expression in infected cells (Figure 4.18) in which it is synthesised in the ER, processed in Golgi and trafficked to the PM. Following PM expression, RABV-G variants with Y_{497} are rapidly internalised through CME and interact with the aforementioned clathrin adaptor proteins to reduce CVS-G levels at the PM (Table 4.1). As identified by their enrichment in CVS-G vs SAD-G datasets, Dynamin and actin filaments are also likely to be involved in this rapid internalisation event (Piccinotti et al., 2013). The absence of these proteins from the SAD-G datasets provide further evidence of its slow PM-associated removal compared to CVS-G.

BioID analysis of CVS-G vs. SAD-G also revealed several adaptor proteins linked to the dynein-mediated anterograde trafficking of cargo from the Golgi apparatus to the ER (Jaarsma and Hoogenraad, 2015). Dynein adaptors mediating this transport that were identified included spectrin, rabankyrin-5 and huntingtin, along with dynactin (Reck-Peterson et al., 2018). Comparison of the trafficking profiles of CVS-G and SAD-G supported these findings as at steady state, a higher distribution of CVS-G with specific Golgi and Golgi-ER associated vesicles were observed (Figure 4.7). CVS-G may therefore be transported to the TGN and then either shuttled back to the ER through COPI-associated coatomer protein complexes including USO1, SEC23IP and SEC24C (also present in the BioID CVS-G datasets), or trafficked towards the secretory pathway through clathrin adaptors AP1 β1 and AP1 γ1 for PM expression and subsequent internalisation (Gravotta et al., 2019). The presence of CVS-G at Golgi to ER trafficking sites may also mediate its interaction with specific host-factors required to sustain virus replication, as previously reported for other negative sense RNA viruses including Hazara virus (Fuller et al., 2020). The localisation of pathogenic CVS-G but not attenuated SAD-G within these ER-Golgi sites may therefore support the sustained levels of virus replication observed for pathogenic RABV strains.

The BioID datasets also suggested a high association of CVS-G but not SAD-G with microtubules and with kinesin variants KIF5B, KIF23 and KIF2C that mediate retrograde transport towards cortical actin. It was speculated from the datasets that vesicles carrying CVS-G may therefore approach cortical actin, and myosin II variants IIA and IIB may then transport CVS-G towards the PM

where it promotes filopodia development through ciliogenesis proteins CLASP1, EXOC4, PLK1 and T-complex proteins, all identified within the BioID datasets (Figures 4.9 and 4.15). Yin and colleagues (2020) fused A FLAG tag to CVS-G and affinity-purified its binding partners, identifying dynamin, dynein, AP2 β1, CLASP2, myosin IIB and several T-complex proteins. These data support many of the features of CVS-G identified through BioID analysis in this Chapter.

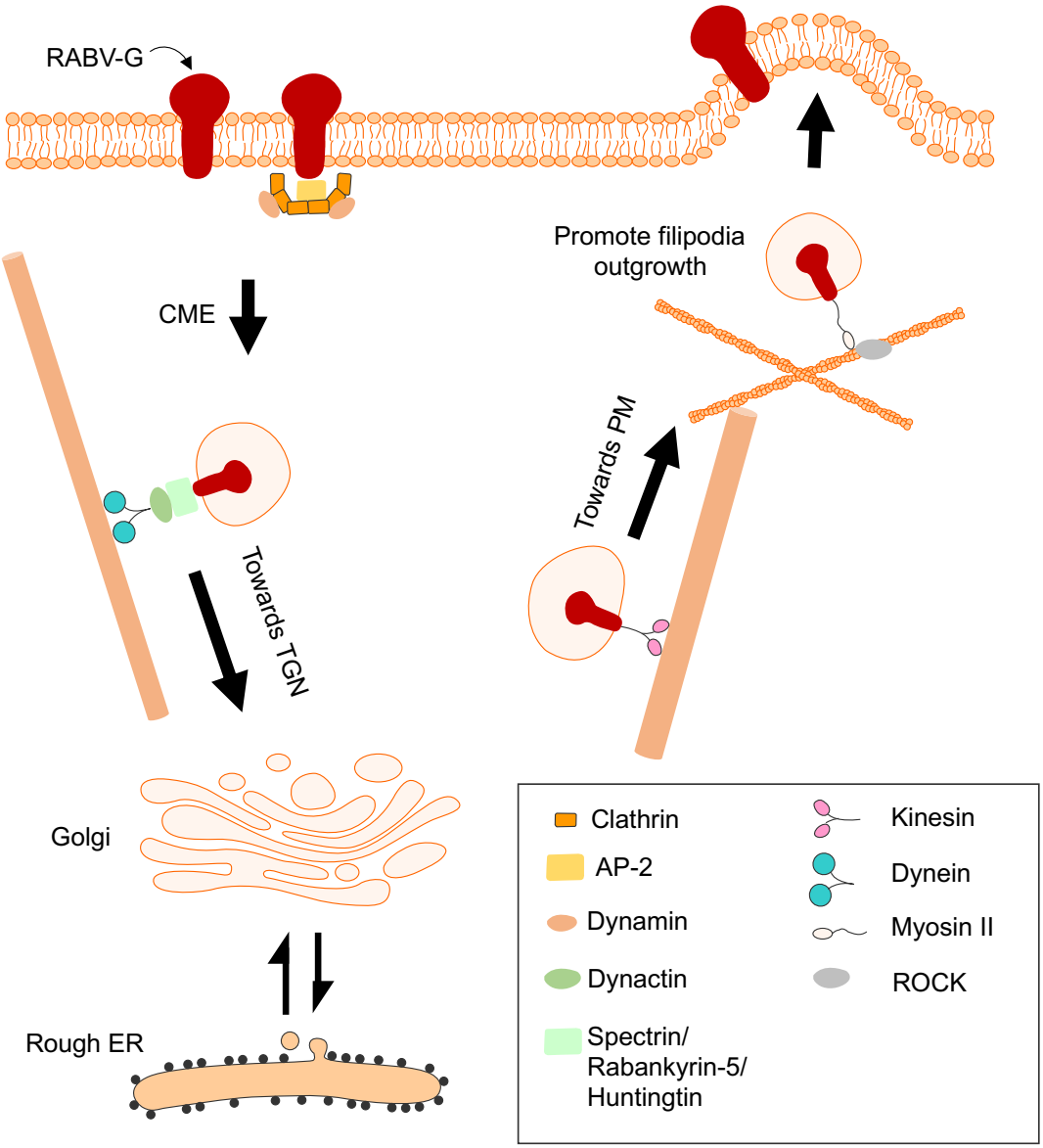

Figure 4.15 Proposed routes of CVS-G intracellular trafficking. CVS-G is synthesised in the ER, processed in Golgi apparatus and trafficked to the PM. RABV-G variants with Y_{497} rapidly internalise from PM through CME and AP2 adaptor proteins. Vesicles with RABV-G cargo are transported through dynein and dynein adaptors to the TGN and may be either trafficked back to ER or are shuttled towards the secretory pathway. Kinesins may CVS-G transport towards the PM and myosin II may regulate CVS-G movement on cortical actin. Once CVS-G is close to the PM, it mediates filopodia outgrowth through ROCK activation of actomyosin filaments. This differs for SAD-G which shows minimal Golgi association, high PM expression, and induces filopodia formation through a mostly ROCK independent mechanism.

4.7.3 Glycoprotein mediated filipodia and antiviral therapy

Many viruses exploit filopodia protrusions to enhance their capability to invade host cells vertically through primary infection or horizontally though cell-to-cell spread (Chang et al., 2016). Viruses exploit filopodia to move towards the attached cell body or 'surf' on filopodia prior to entry. This was reported for murine leukemia virus (Lehmann et al., 2005), HPV (Bienkowska-Haba and Sapp, 2011), Marburg virus (Schudt et al., 2013), HSV-1 (Oh et al., 2010) and RABV (Xu et al., 2015). In the case of HIV-1, the filopodia projections were partially induced by HIV-Nef (Nobile et al., 2010; Aggarwal et al., 2012), whilst in the case of Merkel cell polyomavirus, the small tumor antigen (ST) induces the formation of filopodia projections to promote tumorigenesis (Stakaitytė et al., 2017). In this chapter, the ability of both CVS-G and SAD-G to induce the filopodia observed in RABV infection was confirmed, though the requirement for ROCK during CVS-G induced filopodia formation suggested subtle differences between pathogenic and attenuated RABV strains.

How viruses promote filopodia outgrowth is still debated. HSV-1 gB interacts with Cdc42 (Oh et al., 2010) or myosin IIA/IIB (Arii et al., 2015) to promote filopodia outgrowth. HIV *env* interacts with Cdc42 and activates Src kinase, Pak1 and Wasp (Nikolic et al., 2011) or Diaph2 (Aggarwal et al., 2012) to promote filopodia outgrowth. Wen and colleagues showed that cofilin, LIMK1 and ROCK1 regulate HIV mediated filopodia protrusions and cell-to-cell spread (Wen et al., 2014). Marburg virus utilises Cdc42 and myosin X (*Myo10*) (Kolesnikova et al., 2007) whilst Merkel cell polyomavirus utilises Cdc42 and RhoA (Stakaitytė et al., 2017) to promote filopodia growth. In the BioID screen of CVS-G, myosin IIA, myosin IIB, ROCK and cofilin-1 were identified (Figure 4.9), all representing potential mediators of CVS-G-mediated filopodia

outgrowth. Treatment with blebbistatin disrupted both CVS-G and SAD-G mediated filipodia outgrowth, also shown to inhibit murine leukemia virus (Lehmann et al., 2005), HPV-16 (Schelhaas et al., 2008), and Kaposi's sarcoma-associated herpesvirus (Valiya Veettil et al., 2010) filopodia-like projections. A key finding was however that CVS-G filopodia outgrowth was dependent on ROCK activity, whilst SAD-G retained the ability to induce filopodia during successful ROCK inhibition. Further studies are now required to validate the roles of these divergent filopodia in CVS vs SAD infections, and to assess the antiviral activity of filopodia-inhibiting agents, including Y-27632 against pathogenic RABV infections.

Chapter 5 | Palmitoylation and lipid raft association contribute to the differential trafficking phenotypes of CVS-G and SAD-G

5.1 Introduction

Many virus glycoproteins are post translationally S-acylated. Protein S-acylation describes the attachment of long hydrophobic fatty acids to cysteine residues through thioester linkages (Roth et al., 2002). These fatty acids include palmitic acid, stearic acid or oleic acid, amongst others. Of these modifications, the attachment of palmitic acid (or palmitoylation) is the most common, with ~10% of cell proteins and ~41% of synaptic proteins subject to palmitoylation events (Sanders et al., 2015). Protein palmitoylation is catalysed by palmitoyltransferases (Roth et al., 2002) at the ER and Golgi, enhancing the tethering of proteins to membranes (Ohno et al., 2006; Veit, 2012).

Palmitoylation was first discovered for VSV-G at a single cysteine at the transmembrane-cytoplasmic tail interface (C_{473}) (Schmidt and Schlesinger, 1979). VSV-G is a RABV-G-like rhabdovirus glycoprotein with many shared characteristics (Gaudin and Whitt, 2014). CVS-G was subsequently shown to undergo palmitoylation at a similar position (C_{461}) (Gaudin et al., 1991). Despite these discoveries, mutation of the VSV-G palmitoylation site had no functional effect on virus assembly or fusion activity (Whitt and Rose, 1991), and specific VSV strains such as the Glasgow isolate of VSV Indiana harbour a natural C473Y mutation at this position. SAD-G possesses two cysteine residues at $CC_{460\text{-}461}$ (Gaudin et al., 1991) but palmitoylation at C_{460} has not been investigated (Gadalla and Veit, 2020).

The palmitoylation of other virus glycoproteins have been shown to be associated with virus budding and cell-to-cell spread. SARS-CoV Spike (S) contains nine palmitoylation sites, with the deletion of C1234/1235A attenuating the incorporation of S into virions (Ujike et al., 2012). Similarly the deletion of two key palmitoylation sites in the HA protein of influenza virus attenuates its release from the PM (Chen et al., 2005). Removal of palmitoylated cysteines from measles virus F protein reduces its cell-to-cell fusion activity (Caballero et al., 1998). Deletion of palmitoylation sites from murine leukaemia virus env reduces its ability to induce syncytia (Li et al., 2002).

Palmitoylation is one of the best characterised signals for the lipid raft localisation of proteins (Levental et al., 2010). The deletion of the palmitoylation sites in influenza virus HA also abolishes its incorporation into membrane-raft regions (Chen et al., 2005). Deletion of the palmitoylation sites in HIV *env* and mouse leukaemia virus *env* protein were also reported to abolish their retention at lipid rafts (Rousso et al., 2000; Li et al., 2002; Bhattacharya et al., 2004), though these findings have been questioned for the *env* proteins of HIV and SIV (Chan et al., 2005; Vzorov et al., 2007).

Protein palmitoylation also affects the internalisation and PM expression of both cellular and viral proteins. Deletion of palmitoylation sites in HA increases its mobility in the PM as shown through FILM-FRET and FRAP (Engel et al., 2010). Deletion of the palmitoylation sites in murine leukaemia virus *env* and Sindbis virus small membrane protein (TF) increased their rates of internalisation and reduced their surface expression (Li et al., 2002; Ramsey et al., 2017). RSV *env* harbouring a C167G mutation internalised at a greater rate than WT *env* that had no loss of its palmitoylation event. Double palmitoylation deletions in RSV *env* C164/167G further enhanced this endocytic event (Ochsenbauer et al., 2000). These studies highlight the potential involvement of palmitoylation in the lipid-raft localisation and internalisation of RABV-G proteins.

The main function of palmitoylation is during membrane anchorage (Resh, 2004). Some common characteristics have been reported as associated with palmitoylation, such as the presence of distant myristoylation sites or proximity to basic or hydrophobic amino acids (Resh, 2004; Veit, 2012). In CVS-G, the palmitoylation site at residue 461 exists as a single cysteine, compared to SAD-G in which a second potential palmitoylation site at C_{460} is present. Of note, the palmitoylation of SAD-G has not been reported. In this chapter, the palmitoylation of CVS-G and SAD-G were explored in further detail to investigate its contribution to the trafficking and membrane anchorage of these proteins. Herein, data is provided showing that SAD-G undergoes a dual palmitoyaltion event at $CC_{460\text{-}461}$ and its contribution to the trafficking phenotypes of SAD-G are discussed.

5.2 Palmitoylation of CVS-G and SAD-G

5.2.1 Mutagenesis analysis

Gaudin and colleagues (1991) reported that pathogenic CVS-G possesses a single palmitoylation site at C_{461}. Attenuated SAD-G has C_{460} in addition to C_{461} (Figure 5.1A-B). The second cysteine at 460 is potentially palmitoylated due to its close proximity to C_{461} and presence between the transmembrane and cytoplasmic domains of SAD-G (Veit, 2012). It would be hypothesised that the presence of two palmitoylation sites for SAD-G would make the protein more hydrophobic and potentially increase its association with cellular membranes.

The palmitoylation sites were first investigated through mutagenesis analysis. CVS-G W_{460} was mutated to C_{460} to hypothetically introduce a second palmitoylation site into this protein. The single palmitoylation site in CVS-G was also mutated to alanine (C_{461}) to prevent the palmitoylation event in CVS-G (Figure 5.1C). SAD-G C_{460} was mutated to W_{460} to mimic CVS-G, whilst C_{461} was mutated to A_{461} either alone or in combination with C460A to completely abrogate palmitoylation.

As reported in Chapter 3, $CVSG_{SADT}$ that consists of the SAD-G C-terminus fused to CVS-G reduced the levels of CVS-G internalisation, but did not completely revert its trafficking phenotype back to that of SAD-G. This suggested that factors in addition to the C-terminus dictate the internalisation behaviour of these proteins. $EBLVG_{SADT}$ that contains the substituted SAD-G C-terminus fused to EBLV-G, did however show reduced internalisation levels that were comparable to SAD-G (see Chapter 3, Figure 3.14). SAD-G and EBLV-G possess dual cysteines at $CC_{460-461}$ whilst $CVSG_{SADT}$ has $WC_{460-461}$, and so it was hypothesised that W_{460} in $CVSG_{SADT}$ may lack the membrane anchorage phenotype of SAD-G which may prevent its complete reversion to SAD-G phenotype. A W460C mutation was therefore introduced into $CVSG_{SADT}$ (Figure 5.1C) to investigate this effect.

A

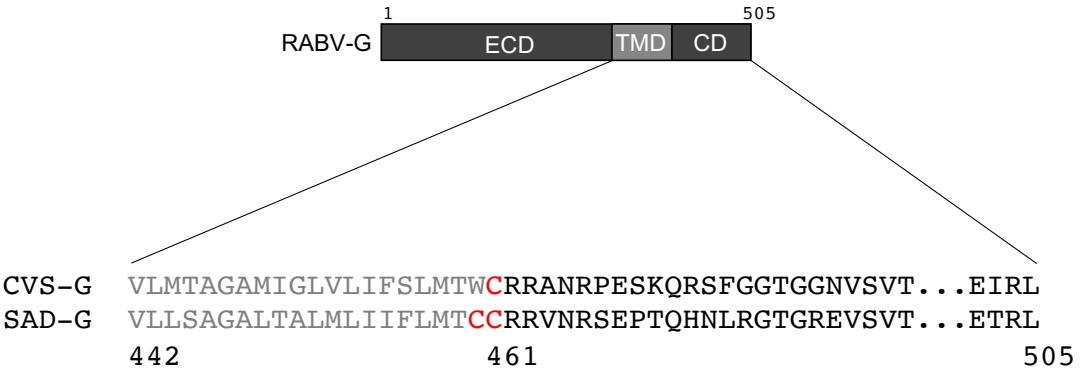

B(i)

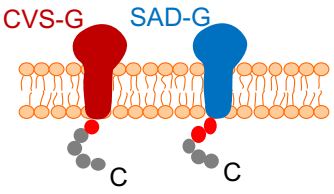

(ii)

Strain	Motif	Palmitoylation
CVS-G	WC	Single palmitoylation event
SAD-G	CC	Double palmitoylation event

C

Strain	Mutant	Intended palmitoylation disruption	Predicted effect
CVS-G	W460C	Second palmitoylation site introduced	Enhanced lipid-raft association
CVS-G	C461A	Deleted palmitoylation site	Reduced lipid-raft association
SAD-G	C460W	First palmitoylation site deleted	Reduced lipid-raft association
SAD-G	C461A	Second palmitoylation site deleted	Reduced lipid-raft association
SAD-G	C460A/C461A	Deleted palmitoylation sites	Reduced lipid-raft association
$CVSG_{SADT}$	W460C	Second palmitoylation site introduced	Enhanced lipid-raft association

Figure 5.1 CVS-G and SAD-G palmitoylation and mutagenesis analysis. (A) Presence of palmitoylated cysteine(s) at the interface of the transmembrane and cytoplasmic domains. CVS-G has a single palmitoylation site at 461, whilst SAD-G display a hypothesised double palmitoylation at 460 and 461. **(B)** Palmitoylated cysteines are long hydrophobic side chains that anchor RABV-G to the cytosolic side of the PM. It is hypothesised that a double palmitoylation event in SAD-G may enhance its membrane association due to this palmitoylation anchorage. **(C)** Mutagenesis of CVS-G, SAD-G and $CVSG_{SADT}$ were performed to investigate the contribution of palmitoylation to both CVS-G and SAD-G proteins.

5.2.2 Expression of the palmitoylation mutants of CVS-G and SAD-G

The palmitoylation mutants CVS-G W460C, CVS-G C461A, SAD-G C460A, SAD-G C461A and SAD-G C460/461A were first produced by mutagenesis and their expression was assessed alongside WT CVS-G, SAD-G and $CVSG_{SADT}$. For western blotting, cells were lysed 16 h post-transfection in a triton-based lysis buffer (See Materials and Methods 2.6.1) and proteins were resolved by SDS-PAGE. Proteins were then transferred onto PVDF membranes and probed with P160 polyclonal anti-RABV-G antibodies (1:250). The results showed ~58 kDa band for CVS-G and ~63 kDa band for SAD-G as previously observed (see Chapter 3, Figure 3.1A). However and of note, some differences in the intensity of expression were observed for the mutants. $CVSG_{SADT}$ and CVS-G C461A bands were of higher intensity in the lysates than CVS-G, which further increased for the CVS-G W460C mutant (Figure 5.2A). SAD-G C460W and SAD-G C461A showed comparable expression to WT SAD-G, however the dual-palmitoylation mutant SAD-G C460/C461A was the most highly expressed of all SAD-G variants (Figure 5.2A).

To investigate whether these differences in expression were an artefact of the transfection efficiency or western blot conditions, SVG-A cells expressing each mutant were live labelled with E559 anti RABV-G antibodies, fixed, and imaged using an IncuCyte plate reader. Widefield images showed an equivalent number of transfected cells for all mutants, suggesting that the changes in the expression profiles may reflect their susceptibility to solubilisation in the triton-based lysis buffer (Figure 5.2B). These results suggest that the introduction or deletion of palmitoylated cysteines may directly affect the membrane localisation of the RABV-G variants.

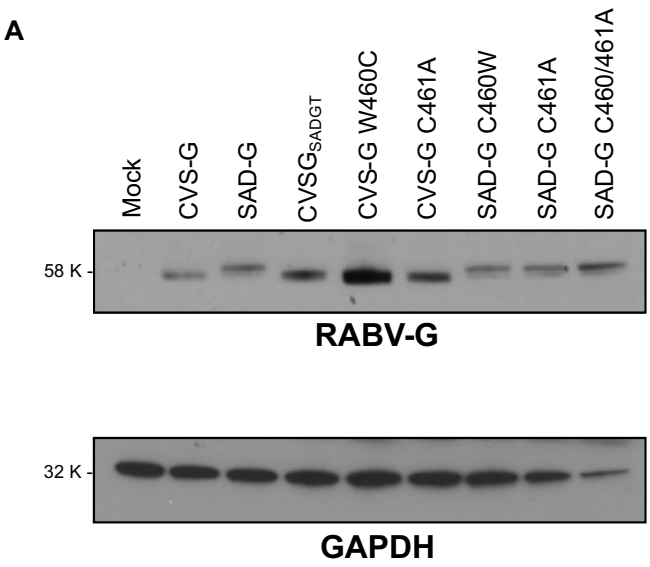

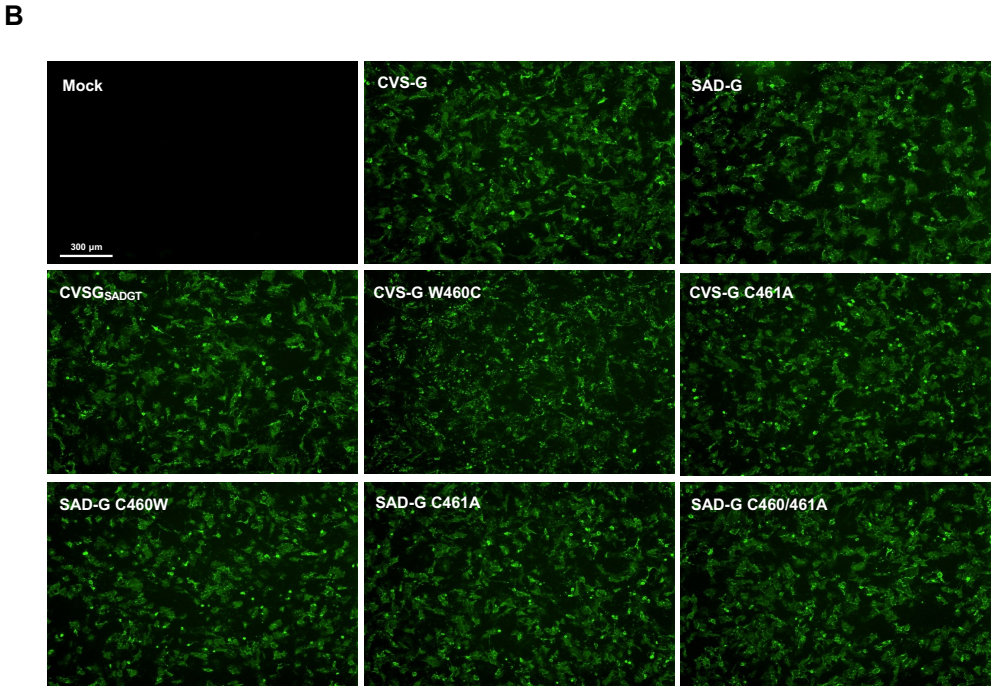

Figure 5.2 Expression of RABV-G palmitoylation mutants in mammalian cells. (A) HEK293T cells were transfected, lysed and probed with P160 polyclonal anti RABV-G. GAPDH was probed as a loading control. Results are representative of 3 blots. **(B)** Live labelled SVG-A cells were fixed and imaged through IncuCyte plate reader. Widefield images showed equal expression levels for RABV-G mutants. Scale bar = 300 µm.

5.2.3 Palmitoylation levels

The palmitoylation status of the mutants were next assessed using the Badrilla's CAPTUREome S-Palmitoylated Protein kit. This method involves exchanging cysteine-bound fatty acids on proteins with a biotin derivative which is then captured using streptavidin beads. All proteins present within the streptavidin samples are therefore palmitoylated (Figure 5.3A). Assays were performed in HEK293T cells expressing each palmitoylation mutant of CVS-G and SAD-G. Once captured, proteins were resolved through SDS-PAGE and probed with anti-RABV-G antibodies. WT CVS-G showed a band at ~58 kDa and SAD-G showed a band at ~63 kDa (Figure 5.3B), confirming that both proteins are palmitoylated. $CVSG_{SADT}$ also showed a band at ~58 kDa. Of interest, the introduction of the CC motif into CVS-G (W460C) increased its expression in the immunoprecipates, suggestive of an additional palmitoylation event. Importantly, both mutation of the single palmitoylation site in CVS-G (C461A) and the double palmitoylation site in SAD-G C460/461A to alanine prevented the palmitoylation of both proteins, evidenced by their absence in the streptavidin immunoprecipitates. SAD-G C460W and SAD-G C461A showed evidence of palmitoylation, albeit to lower levels in the SAD-G C461A mutant, confirming that the deletion of both cysteine residues are required to completely inhibit its palmitoylation, suggesting that the CC motif is a site of dual palmitoylation (Figure 5.3B). Taken together, these data confirm that CVS-G possesses a single palmitoylation site at C_{461} as previously described, but reveals for the first time that SAD-G possesses a double palmitoylation site at $CC_{460\text{-}461}$, highlighting key differences between the lipidation of these proteins.

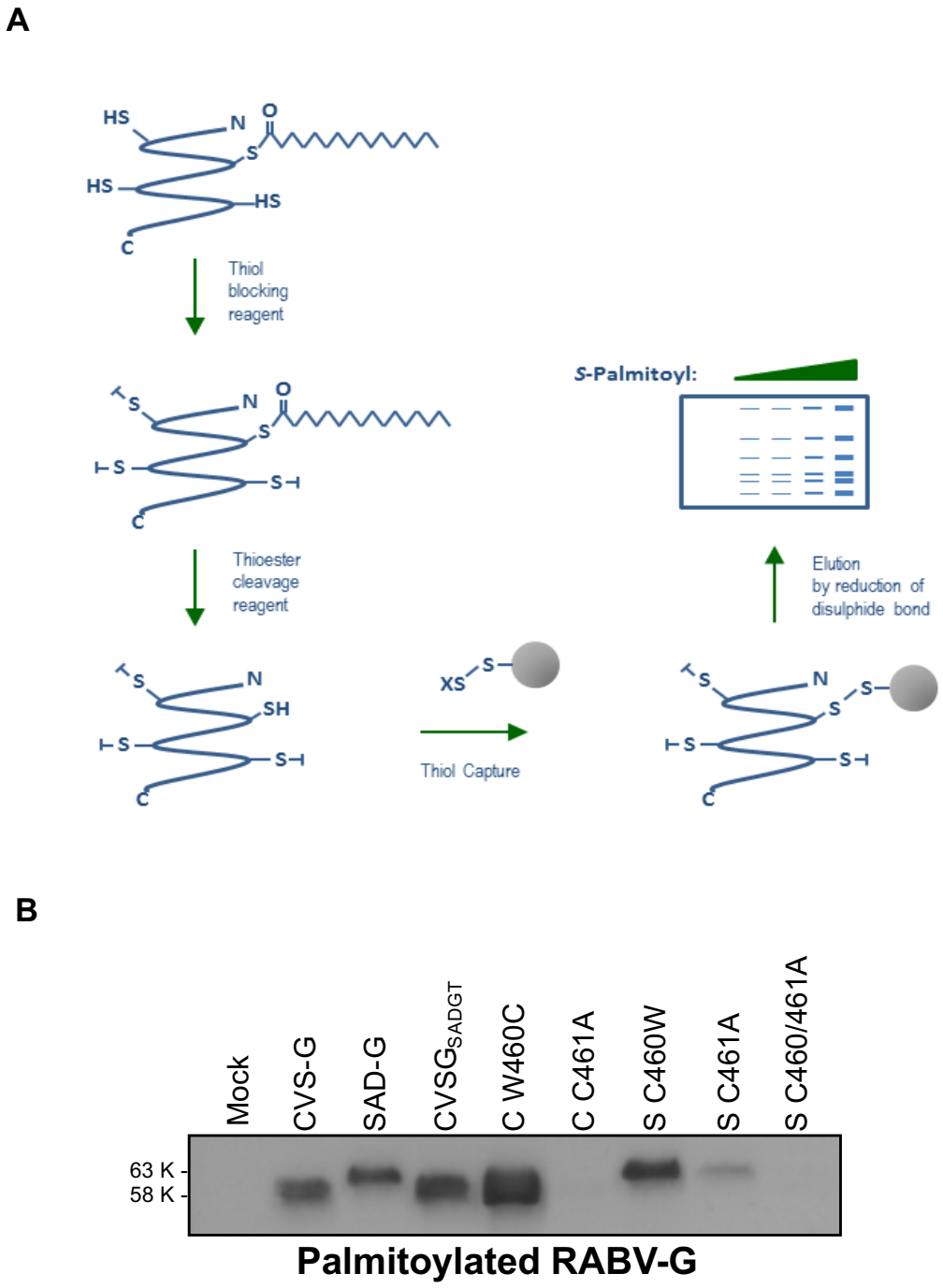

Figure 5.3 SAD-G possesses a double palmitoylation site that is absent in CVS-G. (A) Commercially available palmitoylation isolation kits involve blocking all potential thiol sites. Thioester sites on the cysteines are then cleaved and the fatty acids are replaced with a biotin-derivative. Proteins tagged with this biotin derivative can then be eluted using a streptavidin resin. **(B)** Isolated palmitoylated proteins were resolved through SDS-PAGE and probed with anti RABV-G. Resulting bands of ~58 kDa for CVS-G and ~63 kDa for SAD-G were observed. Importantly, the dual mutation of SAD-G C460A and C461A were required to completely inhibit SAD-G palmitoylation, confirming the presence of a dual palmitoylation site within this protein.

5.3 RABV-G palmitoylation and surface expression

5.3.1 Lipid raft localisation

Highly palmitoylated viral glycoproteins such as influenza HA, HIV env and mouse leukaemia virus env proteins are often associated with lipid rafts (Li et al., 2002; Bhattacharya et al., 2004; Chen et al., 2005). For influenza HA, the palmitoylation profile in relation to lipid rafts localisation identified a C_{551} at the interface of transmembrane and cytoplasmic domain to have the most pronounced effect on lipid raft localisation, as opposed to distant cytoplasmic cysteines C_{559} and C_{562} (Scolari et al., 2016). It can be thus implied that the palmitoylated sites in RABV-G may influence its association with lipid rafts.

The lipid raft localisation of both CVS-G and SAD-G palmitoylation mutants were therefore investigated using the G-Biosciences' FOCUS lipid raft isolation kit. This method involves the fractionation of cell lysates into soluble and membrane-bound proteins (Figure 5.4A), from which membrane-bound proteins are fractionated and treated with non-ionic detergents. Membrane-bound proteins that are insoluble in non-ionic detergents, such as those in lipid rafts (Low, 1989) are then extracted with ionic detergents (FBS buffer). Both soluble and lipid rafts fractions were resolved by SDS-PAGE and western blotting was performed using anti-RABV-G antibodies. Interestingly, CVS-G showed a band in the soluble fraction (non-membrane bound proteins) whereas SAD-G did not, which is suggestive of higher CVS-G intracellular expression. Upon comparison, SAD-G showed more intense expression in raft fractions compared to CVS-G (2-fold higher expression, n = 3, Figure 5.4B). GAPDH labelling showed no bands in the raft fractions, confirming the specificity of the raft isolations (Figure 5.4B, Cho et al., 2019).

Upon analysis of $CVSG_{SADT,}$ comparable levels of raft-association were observed to WT CVS-G, confirming that the raft association of SAD-G was not dictated by its C-terminus (Figure 5.4C-D). However and somewhat surprisingly, the addition of an additional cysteine in CVS-G (W460C) and mutation of the sole palmitoylation site in CVS-G (C461A) both reduced its association with lipid raft-regions (Figure 5.4C-D). Whilst this may be expected for C461A as it abrogates CVS-G palmitoylation, the effects of the addition of

the additional palmitic acid at W460C predicted to increase the hydrophobicity of the protein, were unexpected (Blaskovic et al., 2013; Sobocinska et al., 2018). Mutation of only the first palmitoylated cysteine in SAD-G (C460W) did not reduce its lipid raft association (Figure 5.4C-D). However, mutation of the second palmitoylated cysteine (C461A) or double mutation of the dual palmitoylation site in SAD-G C460/461A led to a loss of raft localisation, confirming a key role for C461 in the raft-association (Figure 5.4C-D). These data confirmed differences in the raft-association of both CVS-G and SAD-G and the influence of palmitoylation on this association.

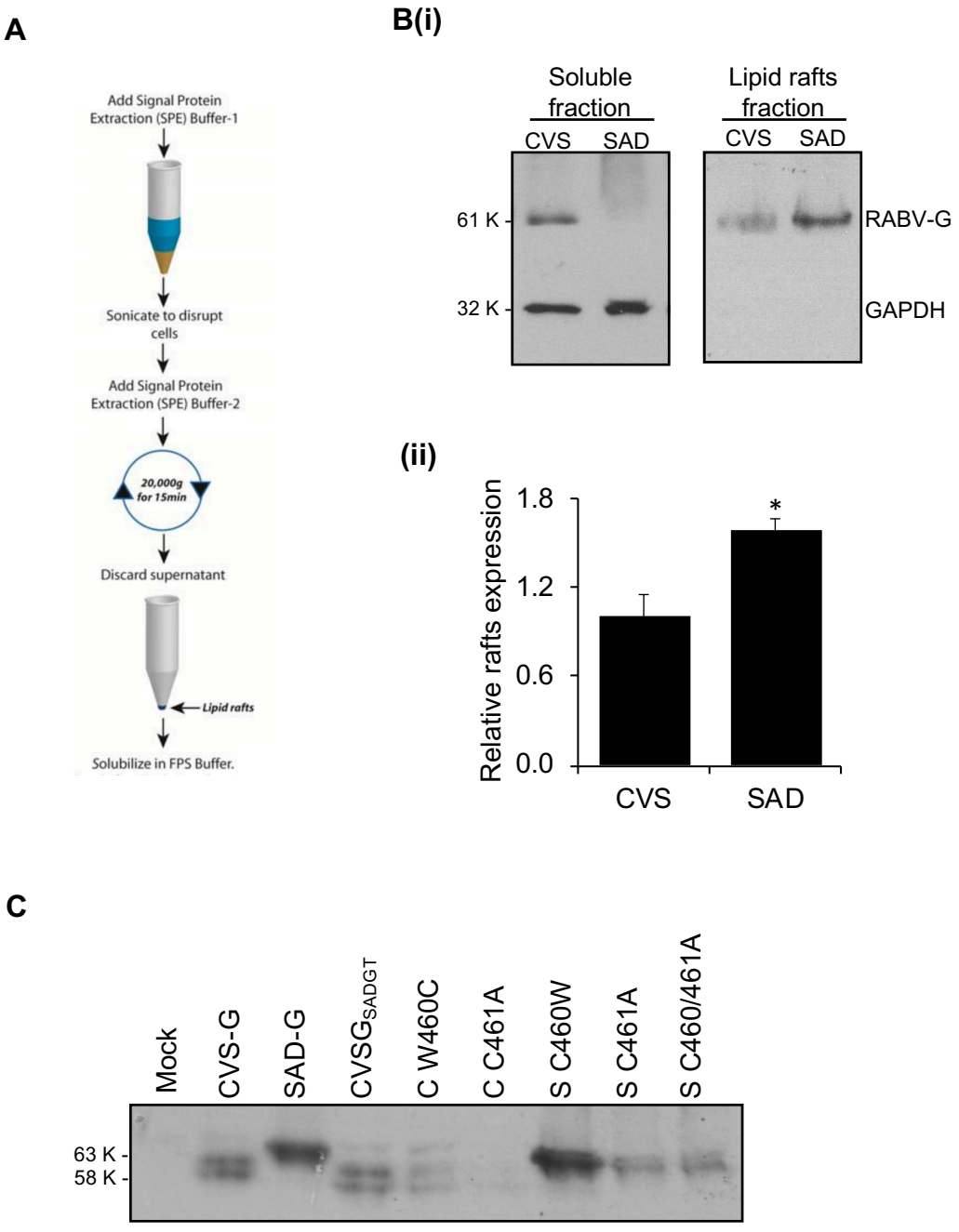

D

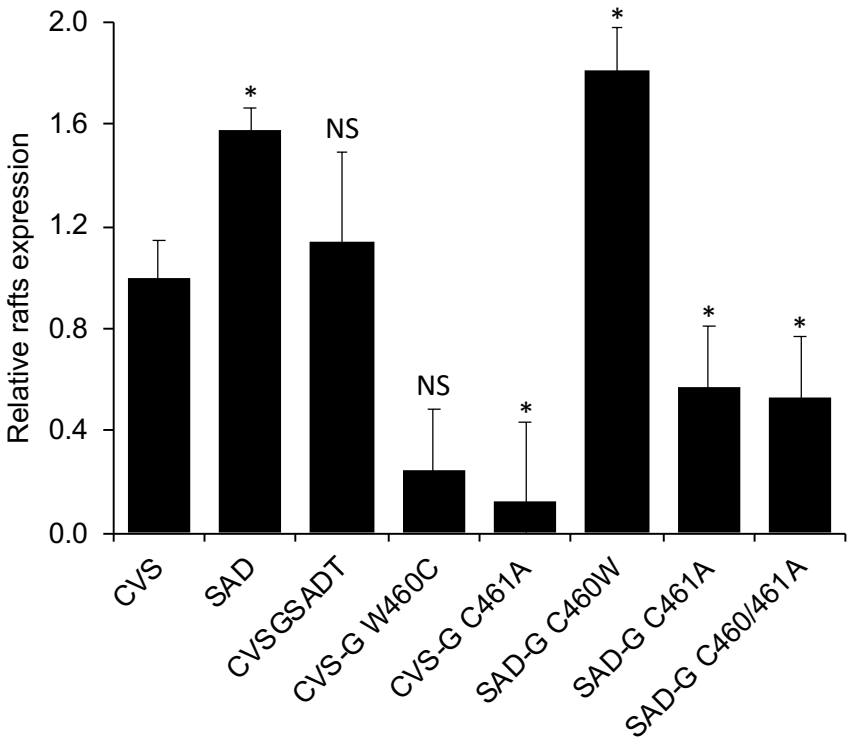

Figure 5.4 SAD-G has higher lipid rafts localisation than CVS-G and mutants display an unusual phenotype. (A) Lipid rafts isolation kit involves solubilisation of cell lysates in three different buffers to extract membrane proteins insoluble in non-ionic detergents - proteins localised at lipid rafts. **(B)** From the rafts kit, CVS-G was **(i)** shown to be present in soluble fraction where SAD-G was absent, reflecting their intracellular distribution. Rafts fraction had more SAD-G expression and **(ii)** upon quantification, SAD-G displayed 2-fold expression intensity of CVS-G (n = 3). **(C)** The rafts fraction was probed with anti-RABV-G to **(i)** show ~58 kDa expression for CVS-G and $CVSG_{SADT}$, very low signal both CVS-G W460C and C461A whereas SAD-G and SAD-G C460W had a ~63 kDa expression that is lower for the two other SAD-G mutants. **(D)** Quantifications of mutants in relation to CVS-G. Results are representative of 3 blots. Error bars indicate mean ± SEM. *significant difference between CVS-G and mutants ($P < 0.05$).

5.3.2 Addition of the dual palmitoylation motif to CVS-G enhances its removal from the PM

CVS-G internalises to higher levels than SAD-G. Given the known correlation between the lipid raft localisation of cellular proteins and their slower removal from the PM, the effects of the palmitoylation mutants on the removal of CVS-G and SAD-G from the plasma membrane were next investigated. Upon the introduction of the dual palmitoylation site (W460C) into CVS-G, thereby introducing a second palmitoylation event, live-surface labelling (Figure 5.5A) showed a vast number of internalised intracellular puncta, indicative of the rapid surface removal of this mutant from the PM (white arrowheads, 3-fold higher number of intracellular puncta compared to WT CVS-G, Figure 5.5B). Given that this mutant shifted the majority of CVS-G to non-lipid-raft like regions, this suggested that the introduction of a second cysteine to CVS-G enhanced its internalisation from the PM, most likely due to the more rapid removal rates of PM proteins from non-raft regions through CME.

A

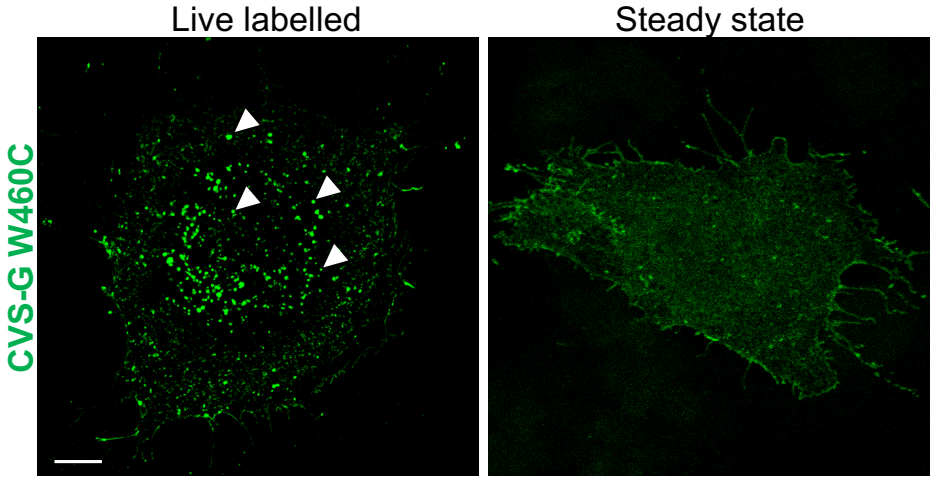

B

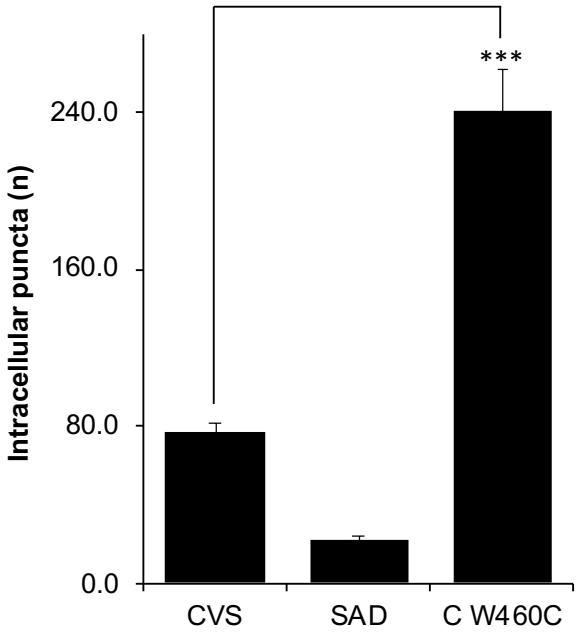

Figure 5.5 CVS-G W460C enhances the internalisation of CVS-G. (A) SVG-A cells were transfected with CVS-G W460C and either live-labelled or labelled at steady state labelled as described previously. Live labelled cells showed higher levels of internalisation from the PM (white arrowheads). Scale bar = 10 μm. **(B)** Quantification of intracellular puncta (n=25 cells). Error bars indicate mean ± SEM. ***significant difference between CVS-G and CVS-G W460C ($P < 0.0005$).

5.3.3 Removal of CVS-G palmitoylation also enhances surface removal

Given these findings, the C461A CVS-G mutant was next investigated to assess the effects of removal of the single palmitoylation site on its internalisation. In the experiments that followed, SVG-A cells expressing the C461A mutant were either live-labelled or labelled at steady state. The C461A mutant showed a diffuse steady-state distribution with evidence of PM staining (Figure 5.6A). Upon assessment of its internalisation profile and quantification of the total number of internalised puncta, CVS-G C461A showed almost twice the number of intracellular puncta compared to WT CVS-G (Figure 5.6B), suggesting that the removal of the single cysteine residue enhanced the internalisation of CVS-G (white arrows). Since like the W460C mutant, the C461A mutant decreased the association of CVS-G with lipid rafts, it was again reasoned that both these mutants internalise more rapidly due to their absence from lipid rafts.

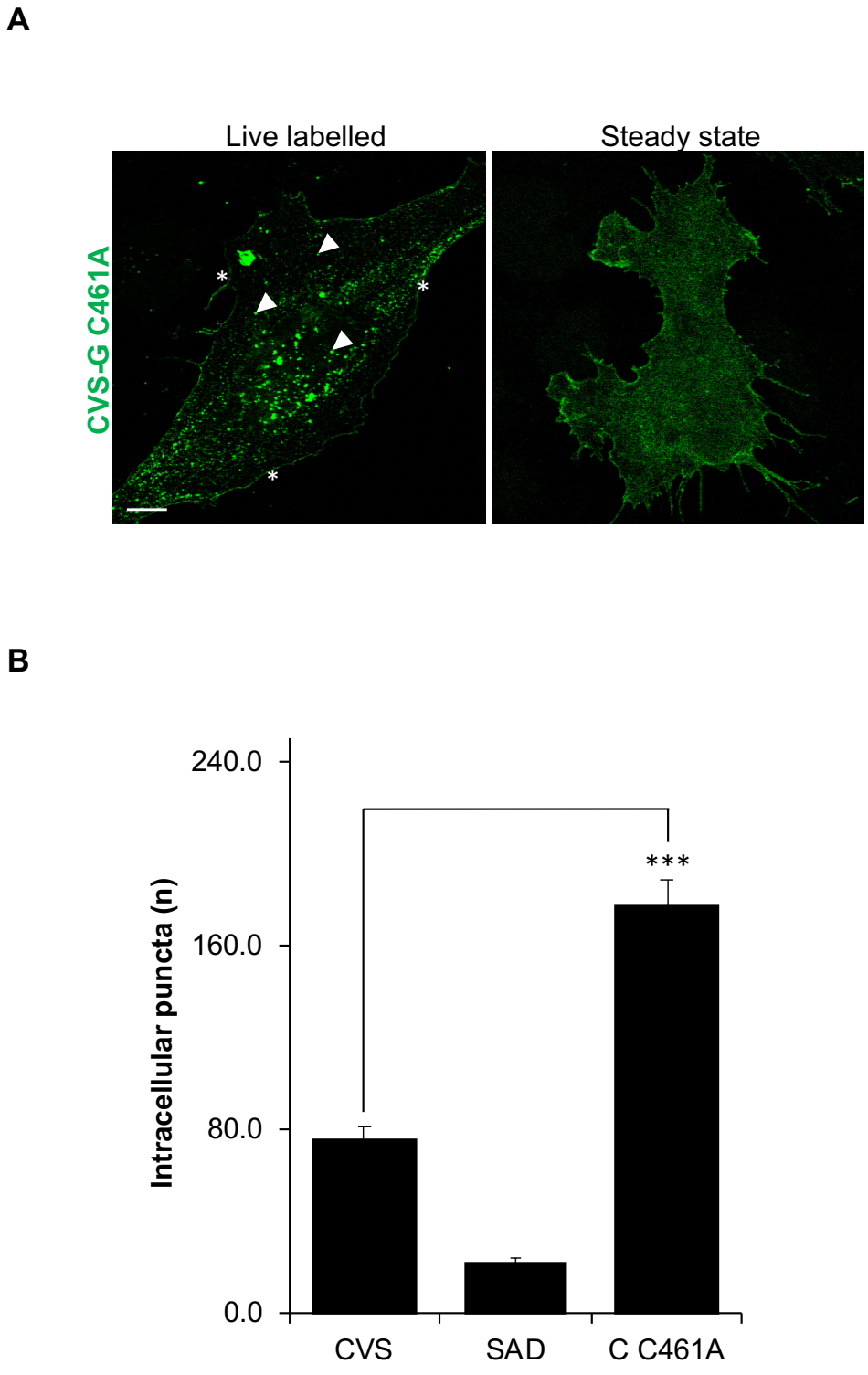

Figure 5.6 CVS-G C461A shows higher levels of internalisation than WT CVS-G. (A) SVG-A cells were transfected with CVS-G C461A and labelled in live-cells or at steady state as described previously. Scale bar = 10 µm. **(B)** Quantification of intracellular puncta from n=25 cells. Error bars indicate mean ± SEM. ***significant difference between CVS-G and CVS-G C461A ($P < 0.0005$).

5.3.4 Removal of the first palmitoylation site does not significantly affect SAD-G internalisation

SAD-G possesses two palmitoylation sites at C_{460} and C_{461} (Figure 5.3). Upon investigation of mutation of the first palmitoylation site (C460W) with its mutation to W to mimic that of CVS-G at this site, low levels of internalisation were observed, with minimal evidence of internalised puncta and high levels of protein clustering at the PM (Figure 5.7A). Quantification of these internalised puncta showed that these structures were ~20% less in abundance when observed for SAD-G (Figure 5.7B). Given that this mutant enhanced the localisation of SAD-G within raft like-regions, this strengthened the premise that the high levels of SAD-G in raft-like regions impairs its removal from the PM (Figure 5.4).

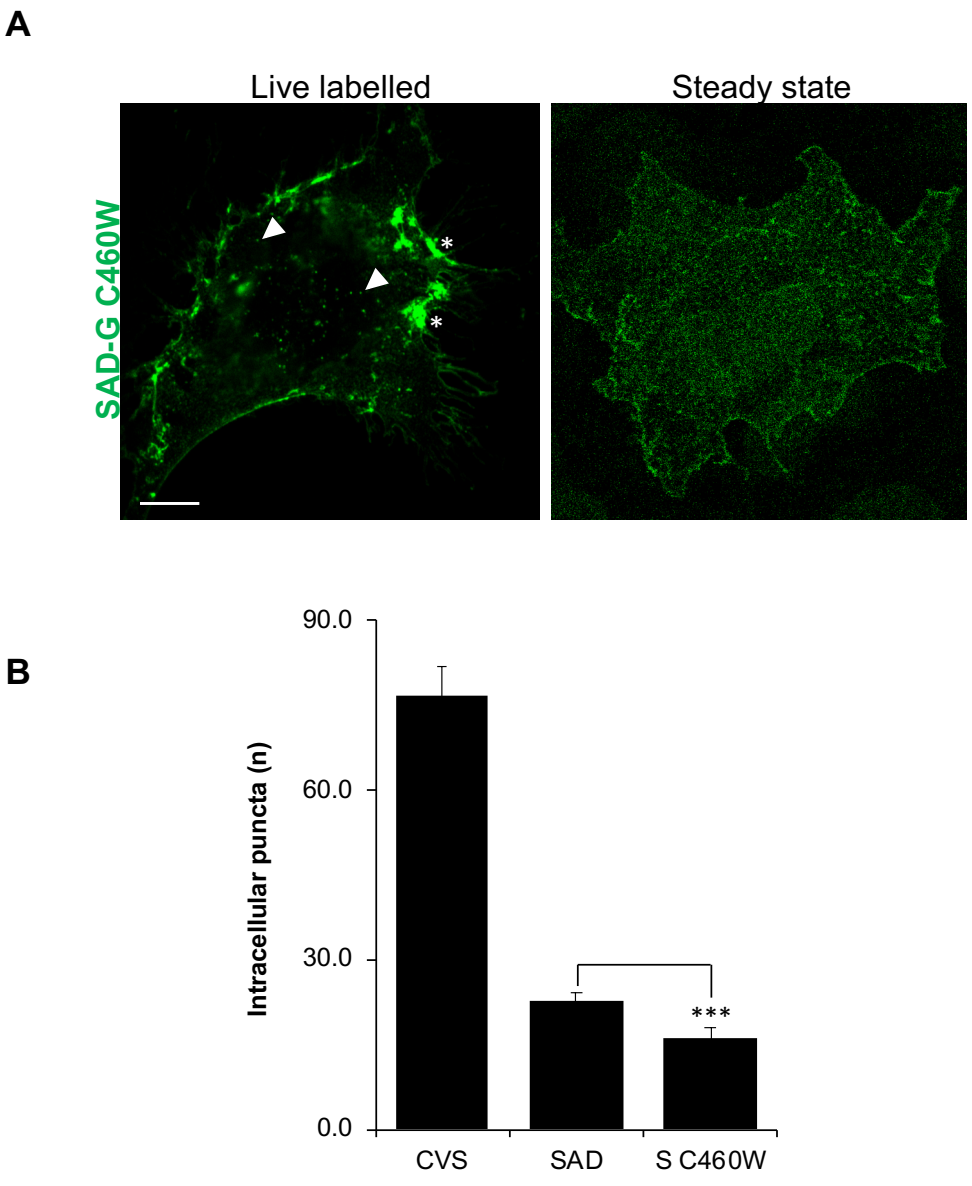

Figure 5.7 SAD-G C460W impairs the low levels of internalisation observed for WT SAD-G. (A) SVG-A cells transfected with SAD-G C460W were live- or steady-state labelled as described previously. Live labelled cells showed pronounced PM localisation, with minimal levels of internalised puncta. Scale bar = 10 μm. **(B)** Quantification of the number of intracellular puncta from n=25 cells, error bars indicate mean ± SEM. ***significant difference between SAD-G and SAD-G C460W ($P < 0.0005$).

5.3.5 Removal of the second palmitoylation site from SAD-G enhances its internalisation

SAD-G undergoes a dual palmitoylation event (Figure 5.3). Of note, the single mutation at residue C461A and the C460A-C461A mutant both reduced the levels of SAD-G in lipid rafts (Figure 5.4). Given that both these mutants transitioned SAD-G into non-raft regions, their effects on SAD-G removal from the PM were next investigated.

Assessment of the internalisation profiles of the C461A and the C460A-C461A mutants showed an increase in the internalisation of SAD-G, with the number of internalised intracellular puncta per-cell showing ~2-fold higher values for both mutants compared to WT SAD-G (Figure 5.8A-B). These data supported the notion that when SAD-G is not associated with lipid rafts, it is subject to internalisation from the plasma membrane.

These results show that whilst SAD-G is dual palmitoylated, mutation of the palmitoylation site at 461 is sufficient to disrupt its association with lipid rafts. Importantly, mutation of C461A in either CVS-G or SAD-G shifted both proteins into non-lipid raft regions and enhanced their removal from the PM. Whilst the contribution of the dual palmitoylation event to enhanced lipid-raft association of SAD-G remains unclear, these data highlight that the differential internalisation profiles of CVS-G and SAD-G are in-part dictated by the PM micro domains at which both proteins reside.

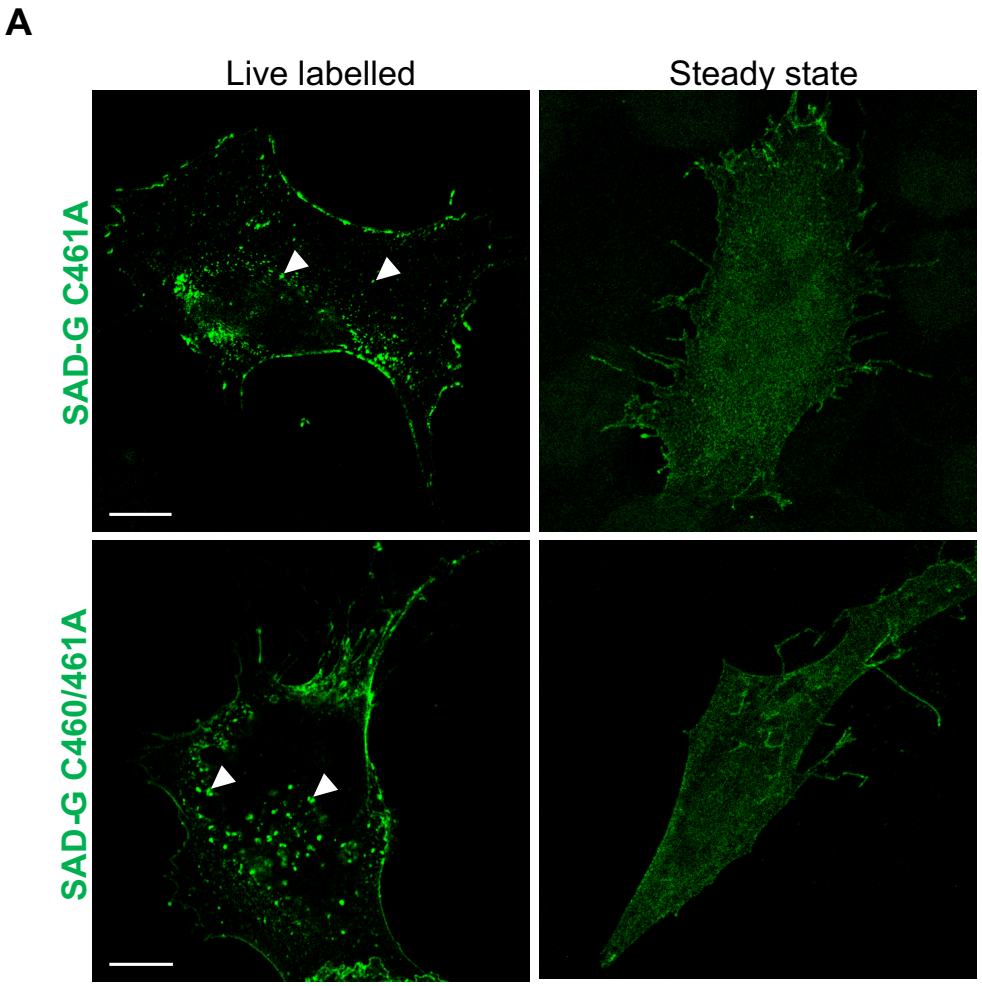
A
Live labelled
Steady state
SAD-G C461A
SAD-G C460/461A

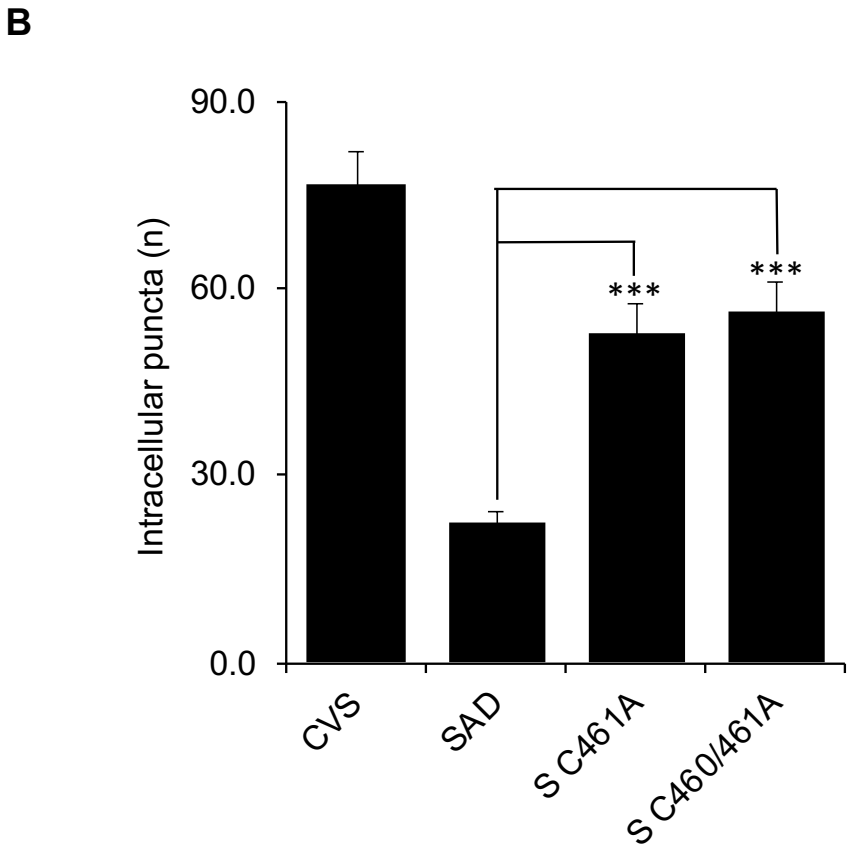
B
90.0
60.0
30.0
0.0
Intracellular puncta (n)
***
***
CVS
SAD
S C461A
S C460/461A

Figure 5.8 SAD-G removal of second palmitoylation site increases rate of internalisation. (A) SVG-A cells transfected with SAD-G C461A or C460/461A were live- or steady-state labelled as described previously. Live labelled cells from PM showed an increase in the rate of internalisation (white arrowhead) as compared to SAD-G but retained surface expression (white star). Scale bar = 10 µm. **(B)** Quantification of intracellular puncta from n=25 cells, error bars indicate mean ± SEM. ***significant difference between SAD-G and SAD-G C461A or C460/461A ($P < 0.0005$).

5.4 Both the CC motif and C-terminal tail of SAD-G contribute to its surface retention

An important but unexplained observation of the data presented in Chapter 3 was the complete inhibition of the internalisation of EBLV-G upon replacement of its C-terminal domain with that of SAD-G ($ELBV_{SADT}$), which contrasted the replacement of the C-terminal tail of CVS-G with that of SAD-G ($CVSG_{SADT}$) that showed only a partial inhibition of the internalisation profile of the chimeric protein (Figure 3.14). Importantly, EBLV-G contains the same dual CC motif ($CC_{460\text{-}461}$) as SAD-G whilst CVS-G possesses WC at this region. It was reasoned that the $CC_{460\text{-}461}$ domain may therefore be required in combination with the C-terminus of SAD-G to completely ablate internalisation. To investigate this, the WC residues in $CVSG_{SADT}$ were mutated to a dual cysteine motif CC (W460C, Figure 5.9) and the internalisation profile of this chimeric mutant investigated. The data revealed that the CC-$CVSG_{SADT}$ mutant showed significantly lower levels of internalisation than WT $CVSG_{SADT}$, and thus a more complete reversion to a SAD-G-like internalisation phenotype (Figure 5.9B-C). This observation suggests that both the CC motif and the C-terminus of SAD-G contribute to its lower levels of internalisation and high levels of surface retention compared to CVS-G.

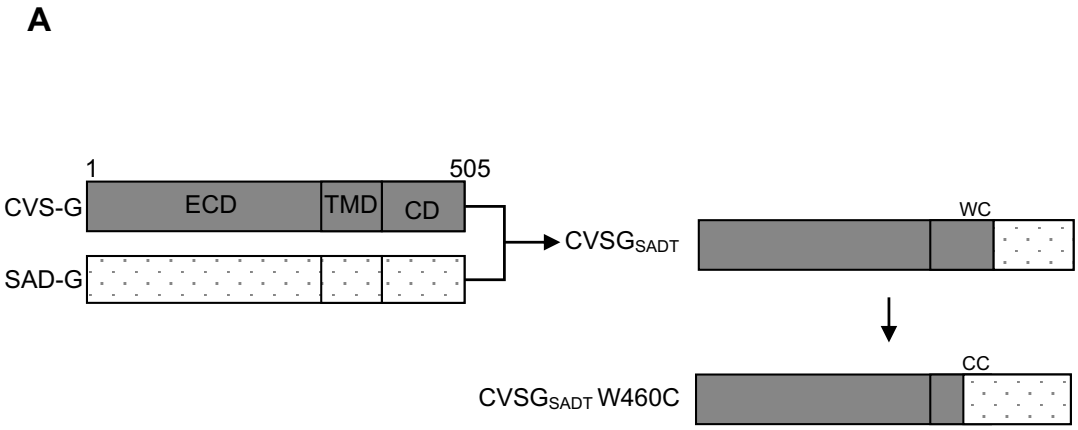
A
1
505
CVS-G
ECD
TMD
CD
SAD-G
CVSG$_{SADT}$
WC
CC
CVSG$_{SADT}$ W460C

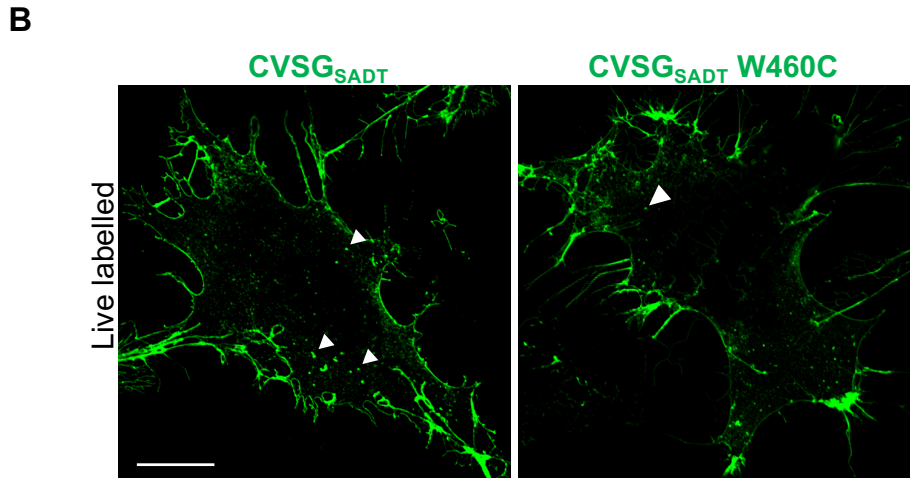
B
CVSG$_{SADT}$
CVSG$_{SADT}$ W460C
Live labelled

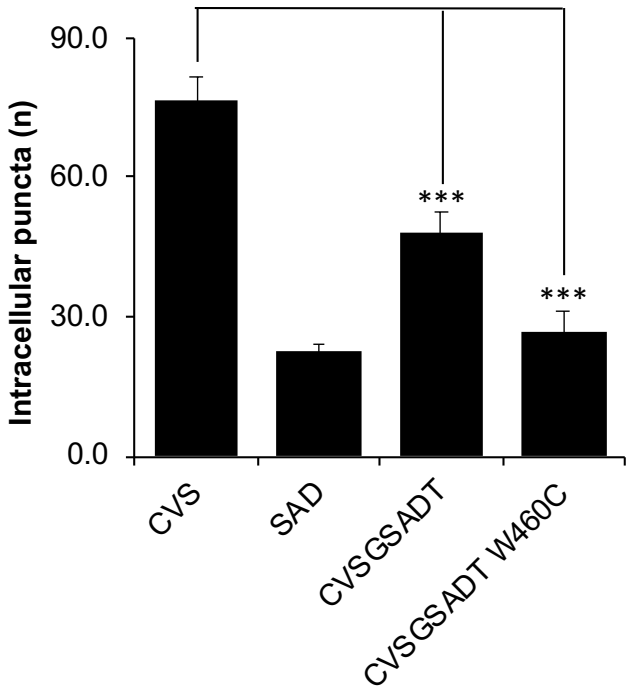
C
Intracellular puncta (n)
90.0
60.0
30.0
0.0
***
***
CVS
SAD
CVSGSADT
CVSGSADT W460C

Figure 5.9 SAD-G cytoplasmic tail works in synergy with cysteines 460 and 461 of the transmembrane domain to retain SAD-G at the PM. (A) $CVSG_{SADT}$ was created by replacing the CVS-G cytoplasmic tail with that of SAD-G. This construct contains $WC_{460-461}$ at the end of CVS-G derived transmembrane domain. $CVSG_{SADT}$ W460C was created to introduce a CC motif into the chimera. **(B)** Live labelled cells showing lower numbers of intracellular puncta for $CVSG_{SADT}$. Scale bar = 10 μm. **(C)** Quantification of intracellular puncta from 25 images. Error bars indicate mean ± SEM. ***significant difference from CVS-G ($P < 0.0005$).

5.5 Discussion

This Chapter investigated the last two residues of the RABV-G transmembrane domain, namely $WC_{460-461}$ in CVS-G and $CC_{460-461}$ in SAD-G. The latter residue was previously shown to be palmitoylated (Gaudin et al., 1991) and both residues potentially contribute to virus budding efficiency (Mebatsion et al., 1996). Here, it is shown that only palmitoylated C_{461} contributes to the lipid raft association of both CVS-G and SAD-G, which contrasts that of the equivalent residue in VSV-G (C_{473}) that showed no functional effects (Brown and Lyles, 2003). The adjacent C_{460} in SAD-G was also shown to be palmitoylated but it did not affect the lipid raft association or internalisation of SAD-G. Surprisingly, mutation of W_{460} in CVS-G to create the CC motif enhanced its palmitoylation but decreased its association with lipid rafts. This mutant showed higher levels of internalisation than WT CVS-G, suggesting that by decreasing the association of CVS-G with raft-like regions, its removal from the cell surface is enhanced.

The palmitoylation mutants of both CVS-G and SAD-G altered their rates of internalisation from the PM (Table 5.1). A common feature was that when the mutants showed lower levels of association with lipid raft regions, their internalisation rates increased. Upon analysis, WT CVS-G was localised to both lipid-raft microdomains (lipid rafts) and non-raft regions in the plasma membrane and was internalised from the cell surface through both clathrin- and cholesterol-dependent pathways. The internalisation of CVS-G was also dependent upon a number of residues in its cytoplasmic domain, most notably its tyrosine-based motif, presumed to interact with the μ subunits of the AP2 and AP1 adaptor complexes to mediate rapid removal (Chapter 4). Collectively, these data indicate that CVS-G is internalised by multiple routes,

but that the clathrin-mediated internalisation of CVS-G occurs more efficiently if CVS-G is not localised to lipid rafts.

Table 5.1 Last two residues of RABV-G TM domain mutagenesis and effect on internalisation.

Strain	Mutant	Palmitoylation profile	Lipid raft association	Effect on internalisation
CVS-G	W460C	$CC_{460-461}$	Significantly decreased	Significantly increased
CVS-G	C461A	No palmitoylation	Significantly decreased	Significantly increased
SAD-G	C460W	$WC_{460-461}$	Increased	Decreased
SAD-G	C461A	$CA_{460-461}$	Lower than SAD-G	Increased
SAD-G	C460A/ C461A	No palmitoylation	Lower than SAD-G	Increased
$CVSG_{SADT}$	-	$WC_{460-461}$	Similar to CVS-G	Higher than SAD-G but lower than CVS-G
$CVSG_{SADT}$	W460C	$CC_{460-461}$	-	Decreased to SAD-G levels

The situation for SAD-G is different. The majority of the SAD-G protein was present in lipid-raft regions of the plasma membrane which was dependent on the palmitoylation event at C_{461}. Mutation of this site in SAD-G enhanced its removal from the plasma membrane, consistent with the notion that WT SAD-G undergoes lower levels of internalisation due to its localisation in raft-like regions. Studies on the uptake of raft associated proteins have revealed a diversity of internalisation methods (Kumari et al., 2010). Although lipid raft proteins are recognised by the endocytic machinery, the low levels of native SAD-G that did internalise could be blocked by CME inhibitors but not cholesterol depletion (see Chapter 3, Figure 3.10). These data are consistent with the notion that the SAD-G C-terminal tail lacks a raft-specific or raft-dependent endocytic signal, meaning that the protein can only internalise in non-raft associated PM regions. These data suggest that the palmitoyaltion of RABV-G proteins through dictating the PM regions in which the protein resides also contributes to internalisation. In the case of CVS-G and SAD-G, CVS-G is resident in both raft and non-raft regions from which it can internalise, whilst SAD-G is predominantly localised in rafts leading to a lack of PM removal. This raft like association is in-part governed by palmitoylation.

Differential palmitoylation sites have different levels of contribution to virus cell biology. Feline immunodeficiency virus *env* contains four palmitoylated cysteines within its cytoplasmic tail. Deletion of transmembrane-proximate C_{804} reduced env fusiogenic capability by more than 93%. This is in contrast to transmembrane-distant C_{815} that reduced *env* fusiogenic capability by just 50% (González et al., 2012). This study along with those of Scolari el al. (2016) (discussed in 5.3.1) suggest that palmitoylation sites approximate to the transmembrane-cytoplasmic interface are more functionally involved than distant palmitoylation sites and it can be argued that residue C_{461} that is more proximate to the transmembrane-cytoplasmic interface is more functionally involved than C_{460} that is slightly more distant.

At the time this thesis was written, the palmitoylation mutants have been introduced into both rabies CVS and SAD strains with collaborator Prof Stefan Finke to reveal the role of dual or single palmitoylation events *in vivo*. If confirmed, these results will have major impact on our understanding of the rabies glycoproteins and the role of palmitoylation in virus pathogenesis.

Chapter 6 | Final Discussion

6.1 RABV-G and pathogenesis

RABV infection in humans results in a case fatality rate of nearly 100% but upon timely vaccination, it can be effectively prevented (Fooks et al., 2014). Attenuated strains such as SAD share ~80% homology with pathogenic RABV but they are rapidly detected and cleared by host immune defences. Their use as live vaccines for wild animals is well-established and led to the eradication of canine rabies from Western Europe (Rupprecht et al., 2005). Nevertheless, RABV remains an endemic viral infection leading to 60,000 deaths per year, as PEP treatments are unaffordable and/or unavailable to many. The re-emergence of RABV has also been reported in some regions, making this virus a continuing threat to human health (Fisher et al., 2018).

Many of the challenges with RABV could be circumvented if the PEP regimen was affordable and not subject to cold chain storage issues. Alternatively, the development of shelf-stable antiviral therapies could act as a first-line of defence against RABV infections. RABV pathogenesis is primarily mediated by RABV-G that protrudes from the bullet-shaped virion and mediates virus entry and spread. RABV-G has been traditionally studied in invading RABV virions (requiring BSL3/SAPO 4 facilities) or as a single-cycle trans-supplemented to ΔG RABV or engineered into VSV. These studies have identified a range of entry factors for RABV-G including nAChR, NCAM, $p75^{NTR}$ and mGluR2 (Guo et al., 2019) and have revealed many of the entry characteristics of pathogenic RABV infections.

In this thesis, the role(s) of RABV-G in virus pathogenesis once expressed in cells were investigated. RABV-G proteins from CVS and SAD viruses were exogenously expressed in cells and their trafficking profiles and proximal proteins were investigated and compared to reveal new determinants of RABV pathogenicity. CVS and SAD were selected as the prototypical strains of pathogenic and attenuated RABV, respectively. In Chapter 3, it was identified that the rapid internalisation of pathogenic CVS-G occurred, whilst the PM removal of SAD-G was comparably slow. In Chapter 4, BioID proximal labelling analysis revealed a range of novel proteins proximal to CVS-G that mediated distinct cell biological phenotypes that were absent in SAD-G, namely the ROCK dependent production of filopodia and neurite outgrowth.

Finally in Chapter 5, a dual palmitoylated $CC_{460-461}$ motif was identified in the interface of the SAD-G transmembrane domain and cytoplasmic tail that is absent in CVS-G. This CC motif was shown to enhance SAD-G localisation at lipid rafts which in turn enhanced its surface expression, as opposed to CVS-G that had lower lipid raft expression and more rapid surface removal. Thus, a range of distinctive phenotypes between CVS-G and SAD-G were identified that may dictate the role of CVS-G in pathogenic RABV infection.

Approaches taken here are not without limitations. RABV-G expression alone may have introduced artificial overexpression phenotypes in its trafficking and cellular localisation. RABV-G also binds to RABV-M in infected cells, an interaction not investigated in this thesis. Many of these limitations were however circumvented by the direct comparison of CVS-G to SAD-G, in which key differences in cell behaviours were not limited to their differential expression levels, with comparable CVS-G to SAD-G levels observed throughout the experiment data reported in this thesis. The identified phenotypes that differed between CVS-G and SAD-G do however require transition into RABV infectious virus assays and the assessment of their specific effects on RABV *in vivo.* These experiments are challenging to perform due to the high containment status of the virus (limited to a single site in the UK), but are in progress using the reverse genetics system designed by collaborator Prof Stefan Finke (Friedrich Loeffler institute, Germany).

6.2 Are the more rapid internalisation rates of pathogenic RABV-G a hallmark of fatal RABV infections?

Following transfection of known RABV-susceptible cell lines HEK293T, SVG-A and SH-SY5Y with CVS-G and SAD-G, it was shown that CVS-G internalised at a greater rate from the PM than SAD-G. This was shown to correlate with Y_{497} of the cytoplasmic tail as the introduction of Y497A mutation significantly attenuated CVS-G internalisation. Live attenuated strains possess a conserved H_{497} at this position, losing the only tyrosine in cytoplasmic tail, which correlates with CME mediated PM removal in many other cellular and viral proteins (Ochsenbauer et al., 2000; Favoreel et al.,

2002; Ilinskaya et al., 2010). Of note, the BioID screen in Chapter 4 identified many CME components that were more highly associated with CVS-G, namely CME adaptors AP2 α1, AP2 α2, AP2 β1 and AP2 μ, consistent with a probable role for CME in the specific PM removal of CVS-G.

This study is not the first to compare pathogenic RABV-G to attenuated RABV-G strains. Previously, R333Q in apathogenic HEP-Flury was identified as key attenuation residue that reduces neuroinvasiveness (Seif et al., 1985) through abolishment of RABV binding to entry receptor $p75^{NTR}$ (Tuffereau et al., 1998). This mutation when introduced into CVS-G reduced its pathogenicity (Lafon, 2008), but a complementary N194K mutation developed after several passages (Tao et al., 2010). Introduction of an N194S mutation into CVS-G could prevent the pathogenic reversion (Faber et al., 2005). These attenuation studies were limited to the RABV-G ectodomain and virus entry studies.

In this thesis, a potential mechanism of attenuation was identified in which SAD-G fails to undergo rapid cell surface removal. Many virus glycoproteins expressed at the cell surface undergo a similar internalisation event. HIV gp41 is subject to rapid PM removal which correlates with its ability to avoid immune detection (von Bredow et al., 2015). In RABV, low RABV-G surface levels have similarly been linked to immune avoidance (Yang et al., 2015; Li et al., 2019). It is proposed here that surface-expressed SAD-G is readily detected by host APCs and cleared from infected host cells. CVS-G however undergoes rapid internalisation to avoid surface exposure, a hypothesis strengthened by the observation that the introduction of a dual copy of RABV-G into pathogenic RABV strains increases its surface expression and reduces its pathogenicity (Faber et al., 2002; Cenna et al., 2008). Furthermore, when the cytoplasmic tail of SAD-G was replaced with that of pathogenic SHBRV-G, the chimeric glycoprotein $SAD\text{-}G_{SHBRVT}$ had lower surface levels than SAD-G (Morimoto et al., 2000). Of note, pathogenic SHBRV-G possesses a $Y_{497,}$ further implicating this residue in the control of RABV-G PM expression.

In Chapter 5, two residues that followed the transmembrane domain $WC_{460\text{-}461}$ or $CC_{460\text{-}461}$ were also implicated in the CVS-G internalisation event. The cysteine(s) in this motif was confirmed to be palmitoylated and through hydrophobic association caused enhanced SAD-G trafficking to lipid rafts. It

is not known whether lipid raft association dictates RABV pathogenesis at this stage, but ~41% of synaptic genes encode a palmitoylated protein (Sanders et al., 2015), suggesting this post-translational modification as a key regulator of protein functionality in the CNS. This may suggest that loss of this palmitoylation of CVS-G may attenuate its activity in infected neurons, altering pathogenicity. Of-note, the related non-neurotropic VSV-G does not traffic to lipid rafts and its equivalent palmitoylated cysteine shows no functional effect (Whitt and Rose, 1991). This may further highlight a neuronal specific effect of the palmitoylation of virus glycoproteins.

In summary, CVS-G internalises faster than SAD-G due to its cytoplasmic tyrosine that is likely to interact with the μ subunits of the AP2 and AP1 adaptor complexes mediating CME. CVS-G might also internalise through cholesterol-dependent pathway but clathrin-mediated internalisation occurs more efficiently if CVS-G is not localised to lipid rafts.

6.3 Does filopodia and neurite outgrowth contribute to RABV pathogenesis?

It was previously shown that RABV infection leads to the development of filopodia in epithelial cells (Xu et al., 2015). CVS-G and ERA-G has been shown to induce the formation of neurites that are themselves enriched with RABV-G proteins (Seo et al., 2017). In Chapter 4, it was shown that RABV-G from both CVS and SAD strains can induce filopodia formation in SVG-A astrocytes and promote neurite outgrowth in SH-SY5Y neuroblasts. This was true for almost all cell lines assayed (data not shown). These cell protrusions may result from either cell stress pathways (Shneyer et al., 2017), or as the result of an active mechanism of pathogenesis (Chang et al., 2016).

Whilst filopodia/neurite outgrowth have yet to be directly linked to RABV pathogenesis, *in vivo* RABV infection causes the degeneration of neurites (Li et al., 2005; Wang et al., 2005) as a result of F-actin depolymerisation (Song et al., 2013). This effect was ascribed to the activity of RABV-G for the first time in this thesis. Several viruses have been shown to surf on filopodia prior to entry (Lehmann et al., 2005; Bienkowska-Haba and Sapp, 2011; Schudt et

al., 2013) whilst others actively induce filopodia (Nobile et al., 2010; Aggarwal et al., 2012; Stakaitytė et al., 2017). The roles of these filopodia in RABV are to-date undefined, but may facilitate the cell to cell spread of newly assembled virions as a further mechanism of immune evasion. RABV has also been shown to induce syncytium through the action of RABV-G (Morimoto et al., 1992) due to its known fusogenic activity (Dietzschold et al., 2008). The presence of filopodia that are extensively enriched with RABV-G proteins in infected cells may contribute to this syncytia formation.

The BioID screen revealed a cluster of actomyosin proteins including myosin II (IIA, IIB and IIC), ROCK enzymes 1 and 2 and cofilin-1 as proximal to CVS-G. Myosin II and ROCK are associated with filopodia outgrowth (Alieva et al., 2019) and when myosin II was inactivated by blebbistatin, CVS-G and SAD-G expressing cells showed fewer filopodia, but their length increased to almost 2-fold the size of no-drug cells. When ROCK was targeted with Y-27632, CVS-G expressing cells showed a complete retraction of their filopodia as opposed to SAD-G that retained its filopodia outgrowth (Chapter 4, Figure 4.14). The specific inhibition of CVS-G associated filopodia with Y-27632 hinted at a ROCK-mediated mechanism of induction that exists only for CVS-G but not SAD-G. This may highlight subtle differences in the mechanism(s) of filopodia production between attenuated and pathogenic RABV strains. In the context of CVS infection, it is noteworthy that the Y-27632-like ROCK inhibitors fasudil and netarsudil are clinically approved for the prevention of cerebral vasospasm and glaucoma, respectively (Doggrell, 2005; Kopczynski and Heah, 2018). Future studies should focus on the anti-viral activity of these compounds in pathogenic RABV strains.

6.4 RABV-G trafficking and neurotropism

Pathogenic strains of RABV are highly neurotropic whereas attenuated strains are not. This is evidenced by neurotrancing studies showing that CVS preferentially spreads neuron-to-neuron (Reardon et al., 2016) whereas SAD spreads almost uniformly throughout the CNS (Wickersham et al., 2007). Cell lines used in this project were mostly derived from the CNS such as SVG-A

astrocytes and SH-SY5Y neuroblasts. RABV was recently shown to efficiently infect astrocytes (Potratz et al., 2020) and whilst these cell lines are not directly reflective of RABV-G infection, evidence generated in this thesis may explain some aspects of RABV-G mediated neuroinvasiveness. Measles virus avoids immune detection in the CNS by restricting the surface expression of its two surface glycoproteins (Griffin et al., 2012) and herein, it is shown for the first time that pathogenic, neurotropic CVS-G is rapidly removed from the cell surface whereas attenuated non-neurotropic SAD-G is not, a phenotype validated in differentiated neuronal-like SH-SY5Y cells (Chapter 3, Figure 3.12).

Cells of the CNS are highly lapidated (Sanders et al., 2015) and most RABV neuronal entry receptors cluster in lipid rafts (see Chapter 1, 1.3.2). Of note, VSV is not neurotropic and VSV-G's single palmitoylated cysteine is not functional. When VSV is pseudotyped with CVS-G, it became neurotropic (Beier et al., 2013) and here, it is shown that RABV-G palmitoylation influences its lipid raft localisation. It can be speculated that the partial lipid raft association of CVS-G may facilitate synaptic spread by permitting CVS budding from raft regions of the surface, whilst those in non-raft regions are rapidly internalised. Further studies assessing the enrichment of raft-like proteins in the envelopes of pathogenic RABV strains may further implicate this site as key to RABV budding.

6.5 Conclusions

Lyssaviruses such as RABV are dangerous pathogens that require immediate medical attention upon exposure. Their mechanism(s) of pathogenesis are not well-understood and many of the characteristics of RABV-G are not well-characterised. Current treatment options are unaffordable to many. The development of improved therapeutics may afford protection from fatal rabies encephalitis.

The work outlined in this thesis sought to identify the mechanisms of RABV pathogenesis in order to reveal new targeted treatment strategies. Chapter 3 identified the rapid internalisation of surface expressed CVS-G as potential

RABV mechanism of pathogenesis. Pathogenic strains such as CVS-G, EBLV-G and DOG-G undergo rapid internalisation whereas SAD-G does not, instead remaining mostly surface associated. This rapid internalisation event was shown to not be the result of expressional differences, and highlighted a key phenotypic difference between pathogenic and non-pathogenic proteins.

In Chapter 4, a BioID screen of proximate host proteins to CVS-G and SAD-G showed a range of cellular proteins, including a multitude of CME adaptors with higher proximity to CVS-G than SAD-G. The BioID screen also revealed that CVS-G is proximate to proteins implicated in ciliogenesis and filopodia outgrowth, with the disruption of myosin IIA and ROCK shown to disrupt the development of CVS-G induced filopodia. Of note, SAD-G retained its ability to induce filopodia in the face of ROCK inhibition. Whether the dependence of ROCK activity is a key feature of pathogenic RABV strains now warrants further studies in *in vivo* RABV systems.

In Chapter 5, palmitoylated cysteines in CVS-G $WC_{460\text{-}461}$ or SAD-G $CC_{460\text{-}461}$ were shown to enhance lipid raft localisation. This raft localisation inversely correlated with the ability of RABV-G to internalise. Disruption of C_{461} made both glycoproteins internalise faster. This Chapter suggests that in addition to the cytoplasmic tail, the last two residues from the transmembrane domain influence the rate of RABV-G internalisation.

The data presented in this thesis identified rapid internalisation, filipodia outgrowth and lipid raft localisation as three cellular trafficking pathways that may dictate the pathogenesis of RABV strains. Efforts to develop antiviral therapies for RABV are ongoing, but the most promising drugs colchicine, favipiravir and emetine only delay RABV infection rather than clear the virus from infected hosts (Du Pont et al., 2019). It is likely that multiple RABV processes must be targeted in combination to prevent its transmission and survival *in vivo*. Thus, methods to specifically block the rapid internalisation of pathogenic RABV-G proteins and its ability to induce filopodia outgrowth may add to the arsenal of anti-RABV strategies.

Appendix

Table A1 RABV gene replacement show RABV-G has the highest impact on pathogenicity.

Replaced gene	Virus strain backbone	Introduced gene source	Chimeric glycoproteins	Effect on pathogenesis (route of infection)	Note	Source
-	SAD L16	-	-	Apathogenic (im)	-	Morimoto et al., 2000
RABV-G	SAD L16	CVS-N2c	SAD G_{CVSn}	Became pathogenic (im)	Delayed death by 4 days	
		CVS-B2c	SAD G_{CVSb}	Became pathogenic (im)	10 times less pathogenic than SAD G_{CVSn}	
		SHBRV-18	SAD G_{SHBRV}	Remained apathogenic (im)	Higher RABV-G PM expression than SHBRV-18	
		SHBRV-18 with SAD_{CD}	SAD G_{SHBRVT}	Remained apathogenic (im)	Lower PM expression levels than SAD G_{SHBRV}	
-	RC-HL	-	-	Apathogenic (ic)	-	Ito et al., 2001
RABV-G	RC-HL	Nishigahara	RC-HL G_{NISHI}	Became pathogenic (ic)	Delayed death by 3 days	
-	SAD L16	-	-	Apathogenic (im) and pathogenic (ic)	-	Faber et al., 2004
RABV N, P and M		SHBRV-18	pSB 4	10% became pathogenic (im)	Delayed death by 8 days	
RABV N, P, M and G			pSB 3	60% became pathogenic (im)	Delayed death by 2 days	
RABV N, P, M, G and ψ			pSB 2	90% became pathogenic (im)	Delayed death by 2-8 days	

RABV-G			SN-BG	20% became pathogenic (im)	Lower RABV-G PM expression	Pulmanausahakul et al., 2008
RABV-M			SN-BM	Remained apathogenic (im)	Highest RABV-G PM expression	
RABV G and M			SN-BMBG	40% became pathogenic (im)	Lowest RABV-G PM expression	
-	HEP-Flury	-	-	Apathogenic (ic)	-	Tao et al., 2010
RABV-G		LEP-Flurry	HEP-G(L)	Became pathogenic through (im) but not through (ic)*		
RABV-G	LEP-Flury	HEP-Flury	LEP-G(H)	Became attenuated through (im) but not (ic)		
-	SAD-B19	-	-	Apathogenic (im)	-	Marston et al., 2013
RABV-G		EBLV-1	SN-1	Remained apathogenic (im)		
		EBLV-2	SN-2	Remained apathogenic (im)		

*HEP-G(L) is actually HEP-G_{Q333R}, a single amino acid substitution naturally found in LEP and implicated in pathogenesis. At relatively high viral load (10^6 FFU), HEP-G(L) becomes pathogenic even through peripheral intramuscular injection.

Table A2 Reagents, kits and instruments.

Reagent type (usage)	Designation	Source	Identifier	Additional information
Media (Cloning)	SOC	NEB	Cat. #: B9020S	
Kit (Cloning)	QuickLyse	Qiagen	Cat. #: 27405	
Kit (Cloning)	Miniprep	Qiagen	Cat. #: 27104	QIAprep spin variant
Kit (Cloning)	Maxiprep	Qiagen	Cat. #: 12162	
Kit (Cloning)	Q5 Site-Directed Mutagenesis	NEB	Cat. #: E0554	
Kit (Cloning)	QIAquick Gel Extraction Kit	Qiagen	Cat. #: 28704	
Enzyme (Cloning)	T4 ligase	NEB	Cat. #: M0202	
Reagent (Cloning)	Gel Loading Dye	NEB	Cat. #: B7025S	Purple, no SDS
Reagent (Cloning)	SYBR safe DNA stain	Thermo Fisher	Cat. #: S33102	
Reagent (Cloning)	CutSmart buffer	NEB	Cat. #: B7204S	
Reagent (Cloning)	3.1 Buffer	NEB	Cat. #: B7203S	
Reagent (Cell culture)	DMEM	Gibco	Cat. #: 41965062	
Reagent (Cell culture)	FBS (serum)	Gibco	Cat. #: 26140	

Reagent (Cell culture)	Penicillin/Streptomycin (P/S)	Gibco	Cat. #: 15140148	
Reagent (Cell culture)	Trypsin-EDTA	Gibco	Cat. #: 15400054	
Reagent (Cell culture)	Opti-MEM	Gibco	Cat. #: 31985062	
Reagent (Cell culture)	Protease inhibitor cocktail	Thermo Fisher	Cat. #: 78429	
Reagent (Cell culture)	Laminin	Sigma	Cat. #: L2020-1MG	
Reagent (Cell culture)	IGF-I	PeproTech	Cat. #: 100-11	
Reagent (Cell culture)	poly-L-lysine	Sigma	Cat. #: P8920	
Reagent (Cell culture)	ProLong Gold with DAPI	Thermo Fisher	Cat. #: P36931	
Kit (Biochemistry)	BCA assay	Thermo Fisher	Cat. #: 23225	
Reagent (Biochemistry)	4x Laemmli sample buffer	Bio-Rad	Cat. #: 1610747	
Miscellaneous (Biochemistry)	PVDF membrane	Millipore	Cat. #: IPVH00010	
Reagent (Biochemistry)	ECL	Thermo Fisher	Cat. #: 32106	
Reagent (BioID)	Biotin	Sigma	Cat. #: B4639	
Equipment (ddH_2O)	Elga Purelab Ultra Genetic	Elga	Cat. #: ULXXXGEM2	
Equipment (Cloning)	NanoDrop	Thermo Fisher	Cat. #: ND-ONE-W	

Equipment (Cloning)	Veriti 96-well thermocycler	Thermo Fisher	Cat. #: 4375305	
Equipment (Cloning)	InGenuis3 gel documentation	Syngene	Cat. #: MB0810	
Equipment (Cell culture)	CO2 incubator	Sanyo	Model: MCO-18AIC	
Equipment (Cell culture)	Airstream BSL2 biological safety cabinet	Esco	Code: CAB7504	
Equipment (Cell culture)	IncuCyte Zoom	Essen BioScience	Model: 8000-0338-B00	
Equipment (Biochemistry)	Trans-blot Turbo	Bio-Rad	Cat. #: 1704150	
Equipment (Biochemistry)	Thermomixer C	Eppendorf	Cat. #: 5382000031	

Table A3 Interactomics dataset that compares CVS-G proximate proteins to SAD-G in HEK293T cells.

Accession	Description	Unique Peptides #	CVS/SAD abundance ratio	Sequest score
P78527	DNA-dependent protein kinase catalytic subunit OS=Homo sapiens OX=9606 GN=PRKDC PE=1 SV=3	208	3.101	1211.39
Q14204	Cytoplasmic dynein 1 heavy chain 1 OS=Homo sapiens OX=9606 GN=DYNC1H1 PE=1 SV=5	227	2.794	1174.2
P49327	Fatty acid synthase OS=Homo sapiens OX=9606 GN=FASN PE=1 SV=3	104	3.546	804.98
A0A024R1N1	Myosin, heavy polypeptide 9, non-muscle, isoform CRA_a OS=Homo sapiens OX=9606 GN=MYH9 PE=3 SV=1	100	2.389	755.87
P46013	Proliferation marker protein Ki-67 OS=Homo sapiens OX=9606 GN=MKI67 PE=1 SV=2	141	3.333	722.45
A0A024R3T8	Poly [ADP-ribose] polymerase OS=Homo sapiens OX=9606 GN=PARP1 PE=4 SV=1	76	2.802	710.75
A0A087WVQ6	Clathrin heavy chain OS=Homo sapiens OX=9606 GN=CLTC PE=1 SV=1	63	2.782	676.92
Q09666	Neuroblast differentiation-associated protein AHNAK OS=Homo sapiens OX=9606 GN=AHNAK PE=1 SV=2	164	1.054	675.49
P35580	Myosin-10 OS=Homo sapiens OX=9606 GN=MYH10 PE=1 SV=3	89	2.468	619.76
P13639	Elongation factor 2 OS=Homo sapiens OX=9606 GN=EEF2 PE=1 SV=4	50	2.83	618.27
A0A140VK53	Testicular secretory protein Li 53 OS=Homo sapiens OX=9606 PE=2 SV=1	105	3.087	604.28
E1NZA1	Peroxisome proliferator activated receptor interacting complex protein GN=PRIC295	133	3.049	590.69
Q6P2Q9	Pre-mRNA-processing-splicing factor 8 OS=Homo sapiens OX=9606 GN=PRPF8 PE=1 SV=2	105	3.326	560.76
P49792	E3 SUMO-protein ligase RanBP2 OS=Homo sapiens OX=9606 GN=RANBP2 PE=1 SV=2	79	2.246	556.3
A7BI36	p180/ribosome receptor OS=Homo sapiens OX=9606 GN=RRBP1 PE=2 SV=2	50	0.614	532.16
A0A024R5M9	Nuclear mitotic apparatus protein 1, isoform CRA_a OS=Homo sapiens OX=9606 GN=NUMA1 PE=4 SV=1	108	2.535	523.18
P10412	Histone H1.4 OS=Homo sapiens OX=9606 GN=HIST1H1E PE=1 SV=2	12	1.164	519.86
P07437	Tubulin beta chain OS=Homo sapiens OX=9606 GN=TUBB PE=1 SV=2	4	2.304	506.03
P68371	Tubulin beta-4B chain OS=Homo sapiens OX=9606 GN=TUBB4B PE=1 SV=1	1	2.281	502.63
O75643	U5 small nuclear ribonucleoprotein 200 kDa helicase OS=Homo sapiens OX=9606 GN=SNRNP200 PE=1 SV=2	90	2.438	485.04
A0A024R9W5	HECT, UBA and WWE domain containing 1, isoform CRA_b OS=Homo sapiens OX=9606 GN=HUWE1 PE=4 SV=1	28	3.128	466.95
P16403	Histone H1.2 OS=Homo sapiens OX=9606 GN=HIST1H1C PE=1 SV=2	10	1.778	459.27
Q13428	Treacle protein OS=Homo sapiens OX=9606 GN=TCOF1 PE=1 SV=3	7	0.676	454.09
Q4LE36	ACLY variant protein (Fragment) OS=Homo sapiens OX=9606 GN=ACLY variant protein PE=2 SV=1	1	3.435	444.66
A0A024R1Y2	ATP-citrate synthase OS=Homo sapiens OX=9606 GN=ACLY PE=3 SV=1	1	2.221	442.25
Q08211	ATP-dependent RNA helicase A OS=Homo sapiens OX=9606 GN=DHX9 PE=1 SV=4	64	2.915	442.2
P07814	Bifunctional glutamate/proline--tRNA ligase OS=Homo sapiens OX=9606 GN=EPRS PE=1 SV=5	75	2.638	440.49
Q13885	Tubulin beta-2A chain OS=Homo sapiens OX=9606 GN=TUBB2A PE=1 SV=1	1	2.424	436.14
Q9BVA1	Tubulin beta-2B chain OS=Homo sapiens OX=9606 GN=TUBB2B PE=1 SV=1	1	2.673	436.06
P16402	Histone H1.3 OS=Homo sapiens OX=9606 GN=HIST1H1D PE=1 SV=2	13	1.629	433.51
E7ETY2	Treacle protein OS=Homo sapiens OX=9606 GN=TCOF1 PE=1 SV=1	4	0.688	411.98

P04350	Tubulin beta-4A chain OS=Homo sapiens OX=9606 GN=TUBB4A PE=1 SV=2	3	2.28	408.52
Q53G89	Elongation factor 1-alpha (Fragment) OS=Homo sapiens OX=9606 PE=2 SV=1	4	2.246	405.92
A0A0G2JIW1	Heat shock 70 kDa protein 1B OS=Homo sapiens OX=9606 GN=HSPA1B PE=1 SV=1	29	1.18	398.51
E5KNY5	Leucine-rich PPR-motif containing OS=Homo sapiens OX=9606 GN=LRPPRC PE=4 SV=1	81	1.848	396.99
Q9NR30	Nucleolar RNA helicase 2 OS=Homo sapiens OX=9606 GN=DDX21 PE=1 SV=5	47	1.944	396.58
Q9BQG0	Myb-binding protein 1A OS=Homo sapiens OX=9606 GN=MYBBP1A PE=1 SV=2	59	2.392	396.11
A0A024RD80	Heat shock protein 90kDa alpha (Cytosolic), class B member 1, isoform CRA_a GN=HSP90AB1	25	1.709	391.07
Q15149	Plectin OS=Homo sapiens OX=9606 GN=PLEC PE=1 SV=3	119	1.714	390.7
Q9NU22	Midasin OS=Homo sapiens OX=9606 GN=MDN1 PE=1 SV=2	106	2.698	387.47
V9HWB8	Pyruvate kinase OS=Homo sapiens OX=9606 GN=HEL-S-30 PE=1 SV=1	4	2.734	384.66
Q14008	Cytoskeleton-associated protein 5 OS=Homo sapiens OX=9606 GN=CKAP5 PE=1 SV=3	91	2.669	384.23
P21333	Filamin-A OS=Homo sapiens OX=9606 GN=FLNA PE=1 SV=4	73	0.713	384.2
P27708	CAD protein OS=Homo sapiens OX=9606 GN=CAD PE=1 SV=3	74	2.782	379.21
P11388	DNA topoisomerase 2-alpha OS=Homo sapiens OX=9606 GN=TOP2A PE=1 SV=3	62	2.369	374.14
P22626	Heterogeneous nuclear ribonucleoproteins A2/B1 OS=Homo sapiens OX=9606 GN=HNRNPA2B1 PE=1 SV=2	19	2.879	373.09
A0A024R663	Kinectin 1 (Kinesin receptor), isoform CRA_a OS=Homo sapiens OX=9606 GN=KTN1 PE=4 SV=1	82	0.526	368.86
P53621	Coatomer subunit alpha OS=Homo sapiens OX=9606 GN=COPA PE=1 SV=2	64	3.142	366.23
J9R021	Eukaryotic translation initiation factor 3 subunit A OS=Homo sapiens OX=9606 GN=eIF3a PE=2 SV=1	71	2.376	363.53
O75533	Splicing factor 3B subunit 1 OS=Homo sapiens OX=9606 GN=SF3B1 PE=1 SV=3	62	2.21	363.45
A0A0C4DGG9	Chromodomain-helicase-DNA-binding protein 4 OS=Homo sapiens OX=9606 GN=CHD4 PE=1 SV=1	1	1.524	360.97
V9HW22	Epididymis luminal protein 33 OS=Homo sapiens OX=9606 GN=HEL-S-72p PE=2 SV=1	22	1.647	357.71
Q5H924	HECT, UBA and WWE domain containing 1 (Fragment) OS=Homo sapiens OX=9606 GN=HUWE1 PE=4 SV=1	1		357.09
B3KY63	cDNA FLJ16830 fis, clone UTERU3022536, highly similar to Chromodomain helicase-DNA-binding protein 4 OX=9606	1	2.367	357.04
A0A3B3IUD7	Programmed cell death 11, isoform CRA_a OS=Homo sapiens OX=9606 GN=PDCD11 PE=1 SV=1	84	2.773	353.27
P18583	Protein SON OS=Homo sapiens OX=9606 GN=SON PE=1 SV=4	21	2.46	338.7
A0A024RC65	HCG1991735, isoform CRA_a OS=Homo sapiens OX=9606 GN=hCG_1991735 PE=4 SV=1	60	2.439	335.98
Q00839	Heterogeneous nuclear ribonucleoprotein U OS=Homo sapiens OX=9606 GN=HNRNPU PE=1 SV=6	6	2.309	333.01
A0A024R5Z9	Pyruvate kinase OS=Homo sapiens OX=9606 GN=PKM2 PE=3 SV=1	1	1.488	331.83
K9JA46	Epididymis luminal secretory protein 52 OS=Homo sapiens OX=9606 GN=EL52 PE=2 SV=1	25	1.716	330.46
P08670	Vimentin OS=Homo sapiens OX=9606 GN=VIM PE=1 SV=4	33	1.508	327.06
B4DLR3	cDNA FLJ54020, highly similar to Heterogeneous nuclear ribonucleoprotein U OS=Homo sapiens OX=9606 PE=2 SV=1	2	1.987	326.63
A0A087WUT6	Eukaryotic translation initiation factor 5B OS=Homo sapiens OX=9606 GN=EIF5B PE=1 SV=1	62	1.072	320.66
A0A1S5UZ07	Talin-1 OS=Homo sapiens OX=9606 GN=TLN1 PE=2 SV=1	83	2.006	317.41
P12956	X-ray repair cross-complementing protein 6 OS=Homo sapiens OX=9606 GN=XRCC6 PE=1 SV=2	39	2.527	314.33
F5H5D3	Tubulin alpha chain OS=Homo sapiens OX=9606 GN=TUBA1C PE=1 SV=1	7	2.103	309.34
Q5T4S7	E3 ubiquitin-protein ligase UBR4 OS=Homo sapiens OX=9606 GN=UBR4 PE=1 SV=1	42	2.847	309.11

J3KN16	Proteasome adapter and scaffold protein ECM29 OS=Homo sapiens OX=9606 GN=ECPAS PE=1 SV=1	62	2.858	307.01
P68366	Tubulin alpha-4A chain OS=Homo sapiens OX=9606 GN=TUBA4A PE=1 SV=1	4	2.401	301.05
A0A024RAZ7	Heterogeneous nuclear ribonucleoprotein A1, isoform CRA_b OS=Homo sapiens OX=9606 GN=HNRPA1 PE=4 SV=1	17	3.224	299.62
A0A384N6C7	Epididymis secretory sperm binding protein OS=Homo sapiens OX=9606 PE=2 SV=1	7	3.019	298.48
Q02880	DNA topoisomerase 2-beta OS=Homo sapiens OX=9606 GN=TOP2B PE=1 SV=3	56	2.404	297.09
A8K7F6	cDNA FLJ78244, highly similar to Homo sapiens eukaryotic translation initiation factor 4A, isoform 1 (EIF4A1), mRNA	13	1.987	296.74
F4ZW66	NF110b OS=Homo sapiens OX=9606 PE=2 SV=1	1	3.073	296.61
A0A0S2Z4Z9	Non-POU domain containing octamer-binding isoform 1 (Fragment) OS=Homo sapiens OX=9606 GN=NONO PE=2 SV=1	25	2.205	296.58
Q9NYF8	Bcl-2-associated transcription factor 1 OS=Homo sapiens OX=9606 GN=BCLAF1 PE=1 SV=2	3	1.37	294.51
A0A0D9SF53	ATP-dependent RNA helicase DDX3X OS=Homo sapiens OX=9606 GN=DDX3X PE=1 SV=1	13	2.318	294.49
Q59FF0	EBNA-2 co-activator variant (Fragment) OS=Homo sapiens OX=9606 PE=2 SV=1	43	2.607	291.06
B2RWN5	HEAT repeat containing 1 OS=Homo sapiens OX=9606 GN=HEATR1 PE=2 SV=1	7	2.246	290.75
P11586	C-1-tetrahydrofolate synthase, cytoplasmic OS=Homo sapiens OX=9606 GN=MTHFD1 PE=1 SV=3	48	2.904	289.64
Q93008	Probable ubiquitin carboxyl-terminal hydrolase FAF-X OS=Homo sapiens OX=9606 GN=USP9X PE=1 SV=3	66	3.051	287
Q53HV2	T-complex protein 1 subunit eta (Fragment) OS=Homo sapiens OX=9606 PE=2 SV=1	36	2.533	284.32
Q5UIP0	Telomere-associated protein RIF1 OS=Homo sapiens OX=9606 GN=RIF1 PE=1 SV=2	73	2.355	282.86
E9PK91	Bcl-2-associated transcription factor 1 OS=Homo sapiens OX=9606 GN=BCLAF1 PE=1 SV=1	1	1.65	281.52
A0A024RDY0	RAN binding protein 5, isoform CRA_d OS=Homo sapiens OX=9606 GN=RANBP5 PE=4 SV=1	39	2.259	281.39
V9HWB4	Epididymis secretory sperm binding protein Li 89n OS=Homo sapiens OX=9606 GN=HEL-S-89n PE=2 SV=1	39	1.054	277.88
P13010	X-ray repair cross-complementing protein 5 OS=Homo sapiens OX=9606 GN=XRCC5 PE=1 SV=3	40	2.345	277.21
A0A024R3R7	HEAT repeat containing 1, isoform CRA_b OS=Homo sapiens OX=9606 GN=HEATR1 PE=4 SV=1	3	2.578	276.9
O43390	Heterogeneous nuclear ribonucleoprotein R OS=Homo sapiens OX=9606 GN=HNRNPR PE=1 SV=1	4	5.343	275.53
A8K8U1	cDNA FLJ77762, highly similar to Homo sapiens cullin-associated and neddylation-dissociated 1 (CAND1), mRNA	45	2.345	271.4
B2RCM2	cDNA, FLJ96156, highly similar to Homo sapiens leucyl-tRNA synthetase (LARS), mRNA	50	1.976	268.95
Q92621	Nuclear pore complex protein Nup205 OS=Homo sapiens OX=9606 GN=NUP205 PE=1 SV=3	59	3.027	268.88
P17987	T-complex protein 1 subunit alpha OS=Homo sapiens OX=9606 GN=TCP1 PE=1 SV=1	32	2.113	268.56
P53618	Coatomer subunit beta OS=Homo sapiens OX=9606 GN=COPB1 PE=1 SV=3	42	2.441	266.45
A0A384MR33	Structural maintenance of chromosomes protein OS=Homo sapiens OX=9606 GN=SMC1L1 PE=2 SV=1	71	2.4	266.37
Q1ED39	Lysine-rich nucleolar protein 1 OS=Homo sapiens OX=9606 GN=KNOP1 PE=1 SV=1	42	0.785	263.71
P22314	Ubiquitin-like modifier-activating enzyme 1 OS=Homo sapiens OX=9606 GN=UBA1 PE=1 SV=3	37	2.368	262.64
O60264	SWI/SNF-related matrix-associated actin-dependent regulator of chromatin subfamily A member 5 GN=SMARCA5	42	2.27	261.96
Q9Y2L1	Exosome complex exonuclease RRP44 OS=Homo sapiens OX=9606 GN=DIS3 PE=1 SV=2	3	2.825	260.69
A1A5C5	RRBP1 protein OS=Homo sapiens OX=9606 GN=RRBP1 PE=2 SV=1	1	0.448	260.64
P39023	60S ribosomal protein L3 OS=Homo sapiens OX=9606 GN=RPL3 PE=1 SV=2	11	2.293	259.52

Q6MZS5	Uncharacterized protein DKFZp686A13234 (Fragment) OS=Homo sapiens OX=9606 GN=DKFZp686A13234 PE=2 SV=1	1	7.35	257.4
P55060	Exportin-2 OS=Homo sapiens OX=9606 GN=CSE1L PE=1 SV=3	43	2.58	253.12
Q59G75	Isoleucyl-tRNA synthetase, cytoplasmic variant (Fragment) OS=Homo sapiens OX=9606 PE=2 SV=1	48	2.535	253.05
P50990	T-complex protein 1 subunit theta OS=Homo sapiens OX=9606 GN=CCT8 PE=1 SV=4	38	1.877	251.61
B7ZLZ7	Structural maintenance of chromosomes protein OS=Homo sapiens OX=9606 GN=SMC2 PE=2 SV=1	62	2.012	251.35
P54886	Delta-1-pyrroline-5-carboxylate synthase OS=Homo sapiens OX=9606 GN=ALDH18A1 PE=1 SV=2	41	2.116	251.31
P52701	DNA mismatch repair protein Msh6 OS=Homo sapiens OX=9606 GN=MSH6 PE=1 SV=2	51	3.312	251.09
Q59HH3	Trifunctional purine biosynthetic protein adenosine-3 (Fragment) OS=Homo sapiens OX=9606 PE=2 SV=1	1	2.601	249.59
A0A0C4DG89	Probable ATP-dependent RNA helicase DDX46 OS=Homo sapiens OX=9606 GN=DDX46 PE=1 SV=1	1	6.223	249.35
O14980	Exportin-1 OS=Homo sapiens OX=9606 GN=XPO1 PE=1 SV=1	37	2.757	247.29
Q7L2E3	ATP-dependent RNA helicase DHX30 OS=Homo sapiens OX=9606 GN=DHX30 PE=1 SV=1	57	2.509	247.23
O14654	Insulin receptor substrate 4 OS=Homo sapiens OX=9606 GN=IRS4 PE=1 SV=1	41	2.222	246.79
Q7L014	Probable ATP-dependent RNA helicase DDX46 OS=Homo sapiens OX=9606 GN=DDX46 PE=1 SV=2	1	2.144	246.65
P07197	Neurofilament medium polypeptide OS=Homo sapiens OX=9606 GN=NEFM PE=1 SV=3	36	1.581	246.58
A0A024R4E5	High density lipoprotein binding protein (Vigilin), isoform CRA_a OS=Homo sapiens OX=9606 GN=HDLBP PE=1 SV=1	57	1.283	244.47
P52272	Heterogeneous nuclear ribonucleoprotein M OS=Homo sapiens OX=9606 GN=HNRNPM PE=1 SV=3	44	1.96	244.46
P11498	Pyruvate carboxylase, mitochondrial OS=Homo sapiens OX=9606 GN=PC PE=1 SV=2	52	2.609	243.94
P50991	T-complex protein 1 subunit delta OS=Homo sapiens OX=9606 GN=CCT4 PE=1 SV=4	33	2.42	243.51
Q59H77	T-complex protein 1 subunit gamma (Fragment) OS=Homo sapiens OX=9606 PE=2 SV=1	38	2.203	242.43
P34932	Heat shock 70 kDa protein 4 OS=Homo sapiens OX=9606 GN=HSPA4 PE=1 SV=4	44	1.907	241.14
P05023	Sodium/potassium-transporting ATPase subunit alpha-1 OS=Homo sapiens OX=9606 GN=ATP1A1 PE=1 SV=1	46	1.546	240.98
A8K3K1	cDNA FLJ78096, highly similar to Homo sapiens actin, alpha, cardiac muscle (ACTC), mRNA	1	2.022	240.46
A8QI98	DIS3 OS=Homo sapiens OX=9606 PE=2 SV=1	1	2.931	239.69
Q13085	Acetyl-CoA carboxylase 1 OS=Homo sapiens OX=9606 GN=ACACA PE=1 SV=2	71	2.805	236.4
P11387	DNA topoisomerase 1 OS=Homo sapiens OX=9606 GN=TOP1 PE=1 SV=2	49	0.703	234.49
A0A3B3ITJ4	Heterogeneous nuclear ribonucleoprotein L (Fragment) OS=Homo sapiens OX=9606 GN=HNRNPL PE=1 SV=1	2	3.772	233.24
A5YKK6	CCR4-NOT transcription complex subunit 1 OS=Homo sapiens OX=9606 GN=CNOT1 PE=1 SV=2	60	3.023	232.4
B3KMS0	Condensin complex subunit 1 OS=Homo sapiens OX=9606 PE=2 SV=1	1	2.76	230.37
P17844	Probable ATP-dependent RNA helicase DDX5 OS=Homo sapiens OX=9606 GN=DDX5 PE=1 SV=1	29	2.17	229.26
Q86VX4	Structural maintenance of chromosomes protein OS=Homo sapiens OX=9606 GN=SMC3 PE=2 SV=1	55	2.25	227.38
P57053	Histone H2B type F-S OS=Homo sapiens OX=9606 GN=H2BFS PE=1 SV=2	5	0.562	225.12
Q9UIG0	Tyrosine-protein kinase BAZ1B OS=Homo sapiens OX=9606 GN=BAZ1B PE=1 SV=2	58	2.036	224.35
A0A0S2Z3L2	ATPase Ca++ transporting cardiac muscle slow twitch 2 isoform 1 (Fragment) GN=ATP2A2	42	1.915	224.17
P33993	DNA replication licensing factor MCM7 OS=Homo sapiens OX=9606 GN=MCM7 PE=1 SV=4	44	2.898	223.65
Q59F66	DEAD box polypeptide 17 isoform p82 variant (Fragment) OS=Homo sapiens OX=9606 PE=2 SV=1	25	2.672	223.61

Q9H0A0	RNA cytidine acetyltransferase OS=Homo sapiens OX=9606 GN=NAT10 PE=1 SV=2	26	1.84	222.65
P11940	Polyadenylate-binding protein 1 OS=Homo sapiens OX=9606 GN=PABPC1 PE=1 SV=2	25	2.685	221.45
A0A384MDY8	Epididymis secretory sperm binding protein OS=Homo sapiens OX=9606 PE=2 SV=1	35	0.365	221.08
B3KS36	cDNA FLJ35376 fis, clone SKMUS2004044, highly similar to ribosomal protein L3 (RPL3), transcript variant 2, mRNA	1	2.602	220.12
Q8N257	Histone H2B type 3-B OS=Homo sapiens OX=9606 GN=HIST3H2BB PE=1 SV=3	6	0.496	220.06
Q9NTJ3	Structural maintenance of chromosomes protein 4 OS=Homo sapiens OX=9606 GN=SMC4 PE=1 SV=2	55	2.413	219.97
O43143	Pre-mRNA-splicing factor ATP-dependent RNA helicase DHX15 OS=Homo sapiens OX=9606 GN=DHX15 PE=1 SV=2	36	2.719	219.91
O60506	Heterogeneous nuclear ribonucleoprotein Q OS=Homo sapiens OX=9606 GN=SYNCRIP PE=1 SV=2	18	2.901	219.24
Q59GY2	Ribosomal protein L4 variant (Fragment) OS=Homo sapiens OX=9606 PE=2 SV=1	35	2.038	218.82
Q01780	Exosome component 10 OS=Homo sapiens OX=9606 GN=EXOSC10 PE=1 SV=2	48	2.737	218.67
A8MQ02	Afadin OS=Homo sapiens OX=9606 GN=AFDN PE=1 SV=2	35	1.284	218.44
O14617	AP-3 complex subunit delta-1 OS=Homo sapiens OX=9606 GN=AP3D1 PE=1 SV=1	41	1.708	216.11
A8K492	cDNA FLJ76789, highly similar to Homo sapiens methionine-tRNA synthetase (MARS), mRNA	37	2.69	216.02
F2Z2U4	Transformation/transcription domain-associated protein OS=Homo sapiens OX=9606 GN=TRRAP PE=1 SV=3	66	3.027	215.52
H0YFD6	Trifunctional enzyme subunit alpha, mitochondrial OS=Homo sapiens OX=9606 GN=HADHA PE=1 SV=2	35	2.281	214.54
P54136	Arginine--tRNA ligase, cytoplasmic OS=Homo sapiens OX=9606 GN=RARS PE=1 SV=2	38	2.584	213.97
Q9Y5B9	FACT complex subunit SPT16 OS=Homo sapiens OX=9606 GN=SUPT16H PE=1 SV=1	47	2.397	213.43
Q9UPU5	Ubiquitin carboxyl-terminal hydrolase 24 OS=Homo sapiens OX=9606 GN=USP24 PE=1 SV=3	59	3.06	212.6
Q9NX58	Cell growth-regulating nucleolar protein OS=Homo sapiens OX=9606 GN=LYAR PE=1 SV=2	3	0.258	212.43
Q92878	DNA repair protein RAD50 OS=Homo sapiens OX=9606 GN=RAD50 PE=1 SV=1	65	2.118	212.42
B0I1S0	DYNC2H1 variant protein OS=Homo sapiens OX=9606 PE=2 SV=1	71	2.968	212.19
A0A024R071	Nucleoporin 155kDa, isoform CRA_a OS=Homo sapiens OX=9606 GN=NUP155 PE=4 SV=1	43	2.525	211.85
V9HW37	Epididymis secretory protein Li 69 OS=Homo sapiens OX=9606 GN=HEL-S-69 PE=1 SV=1	33	1.472	210.66
O76021	Ribosomal L1 domain-containing protein 1 OS=Homo sapiens OX=9606 GN=RSL1D1 PE=1 SV=3	39	1.831	210.51
Q12789	General transcription factor 3C polypeptide 1 OS=Homo sapiens OX=9606 GN=GTF3C1 PE=1 SV=4	59	2.793	210.03
A0A384N5Z8	Epididymis secretory sperm binding protein OS=Homo sapiens OX=9606 PE=2 SV=1	29	2.473	208.09
P15924	Desmoplakin OS=Homo sapiens OX=9606 GN=DSP PE=1 SV=3	74	2.878	206.49
O00567	Nucleolar protein 56 OS=Homo sapiens OX=9606 GN=NOP56 PE=1 SV=4	33	0.729	205.19
A0A384ME17	Elongation factor Tu OS=Homo sapiens OX=9606 GN=TUFM PE=2 SV=1	27	2.38	205.07
Q9ULT8	E3 ubiquitin-protein ligase HECTD1 OS=Homo sapiens OX=9606 GN=HECTD1 PE=1 SV=3	59	2.562	203.36
B2RBE5	cDNA, FLJ95468, highly similar to Homo sapiens transcriptional coactivator tubedown-100 (TBDN100)	1	1.501	202.76
E7EQT4	Apoptotic chromatin condensation inducer in the nucleus OS=Homo sapiens OX=9606 GN=ACIN1 PE=1 SV=2	14	2.314	202.71
Q12931	Heat shock protein 75 kDa, mitochondrial OS=Homo sapiens OX=9606 GN=TRAP1 PE=1 SV=3	35	2.22	201.82
Q29RF7	Sister chromatid cohesion protein PDS5 homolog A OS=Homo sapiens OX=9606 GN=PDS5A PE=1 SV=1	42	2.608	201.55
A8MXP9	Matrin-3 OS=Homo sapiens OX=9606 GN=MATR3 PE=1 SV=1	42	1.787	201.1

E7EX90	Dynactin subunit 1 OS=Homo sapiens OX=9606 GN=DCTN1 PE=1 SV=1	43	2.37	200.49
Q16891	MICOS complex subunit MIC60 OS=Homo sapiens OX=9606 GN=IMMT PE=1 SV=1	1	1.881	199.4
A0A0B4J1W3	N-alpha-acetyltransferase 15, NatA auxiliary subunit OS=Homo sapiens OX=9606 GN=NAA15 PE=1 SV=1	1	2.308	199.4
Q8WYP5	Protein ELYS OS=Homo sapiens OX=9606 GN=AHCTF1 PE=1 SV=3	56	1.501	198.52
A8K3Y5	cDNA FLJ78186 OS=Homo sapiens OX=9606 PE=2 SV=1	1	0.307	198.29
A0A024R753	RNA binding motif protein 28 isoform 1 OS=Homo sapiens OX=9606 GN=RBM28 PE=2 SV=1	39	2.538	198.24
A0A024R7U6	DNA helicase OS=Homo sapiens OX=9606 GN=MCM4 PE=3 SV=1	42	2.561	197.96
P06737	Glycogen phosphorylase, liver form OS=Homo sapiens OX=9606 GN=PYGL PE=1 SV=4	35	2.487	197.37
B2RBD5	Tubulin beta chain OS=Homo sapiens OX=9606 PE=2 SV=1	2		197.18
Q7Z6E9	E3 ubiquitin-protein ligase RBBP6 OS=Homo sapiens OX=9606 GN=RBBP6 PE=1 SV=1	57	1.221	196.86
B7ZKR9	DNA-directed RNA polymerase subunit OS=Homo sapiens OX=9606 GN=POLR1A PE=2 SV=1	45	2.998	194.18
G8JLB6	Heterogeneous nuclear ribonucleoprotein H OS=Homo sapiens OX=9606 GN=HNRNPH1 PE=1 SV=1	1	2.226	194.16
P63244	Receptor of activated protein C kinase 1 OS=Homo sapiens OX=9606 GN=RACK1 PE=1 SV=3	19	1.934	192.7
A0A384P5G6	Epididymis secretory sperm binding protein OS=Homo sapiens OX=9606 PE=2 SV=1	41	1.756	192.6
Q9NZI8	Insulin-like growth factor 2 mRNA-binding protein 1 OS=Homo sapiens OX=9606 GN=IGF2BP1 PE=1 SV=2	28	2.809	192.34
P46087	Probable 28S rRNA (cytosine(4447)-C(5))-methyltransferase OS=Homo sapiens OX=9606 GN=NOP2 PE=1 SV=2	29	1.721	192.01
B4DJ30	cDNA FLJ61290, highly similar to Neutral alpha-glucosidase AB OS=Homo sapiens OX=9606 PE=2 SV=1	5	1.877	191.22
Q9NTI5	Sister chromatid cohesion protein PDS5 homolog B OS=Homo sapiens OX=9606 GN=PDS5B PE=1 SV=1	30	2.61	190.87
Q9HAV4	Exportin-5 OS=Homo sapiens OX=9606 GN=XPO5 PE=1 SV=1	37	2.764	189.18
B7ZM99	MTHFD1L protein OS=Homo sapiens OX=9606 GN=MTHFD1L PE=1 SV=1	36	2.59	188.86
A0A024RAC9	Zinc finger, UBR1 type 1, isoform CRA_c OS=Homo sapiens OX=9606 GN=ZUBR1 PE=4 SV=1	1	2.269	188.77
Q8WUM4	Programmed cell death 6-interacting protein OS=Homo sapiens OX=9606 GN=PDCD6IP PE=1 SV=1	1	2.329	188.35
P07195	L-lactate dehydrogenase B chain OS=Homo sapiens OX=9606 GN=LDHB PE=1 SV=2	18	2.368	188.35
Q4W4Y1	Dopamine receptor interacting protein 4 OS=Homo sapiens OX=9606 GN=DRIP4 PE=2 SV=1	1	2.627	186.75
Q8N3C0	Activating signal cointegrator 1 complex subunit 3 OS=Homo sapiens OX=9606 GN=ASCC3 PE=1 SV=3	58	3.144	186.46
P54577	Tyrosine--tRNA ligase, cytoplasmic OS=Homo sapiens OX=9606 GN=YARS PE=1 SV=4	45	2.552	185.87
Q7Z3J3	RanBP2-like and GRIP domain-containing protein 4 OS=Homo sapiens OX=9606 GN=RGPD4 PE=2 SV=3	2	2.251	184.91
V9HW96	Chaperonin containing TCP1, subunit 2 (Beta), isoform CRA_b OS=Homo sapiens OX=9606 GN=HEL-S-100n PE=2 SV=1	32	2.062	184.77
Q9BSJ8	Extended synaptotagmin-1 OS=Homo sapiens OX=9606 GN=ESYT1 PE=1 SV=1	2	0.604	184.73
O75691	Small subunit processome component 20 homolog OS=Homo sapiens OX=9606 GN=UTP20 PE=1 SV=3	53	2.391	184.41
B7ZMF2	Fanconi anemia, complementation group I OS=Homo sapiens OX=9606 GN=FANCI PE=2 SV=1	45	3.343	183.63
Q14684	Ribosomal RNA processing protein 1 homolog B OS=Homo sapiens OX=9606 GN=RRP1B PE=1 SV=3	30	0.92	183.18
B4DY08	Heterogeneous nuclear ribonucleoproteins C1/C2 OS=Homo sapiens OX=9606 GN=HNRNPC PE=1 SV=1	27	1.627	183.17
A8K8N7	Phosphoribosylformylglycinamidine synthase (FGAR amidotransferase), isoform CRA_b GN=PFAS	37	2.54	182.81
B3KQ33	cDNA FLJ32715 fis, clone TESTI2000784, highly similar to Importin-4 OS=Homo sapiens OX=9606 PE=2 SV=1	33	2.663	182.66

A0A024R0E2	Cold shock domain containing E1, RNA-binding, isoform CRA_a OS=Homo sapiens OX=9606 GN=CSDE1 PE=4 SV=1	42	1.598	182.62
Q99666	RANBP2-like and GRIP domain-containing protein 5/6 OS=Homo sapiens OX=9606 GN=RGPD5 PE=1 SV=3	2	2.217	182.59
P00338	L-lactate dehydrogenase A chain OS=Homo sapiens OX=9606 GN=LDHA PE=1 SV=2	24	2.639	182.51
A0A024R2Z6	Guanine nucleotide binding protein-like 3 (Nucleolar), isoform CRA_b GN=GNL3	29	0.304	182.12
Q8N1F7	Nuclear pore complex protein Nup93 OS=Homo sapiens OX=9606 GN=NUP93 PE=1 SV=2	42	2.522	182
A0A024RB16	Family with sequence similarity 62 (C2 domain containing), member A, isoform CRA_a GN=FAM62A	1	0.476	180.73
A0A024R4A0	Nucleolin, isoform CRA_b OS=Homo sapiens OX=9606 GN=NCL PE=4 SV=1	24	1.678	179.07
P51991	Heterogeneous nuclear ribonucleoprotein A3 OS=Homo sapiens OX=9606 GN=HNRNPA3 PE=1 SV=2	11	3.237	179.05
Q8WUM0	Nuclear pore complex protein Nup133 OS=Homo sapiens OX=9606 GN=NUP133 PE=1 SV=2	38	2.578	178.94
P26599	Polypyrimidine tract-binding protein 1 OS=Homo sapiens OX=9606 GN=PTBP1 PE=1 SV=1	2	3.111	178.74
G5E9E7	Tight junction protein 1 (Zona occludens 1), isoform CRA_e OS=Homo sapiens OX=9606 GN=TJP1 PE=1 SV=1	42	0.57	178.5
O14715	RANBP2-like and GRIP domain-containing protein 8 OS=Homo sapiens OX=9606 GN=RGPD8 PE=1 SV=2	1	4.39	178.38
A3F769	NF-kappaB repressing factor OS=Homo sapiens OX=9606 GN=NRF PE=2 SV=1	40	2.904	178.29
B3KMC9	5'-3' exoribonuclease OS=Homo sapiens OX=9606 PE=2 SV=1	35	2.62	177.72
O75592	E3 ubiquitin-protein ligase MYCBP2 OS=Homo sapiens OX=9606 GN=MYCBP2 PE=1 SV=4	44	2.878	177.05
V9HWF4	Phosphoglycerate kinase OS=Homo sapiens OX=9606 GN=HEL-S-68p PE=2 SV=1	20	2.588	175.61
P31939	Bifunctional purine biosynthesis protein PURH OS=Homo sapiens OX=9606 GN=ATIC PE=1 SV=3	29	3.03	175.29
A0A090N7U0	Cullin 1 OS=Homo sapiens OX=9606 GN=CUL1 PE=3 SV=1	44	2.735	174.67
B2R491	40S ribosomal protein S4 OS=Homo sapiens OX=9606 GN=RPS4X PE=2 SV=1	21	2.615	174.62
P26641	Elongation factor 1-gamma OS=Homo sapiens OX=9606 GN=EEF1G PE=1 SV=3	23	2.529	174.54
Q9BPX3	Condensin complex subunit 3 OS=Homo sapiens OX=9606 GN=NCAPG PE=1 SV=1	36	2.441	174.46
P55265	Double-stranded RNA-specific adenosine deaminase OS=Homo sapiens OX=9606 GN=ADAR PE=1 SV=4	1	3.033	174.04
Q14566	DNA replication licensing factor MCM6 OS=Homo sapiens OX=9606 GN=MCM6 PE=1 SV=1	40	2.358	173.7
A0A140VJE8	AP complex subunit beta OS=Homo sapiens OX=9606 GN=AP2B1 PE=2 SV=1	18	2.724	173.46
P61247	40S ribosomal protein S3a OS=Homo sapiens OX=9606 GN=RPS3A PE=1 SV=2	24	1.676	173.33
Q14974	Importin subunit beta-1 OS=Homo sapiens OX=9606 GN=KPNB1 PE=1 SV=2	27	2.013	173.3
B1AHB0	DNA helicase OS=Homo sapiens OX=9606 GN=MCM5 PE=2 SV=1	39	2.572	172.77
A0A0S2Z4T1	DNA helicase (Fragment) OS=Homo sapiens OX=9606 GN=MCM3 PE=2 SV=1	38	2.531	172.71
Q59EC0	Adenosine deaminase, RNA-specific isoform ADAR-a variant (Fragment) OS=Homo sapiens OX=9606 PE=2 SV=1	1	3.099	172.26
Q7Z478	ATP-dependent RNA helicase DHX29 OS=Homo sapiens OX=9606 GN=DHX29 PE=1 SV=2	46	1.965	172.14
Q01813	ATP-dependent 6-phosphofructokinase, platelet type OS=Homo sapiens OX=9606 GN=PFKP PE=1 SV=2	28	2.661	172.1
Q8IY81	pre-rRNA 2'-O-ribose RNA methyltransferase FTSJ3 OS=Homo sapiens OX=9606 GN=FTSJ3 PE=1 SV=2	29	1.033	172.02
P25705	ATP synthase subunit alpha, mitochondrial OS=Homo sapiens OX=9606 GN=ATP5F1A PE=1 SV=1	28	1.942	171.73
A0A0U1RRM4	Polypyrimidine tract-binding protein 1 OS=Homo sapiens OX=9606 GN=PTBP1 PE=1 SV=1	1	1.848	171.25
P62424	60S ribosomal protein L7a OS=Homo sapiens OX=9606 GN=RPL7A PE=1 SV=2	21	1.687	170.75

Q14151	Scaffold attachment factor B2 OS=Homo sapiens OX=9606 GN=SAFB2 PE=1 SV=1	23	2.249	170.51
Q8NE71	ATP-binding cassette sub-family F member 1 OS=Homo sapiens OX=9606 GN=ABCF1 PE=1 SV=2	16	1.672	170.47
A0A0A0MRM8	Unconventional myosin-VI OS=Homo sapiens OX=9606 GN=MYO6 PE=1 SV=1	46	2.931	169.24
A0A024R7E3	DNA (cytosine-5)-methyltransferase OS=Homo sapiens OX=9606 GN=DNMT1 PE=3 SV=1	1	3.387	168.76
Q8TEQ6	Gem-associated protein 5 OS=Homo sapiens OX=9606 GN=GEMIN5 PE=1 SV=3	40	1.956	168.63
O15042	U2 snRNP-associated SURP motif-containing protein OS=Homo sapiens OX=9606 GN=U2SURP PE=1 SV=2	39	1.797	168.58
Q9NRL2	Bromodomain adjacent to zinc finger domain protein 1A OS=Homo sapiens OX=9606 GN=BAZ1A PE=1 SV=2	39	2.495	168.26
Q14126	Desmoglein-2 OS=Homo sapiens OX=9606 GN=DSG2 PE=1 SV=2	33	1.242	168.11
P42285	Exosome RNA helicase MTR4 OS=Homo sapiens OX=9606 GN=MTREX PE=1 SV=3	40	2.508	167.79
Q59FD4	Hexokinase 1 isoform HKI variant (Fragment) OS=Homo sapiens OX=9606 PE=2 SV=1	35	2.335	167.19
A0A024RAH8	RNA helicase OS=Homo sapiens OX=9606 GN=DDX18 PE=3 SV=1	33	1.592	167.17
B4DZF2	cDNA FLJ59571, highly similar to Eukaryotic translation initiation factor 4gamma 2	42	1.677	167.09
A0A024RB85	Proliferation-associated 2G4, 38kDa, isoform CRA_a OS=Homo sapiens OX=9606 GN=PA2G4 PE=4 SV=1	22	1.69	167.08
Q9Y520	Protein PRRC2C OS=Homo sapiens OX=9606 GN=PRRC2C PE=1 SV=4	29	1.387	166.08
Q96T58	Msx2-interacting protein OS=Homo sapiens OX=9606 GN=SPEN PE=1 SV=1	53	2.114	165.62
Q9BUF5	Tubulin beta-6 chain OS=Homo sapiens OX=9606 GN=TUBB6 PE=1 SV=1	9	2.073	165.47
Q7Z2W4	Zinc finger CCCH-type antiviral protein 1 OS=Homo sapiens OX=9606 GN=ZC3HAV1 PE=1 SV=3	2	1.349	165.41
Q96N67	Dedicator of cytokinesis protein 7 OS=Homo sapiens OX=9606 GN=DOCK7 PE=1 SV=4	22	3.027	164.78
Q15365	Poly(rC)-binding protein 1 OS=Homo sapiens OX=9606 GN=PCBP1 PE=1 SV=2	11	2.287	164.42
A0A2U3TZH3	Elongation factor 1-alpha OS=Homo sapiens OX=9606 GN=EEF1A2 PE=1 SV=1	13	2.44	164.27
P49915	GMP synthase [glutamine-hydrolyzing] OS=Homo sapiens OX=9606 GN=GMPS PE=1 SV=1	31	2.49	163.57
Q8NI27	THO complex subunit 2 OS=Homo sapiens OX=9606 GN=THOC2 PE=1 SV=2	52	2.444	163.42
A0A024R9D2	Metadherin, isoform CRA_a OS=Homo sapiens OX=9606 GN=MTDH PE=4 SV=1	26	0.289	162.81
O43242	26S proteasome non-ATPase regulatory subunit 3 OS=Homo sapiens OX=9606 GN=PSMD3 PE=1 SV=2	33	2.413	162.69
Q5JTH9	RRP12-like protein OS=Homo sapiens OX=9606 GN=RRP12 PE=1 SV=2	42	2.054	162.59
B5ME19	Eukaryotic translation initiation factor 3 subunit C-like protein OS=Homo sapiens OX=9606 GN=EIF3CL PE=1 SV=1	36	2.209	162.47
Q59FP7	DNA (Cytosine-5-)-methyltransferase 1 variant (Fragment) OS=Homo sapiens OX=9606 PE=2 SV=1	1	1.894	161.98
Q9H2U1	ATP-dependent DNA/RNA helicase DHX36 OS=Homo sapiens OX=9606 GN=DHX36 PE=1 SV=2	34	3.269	161.27
Q12830	Nucleosome-remodeling factor subunit BPTF OS=Homo sapiens OX=9606 GN=BPTF PE=1 SV=3	51	1.737	161.19
E9PKU7	Neutral alpha-glucosidase AB OS=Homo sapiens OX=9606 GN=GANAB PE=1 SV=1	1		161.03
P26038	Moesin OS=Homo sapiens OX=9606 GN=MSN PE=1 SV=3	29	2.247	160.41
A0A4D5RAB6	Uncharacterized protein OS=Homo sapiens OX=9606 PE=4 SV=1	2	2.135	160.25
B4DUQ1	cDNA FLJ54552, highly similar to Heterogeneous nuclear ribonucleoprotein K OS=Homo sapiens OX=9606 PE=2 SV=1	1	1.409	160
A0A024QZW7	Nucleoporin 153kDa, isoform CRA_a OS=Homo sapiens OX=9606 GN=NUP153 PE=4 SV=1	45	2.476	159.9
P47897	Glutamine--tRNA ligase OS=Homo sapiens OX=9606 GN=QARS PE=1 SV=1	2	2.528	159.75

A8K329	cDNA FLJ76656, highly similar to Homo sapiens scaffold attachment factor B (SAFB), mRNA	21	1.975	159.59
A0A090N7Y2	ATP-binding cassette, sub-family F (GCN20), member 2 OS=Homo sapiens OX=9606 GN=ABCF2 PE=4 SV=1	30	2.337	159.15
A0A024RDS1	Heat shock 105kDa/110kDa protein 1, isoform CRA_c OS=Homo sapiens OX=9606 GN=HSPH1 PE=3 SV=1	31	1.796	158.06
P38919	Eukaryotic initiation factor 4A-III OS=Homo sapiens OX=9606 GN=EIF4A3 PE=1 SV=4	21	2.241	157.96
Q10567	AP-1 complex subunit beta-1 OS=Homo sapiens OX=9606 GN=AP1B1 PE=1 SV=2	6	2.277	157.55
Q641Q2	WASH complex subunit 2A OS=Homo sapiens OX=9606 GN=WASHC2A PE=1 SV=3	8	0.631	157.23
P42345	Serine/threonine-protein kinase mTOR OS=Homo sapiens OX=9606 GN=MTOR PE=1 SV=1	44	2.94	156.74
Q9GZR7	ATP-dependent RNA helicase DDX24 OS=Homo sapiens OX=9606 GN=DDX24 PE=1 SV=1	35	2.458	156.57
O00425	Insulin-like growth factor 2 mRNA-binding protein 3 OS=Homo sapiens OX=9606 GN=IGF2BP3 PE=1 SV=2	21	2.362	156.51
A0A0S2Z4Z6	Serine/arginine repetitive matrix 1 isoform 2 (Fragment) OS=Homo sapiens OX=9606 GN=SRRM1 PE=1 SV=1	5	4.344	156.18
E9PHY5	Band 4.1-like protein 2 OS=Homo sapiens OX=9606 GN=EPB41L2 PE=1 SV=1	26	0.863	156.13
P52789	Hexokinase-2 OS=Homo sapiens OX=9606 GN=HK2 PE=1 SV=2	29	2.289	155.94
Q16577	Elongation factor 1-alpha 1 OS=Homo sapiens OX=9606 GN=PTI-1 PE=2 SV=1	2	2.091	155.74
A0A0S2Z4J1	Epididymis secretory sperm binding protein (Fragment) OS=Homo sapiens OX=9606 GN=HSD17B4 PE=2 SV=1	29	2.919	155.43
A8K9U6	cDNA FLJ76121, highly similar to zinc finger CCCH-type, antiviral 1 (ZC3HAV1), transcript variant 1, mRNA	1	1.116	153.38
A0A024RDL1	Chaperonin containing TCP1, subunit 6A (Zeta 1), isoform CRA_a OS=Homo sapiens OX=9606 GN=CCT6A PE=3 SV=1	28	2.198	153.12
A0A1B0GVU9	Glutamine--tRNA ligase (Fragment) OS=Homo sapiens OX=9606 GN=QARS PE=1 SV=1	1	2.9	152.85
Q14966	Zinc finger protein 638 OS=Homo sapiens OX=9606 GN=ZNF638 PE=1 SV=2	50	1.838	152.47
P33176	Kinesin-1 heavy chain OS=Homo sapiens OX=9606 GN=KIF5B PE=1 SV=1	38	1.732	152.34
B3KT00	cDNA FLJ37368 fis, clone BRAMY2024530, highly similar to Zinc phosphodiesterase ELAC protein 2	29	3.672	151.88
V9HWP2	Epididymis luminal protein 35 OS=Homo sapiens OX=9606 GN=HEL-S-125m PE=2 SV=1	36	1.265	151.59
Q9HBB3	60S ribosomal protein L6 OS=Homo sapiens OX=9606 PE=2 SV=1	26	1.752	151.29
P17812	CTP synthase 1 OS=Homo sapiens OX=9606 GN=CTPS1 PE=1 SV=2	22	2.416	151.04
Q69YJ6	Uncharacterized protein DKFZp667N107 (Fragment) OS=Homo sapiens OX=9606 GN=DKFZp667N107 PE=2 SV=1	1		150.89
Q9Y2A7	Nck-associated protein 1 OS=Homo sapiens OX=9606 GN=NCKAP1 PE=1 SV=1	36	2.952	150.79
O95239	Chromosome-associated kinesin KIF4A OS=Homo sapiens OX=9606 GN=KIF4A PE=1 SV=3	40	2.419	150.74
Q03701	CCAAT/enhancer-binding protein zeta OS=Homo sapiens OX=9606 GN=CEBPZ PE=1 SV=3	3	1.699	150.63
P62917	60S ribosomal protein L8 OS=Homo sapiens OX=9606 GN=RPL8 PE=1 SV=2	17	2.27	150.23
P46777	60S ribosomal protein L5 OS=Homo sapiens OX=9606 GN=RPL5 PE=1 SV=3	2	2.385	150.01
B4DLV7	Rab GDP dissociation inhibitor OS=Homo sapiens OX=9606 PE=2 SV=1	18	2.959	149.84
Q08J23	tRNA (cytosine(34)-C(5))-methyltransferase OS=Homo sapiens OX=9606 GN=NSUN2 PE=1 SV=2	34	1.879	149.75
Q6IQ30	Polyadenylate-binding protein OS=Homo sapiens OX=9606 GN=PABPC4 PE=2 SV=1	21	2.47	149.63
O75400	Pre-mRNA-processing factor 40 homolog A OS=Homo sapiens OX=9606 GN=PRPF40A PE=1 SV=2	32	1.813	149.5
A2A3R6	40S ribosomal protein S6 OS=Homo sapiens OX=9606 GN=RPS6 PE=2 SV=1	17	2.162	149.28

B2R5U7	cDNA, FLJ92633, highly similar to Homo sapiens CCAAT-box-binding transcription factor (CBF2), mRNA	1		148.48
Q16513	Serine/threonine-protein kinase N2 OS=Homo sapiens OX=9606 GN=PKN2 PE=1 SV=1	30	2.568	148.38
O95373	Importin-7 OS=Homo sapiens OX=9606 GN=IPO7 PE=1 SV=1	26	2.039	148.36
Q8IX12	Cell division cycle and apoptosis regulator protein 1 OS=Homo sapiens OX=9606 GN=CCAR1 PE=1 SV=2	39	3.089	147.58
Q9HBD4	SMARCA4 isoform 2 OS=Homo sapiens OX=9606 GN=SMARCA4 PE=1 SV=1	17	1.976	147.58
A8K7D9	Importin subunit alpha OS=Homo sapiens OX=9606 PE=2 SV=1	22	1.822	147.51
B0QY89	Eukaryotic translation initiation factor 3 subunit L OS=Homo sapiens OX=9606 GN=EIF3L PE=1 SV=1	24	2.756	146.26
A0A140VK27	Leukotriene A(4) hydrolase OS=Homo sapiens OX=9606 PE=2 SV=1	28	2.535	145.23
Q12769	Nuclear pore complex protein Nup160 OS=Homo sapiens OX=9606 GN=NUP160 PE=1 SV=3	34	2.47	145.16
O75179	Ankyrin repeat domain-containing protein 17 OS=Homo sapiens OX=9606 GN=ANKRD17 PE=1 SV=3	22	1.121	144.77
O14646	Chromodomain-helicase-DNA-binding protein 1 OS=Homo sapiens OX=9606 GN=CHD1 PE=1 SV=2	36	2.765	144.74
P50570	Dynamin-2 OS=Homo sapiens OX=9606 GN=DNM2 PE=1 SV=2	21	2.819	144.71
O15371	Eukaryotic translation initiation factor 3 subunit D OS=Homo sapiens OX=9606 GN=EIF3D PE=1 SV=1	24	2.547	144.57
A8KAP3	cDNA FLJ78483, highly similar to elongation factor Tu GTP binding domain containing 2 (EFTUD2), mRNA	29	1.763	144.56
Q14240	Eukaryotic initiation factor 4A-II OS=Homo sapiens OX=9606 GN=EIF4A2 PE=1 SV=2	5	1.913	144.47
Q6NVC0	SLC25A5 protein (Fragment) OS=Homo sapiens OX=9606 GN=SLC25A5 PE=2 SV=1	6	1.99	144.47
P55072	Transitional endoplasmic reticulum ATPase OS=Homo sapiens OX=9606 GN=VCP PE=1 SV=4	35	1.292	143.75
B3KWV6	Cytoplasmic FMR1-interacting protein OS=Homo sapiens OX=9606 PE=2 SV=1	20	3.022	143.1
P15880	40S ribosomal protein S2 OS=Homo sapiens OX=9606 GN=RPS2 PE=1 SV=2	18	2.517	142.63
Q9NR09	Baculoviral IAP repeat-containing protein 6 OS=Homo sapiens OX=9606 GN=BIRC6 PE=1 SV=2	42	2.91	142.48
P23396	40S ribosomal protein S3 OS=Homo sapiens OX=9606 GN=RPS3 PE=1 SV=2	17	1.63	142.03
A6NHR9	Structural maintenance of chromosomes flexible hinge domain-containing protein 1 GN=SMCHD1	51	2.388	141.73
E9PK54	Heat shock cognate 71 kDa protein (Fragment) OS=Homo sapiens OX=9606 GN=HSPA8 PE=1 SV=8	1	0.806	140.95
Q2NL82	Pre-rRNA-processing protein TSR1 homolog OS=Homo sapiens OX=9606 GN=TSR1 PE=1 SV=1	30	2.838	140.81
B2R6J2	cDNA, FLJ92973, highly similar to Homo sapiens villin 2 (ezrin) (VIL2), mRNA OS=Homo sapiens OX=9606 PE=2 SV=1	22	2.079	140.66
A0A024RBE7	Thymopoietin, isoform CRA_c OS=Homo sapiens OX=9606 GN=TMPO PE=4 SV=1	8	0.385	140.5
P14868	Aspartate--tRNA ligase, cytoplasmic OS=Homo sapiens OX=9606 GN=DARS PE=1 SV=2	31	1.68	140.15
Q9H9A6	Leucine-rich repeat-containing protein 40 OS=Homo sapiens OX=9606 GN=LRRC40 PE=1 SV=1	27	2.892	139.61
Q53GS0	G protein-binding protein CRFG variant (Fragment) OS=Homo sapiens OX=9606 PE=2 SV=1	29	1.809	139.58
Q96AG4	Leucine-rich repeat-containing protein 59 OS=Homo sapiens OX=9606 GN=LRRC59 PE=1 SV=1	21	0.316	139.05
O14802	DNA-directed RNA polymerase III subunit RPC1 OS=Homo sapiens OX=9606 GN=POLR3A PE=1 SV=2	38	2.704	138.99
Q7Z406	Myosin-14 OS=Homo sapiens OX=9606 GN=MYH14 PE=1 SV=2	21	2.04	138.9
A0A024R8A2	GTPase activating protein and VPS9 domains 1, isoform CRA_d OS=Homo sapiens OX=9606 GN=GAPVD1 PE=4 SV=1	41	2.129	138.75
Q6PKG0	La-related protein 1 OS=Homo sapiens OX=9606 GN=LARP1 PE=1 SV=2	29	1.317	138.59
P61221	ATP-binding cassette sub-family E member 1 OS=Homo sapiens OX=9606 GN=ABCE1 PE=1 SV=1	17	2.922	138.52

P55786	Puromycin-sensitive aminopeptidase OS=Homo sapiens OX=9606 GN=NPEPPS PE=1 SV=2	35	2.606	138.45
Q9H6S0	3'-5' RNA helicase YTHDC2 OS=Homo sapiens OX=9606 GN=YTHDC2 PE=1 SV=2	4	3.103	137.64
A0A0S2Z404	Regulator of chromosome condensation 1 isoform 2 (Fragment) OS=Homo sapiens OX=9606 GN=RCC1 PE=2 SV=1	18	2.916	137.04
P11717	Cation-independent mannose-6-phosphate receptor OS=Homo sapiens OX=9606 GN=IGF2R PE=1 SV=3	42	1.254	136.96
Q59EI9	ADP,ATP carrier protein, liver isoform T2 variant (Fragment) OS=Homo sapiens OX=9606 PE=2 SV=1	2	1.858	136.95
M0R2B7	DNA polymerase OS=Homo sapiens OX=9606 GN=POLD1 PE=1 SV=1	35	2.839	136.92
Q92538	Golgi-specific brefeldin A-resistance guanine nucleotide exchange factor 1 GN=GBF1	34	2.424	136.65
A0A0A6YYL6	Protein RPL17-C18orf32 OS=Homo sapiens OX=9606 GN=RPL17-C18orf32 PE=3 SV=1	13	1.929	136.4
A0A096LPC5	WASH complex subunit 2C OS=Homo sapiens OX=9606 GN=WASHC2C PE=1 SV=1	1	0.585	136.34
O95782	AP-2 complex subunit alpha-1 OS=Homo sapiens OX=9606 GN=AP2A1 PE=1 SV=3	20	2.895	136.22
P53675	Clathrin heavy chain 2 OS=Homo sapiens OX=9606 GN=CLTCL1 PE=1 SV=2	3	1.711	136.05
E7EVA0	Microtubule-associated protein OS=Homo sapiens OX=9606 GN=MAP4 PE=1 SV=1	47	1.099	135.83
O94906	Pre-mRNA-processing factor 6 OS=Homo sapiens OX=9606 GN=PRPF6 PE=1 SV=1	38	2.717	135.8
Q9Y2W1	Thyroid hormone receptor-associated protein 3 OS=Homo sapiens OX=9606 GN=THRAP3 PE=1 SV=2	28	1.013	135.75
A0A024R821	Eukaryotic translation initiation factor 3 subunit B OS=Homo sapiens OX=9606 GN=EIF3S9 PE=3 SV=1	25	1.805	135.74
A0A0J9YVP6	Poly(U)-binding-splicing factor PUF60 (Fragment) OS=Homo sapiens OX=9606 GN=PUF60 PE=1 SV=1	22	1.518	135.66
O60287	Nucleolar pre-ribosomal-associated protein 1 OS=Homo sapiens OX=9606 GN=URB1 PE=1 SV=4	37	3.07	135.61
Q6P2E9	Enhancer of mRNA-decapping protein 4 OS=Homo sapiens OX=9606 GN=EDC4 PE=1 SV=1	31	0.905	134.45
O75152	Zinc finger CCCH domain-containing protein 11A OS=Homo sapiens OX=9606 GN=ZC3H11A PE=1 SV=3	32	2.328	134.28
P27824	Calnexin OS=Homo sapiens OX=9606 GN=CANX PE=1 SV=2	20	0.482	134.24
V9HWK0	Signal recognition particle subunit SRP72 OS=Homo sapiens OX=9606 GN=HEL103 PE=2 SV=1	32	1.401	133.89
Q14692	Ribosome biogenesis protein BMS1 homolog OS=Homo sapiens OX=9606 GN=BMS1 PE=1 SV=1	36	1.903	133.17
P49756	RNA-binding protein 25 OS=Homo sapiens OX=9606 GN=RBM25 PE=1 SV=3	30	1.803	133.14
Q8NI36	WD repeat-containing protein 36 OS=Homo sapiens OX=9606 GN=WDR36 PE=1 SV=1	31	2.68	133.05
Q9Y2X3	Nucleolar protein 58 OS=Homo sapiens OX=9606 GN=NOP58 PE=1 SV=1	26	0.823	133.03
P06733	Alpha-enolase OS=Homo sapiens OX=9606 GN=ENO1 PE=1 SV=2	23	2.035	132.81
Q13618	Cullin-3 OS=Homo sapiens OX=9606 GN=CUL3 PE=1 SV=2	35	2.492	132.5
O43175	D-3-phosphoglycerate dehydrogenase OS=Homo sapiens OX=9606 GN=PHGDH PE=1 SV=4	22	2.556	132
B7ZLQ5	Probable global transcription activator SNF2L1 OS=Homo sapiens OX=9606 GN=SMARCA1 PE=1 SV=1	22	2.616	131.86
P05165	Propionyl-CoA carboxylase alpha chain, mitochondrial OS=Homo sapiens OX=9606 GN=PCCA PE=1 SV=4	30	1.762	131.29
Q09161	Nuclear cap-binding protein subunit 1 OS=Homo sapiens OX=9606 GN=NCBP1 PE=1 SV=1	24	2.508	131.11
A0A024R0Z3	DEAD (Asp-Glu-Ala-Asp) box polypeptide 23, isoform CRA_b OS=Homo sapiens OX=9606 GN=DDX23 PE=4 SV=1	36	2.066	130.84
A0A2R8Y891	ATP-dependent 6-phosphofructokinase OS=Homo sapiens OX=9606 GN=PFKM PE=1 SV=1	26	2.389	130.42
Q9Y678	Coatomer subunit gamma-1 OS=Homo sapiens OX=9606 GN=COPG1 PE=1 SV=1	27	2.507	130.17
Q92973	Transportin-1 OS=Homo sapiens OX=9606 GN=TNPO1 PE=1 SV=2	17	2.13	130.03

Q93009	Ubiquitin carboxyl-terminal hydrolase 7 OS=Homo sapiens OX=9606 GN=USP7 PE=1 SV=2	34	1.893	130.02
Q9HB71	Calcyclin-binding protein OS=Homo sapiens OX=9606 GN=CACYBP PE=1 SV=2	15	2.283	129.92
Q59EG8	Proteasome 26S non-ATPase subunit 2 variant (Fragment) OS=Homo sapiens OX=9606 PE=2 SV=1	30	2.029	129.81
V9HWH2	Creatine kinase brain isoform 1 OS=Homo sapiens OX=9606 GN=HEL-S-29 PE=2 SV=1	15	2.233	129.61
Q643R0	HCTP4 OS=Homo sapiens OX=9606 GN=HCTP4 PE=1 SV=1	36	1.901	129.4
Q99623	Prohibitin-2 OS=Homo sapiens OX=9606 GN=PHB2 PE=1 SV=2	22	1.864	129.27
Q96GQ7	Probable ATP-dependent RNA helicase DDX27 OS=Homo sapiens OX=9606 GN=DDX27 PE=1 SV=2	33	0.815	129.23
F8VZX2	Poly(rC)-binding protein 2 OS=Homo sapiens OX=9606 GN=PCBP2 PE=1 SV=1	3	2.316	129.19
P08243	Asparagine synthetase [glutamine-hydrolyzing] OS=Homo sapiens OX=9606 GN=ASNS PE=1 SV=4	25	2.151	129.07
A8K6G9	cDNA FLJ76871, highly similar to Homo sapiens DEAH (Asp-Glu-Ala-His) box polypeptide 38 (DHX38), mRNA	31	2.792	128.8
Q5SRE5	Nucleoporin NUP188 homolog OS=Homo sapiens OX=9606 GN=NUP188 PE=1 SV=1	33	3.118	128.75
B2RDF5	SUMO-activating enzyme subunit 2 OS=Homo sapiens OX=9606 PE=2 SV=1	29	2.273	128.72
B2RNR6	Zinc finger RNA binding protein OS=Homo sapiens OX=9606 GN=ZFR PE=2 SV=1	26	3.17	127.52
A0A384N6C2	Inosine-5'-monophosphate dehydrogenase OS=Homo sapiens OX=9606 GN=IMPDH PE=2 SV=1	22	2.459	127.38
A0A494C1K3	General transcription factor II-I OS=Homo sapiens OX=9606 GN=GTF2I PE=1 SV=1	33	2.347	127.23
A0A024QZN9	Voltage-dependent anion channel 2, isoform CRA_a OS=Homo sapiens OX=9606 GN=VDAC2 PE=4 SV=1	15	2.391	127.17
Q9NSD9	Phenylalanine--tRNA ligase beta subunit OS=Homo sapiens OX=9606 GN=FARSB PE=1 SV=3	30	2.343	126.01
P30876	DNA-directed RNA polymerase II subunit RPB2 OS=Homo sapiens OX=9606 GN=POLR2B PE=1 SV=1	33	2.469	125.98
O94973	AP-2 complex subunit alpha-2 OS=Homo sapiens OX=9606 GN=AP2A2 PE=1 SV=2	14	2.575	125.84
E7ESC6	Exportin-7 OS=Homo sapiens OX=9606 GN=XPO7 PE=1 SV=1	35	2.795	125.72
Q59GX9	Ribosomal protein L5 variant (Fragment) OS=Homo sapiens OX=9606 PE=2 SV=1	1	2.067	125.51
P52948	Nuclear pore complex protein Nup98-Nup96 OS=Homo sapiens OX=9606 GN=NUP98 PE=1 SV=4	35	1.532	125.16
A0A1W2PNX8	Protein unc-45 homolog A OS=Homo sapiens OX=9606 GN=UNC45A PE=1 SV=1	30	2.355	125.02
P35251	Replication factor C subunit 1 OS=Homo sapiens OX=9606 GN=RFC1 PE=1 SV=4	28	2.376	124.99
A0A024RDF4	Heterogeneous nuclear ribonucleoprotein D (AU-rich element RNA binding protein 1, 37kDa), isoform CRA_e	3	2.404	124.9
P55795	Heterogeneous nuclear ribonucleoprotein H2 OS=Homo sapiens OX=9606 GN=HNRNPH2 PE=1 SV=1	7	2.151	124.65
P50851	Lipopolysaccharide-responsive and beige-like anchor protein OS=Homo sapiens OX=9606 GN=LRBA PE=1 SV=4	39	2.791	124.52
P27635	60S ribosomal protein L10 OS=Homo sapiens OX=9606 GN=RPL10 PE=1 SV=4	5	2.508	124.4
P35998	26S proteasome regulatory subunit 7 OS=Homo sapiens OX=9606 GN=PSMC2 PE=1 SV=3	25	2.207	124.38
A0A1U9XBC0	MDC1 OS=Homo sapiens OX=9606 PE=4 SV=1	38	2.16	124.27
A0A0S2Z4Z0	RNA binding motif protein 14 isoform 1 (Fragment) OS=Homo sapiens OX=9606 GN=RBM14 PE=2 SV=1	25	2.297	124.26
A8K905	Nucleolar complex protein 3 homolog OS=Homo sapiens OX=9606 PE=2 SV=1	28	1.619	124.19
P26639	Threonine--tRNA ligase, cytoplasmic OS=Homo sapiens OX=9606 GN=TARS PE=1 SV=3	25	2.095	123.81
O95071	E3 ubiquitin-protein ligase UBR5 OS=Homo sapiens OX=9606 GN=UBR5 PE=1 SV=2	41	2.213	123.23
B0I1S9	MYO1B variant protein OS=Homo sapiens OX=9606 GN=MYO1B PE=2 SV=1	33	2.72	122.97

P38159	RNA-binding motif protein, X chromosome OS=Homo sapiens OX=9606 GN=RBMX PE=1 SV=3	9	2.146	122.9
P10155	60 kDa SS-A/Ro ribonucleoprotein OS=Homo sapiens OX=9606 GN=RO60 PE=1 SV=2	25	2.8	122.89
Q5JR94	40S ribosomal protein S8 OS=Homo sapiens OX=9606 GN=RPS8 PE=2 SV=1	11	1.085	122.63
Q6ZMY0	cDNA FLJ16598 fis, clone TESTI4006473, weakly similar to ATP-dependent RNA helicase A	1	2.929	122.53
A0A024R4U3	Tubulin tyrosine ligase-like family, member 12, isoform CRA_a OS=Homo sapiens OX=9606 GN=TTLL12 PE=4 SV=1	26	2.922	122.31
O75717	WD repeat and HMG-box DNA-binding protein 1 OS=Homo sapiens OX=9606 GN=WDHD1 PE=1 SV=1	36	2.128	122.31
A0A024RCM3	DDX39B OS=Homo sapiens OX=9606 GN=hCG_2005638 PE=4 SV=1	9	1.869	122.19
Q9Y383	Putative RNA-binding protein Luc7-like 2 OS=Homo sapiens OX=9606 GN=LUC7L2 PE=1 SV=2	11	1.173	122.11
Q13620	Cullin-4B OS=Homo sapiens OX=9606 GN=CUL4B PE=1 SV=4	25	2.195	122.1
A0A2P9DU05	Rho-associated protein kinase OS=Homo sapiens OX=9606 GN=ROCK2 PE=2 SV=1	34	2.49	122.06
Q9UBF2	Coatomer subunit gamma-2 OS=Homo sapiens OX=9606 GN=COPG2 PE=1 SV=1	19	2.655	122.04
P49736	DNA replication licensing factor MCM2 OS=Homo sapiens OX=9606 GN=MCM2 PE=1 SV=4	26	1.928	121.91
Q7LBC6	Lysine-specific demethylase 3B OS=Homo sapiens OX=9606 GN=KDM3B PE=1 SV=2	3	3.024	121.52
Q5T9A4	ATPase family AAA domain-containing protein 3B OS=Homo sapiens OX=9606 GN=ATAD3B PE=1 SV=1	7	1.841	121.11
A0A2R8Y5S7	Radixin OS=Homo sapiens OX=9606 GN=RDX PE=1 SV=1	14	2.278	120.91
O75367	Core histone macro-H2A.1 OS=Homo sapiens OX=9606 GN=H2AFY PE=1 SV=4	17	0.956	120.8
O60832	H/ACA ribonucleoprotein complex subunit DKC1 OS=Homo sapiens OX=9606 GN=DKC1 PE=1 SV=3	27	1.587	120.37
O00116	Alkyldihydroxyacetonephosphate synthase, peroxisomal OS=Homo sapiens OX=9606 GN=AGPS PE=1 SV=1	24	2.8	120.25
P06748	Nucleophosmin OS=Homo sapiens OX=9606 GN=NPM1 PE=1 SV=2	20	1.035	120.19
P43246	DNA mismatch repair protein Msh2 OS=Homo sapiens OX=9606 GN=MSH2 PE=1 SV=1	29	2.426	120.16
Q13151	Heterogeneous nuclear ribonucleoprotein A0 OS=Homo sapiens OX=9606 GN=HNRNPA0 PE=1 SV=1	11	2.42	119.82
Q08945	FACT complex subunit SSRP1 OS=Homo sapiens OX=9606 GN=SSRP1 PE=1 SV=1	29	1.808	119.71
Q96GA3	Protein LTV1 homolog OS=Homo sapiens OX=9606 GN=LTV1 PE=1 SV=1	27	0.4	119.68
A0A0S2Z410	Epididymis secretory sperm binding protein (Fragment) OS=Homo sapiens OX=9606 GN=HSD17B10 PE=2 SV=1	16	2	119.61
Q5T3I0	G patch domain-containing protein 4 OS=Homo sapiens OX=9606 GN=GPATCH4 PE=1 SV=2	20	0.769	119.51
A8K9E1	cDNA FLJ77957, highly similar to Homo sapiens HBS1-like (S. cerevisiae) (HBS1L), mRNA	27	2.11	119.47
Q562R1	Beta-actin-like protein 2 OS=Homo sapiens OX=9606 GN=ACTBL2 PE=1 SV=2	1	1.758	119.29
Q15019	Septin-2 OS=Homo sapiens OX=9606 GN=SEPTIN2 PE=1 SV=1	12	1.503	119.1
P08240	Signal recognition particle receptor subunit alpha OS=Homo sapiens OX=9606 GN=SRPRA PE=1 SV=2	28	0.666	118.91
A0A0B4J1V9	Helicase, lymphoid-specific, isoform CRA_b OS=Homo sapiens OX=9606 GN=HELLS PE=1 SV=1	31	2.513	118.83
Q13823	Nucleolar GTP-binding protein 2 OS=Homo sapiens OX=9606 GN=GNL2 PE=1 SV=1	35	1.286	118.73
P49588	Alanine--tRNA ligase, cytoplasmic OS=Homo sapiens OX=9606 GN=AARS PE=1 SV=2	29	1.654	118.71
A0A024R3X4	Epididymis secretory sperm binding protein OS=Homo sapiens OX=9606 GN=HSPD1 PE=2 SV=1	24	1.283	118.32
A0A384MTI6	Epididymis secretory sperm binding protein OS=Homo sapiens OX=9606 PE=2 SV=1	30	2.211	118.27
B4DLC0	cDNA FLJ58476, highly similar to Poly(rC)-binding protein 2 OS=Homo sapiens OX=9606 PE=2 SV=1	1	2.498	118.13

A0A1U9X9A1	VARS OS=Homo sapiens OX=9606 PE=3 SV=2	33	2.311	118.1
Q53GR7	Solute carrier family 25, member 13 (Citrin) variant (Fragment) OS=Homo sapiens OX=9606 PE=2 SV=1	18	2.322	117.86
D9ZGF8	Rho-associated protein kinase OS=Homo sapiens OX=9606 GN=ROCK1 PE=3 SV=1	32	2.135	117.42
Q96F88	Processing of 1, ribonuclease P/MRP subunit (S. cerevisiae) OS=Homo sapiens OX=9606 GN=POP1 PE=2 SV=1	28	2.123	116.92
P16401	Histone H1.5 OS=Homo sapiens OX=9606 GN=HIST1H1B PE=1 SV=3	3	1.41	116.58
Q9NZB2	Constitutive coactivator of PPAR-gamma-like protein 1 OS=Homo sapiens OX=9606 GN=FAM120A PE=1 SV=2	28	2.948	115.97
Q9UHB9	Signal recognition particle subunit SRP68 OS=Homo sapiens OX=9606 GN=SRP68 PE=1 SV=2	28	2.046	115.92
A8K787	cDNA FLJ75273, highly similar to solute carrier family 25 (mitochondrial carrier; adenine nucleotide translocator)	6	2.046	115.66
Q86XP3	ATP-dependent RNA helicase DDX42 OS=Homo sapiens OX=9606 GN=DDX42 PE=1 SV=1	25	2.446	115.39
A0A024R7L8	UPF1 regulator of nonsense transcripts homolog (Yeast), isoform CRA_a	30	1.569	115.34
A0A024RDB4	Heterogeneous nuclear ribonucleoprotein D (AU-rich element RNA binding protein 1, 37kDa), isoform CRA_c	1	2.726	115.33
P30041	Peroxiredoxin-6 OS=Homo sapiens OX=9606 GN=PRDX6 PE=1 SV=3	16	2.583	115.28
Q15020	Squamous cell carcinoma antigen recognized by T-cells 3 OS=Homo sapiens OX=9606 GN=SART3 PE=1 SV=1	33	1.998	114.9
Q13423	NAD(P) transhydrogenase, mitochondrial OS=Homo sapiens OX=9606 GN=NNT PE=1 SV=3	31	2.229	114.76
A0A087WUZ3	Spectrin beta chain OS=Homo sapiens OX=9606 GN=SPTBN1 PE=1 SV=1	33	1.239	114.65
P05198	Eukaryotic translation initiation factor 2 subunit 1 OS=Homo sapiens OX=9606 GN=EIF2S1 PE=1 SV=3	18	2.241	114.63
E7ERI8	CLIP-associating protein 2 OS=Homo sapiens OX=9606 GN=CLASP2 PE=1 SV=1	2	2.271	114.54
P07355	Annexin A2 OS=Homo sapiens OX=9606 GN=ANXA2 PE=1 SV=2	24	0.668	114.21
P32969	60S ribosomal protein L9 OS=Homo sapiens OX=9606 GN=RPL9 PE=1 SV=1	11	2.172	114.13
Q6IBR8	Eukaryotic translation initiation factor 2, subunit 2 beta, 38kDa OS=Homo sapiens OX=9606 GN=EIF2S2 PE=2 SV=1	19	1.702	113.98
O00267	Transcription elongation factor SPT5 OS=Homo sapiens OX=9606 GN=SUPT5H PE=1 SV=1	29	1.913	113.97
A0A0S2Z5P5	Chromosome 10 open reading frame 119, isoform CRA_c (Fragment) OS=Homo sapiens OX=9606 GN=MCMBP	28	2.628	113.97
B5BUB1	RuvB-like helicase (Fragment) OS=Homo sapiens OX=9606 GN=RUVBL1 PE=2 SV=1	9	1.268	113.6
Q9UKN8	General transcription factor 3C polypeptide 4 OS=Homo sapiens OX=9606 GN=GTF3C4 PE=1 SV=2	26	2.954	113.35
Q15008	26S proteasome non-ATPase regulatory subunit 6 OS=Homo sapiens OX=9606 GN=PSMD6 PE=1 SV=1	23	2.598	113.32
P17858	ATP-dependent 6-phosphofructokinase, liver type OS=Homo sapiens OX=9606 GN=PFKL PE=1 SV=6	17	3.254	113.31
A0A3S6H7X4	Protein arginine N-methyltransferase 1 transcript variant 5 OS=Homo sapiens OX=9606 GN=PRMT1 PE=2 SV=1	17	2.363	113.04
B2RE46	Dolichyl-diphosphooligosaccharide--protein glycosyltransferase subunit 2 OS=Homo sapiens OX=9606 PE=2 SV=1	17	2.638	112.99
Q9UPN3	Microtubule-actin cross-linking factor 1, isoforms 1/2/3/5 OS=Homo sapiens OX=9606 GN=MACF1 PE=1 SV=4	40	1.434	112.66
P16152	Carbonyl reductase [NADPH] 1 OS=Homo sapiens OX=9606 GN=CBR1 PE=1 SV=3	18	2.514	112.59
E9PCT1	Serine/arginine repetitive matrix protein 1 OS=Homo sapiens OX=9606 GN=SRRM1 PE=1 SV=3	1	0.882	112.5
Q7Z460	CLIP-associating protein 1 OS=Homo sapiens OX=9606 GN=CLASP1 PE=1 SV=1	4	2.319	112.49
B0YIW6	Archain 1, isoform CRA_a OS=Homo sapiens OX=9606 GN=ARCN1 PE=1 SV=1	29	1.342	112.47
P62750	60S ribosomal protein L23a OS=Homo sapiens OX=9606 GN=RPL23A PE=1 SV=1	14	0.605	111.99

P48739	Phosphatidylinositol transfer protein beta isoform OS=Homo sapiens OX=9606 GN=PITPNB PE=1 SV=2	18	2.612	111.89
E9PK25	Cofilin-1 OS=Homo sapiens OX=9606 GN=CFL1 PE=1 SV=1	14	1.886	111.74
P22087	rRNA 2'-O-methyltransferase fibrillarin OS=Homo sapiens OX=9606 GN=FBL PE=1 SV=2	14	2.967	111.57
B3KY60	cDNA FLJ16777 fis, clone BRHIP2029567, highly similar to Cell division cycle 5-like protein	28	1.499	111.24
Q9Y230	RuvB-like 2 OS=Homo sapiens OX=9606 GN=RUVBL2 PE=1 SV=3	22	1.009	110.99
Q9NUU7	ATP-dependent RNA helicase DDX19A OS=Homo sapiens OX=9606 GN=DDX19A PE=1 SV=1	3	2.029	110.88
A0A494C0R8	Clustered mitochondria protein homolog OS=Homo sapiens OX=9606 GN=CLUH PE=1 SV=1	33	2.286	110.78
Q15393	Splicing factor 3B subunit 3 OS=Homo sapiens OX=9606 GN=SF3B3 PE=1 SV=4	30	2.05	110.58
J3KR97	Tubulin-specific chaperone D OS=Homo sapiens OX=9606 GN=TBCD PE=1 SV=1	28	3.111	110.12
O00159	Unconventional myosin-Ic OS=Homo sapiens OX=9606 GN=MYO1C PE=1 SV=4	28	2.357	109.89
Q14669	E3 ubiquitin-protein ligase TRIP12 OS=Homo sapiens OX=9606 GN=TRIP12 PE=1 SV=1	24	2.476	109.78
O60343	TBC1 domain family member 4 OS=Homo sapiens OX=9606 GN=TBC1D4 PE=1 SV=2	30	2.802	109.63
A0A2R8Y7R9	Liprin-alpha-1 (Fragment) OS=Homo sapiens OX=9606 GN=PPFIA1 PE=1 SV=1	27	1.885	109.37
Q9UNX4	WD repeat-containing protein 3 OS=Homo sapiens OX=9606 GN=WDR3 PE=1 SV=1	28	2.121	109.33
H7BXI1	Extended synaptotagmin-2 OS=Homo sapiens OX=9606 GN=ESYT2 PE=1 SV=2	21	0.847	109.33
Q5H9N4	Uncharacterized protein DKFZp686L20222 OS=Homo sapiens OX=9606 GN=DKFZp686L20222 PE=3 SV=1	12	2.25	109.33
Q8TDD1	ATP-dependent RNA helicase DDX54 OS=Homo sapiens OX=9606 GN=DDX54 PE=1 SV=2	26	2.801	109.22
E7EPK1	Septin-7 OS=Homo sapiens OX=9606 GN=SEPTIN7 PE=1 SV=2	20	2.049	109.03
O60716	Catenin delta-1 OS=Homo sapiens OX=9606 GN=CTNND1 PE=1 SV=1	31	1.041	108.95
A0A3B3ITK7	Phosphoglucomutase-1 OS=Homo sapiens OX=9606 GN=PGM1 PE=1 SV=1	25	2.94	108.86
P07737	Profilin-1 OS=Homo sapiens OX=9606 GN=PFN1 PE=1 SV=2	10	3.061	108.76
Q5JRX3	Presequence protease, mitochondrial OS=Homo sapiens OX=9606 GN=PITRM1 PE=1 SV=3	33	2.059	108.74
A8KA19	Exportin-T OS=Homo sapiens OX=9606 PE=2 SV=1	23	2.457	108.62
Q9HBB9	HC56 OS=Homo sapiens OX=9606 PE=4 SV=1	30	2.637	108.58
Q8IWZ3	Ankyrin repeat and KH domain-containing protein 1 OS=Homo sapiens OX=9606 GN=ANKHD1 PE=1 SV=1	11	1.067	108.48
A4FUT8	JMJD1B protein (Fragment) OS=Homo sapiens OX=9606 GN=JMJD1B PE=2 SV=1	1	3.026	108.47
P61011	Signal recognition particle 54 kDa protein OS=Homo sapiens OX=9606 GN=SRP54 PE=1 SV=1	22	1.042	108.46
P42695	Condensin-2 complex subunit D3 OS=Homo sapiens OX=9606 GN=NCAPD3 PE=1 SV=2	26	3.286	108.1
Q6PGP7	Tetratricopeptide repeat protein 37 OS=Homo sapiens OX=9606 GN=TTC37 PE=1 SV=1	32	3.042	107.54
Q12873	Chromodomain-helicase-DNA-binding protein 3 OS=Homo sapiens OX=9606 GN=CHD3 PE=1 SV=3	15	1.797	107.46
P23526	Adenosylhomocysteinase OS=Homo sapiens OX=9606 GN=AHCY PE=1 SV=4	18	2.274	107.45
P20700	Lamin-B1 OS=Homo sapiens OX=9606 GN=LMNB1 PE=1 SV=2	22	1.814	107.4
A0A024R233	Tight junction protein 2 (Zona occludens 2), isoform CRA_a OS=Homo sapiens OX=9606 GN=TJP2 PE=3 SV=1	1	0.643	107.33
A8KA74	cDNA FLJ76065 OS=Homo sapiens OX=9606 PE=2 SV=1	32	2.501	107.25
Q6IT96	Histone deacetylase OS=Homo sapiens OX=9606 GN=HDAC1 PE=2 SV=1	14	2.413	107.18
P46063	ATP-dependent DNA helicase Q1 OS=Homo sapiens OX=9606 GN=RECQL PE=1 SV=3	26	2.555	106.47

A0A024R814	Ribosomal protein L7, isoform CRA_a OS=Homo sapiens OX=9606 GN=RPL7 PE=4 SV=1	20	2.212	106.43
Q02241	Kinesin-like protein KIF23 OS=Homo sapiens OX=9606 GN=KIF23 PE=1 SV=3	30	1.917	106.34
O60763	General vesicular transport factor p115 OS=Homo sapiens OX=9606 GN=USO1 PE=1 SV=2	25	1.756	106.13
B7Z5R7	cDNA FLJ61355, highly similar to CLIP-associating protein 1 OS=Homo sapiens OX=9606 PE=2 SV=1	1	2.838	105.93
A0A384NL00	Glucose-6-phosphate 1-dehydrogenase OS=Homo sapiens OX=9606 PE=2 SV=1	21	2.975	105.6
J3KPS3	Fructose-bisphosphate aldolase OS=Homo sapiens OX=9606 GN=ALDOA PE=1 SV=1	13	2.801	105.26
E5KMI6	Lon protease homolog, mitochondrial OS=Homo sapiens OX=9606 GN=LONP1 PE=3 SV=1	24	2.126	105.18
P42858	Huntingtin OS=Homo sapiens OX=9606 GN=HTT PE=1 SV=2	34	2.621	105.05
Q8NEH0	DEAD (Asp-Glu-Ala-Asp) box polypeptide 20 OS=Homo sapiens OX=9606 GN=DDX20 PE=2 SV=1	24	2.593	105.02
A0A140VJS3	Testicular tissue protein Li 149 OS=Homo sapiens OX=9606 PE=2 SV=1	21	1.684	104.83
A0A224AV41	Adenomatous polyposis coli protein isoform t OS=Homo sapiens OX=9606 GN=APC PE=2 SV=1	34	0.844	104.54
A0A2R8YDH4	Uncharacterized protein OS=Homo sapiens OX=9606 PE=1 SV=1	1	0.731	104.5
P21796	Voltage-dependent anion-selective channel protein 1 OS=Homo sapiens OX=9606 GN=VDAC1 PE=1 SV=2	14	2.08	104.42
Q86Y56	Dynein assembly factor 5, axonemal OS=Homo sapiens OX=9606 GN=DNAAF5 PE=1 SV=4	28	2.717	103.73
P11171	Protein 4.1 OS=Homo sapiens OX=9606 GN=EPB41 PE=1 SV=4	28	1.027	103.58
Q12788	Transducin beta-like protein 3 OS=Homo sapiens OX=9606 GN=TBL3 PE=1 SV=2	27	2.07	103.55
Q96P70	Importin-9 OS=Homo sapiens OX=9606 GN=IPO9 PE=1 SV=3	21	2.384	103.52
A0A0S2Z5J4	Adaptor-related protein complex 3 beta 1 subunit isoform 1 (Fragment) OS=Homo sapiens OX=9606 GN=AP3B1	33	2.122	103.47
A0A024R534	Metastasis associated 1 family, member 2, isoform CRA_a OS=Homo sapiens OX=9606 GN=MTA2 PE=4 SV=1	23	2.211	103.46
P27694	Replication protein A 70 kDa DNA-binding subunit OS=Homo sapiens OX=9606 GN=RPA1 PE=1 SV=2	25	2.031	103.45
Q5VT25	Serine/threonine-protein kinase MRCK alpha OS=Homo sapiens OX=9606 GN=CDC42BPA PE=1 SV=1	10	1.358	103.35
A0A024R3R5	Lamin B receptor, isoform CRA_a OS=Homo sapiens OX=9606 GN=LBR PE=4 SV=1	22	1.323	103.17
A0A024RBH2	Cytoskeleton-associated protein 4, isoform CRA_c OS=Homo sapiens OX=9606 GN=CKAP4 PE=4 SV=1	22	0.556	103.07
Q13330	Metastasis-associated protein MTA1 OS=Homo sapiens OX=9606 GN=MTA1 PE=1 SV=2	15	2.568	102.93
Q8N1G2	Cap-specific mRNA (nucleoside-2'-O-)-methyltransferase 1 OS=Homo sapiens OX=9606 GN=CMTR1 PE=1 SV=1	28	3.287	102.87
A3RJH1	ATP-dependent RNA helicase DDX1 OS=Homo sapiens OX=9606 GN=DDX1 PE=2 SV=1	33	2.167	102.71
P26196	Probable ATP-dependent RNA helicase DDX6 OS=Homo sapiens OX=9606 GN=DDX6 PE=1 SV=2	18	2.202	102.36
V9HW31	ATP synthase subunit beta OS=Homo sapiens OX=9606 GN=HEL-S-271 PE=1 SV=1	18	1.733	102.36
F6QDS0	HCG2043426, isoform CRA_b OS=Homo sapiens OX=9606 GN=hCG_2043426 PE=1 SV=1	2	2.073	102.26
P04843	Dolichyl-diphosphooligosaccharide--protein glycosyltransferase subunit 1 GN=RPN1	26	1.038	102.23
A0A087WW66	26S proteasome non-ATPase regulatory subunit 1 OS=Homo sapiens OX=9606 GN=PSMD1 PE=1 SV=1	28	1.669	102.07
Q8IY37	Probable ATP-dependent RNA helicase DHX37 OS=Homo sapiens OX=9606 GN=DHX37 PE=1 SV=1	30	2.358	101.99
Q07864	DNA polymerase epsilon catalytic subunit A OS=Homo sapiens OX=9606 GN=POLE PE=1 SV=5	31	3.351	101.95
B3KNS8	cDNA FLJ30322 fis, clone BRACE2006703, highly similar to Surfeit locus protein 6	18	0.251	101.51
P50748	Kinetochore-associated protein 1 OS=Homo sapiens OX=9606 GN=KNTC1 PE=1 SV=1	32	2.868	101.28

B2RBE0	cDNA, FLJ95462, highly similar to Homo sapiens fatty-acid-Coenzyme A ligase, long-chain 3 (FACL3),mRNA	17	1.465	101.11
P22695	Cytochrome b-c1 complex subunit 2, mitochondrial OS=Homo sapiens OX=9606 GN=UQCRC2 PE=1 SV=3	20	2.091	100.89
A0A024RD93	Phosphoribosylaminoimidazole carboxylase, phosphoribosylaminoimidazole succinocarboxamide synthetase, isoform CRA_c	23	2.636	100.86
B4DLM8	cDNA FLJ56105, highly similar to Nuclear valosin-containing protein-like OS=Homo sapiens OX=9606 PE=2 SV=1	26	1.867	100.69
Q6NX51	Exocyst complex component 4 OS=Homo sapiens OX=9606 GN=EXOC4 PE=2 SV=1	26	2.436	100.69
Q59G12	Lamina-associated polypeptide 2, isoforms beta/gamma variant (Fragment) OS=Homo sapiens OX=9606 PE=2 SV=1	2	0.343	100.6
Q14694	Ubiquitin carboxyl-terminal hydrolase 10 OS=Homo sapiens OX=9606 GN=USP10 PE=1 SV=2	21	2.448	100.43
P41250	Glycine--tRNA ligase OS=Homo sapiens OX=9606 GN=GARS PE=1 SV=3	22	2.209	100.42
O95433	Activator of 90 kDa heat shock protein ATPase homolog 1 OS=Homo sapiens OX=9606 GN=AHSA1 PE=1 SV=1	19	2.365	100.41
P41091	Eukaryotic translation initiation factor 2 subunit 3 OS=Homo sapiens OX=9606 GN=EIF2S3 PE=1 SV=3	20	2.343	100.39
D3DUW7	Dynamin 1-like, isoform CRA_a OS=Homo sapiens OX=9606 GN=DNM1L PE=3 SV=1	1	2.029	100.25
A0A024R1U0	Ran GTPase activating protein 1, isoform CRA_d OS=Homo sapiens OX=9606 GN=RANGAP1 PE=4 SV=1	24	0.758	100
A8K5B6	cDNA FLJ76830, highly similar to SWI/SNF related, matrix associated, actin dependent regulator of chromatin, subfamily a	34	2.848	99.99
Q9H2G2	STE20-like serine/threonine-protein kinase OS=Homo sapiens OX=9606 GN=SLK PE=1 SV=1	29	1.178	99.83
Q6KC79	Nipped-B-like protein OS=Homo sapiens OX=9606 GN=NIPBL PE=1 SV=2	30	2.6	99.56
Q14157	Ubiquitin-associated protein 2-like OS=Homo sapiens OX=9606 GN=UBAP2L PE=1 SV=2	7	0.584	99.52
Q92769	Histone deacetylase 2 OS=Homo sapiens OX=9606 GN=HDAC2 PE=1 SV=2	13	2.081	99.42
Q15436	Protein transport protein Sec23A OS=Homo sapiens OX=9606 GN=SEC23A PE=1 SV=2	1	3.035	99.3
Q9BVJ6	U3 small nucleolar RNA-associated protein 14 homolog A OS=Homo sapiens OX=9606 GN=UTP14A PE=1 SV=1	26	1.179	99.21
B3KXW5	AP-1 complex subunit gamma OS=Homo sapiens OX=9606 PE=2 SV=1	22	2.864	99.18
Q9BYG3	MKI67 FHA domain-interacting nucleolar phosphoprotein OS=Homo sapiens OX=9606 GN=NIFK PE=1 SV=1	18	1.472	99.15
P04406	Glyceraldehyde-3-phosphate dehydrogenase OS=Homo sapiens OX=9606 GN=GAPDH PE=1 SV=3	17	1.595	99.01
A0A384MTT2	Epididymis secretory sperm binding protein OS=Homo sapiens OX=9606 GN=PCK2 PE=2 SV=1	24	2.459	98.73
Q9HCK8	Chromodomain-helicase-DNA-binding protein 8 OS=Homo sapiens OX=9606 GN=CHD8 PE=1 SV=5	28	2.553	98.52
A0A024R1I7	Tuftelin-interacting protein 11 OS=Homo sapiens OX=9606 GN=TFIP11 PE=3 SV=1	27	1.852	98.49
A0A0A0MRM9	Nucleolar and coiled-body phosphoprotein 1 (Fragment) OS=Homo sapiens OX=9606 GN=NOLC1 PE=1 SV=1	25	1.237	98.49
B4E2B5	MICOS complex subunit MIC60 OS=Homo sapiens OX=9606 PE=2 SV=1	2	1.725	98.39
Q9H6R4	Nucleolar protein 6 OS=Homo sapiens OX=9606 GN=NOL6 PE=1 SV=2	27	2.832	98
P51003	Poly(A) polymerase alpha OS=Homo sapiens OX=9606 GN=PAPOLA PE=1 SV=4	28	2.786	97.91
O43290	U4/U6.U5 tri-snRNP-associated protein 1 OS=Homo sapiens OX=9606 GN=SART1 PE=1 SV=1	25	0.517	97.75
P62906	60S ribosomal protein L10a OS=Homo sapiens OX=9606 GN=RPL10A PE=1 SV=2	14	2.688	97.61
Q9Y277	Voltage-dependent anion-selective channel protein 3 OS=Homo sapiens OX=9606 GN=VDAC3 PE=1 SV=1	12	2.249	97.56
A0A0S2Z5M1	SEC63-like (S. cerevisiae) (Fragment) OS=Homo sapiens OX=9606 GN=SEC63 PE=2 SV=1	21	1.197	97.45

P55084	Trifunctional enzyme subunit beta, mitochondrial OS=Homo sapiens OX=9606 GN=HADHB PE=1 SV=3	23	2.274	97.38
Q9P0M6	Core histone macro-H2A.2 OS=Homo sapiens OX=9606 GN=H2AFY2 PE=1 SV=3	17	1.462	97.23
B2RMQ4	Cytoskeleton associated protein 2 OS=Homo sapiens OX=9606 GN=CKAP2 PE=2 SV=1	1	2.863	96.99
Q8WWK9	Cytoskeleton-associated protein 2 OS=Homo sapiens OX=9606 GN=CKAP2 PE=1 SV=1	1	0.912	96.95
A0A0G2JPP5	Protein scribble homolog OS=Homo sapiens OX=9606 GN=SCRIB PE=1 SV=1	31	1.082	96.68
Q14137	Ribosome biogenesis protein BOP1 OS=Homo sapiens OX=9606 GN=BOP1 PE=1 SV=2	21	2.246	96.23
Q06210	Glutamine--fructose-6-phosphate aminotransferase [isomerizing] 1 OS=Homo sapiens OX=9606 GN=GFPT1 PE=1 SV=3	25	2.191	96.22
Q9H2M9	Rab3 GTPase-activating protein non-catalytic subunit OS=Homo sapiens OX=9606 GN=RAB3GAP2 PE=1 SV=1	29	2.158	95.89
B3KNC3	cDNA FLJ14222 fis, clone NT2RP3003992, highly similar to Nucleolar complex protein 2 homolog	21	2.002	95.69
A0A024RAC5	Epididymis secretory sperm binding protein OS=Homo sapiens OX=9606 GN=RCC2 PE=2 SV=1	24	1.922	95.69
A8K4P8	cDNA FLJ75337 OS=Homo sapiens OX=9606 PE=2 SV=1	26	3.251	95.61
B2R791	cDNA, FLJ93335, highly similar to Homo sapiens PRP3 pre-mRNA processing factor 3 homolog (yeast) (PRPF3), mRNA	27	2.153	95.55
P38606	V-type proton ATPase catalytic subunit A OS=Homo sapiens OX=9606 GN=ATP6V1A PE=1 SV=2	25	2.439	95.5
B2RDF2	Pescadillo homolog OS=Homo sapiens OX=9606 GN=PES1 PE=2 SV=1	26	2.741	95.34
P26373	60S ribosomal protein L13 OS=Homo sapiens OX=9606 GN=RPL13 PE=1 SV=4	16	2.305	95.32
Q5U0I6	H.sapiens ras-related Hrab1A protein OS=Homo sapiens OX=9606 GN=RAB1A PE=2 SV=1	6	1.991	95.23
Q96RP9	Elongation factor G, mitochondrial OS=Homo sapiens OX=9606 GN=GFM1 PE=1 SV=2	25	1.479	95.22
D3DUW5	Dynamin 1-like, isoform CRA_c OS=Homo sapiens OX=9606 GN=DNM1L PE=3 SV=1	1	2.262	95.14
Q9Y266	Nuclear migration protein nudC OS=Homo sapiens OX=9606 GN=NUDC PE=1 SV=1	19	0.651	95
A0A024R718	Nicotinamide phosphoribosyltransferase OS=Homo sapiens OX=9606 GN=PBEF1 PE=3 SV=1	24	2.232	94.87
O14744	Protein arginine N-methyltransferase 5 OS=Homo sapiens OX=9606 GN=PRMT5 PE=1 SV=4	24	3.139	94.86
Q9NXF1	Testis-expressed protein 10 OS=Homo sapiens OX=9606 GN=TEX10 PE=1 SV=2	25	1.615	94.71
Q6FHU2	Phosphoglycerate mutase (Fragment) OS=Homo sapiens OX=9606 GN=PGAM1 PE=2 SV=1	14	2.424	94.66
Q9Y3I0	tRNA-splicing ligase RtcB homolog OS=Homo sapiens OX=9606 GN=RTCB PE=1 SV=1	18	2.222	94.49
Q9Y4W2	Ribosomal biogenesis protein LAS1L OS=Homo sapiens OX=9606 GN=LAS1L PE=1 SV=2	25	1.931	94.45
A8K4T8	Condensin complex subunit 2 OS=Homo sapiens OX=9606 PE=2 SV=1	22	2.398	94.44
Q5QJE6	Deoxynucleotidyltransferase terminal-interacting protein 2 OS=Homo sapiens OX=9606 GN=DNTTIP2 PE=1 SV=2	22	1.278	94.35
Q8IWA0	WD repeat-containing protein 75 OS=Homo sapiens OX=9606 GN=WDR75 PE=1 SV=1	23	2.187	94.23
A0A024R8B6	Nucleoporin 214kDa, isoform CRA_b OS=Homo sapiens OX=9606 GN=NUP214 PE=4 SV=1	26	1.36	94.08
J3KPP4	Cisplatin resistance-associated overexpressed protein, isoform CRA_b OS=Homo sapiens OX=9606 GN=LUC7L3 PE=1 SV=1	18	1.419	94.01
Q13206	Probable ATP-dependent RNA helicase DDX10 OS=Homo sapiens OX=9606 GN=DDX10 PE=1 SV=2	23	2.031	93.9
Q6IPH7	RPL14 protein OS=Homo sapiens OX=9606 GN=RPL14 PE=1 SV=1	1	1.529	93.88
Q9BU76	Multiple myeloma tumor-associated protein 2 OS=Homo sapiens OX=9606 GN=MMTAG2 PE=1 SV=1	16	1.143	93.81
Q9BXW9	Fanconi anemia group D2 protein OS=Homo sapiens OX=9606 GN=FANCD2 PE=1 SV=2	24	2.882	93.76

Q9H0U4	Ras-related protein Rab-1B OS=Homo sapiens OX=9606 GN=RAB1B PE=1 SV=1	1	2.272	93.76
Q13045	Protein flightless-1 homolog OS=Homo sapiens OX=9606 GN=FLII PE=1 SV=2	26	2.2	93.73
V9HW01	Epididymis secretory protein Li 310 OS=Homo sapiens OX=9606 GN=HEL-S-310 PE=2 SV=1	13	1.86	93.73
B7Z3V5	cDNA FLJ60617, highly similar to Mitogen-activated protein kinase kinase kinase kinase 4	1	1.549	93.38
V9GYM8	Rho guanine nucleotide exchange factor 2 OS=Homo sapiens OX=9606 GN=ARHGEF2 PE=1 SV=1	27	2.086	93.28
P17980	26S proteasome regulatory subunit 6A OS=Homo sapiens OX=9606 GN=PSMC3 PE=1 SV=3	21	1.597	93.05
Q96QC0	Serine/threonine-protein phosphatase 1 regulatory subunit 10 OS=Homo sapiens OX=9606 GN=PPP1R10 PE=1 SV=1	26	5.914	93.03
Q53TX8	Uncharacterized protein MAP4K4 (Fragment) OS=Homo sapiens OX=9606 GN=MAP4K4 PE=4 SV=1	1		92.94
B7Z6F7	cDNA FLJ61705, highly similar to Symplekin OS=Homo sapiens OX=9606 PE=2 SV=1	28	2.292	92.8
Q4LE38	IKBKAP variant protein (Fragment) OS=Homo sapiens OX=9606 GN=IKBKAP variant protein PE=2 SV=1	24	1.85	92.71
Q96T37	RNA-binding protein 15 OS=Homo sapiens OX=9606 GN=RBM15 PE=1 SV=2	23	2.372	92.66
A0A087WTP3	Far upstream element-binding protein 2 OS=Homo sapiens OX=9606 GN=KHSRP PE=1 SV=1	18	2.22	92.2
A0A140VKF1	Kinesin-like protein OS=Homo sapiens OX=9606 PE=2 SV=1	22	2.325	92.15
H0Y2W2	ATPase family AAA domain-containing protein 3A (Fragment) OS=Homo sapiens OX=9606 GN=ATAD3A PE=1 SV=1	5	1.809	92.03
Q6L8Q7	2',5'-phosphodiesterase 12 OS=Homo sapiens OX=9606 GN=PDE12 PE=1 SV=2	21	3.179	92.03
O00148	ATP-dependent RNA helicase DDX39A OS=Homo sapiens OX=9606 GN=DDX39A PE=1 SV=2	8	1.803	92
J3KQE5	GTP-binding nuclear protein Ran (Fragment) OS=Homo sapiens OX=9606 GN=RAN PE=1 SV=1	11	2.222	91.9
P60891	Ribose-phosphate pyrophosphokinase 1 OS=Homo sapiens OX=9606 GN=PRPS1 PE=1 SV=2	8	2.492	91.81
Q96E39	RNA binding motif protein, X-linked-like-1 OS=Homo sapiens OX=9606 GN=RBMXL1 PE=1 SV=1	1	1.58	91.58
A0A0B4J2E5	Uncharacterized protein OS=Homo sapiens OX=9606 GN=LOC102724159 PE=1 SV=1	19	2.318	91.38
Q9UBU9	Nuclear RNA export factor 1 OS=Homo sapiens OX=9606 GN=NXF1 PE=1 SV=1	21	1.915	91.33
P62263	40S ribosomal protein S14 OS=Homo sapiens OX=9606 GN=RPS14 PE=1 SV=3	7	2.29	91.27
A8K6J9	cDNA FLJ76879, highly similar to Homo sapiens DEAH (Asp-Glu-Ala-His) box polypeptide 8 (DHX8), mRNA	22	2.705	91.24
F8W930	Insulin-like growth factor 2 mRNA-binding protein 2 OS=Homo sapiens OX=9606 GN=IGF2BP2 PE=1 SV=1	20	2.273	90.94
Q1KMD3	Heterogeneous nuclear ribonucleoprotein U-like protein 2 OS=Homo sapiens OX=9606 GN=HNRNPUL2 PE=1 SV=1	25	2.099	90.92
P35606	Coatomer subunit beta' OS=Homo sapiens OX=9606 GN=COPB2 PE=1 SV=2	19	0.993	90.91
P60228	Eukaryotic translation initiation factor 3 subunit E OS=Homo sapiens OX=9606 GN=EIF3E PE=1 SV=1	18	2.669	90.85
P23921	Ribonucleoside-diphosphate reductase large subunit OS=Homo sapiens OX=9606 GN=RRM1 PE=1 SV=1	24	2.566	90.83
A0A0S2Z3X8	Rab GDP dissociation inhibitor (Fragment) OS=Homo sapiens OX=9606 GN=GDI1 PE=2 SV=1	10	2.834	90.81
O95831	Apoptosis-inducing factor 1, mitochondrial OS=Homo sapiens OX=9606 GN=AIFM1 PE=1 SV=1	17	2.036	90.46
P02786	Transferrin receptor protein 1 OS=Homo sapiens OX=9606 GN=TFRC PE=1 SV=2	24	2.114	90.45
A0A384MDZ1	DNA mismatch repair protein OS=Homo sapiens OX=9606 PE=2 SV=1	27	2.22	90.34
B2R841	Serine/threonine-protein kinase PLK OS=Homo sapiens OX=9606 PE=2 SV=1	23	3.117	90.32
A4D212	DKFZP586J0619 protein OS=Homo sapiens OX=9606 GN=DKFZP586J0619 PE=4 SV=1	28	2.769	90.29

Q9H1A4	Anaphase-promoting complex subunit 1 OS=Homo sapiens OX=9606 GN=ANAPC1 PE=1 SV=1	29	3.102	90.26
A0A024QZY5	PRP4 pre-mRNA processing factor 4 homolog B (Yeast), isoform CRA_a OS=Homo sapiens OX=9606 GN=PRPF4B PE=4 SV=1	25	1.473	90.08
Q8NC51	Plasminogen activator inhibitor 1 RNA-binding protein OS=Homo sapiens OX=9606 GN=SERBP1 PE=1 SV=2	20	0.489	89.99
B2R7V4	cDNA, FLJ93619, highly similar to Homo sapiens PRP4 pre-mRNA processing factor 4 homolog (yeast) (PRPF4)	1	2.096	89.95
Q8WXF1	Paraspeckle component 1 OS=Homo sapiens OX=9606 GN=PSPC1 PE=1 SV=1	18	2.489	89.9
B0UZZ8	Chromosome 6 open reading frame 11 OS=Homo sapiens OX=9606 GN=WDR46 PE=2 SV=1	20	2.145	89.86
Q53HB3	Proteasome 26S ATPase subunit 1 variant (Fragment) OS=Homo sapiens OX=9606 PE=1 SV=1	18	1.49	89.56
Q14997	Proteasome activator complex subunit 4 OS=Homo sapiens OX=9606 GN=PSME4 PE=1 SV=2	28	3.283	89.54
P62280	40S ribosomal protein S11 OS=Homo sapiens OX=9606 GN=RPS11 PE=1 SV=3	14	2.944	89.36
A0A0G2JH68	Protein diaphanous homolog 1 OS=Homo sapiens OX=9606 GN=DIAPH1 PE=1 SV=1	25	2.222	89.2
Q9BUJ2	Heterogeneous nuclear ribonucleoprotein U-like protein 1 OS=Homo sapiens OX=9606 GN=HNRNPUL1 PE=1 SV=2	21	2.684	89.11
E9PAU2	Ribonucleoprotein PTB-binding 1 OS=Homo sapiens OX=9606 GN=RAVER1 PE=1 SV=1	18	2.86	89.03
Q96ST3	Paired amphipathic helix protein Sin3a OS=Homo sapiens OX=9606 GN=SIN3A PE=1 SV=2	27	2.579	89
Q59EL4	PRPF4 protein variant (Fragment) OS=Homo sapiens OX=9606 PE=2 SV=1	1	2.202	88.82
A6NMQ1	DNA polymerase OS=Homo sapiens OX=9606 GN=POLA1 PE=1 SV=1	28	2.379	88.82
V9HW98	Epididymis luminal protein 2 OS=Homo sapiens OX=9606 GN=HEL2 PE=1 SV=1	12	1.714	88.79
P51116	Fragile X mental retardation syndrome-related protein 2 OS=Homo sapiens OX=9606 GN=FXR2 PE=1 SV=2	15	1.724	88.7
A0A0S2Z5U6	Pyrroline-5-carboxylate reductase (Fragment) OS=Homo sapiens OX=9606 GN=PYCR2 PE=2 SV=1	12	2.673	88.67
Q9Y5J1	U3 small nucleolar RNA-associated protein 18 homolog OS=Homo sapiens OX=9606 GN=UTP18 PE=1 SV=3	16	1.983	88.66
A0A024R394	Cysteine and histidine-rich domain (CHORD)-containing 1, isoform CRA_c OS=Homo sapiens OX=9606 GN=CHORDC1	16	1.597	88.54
Q13435	Splicing factor 3B subunit 2 OS=Homo sapiens OX=9606 GN=SF3B2 PE=1 SV=2	27	0.776	88.29
Q8IYB8	ATP-dependent RNA helicase SUPV3L1, mitochondrial OS=Homo sapiens OX=9606 GN=SUPV3L1 PE=1 SV=1	25	2.621	88.22
O75165	DnaJ homolog subfamily C member 13 OS=Homo sapiens OX=9606 GN=DNAJC13 PE=1 SV=5	25	2.789	87.99
A0A024R8A7	HCG31253, isoform CRA_a OS=Homo sapiens OX=9606 GN=hCG_31253 PE=4 SV=1	23	2.586	87.8
Q5STZ8	ATP-binding cassette sub-family F member 1 (Fragment) OS=Homo sapiens OX=9606 GN=ABCF1 PE=1 SV=9	2	1.649	87.8
A6NEM2	Host cell factor 1 OS=Homo sapiens OX=9606 GN=HCFC1 PE=1 SV=2	27	2.325	87.65
Q5U5J2	CSNK2A1 protein OS=Homo sapiens OX=9606 GN=CSNK2A1 PE=1 SV=1	14	1.614	87.47
Q9NSE4	Isoleucine--tRNA ligase, mitochondrial OS=Homo sapiens OX=9606 GN=IARS2 PE=1 SV=2	24	2.468	87.44
P31930	Cytochrome b-c1 complex subunit 1, mitochondrial OS=Homo sapiens OX=9606 GN=UQCRC1 PE=1 SV=3	12	2.84	87.28
A0A024QZD5	Small nuclear ribonucleoprotein 70kDa polypeptide (RNP antigen), isoform CRA_b OS=Homo sapiens OX=9606 GN=SNRP70	21	2.472	87.26
Q9BZJ0	Crooked neck-like protein 1 OS=Homo sapiens OX=9606 GN=CRNKL1 PE=1 SV=4	24	2.258	87.19
X5D8S6	Adenylosuccinate lyase (Fragment) OS=Homo sapiens OX=9606 GN=ADSL PE=2 SV=1	20	2.459	87.13
P07196	Neurofilament light polypeptide OS=Homo sapiens OX=9606 GN=NEFL PE=1 SV=3	20	1.989	87.13
P62136	Serine/threonine-protein phosphatase PP1-alpha catalytic subunit OS=Homo sapiens OX=9606 GN=PPP1CA PE=1 SV=1	3	0.783	87.05

E9PFW3	AP-2 complex subunit mu OS=Homo sapiens OX=9606 GN=AP2M1 PE=1 SV=1	23	1.773	86.73
A0A024R8Z9	Aspartyl-tRNA synthetase 2 (Mitochondrial), isoform CRA_b OS=Homo sapiens OX=9606 GN=DARS2 PE=3 SV=1	20	1.986	86.73
F8W7C6	60S ribosomal protein L10 OS=Homo sapiens OX=9606 GN=RPL10 PE=1 SV=2	1	3.742	86.69
A0A087X295	WD repeat-containing protein 6 OS=Homo sapiens OX=9606 GN=WDR6 PE=1 SV=1	22	1.5	86.5
Q96F07	Cytoplasmic FMR1-interacting protein 2 OS=Homo sapiens OX=9606 GN=CYFIP2 PE=1 SV=2	5	3.046	86.49
Q12923	Tyrosine-protein phosphatase non-receptor type 13 OS=Homo sapiens OX=9606 GN=PTPN13 PE=1 SV=2	27	1.995	86.37
Q9BWF3	RNA-binding protein 4 OS=Homo sapiens OX=9606 GN=RBM4 PE=1 SV=1	4	1.89	86.2
Q00325	Phosphate carrier protein, mitochondrial OS=Homo sapiens OX=9606 GN=SLC25A3 PE=1 SV=2	16	2.032	86.2
O60488	Long-chain-fatty-acid--CoA ligase 4 OS=Homo sapiens OX=9606 GN=ACSL4 PE=1 SV=2	16	2.446	86.19
Q9UNY4	Transcription termination factor 2 OS=Homo sapiens OX=9606 GN=TTF2 PE=1 SV=2	24	2.09	86.14
A0A024R250	Nucleolar protein 8, isoform CRA_a OS=Homo sapiens OX=9606 GN=NOL8 PE=4 SV=1	30	2.55	86.12
A0A087X2I1	26S proteasome regulatory subunit 10B OS=Homo sapiens OX=9606 GN=PSMC6 PE=1 SV=1	21	1.956	86.07
M0R2Z9	SURP and G-patch domain-containing protein 2 OS=Homo sapiens OX=9606 GN=SUGP2 PE=1 SV=1	27	2.781	86.03
P30520	Adenylosuccinate synthetase isozyme 2 OS=Homo sapiens OX=9606 GN=ADSS PE=1 SV=3	19	2.178	85.99
P27448	MAP/microtubule affinity-regulating kinase 3 OS=Homo sapiens OX=9606 GN=MARK3 PE=1 SV=5	15	2.527	85.97
A0A087WTW0	E3 ubiquitin-protein ligase UHRF1 OS=Homo sapiens OX=9606 GN=UHRF1 PE=1 SV=1	18	4.198	85.8
Q9Y5M8	Signal recognition particle receptor subunit beta OS=Homo sapiens OX=9606 GN=SRPRB PE=1 SV=3	16	1.262	85.55
J3KPF3	4F2 cell-surface antigen heavy chain OS=Homo sapiens OX=9606 GN=SLC3A2 PE=1 SV=1	19	1.034	85.54
Q02543	60S ribosomal protein L18a OS=Homo sapiens OX=9606 GN=RPL18A PE=1 SV=2	11	2.731	85.42
F1T0L5	ATP-dependent RNA helicase DDX51 OS=Homo sapiens OX=9606 GN=DDX51 PE=2 SV=1	17	2.758	85.41
P62495	Eukaryotic peptide chain release factor subunit 1 OS=Homo sapiens OX=9606 GN=ETF1 PE=1 SV=3	16	2	85.28
A8K7N0	cDNA FLJ75556, highly similar to Homo sapiens ribosomal protein L14, mRNA OS=Homo sapiens OX=9606 PE=2 SV=1	1	1.767	85.18
A0A140VK41	Testicular secretory protein Li 41 OS=Homo sapiens OX=9606 PE=2 SV=1	6	2.5	85.17
P42166	Lamina-associated polypeptide 2, isoform alpha OS=Homo sapiens OX=9606 GN=TMPO PE=1 SV=2	8	1.584	85.05
P11216	Glycogen phosphorylase, brain form OS=Homo sapiens OX=9606 GN=PYGB PE=1 SV=5	24	2.372	85
P36873	Serine/threonine-protein phosphatase PP1-gamma catalytic subunit OS=Homo sapiens OX=9606 GN=PPP1CC PE=1 SV=1	2	0.629	84.98
Q5SQH4	DBP2 protein OS=Homo sapiens OX=9606 GN=DBP2 PE=2 SV=1	23	1.862	84.97
A0A0A0MRF6	A-kinase anchor protein 9 OS=Homo sapiens OX=9606 GN=AKAP9 PE=1 SV=1	27	1.465	84.6
Q9UBD5	Origin recognition complex subunit 3 OS=Homo sapiens OX=9606 GN=ORC3 PE=1 SV=1	20	2.901	84.55
B2R7C2	cDNA, FLJ93375, highly similar to Homo sapiens ZW10, kinetochore associated, homolog (Drosophila) (ZW10), mRNA	19	2.766	84.47
Q7L0Y3	tRNA methyltransferase 10 homolog C OS=Homo sapiens OX=9606 GN=TRMT10C PE=1 SV=2	18	1.937	84.28
Q96SI9	Spermatid perinuclear RNA-binding protein OS=Homo sapiens OX=9606 GN=STRBP PE=1 SV=1	10	2.665	84.22
Q86U86	Protein polybromo-1 OS=Homo sapiens OX=9606 GN=PBRM1 PE=1 SV=1	32	2.249	84.21
Q4G0J3	La-related protein 7 OS=Homo sapiens OX=9606 GN=LARP7 PE=1 SV=1	20	1.896	84.06

Q92576	PHD finger protein 3 OS=Homo sapiens OX=9606 GN=PHF3 PE=1 SV=3	26	2.543	84.01
Q53XM7	VAMP (Vesicle-associated membrane protein)-associated protein B and C OS=Homo sapiens OX=9606 GN=VAPB	12	0.435	83.96
Q5SW79	Centrosomal protein of 170 kDa OS=Homo sapiens OX=9606 GN=CEP170 PE=1 SV=1	29	1.397	83.72
A8K8X0	cDNA FLJ75187, highly similar to Homo sapiens nap1 P120 OS=Homo sapiens OX=9606 PE=2 SV=1	23	2.92	83.4
Q9Y3F4	Serine-threonine kinase receptor-associated protein OS=Homo sapiens OX=9606 GN=STRAP PE=1 SV=1	15	1.107	83.38
Q7KZI7	Serine/threonine-protein kinase MARK2 OS=Homo sapiens OX=9606 GN=MARK2 PE=1 SV=2	17	2.62	83.38
P38432	Coilin OS=Homo sapiens OX=9606 GN=COIL PE=1 SV=1	18	2.719	83.22
Q5VZL5	Zinc finger MYM-type protein 4 OS=Homo sapiens OX=9606 GN=ZMYM4 PE=1 SV=1	27	2.246	83.19
A0A0S2Z2Z6	Annexin (Fragment) OS=Homo sapiens OX=9606 GN=ANXA6 PE=2 SV=1	23	2.828	83.05
Q9P2R3	Rabankyrin-5 OS=Homo sapiens OX=9606 GN=ANKFY1 PE=1 SV=2	24	2.845	83.05
A0A024R9D3	Ribosomal protein L30, isoform CRA_b OS=Homo sapiens OX=9606 GN=RPL30 PE=3 SV=1	9	2.292	82.8
Q15437	Protein transport protein Sec23B OS=Homo sapiens OX=9606 GN=SEC23B PE=1 SV=2	14	2.932	82.76
P62140	Serine/threonine-protein phosphatase PP1-beta catalytic subunit OS=Homo sapiens OX=9606 GN=PPP1CB PE=1 SV=3	4	1.796	82.73
Q07666	KH domain-containing, RNA-binding, signal transduction-associated protein 1 OS=Homo sapiens OX=9606 GN=KHDRBS1	14	2.742	82.6
O15294	UDP-N-acetylglucosamine--peptide N-acetylglucosaminyltransferase 110 kDa subunit OS=Homo sapiens OX=9606 GN=OGT	22	2.894	82.55
A0A024QZY1	JTV1 gene, isoform CRA_a OS=Homo sapiens OX=9606 GN=JTV1 PE=4 SV=1	13	2.247	82.54
A0A024R9L1	RNA helicase aquarius OS=Homo sapiens OX=9606 GN=AQR PE=3 SV=1	24	2.842	82.52
Q2NKX8	DNA excision repair protein ERCC-6-like OS=Homo sapiens OX=9606 GN=ERCC6L PE=1 SV=1	28	1.538	82.22
A0A024R7X0	ADP-ribosylation factor guanine nucleotide-exchange factor 1(Brefeldin A-inhibited), isoform CRA_a	14	2.667	82.21
Q7Z417	Nuclear fragile X mental retardation-interacting protein 2 OS=Homo sapiens OX=9606 GN=NUFIP2 PE=1 SV=1	22	1.166	82.21
A0A024R419	KIAA0971, isoform CRA_b OS=Homo sapiens OX=9606 GN=KIAA0971 PE=4 SV=1	20	2.037	82.19
K7ER00	Phenylalanine--tRNA ligase alpha subunit OS=Homo sapiens OX=9606 GN=FARSA PE=1 SV=1	15	2.125	82.01
Q53H12	Acylglycerol kinase, mitochondrial OS=Homo sapiens OX=9606 GN=AGK PE=1 SV=2	18	2.477	81.89
Q9Y295	Developmentally-regulated GTP-binding protein 1 OS=Homo sapiens OX=9606 GN=DRG1 PE=1 SV=1	17	2.411	81.87
A0A1U9X972	PRRC2A OS=Homo sapiens OX=9606 PE=4 SV=1	24	1.046	81.87
P13489	Ribonuclease inhibitor OS=Homo sapiens OX=9606 GN=RNH1 PE=1 SV=2	18	2.025	81.83
B9A6J2	RAB3 GTPase activating protein subunit 1 OS=Homo sapiens OX=9606 GN=RAB3GAP1 PE=2 SV=1	24	2.049	81.8
A0A024R3P9	Acyl-Coenzyme A binding domain containing 3, isoform CRA_a OS=Homo sapiens OX=9606 GN=ACBD3 PE=4 SV=1	18	0.558	81.76
P53992	Protein transport protein Sec24C OS=Homo sapiens OX=9606 GN=SEC24C PE=1 SV=3	21	3.661	81.72
A0A286YFF8	Protein MON2 homolog OS=Homo sapiens OX=9606 GN=MON2 PE=1 SV=1	29	2.568	81.68
P20020	Plasma membrane calcium-transporting ATPase 1 OS=Homo sapiens OX=9606 GN=ATP2B1 PE=1 SV=4	12	1.553	81.65
Q96SB4	SRSF protein kinase 1 OS=Homo sapiens OX=9606 GN=SRPK1 PE=1 SV=2	18	1.38	81.64
D0PNI1	Epididymis luminal protein 4 OS=Homo sapiens OX=9606 GN=YWHAZ PE=2 SV=1	11	2.186	81.61
Q96EE3	Nucleoporin SEH1 OS=Homo sapiens OX=9606 GN=SEH1L PE=1 SV=3	16	2.323	81.59

P57740	Nuclear pore complex protein Nup107 OS=Homo sapiens OX=9606 GN=NUP107 PE=1 SV=1	23	2.445	81.56
Q6P158	Putative ATP-dependent RNA helicase DHX57 OS=Homo sapiens OX=9606 GN=DHX57 PE=1 SV=2	18	3.002	81.53
B3KRB2	cDNA FLJ33964 fis, clone CTONG2019029, highly similar to Pseudouridylate synthase 7 homolog	19	2.262	81.34
Q9NYU2	UDP-glucose:glycoprotein glucosyltransferase 1 OS=Homo sapiens OX=9606 GN=UGGT1 PE=1 SV=3	26	1.912	81.29
B3KQ21	cDNA FLJ32640 fis, clone SYNOV2001033, highly similar to U3 small nucleolar RNA-associated protein 6 homolog	21	2.267	81.19
A0JP11	Phosphoinositide-3-kinase, regulatory subunit 4 OS=Homo sapiens OX=9606 GN=PIK3R4 PE=2 SV=1	23	2.55	81.16
P0DN79	Cystathionine beta-synthase-like protein OS=Homo sapiens OX=9606 GN=CBSL PE=1 SV=1	20	2.425	81.11
I3L504	Eukaryotic translation initiation factor 5A-1 OS=Homo sapiens OX=9606 GN=EIF5A PE=1 SV=1	10	0.838	81.06
Q9NQ29	Putative RNA-binding protein Luc7-like 1 OS=Homo sapiens OX=9606 GN=LUC7L PE=1 SV=1	6	2.034	80.93
A0A024R1X8	Junction plakoglobin, isoform CRA_a OS=Homo sapiens OX=9606 GN=JUP PE=4 SV=1	16	2.22	80.83
A0A384NPU5	Epididymis secretory sperm binding protein OS=Homo sapiens OX=9606 PE=2 SV=1	18	1.739	80.72
P24752	Acetyl-CoA acetyltransferase, mitochondrial OS=Homo sapiens OX=9606 GN=ACAT1 PE=1 SV=1	16	2.599	80.67
P51812	Ribosomal protein S6 kinase alpha-3 OS=Homo sapiens OX=9606 GN=RPS6KA3 PE=1 SV=1	12	2.454	80.45
J3KN66	Torsin-1A-interacting protein 1 OS=Homo sapiens OX=9606 GN=TOR1AIP1 PE=1 SV=1	15	0.463	80.28
Q6PUJ7	Epididymis luminal protein 215 OS=Homo sapiens OX=9606 GN=HEL-215 PE=2 SV=1	1	2.016	80.23
P30260	Cell division cycle protein 27 homolog OS=Homo sapiens OX=9606 GN=CDC27 PE=1 SV=2	18	2.32	80.21
P42696	RNA-binding protein 34 OS=Homo sapiens OX=9606 GN=RBM34 PE=1 SV=2	23	2.586	80.2
Q15717	ELAV-like protein 1 OS=Homo sapiens OX=9606 GN=ELAVL1 PE=1 SV=2	14	2.418	80.17
Q969X6	U3 small nucleolar RNA-associated protein 4 homolog OS=Homo sapiens OX=9606 GN=UTP4 PE=1 SV=1	19	2.221	80.16
P28288	ATP-binding cassette sub-family D member 3 OS=Homo sapiens OX=9606 GN=ABCD3 PE=1 SV=1	15	2.174	80.06
Q9Y6Y8	SEC23-interacting protein OS=Homo sapiens OX=9606 GN=SEC23IP PE=1 SV=1	23	2.536	79.91
Q6P1J9	Parafibromin OS=Homo sapiens OX=9606 GN=CDC73 PE=1 SV=1	22	2.383	79.82
O00231	26S proteasome non-ATPase regulatory subunit 11 OS=Homo sapiens OX=9606 GN=PSMD11 PE=1 SV=3	19	2.253	79.79
P49916	DNA ligase 3 OS=Homo sapiens OX=9606 GN=LIG3 PE=1 SV=2	30	2.638	79.77
O95714	E3 ubiquitin-protein ligase HERC2 OS=Homo sapiens OX=9606 GN=HERC2 PE=1 SV=2	23	2.716	79.69
O14979	Heterogeneous nuclear ribonucleoprotein D-like OS=Homo sapiens OX=9606 GN=HNRNPDL PE=1 SV=3	13	1.818	79.67
P26368	Splicing factor U2AF 65 kDa subunit OS=Homo sapiens OX=9606 GN=U2AF2 PE=1 SV=4	16	1.12	79.65
P33981	Dual specificity protein kinase TTK OS=Homo sapiens OX=9606 GN=TTK PE=1 SV=2	23	2.488	79.5
A0A024RDB2	Ras-GTPase activating protein SH3 domain-binding protein 2, isoform CRA_b OS=Homo sapiens OX=9606 GN=G3BP2	13	1.372	79.5
Q05519	Serine/arginine-rich splicing factor 11 OS=Homo sapiens OX=9606 GN=SRSF11 PE=1 SV=1	12	1.536	79.49
Q9H307	Pinin OS=Homo sapiens OX=9606 GN=PNN PE=1 SV=5	18	2.379	79.22
Q9BXW7	Haloacid dehalogenase-like hydrolase domain-containing 5 OS=Homo sapiens OX=9606 GN=HDHD5 PE=1 SV=1	14	3.569	79.11
Q5U0F4	Eukaryotic translation initiation factor 3 subunit I OS=Homo sapiens OX=9606 GN=EIF3S2 PE=2 SV=1	16	1.758	78.94
Q96A33	Coiled-coil domain-containing protein 47 OS=Homo sapiens OX=9606 GN=CCDC47 PE=1 SV=1	18	0.431	78.9
P50454	Serpin H1 OS=Homo sapiens OX=9606 GN=SERPINH1 PE=1 SV=2	16	2.104	78.85

A0A024R2Q4	Ribosomal protein L15 OS=Homo sapiens OX=9606 GN=RPL15 PE=3 SV=1	11	2.922	78.8
A8K401	Epididymis secretory sperm binding protein OS=Homo sapiens OX=9606 GN=PHB PE=2 SV=1	1	4.44	78.76
A0A1B0GUA3	KIF1-binding protein OS=Homo sapiens OX=9606 GN=KIF1BP PE=1 SV=1	22	2.353	78.64
Q05CW7	NAT10 protein (Fragment) OS=Homo sapiens OX=9606 GN=NAT10 PE=2 SV=1	1	2.02	78.45
A0A384NQ03	Epididymis secretory sperm binding protein OS=Homo sapiens OX=9606 PE=2 SV=1	14	1.794	78.44
B0AZS5	Kinesin-like protein OS=Homo sapiens OX=9606 PE=2 SV=1	18	2.125	78.34
P24928	DNA-directed RNA polymerase II subunit RPB1 OS=Homo sapiens OX=9606 GN=POLR2A PE=1 SV=2	26	2.312	78.27
B2RAM6	cDNA, FLJ95005, highly similar to Homo sapiens kinesin family member 11 (KIF11), mRNA	27	2.242	78.26
Q8NCK5	cDNA FLJ90195 fis, clone MAMMA1001310 OS=Homo sapiens OX=9606 PE=2 SV=1	11	2.384	78.23
A0A024RDW4	Uncharacterized protein OS=Homo sapiens OX=9606 GN=FLJ10154 PE=4 SV=1	23	0.87	78.12
Q96Q15	Serine/threonine-protein kinase SMG1 OS=Homo sapiens OX=9606 GN=SMG1 PE=1 SV=3	29	2.264	78.02
P62829	60S ribosomal protein L23 OS=Homo sapiens OX=9606 GN=RPL23 PE=1 SV=1	7	2.371	77.88
P23284	Peptidyl-prolyl cis-trans isomerase B OS=Homo sapiens OX=9606 GN=PPIB PE=1 SV=2	14	2.161	77.86
Q15813	Tubulin-specific chaperone E OS=Homo sapiens OX=9606 GN=TBCE PE=1 SV=1	23	2.308	77.83
Q9UNF1	Melanoma-associated antigen D2 OS=Homo sapiens OX=9606 GN=MAGED2 PE=1 SV=2	22	1.804	77.79
Q12904	Aminoacyl tRNA synthase complex-interacting multifunctional protein 1	14	1.536	77.69
Q9Y5A9	YTH domain-containing family protein 2 OS=Homo sapiens OX=9606 GN=YTHDF2 PE=1 SV=2	11	2.369	77.61
A0A024RAI1	ARP3 actin-related protein 3 homolog (Yeast), isoform CRA_a OS=Homo sapiens OX=9606 GN=ACTR3 PE=3 SV=1	16	2.689	77.58
A0A1B2JLU7	Pyrroline-5-carboxylate reductase OS=Homo sapiens OX=9606 GN=PYCR1 PE=3 SV=1	9	1.898	77.58
Q15417	Calponin-3 OS=Homo sapiens OX=9606 GN=CNN3 PE=1 SV=1	13	0.357	77.26
Q9UKY7	Protein CDV3 homolog OS=Homo sapiens OX=9606 GN=CDV3 PE=1 SV=1	12	0.406	77.09
Q53FE8	cDNA FLJ36526 fis, clone TRACH2003347, highly similar to NSFL1 cofactor p47 (Fragment)	15	0.505	77.09
B4DUP2	UTP--glucose-1-phosphate uridylyltransferase OS=Homo sapiens OX=9606 PE=2 SV=1	19	2.783	77.08
Q9BQ39	ATP-dependent RNA helicase DDX50 OS=Homo sapiens OX=9606 GN=DDX50 PE=1 SV=1	18	2.195	77.06
P52209	6-phosphogluconate dehydrogenase, decarboxylating OS=Homo sapiens OX=9606 GN=PGD PE=1 SV=3	17	2.671	77.03
Q15386	Ubiquitin-protein ligase E3C OS=Homo sapiens OX=9606 GN=UBE3C PE=1 SV=3	22	2.903	76.99
J3KQ32	Obg-like ATPase 1 OS=Homo sapiens OX=9606 GN=OLA1 PE=1 SV=1	16	2.289	76.96
A0A024R4X7	HCG1989366, isoform CRA_a OS=Homo sapiens OX=9606 GN=hCG_1989366 PE=4 SV=1	18	1.81	76.95
Q7Z3R8	DNA-directed RNA polymerase subunit beta OS=Homo sapiens OX=9606 GN=DKFZp686D10173 PE=2 SV=1	22	2.476	76.53
Q12905	Interleukin enhancer-binding factor 2 OS=Homo sapiens OX=9606 GN=ILF2 PE=1 SV=2	15	2.247	76.46
Q93034	Cullin-5 OS=Homo sapiens OX=9606 GN=CUL5 PE=1 SV=4	19	2.421	76.44
L7RRS0	Phosphatidylinositol-4-phosphate 3-kinase, catalytic subunit type 2 alpha OS=Homo sapiens OX=9606 GN=PIK3C2A	25	2.485	76.39
B4DZJ6	cDNA FLJ54706, highly similar to Ubiquitin-associated protein 2-like OS=Homo sapiens OX=9606 PE=2 SV=1	1		76.35
B4DU42	cDNA FLJ56153, highly similar to transforming growth factor beta regulator 4 (TBRG4), transcript variant 1, mRNA	22	2.507	76.32
Q9BTC0	Death-inducer obliterator 1 OS=Homo sapiens OX=9606 GN=DIDO1 PE=1 SV=5	26	2.239	76.27

Q9NZJ4	Sacsin OS=Homo sapiens OX=9606 GN=SACS PE=1 SV=2	30	2.045	76.22
Q9UHD8	Septin-9 OS=Homo sapiens OX=9606 GN=SEPTIN9 PE=1 SV=2	21	2.105	75.98
O00178	GTP-binding protein 1 OS=Homo sapiens OX=9606 GN=GTPBP1 PE=1 SV=3	17	2.702	75.86
O00232	26S proteasome non-ATPase regulatory subunit 12 OS=Homo sapiens OX=9606 GN=PSMD12 PE=1 SV=3	18	2.028	75.67
V9HW74	Ubiquitin carboxyl-terminal hydrolase OS=Homo sapiens OX=9606 GN=HEL-117 PE=2 SV=1	12	2.7	75.65
O00299	Chloride intracellular channel protein 1 OS=Homo sapiens OX=9606 GN=CLIC1 PE=1 SV=4	12	2.565	75.46
Q8IWX8	Calcium homeostasis endoplasmic reticulum protein OS=Homo sapiens OX=9606 GN=CHERP PE=1 SV=3	19	2.12	75.46
A0A0A0MRA8	Band 4.1-like protein 3 OS=Homo sapiens OX=9606 GN=EPB41L3 PE=1 SV=1	16	1.007	75.29
Q8TA92	Similar to AFG3 ATPase family gene 3-like 2 (Yeast) (Fragment) OS=Homo sapiens OX=9606 PE=2 SV=1	23	1.686	75.02
A8K0P8	cDNA FLJ78223 OS=Homo sapiens OX=9606 PE=2 SV=1	23	2.863	75.01
Q86WJ1	Chromodomain-helicase-DNA-binding protein 1-like OS=Homo sapiens OX=9606 GN=CHD1L PE=1 SV=3	24	2.361	75.01

References

Aggarwal, A., Iemma, T.L., Shih, I., Newsome, T.P., McAllery, S., Cunningham, A.L. and Turville, S.G. 2012. Mobilization of HIV spread by diaphanous 2 dependent filopodia in infected dendritic cells. *PLoS Pathogens*. **8**(6).

Al-Shamahy, H.A., Sunhope, A. and Al-Moyed, K.A. 2013. Prevalence of rabies in various species in Yemen and risk factors contributing to the spread of the disease. *Sultan Qaboos University Medical Journal*. **13**(3), pp.404–410.

Albertini, A.A. V., Baquero, E., Ferlin, A. and Gaudin, Y. 2012. Molecular and Cellular Aspects of Rhabdovirus Entry. *Viruses*. **4**(1), pp.117–139.

Albertini, A.A.V., Ruigrok, R.W.H. and Blondel, D. 2011. *Rabies Virus Transcription and Replication*. Academic Press.

Albertini, A.A.V., Wernimont, A.K., Muziol, T., Ravelli, R.B.G., Clapier, C.R., Schoehn, G., Weissenhorn, W. and Ruigrok, R.W.H. 2006. Crystal structure of the rabies virus nucleoprotein-RNA complex. *Science*. **313**(5785), pp.360–363.

Alieva, N.O., Efremov, A.K., Hu, S., Oh, D., Chen, Z., Natarajan, M., Ong, H.T., Jégou, A., Romet-Lemonne, G., Groves, J.T., Sheetz, M.P., Yan, J. and Bershadsky, A.D. 2019. Myosin IIA and formin dependent mechanosensitivity of filopodia adhesion. *Nature Communications*. **10**(1), pp.1–14.

Amarasinghe, G.K., Aréchiga Ceballos, N.G., Banyard, A.C., ... and Kuhn, J.H. 2018. Taxonomy of the order Mononegavirales: update 2018. *Archives of Virology*. **163**(8), pp.2283–2294.

Anilionis, A., Wunner, W.H. and Curtis, P.J. 1982. Amino acid sequence of the rabies virus glycoprotein deduced from its cloned gene. *Comparative Immunology, Microbiology and Infectious Diseases*. **5**(1–3), pp.27–32.

Anilionis, A., Wunner, W.H. and Curtis, P.J. 1981. Structure of the glycoprotein gene in rabies virus. *Nature*. **294**(5838), pp.275–278.

Arii, J., Hirohata, Y., Kato, A. and Kawaguchi, Y. 2015. Nonmuscle Myosin Heavy Chain IIB Mediates Herpes Simplex Virus 1 Entry. *Journal of*

Virology. **89**(3), pp.1879–1888.

Atanasiu, P., Tsiang, H. and Gamet, A. 1974. NOUVEAU VACCIN ANTIRABIQUE HUMAIN DE CULTURE CELLULAIRE PRIMAIRE. *COLLECT.ANN.INST.PASTEUR*. **125 B**(3), pp.419–432.

Badrane, H., Bahloul, C., Perrin, P. and Tordo, N. 2001. Evidence of Two Lyssavirus Phylogroups with Distinct Pathogenicity and Immunogenicity. *Journal of Virology*. **75**(7), pp.3268–3276.

Badrane, H. and Tordo, N. 2001. Host Switching in Lyssavirus History from the Chiroptera to the Carnivora Orders. *Journal of Virology*. **75**(17), pp.8096–8104.

Baer, G.M. 2007. The History of Rabies *In*: *Rabies*. Elsevier Ltd, pp.1–22.

Baer, G.M. and Fishbein, D.B. 1987. Rabies Post-Exposure Prophylaxis. *New England Journal of Medicine*. **316**(20), pp.1270–1272.

Baquero, E., Albertini, A.A., Raux, H., Abou-Hamdan, A., Boeri-Erba, E., Ouldali, M., Buonocore, L., Rose, J.K., Lepault, J., Bressanelli, S. and Gaudin, Y. 2017. Structural intermediates in the fusion-associated transition of vesiculovirus glycoprotein. *The EMBO Journal*. **36**(5), pp.679–692.

Barr, J.N., Whelan, S.P. and Wertz, G.W. 1997. cis-Acting signals involved in termination of vesicular stomatitis virus mRNA synthesis include the conserved AUAC and the U7 signal for polyadenylation. *Journal of Virology*. **71**(11), pp.8718–8725.

Barr, J.N., Whelan, S.P.J. and Wertz, G.W. 2002. Transcriptional control of the RNA-dependent RNA polymerase of vesicular stomatitis virus. *Biochimica et Biophysica Acta - Gene Structure and Expression*. **1577**(2), pp.337–353.

Beier, K.T., Saunders, A.B., Oldenburg, I.A., Sabatini, B.L. and Cepko, C.L. 2013. Vesicular stomatitis virus with the rabies virus glycoprotein directs retrograde transsynaptic transport among neurons in vivo. *Frontiers in Neural Circuits*. **7**(JAN).

Benmansour, A., Leblois, H., Coulon, P., Tuffereau, C., Gaudin, Y., Flamand, A. and Lafay, F. 1991. Antigenicity of rabies virus glycoprotein. *Journal of Virology*. **65**(8), pp.4198–4203.

Bhattacharya, J., Peters, P.J. and Clapham, P.R. 2004. Human Immunodeficiency Virus Type 1 Envelope Glycoproteins That Lack Cytoplasmic Domain Cysteines: Impact on Association with Membrane Lipid Rafts and Incorporation onto Budding Virus Particles. *Journal of Virology*. **78**(10), pp.5500–5506.

Bienkowska-Haba, M. and Sapp, M. 2011. The cytoskeleton in papillomavirus infection. *Viruses*. **3**(3), pp.260–271.

Bijlenga, G. and Heaney, T. 1978. Post-exposure Local Treatment of Mice Infected with Rabies with Two Axonal Flow Inhibitors, Colchicine and Vinblastine. *Journal of General Virology*. **39**(2), pp.381–385.

Blaskovic, S., Blanc, M. and Van Der Goot, F.G. 2013. What does S-palmitoylation do to membrane proteins? *FEBS Journal*. **280**(12), pp.2766–2774.

Bonifacino, J.S. and Glick, B.S. 2004. The Mechanisms of Vesicle Budding and Fusion. *Cell*. **116**(2), pp.153–166.

Bourhy, H., Goudal, M., Mailles, A., Sadkowska-Todys, M., Dacheux, L. and Zeller, H. 2009. Is there a need for anti-rabies vaccine and immunoglobulins rationing in Europe? *Euro surveillance : bulletin européen sur les maladies transmissibles = European communicable disease bulletin*. **14**(13), p.19166.

Brandizzi, F. and Barlowe, C. 2013. Organization of the ER-Golgi interface for membrane traffic control. *Nature Reviews Molecular Cell Biology*. **14**(6), pp.382–392.

von Bredow, B., Arias, J.F., Heyer, L.N., Gardner, M.R., Farzan, M., Rakasz, E.G. and Evans, D.T. 2015. Envelope Glycoprotein Internalization Protects Human and Simian Immunodeficiency Virus-Infected Cells from Antibody-Dependent Cell-Mediated Cytotoxicity. *Journal of Virology*. **89**(20), pp.10648–10655.

Bronnert, J., Wilde, H., Tepsumethanon, V., Lumlertdacha, B. and Hemachudha, T. 2007. Organ Transplantations and Rabies Transmission: Table 1. *Journal of Travel Medicine*. **14**(3), pp.177–180.

Brown, E.L. and Lyles, D.S. 2003. A novel method for analysis of membrane microdomains: Vesicular stomatitis virus glycoprotein microdomains change in size during infection, and those outside of budding sites resemble sites of virus budding. *Virology*. **310**(2), pp.343–358.

Brusés, J.L., Chauvet, N. and Rutishauser, U. 2001. Membrane lipid rafts are necessary for the maintenance of the α7 nicotinic acetylcholine receptor in somatic spines of ciliary neurons. *Journal of Neuroscience*. **21**(2), pp.504–512.

Bu, Z., Ye, L., Vzorov, A., Taylor, D., Compans, R.W. and Yang, C. 2004. Enhancement of immunogenicity of an HIV Env DNA vaccine by mutation of the Tyr-based endocytosis motif in the cytoplasmic domain. *Virology*. **328**(1), pp.62–73.

Burrage, T.G., Tignor, G.H. and Smith, A.L. 1985. Rabies virus binding at neuromuscular junctions. *Virus Research*. **2**(3), pp.273–289.

Caballero, M., Carabaña, J., Ortego, J., Fernández-Muñoz, R. and Celma, M.L. 1998. Measles virus fusion protein is palmitoylated on transmembrane-intracytoplasmic cysteine residues which participate in cell fusion. *Journal of virology*. **72**(10), pp.8198–204.

Cai, Qingxian, Yang, M., Liu, D., Chen, J., Shu, D., Xia, J., Liao, X., Gu, Y., Cai, Qiue, Yang, Y., Shen, C., Li, X., Peng, L., Huang, D., Zhang, J., Zhang, S., Wang, F., Liu, J., Chen, L., Chen, S., Wang, Z., Zhang, Z., Cao, R., Zhong, W., Liu, Y. and Liu, L. 2020. Experimental Treatment with Favipiravir for COVID-19: An Open-Label Control Study. *Engineering*.

Caillet-Saguy, C., Maisonneuve, P., Delhommel, F., Buc, H., Lafon, M., Delepierre, M., Cordier, F. and Wolff, N. 2016. Pleiotropic Role Played by the PDZ Domain in Neuronal Signaling Pathways. *Biophysical Journal*. **110**(3), p.362a.

De Camilli, P. and Takei, K. 1996. Molecular mechanisms in synaptic vesicle endocytosis and recycling. *Neuron*. **16**(3), pp.481–486.

Castellanos, J.E., Castañeda, D.R., Velandia, A.E. and Hurtado, H. 1997. Partial inhibition of the in vitro infection of adult mouse dorsal root ganglion neurons by rabies virus using nicotinic antagonists. *Neuroscience Letters*. **229**(3), pp.198–200.

Ceccaldi, P.E., Fayet, J., Conzelmann, K.K. and Tsiang, H. 1998. Infection characteristics of rabies virus variants with deletion or insertion in the pseudogene sequence. *Journal of NeuroVirology*. **4**(1), pp.115–119.

Ceccaldi, P.E., Gillet, J.P. and Tsiang, H. 1989. Inhibition of the Transport of Rabies Virus in the Central Nervous System. *Journal of Neuropathology*

& Experimental Neurology. **48**(6), pp.620–630.

Ceccaldi, P.E., Valtorta, F., Braud, S., Hellio, R. and Tsiang, H. 1997. Alteration of the actin-based cytoskeleton by rabies virus. *Journal of General Virology*. **78**(11), pp.2831–2835.

Cenna, J., Hunter, M., Tan, G.S., Papaneri, A.B., Ribka, E.P., Schnell, M.J., Marx, P.A. and McGettigan, J.P. 2009. Replication-Deficient Rabies Virus–Based Vaccines Are Safe and Immunogenic in Mice and Nonhuman Primates. *The Journal of Infectious Diseases*. **200**(8), pp.1251–1260.

Cenna, J., Tan, G.S., Papaneri, A.B., Dietzschold, B., Schnell, M.J. and McGettigan, J.P. 2008. Immune modulating effect by a phosphoprotein-deleted rabies virus vaccine vector expressing two copies of the rabies virus glycoprotein gene. *Vaccine*. **26**(50), pp.6405–6414.

Chan, W.-E., Lin, H.-H. and Chen, S.S.-L. 2005. Wild-Type-Like Viral Replication Potential of Human Immunodeficiency Virus Type 1 Envelope Mutants Lacking Palmitoylation Signals. *Journal of Virology*. **79**(13), pp.8374–8387.

Chang, K., Baginski, J., Hassan, S.F., Volin, M., Shukla, D. and Tiwari, V. 2016. Filopodia and viruses: An analysis of membrane processes in entry mechanisms. *Frontiers in Microbiology*. **7**(MAR), p.300.

Charrin, S., Latil, M., Soave, S., Polesskaya, A., Chrétien, F., Boucheix, C. and Rubinstein, E. 2013. Normal muscle regeneration requires tight control of muscle cell fusion by tetraspanins CD9 and CD81. *Nature Communications*. **4**(1), pp.1–12.

Chatterjee, S., Sullivan, H.A., MacLennan, B.J., Xu, R., Hou, Y.Y., Lavin, T.K., Lea, N.E., Michalski, J.E., Babcock, K.R., Dietrich, S., Matthews, G.A., Beyeler, A., Calhoon, G.G., Glober, G., Whitesell, J.D., Yao, S., Cetin, A., Harris, J.A., Zeng, H., Tye, K.M., Reid, R.C. and Wickersham, I.R. 2018. Nontoxic, double-deletion-mutant rabies viral vectors for retrograde targeting of projection neurons. *Nature Neuroscience*. **21**(4), pp.638–646.

Chen, B.J., Takeda, M. and Lamb, R.A. 2005. Influenza Virus Hemagglutinin (H3 Subtype) Requires Palmitoylation of Its Cytoplasmic Tail for Assembly: M1 Proteins of Two Subtypes Differ in Their Ability To Support Assembly. *Journal of Virology*. **79**(21), pp.13673–13684.

Chenik, M., Schnell, M., Conzelmann, K.K. and Blondel, D. 1998. Mapping the interacting domains between the rabies virus polymerase and phosphoprotein. *Journal of virology*. **72**(3), pp.1925–1930.

Cho, Y.Y., Kwon, O.H., Park, M.K., Kim, T.W. and Chung, S. 2019. Elevated cellular cholesterol in Familial Alzheimer's presenilin 1 mutation is associated with lipid raft localization of β-amyloid precursor protein M. K. Lakshmana, ed. *PLoS ONE*. **14**(1), p.e0210535.

Chulasugandha, P., Khawplod, P., Havanond, P. and Wilde, H. 2006. Cost comparison of rabies pre-exposure vaccination with post-exposure treatment in Thai children. *Vaccine*. **24**(9), pp.1478–1482.

Constantine, D. 1967. *Rabies transmission by air in bat caves*. Atlanta: National Communicable Disease Center; [for sale by the Supt. of Docs. U.S. Govt. Print. Off.

Conzelmann, K.-K.K., Cox, J.H., Schneider, L.G. and Thiel, H.-J.J. 1990. Molecular cloning and complete nucleotide sequence of the attenuated rabies virus SAD B19. *Virology*. **175**(2), pp.485–499.

Coyaud, E., Ranadheera, C., Cheng, D., Gonçalves, J., Dyakov, B.J.A., Laurent, E.M.N., St-Germain, J., Pelletier, L., Gingras, A.C., Brumell, J.H., Kim, P.K., Safronetz, D. and Raught, B. 2018. Global interactomics uncovers extensive organellar targeting by Zika Virus. *Molecular and Cellular Proteomics*. **17**(11), pp.2242–2255.

Dacheux, L., Larrous, F., Mailles, A., Boisseleau, D., Delmas, O., Biron, C., Bouchier, C., Capek, I., Muller, M., Ilari, F., Lefranc, T., Raffi, F., Goudal, M. and Bourhy, H. 2009. European bat lyssavirus transmission among cats, Europe. *Emerging Infectious Diseases*. **15**(2), pp.280–284.

Davis, B.M., Rall, G.F. and Schnell, M.J. 2015. Everything You Always Wanted to Know About Rabies Virus (But Were Afraid to Ask). *Annual Review of Virology*. **2**(1), pp.451–471.

Dechant, G. and Barde, Y.-A. 2002. The neurotrophin receptor p75NTR: novel functions and implications for diseases of the nervous system. *Nature neuroscience*. **5**(11), pp.1131–1136.

Deinhardt, K., Reversi, A., Berninghausen, O., Hopkins, C.R. and Schiavo, G. 2007. Neurotrophins Redirect p75 ^{NTR} from a Clathrin-Independent to a Clathrin-Dependent Endocytic Pathway Coupled to Axonal Transport. *Traffic*. **8**(12), pp.1736–1749.

Descamps, V., Helle, F., Louandre, C., Martin, E., Brochot, E., Izquierdo, L., Fournier, C., Hoffmann, T.W., Castelain, S., Duverlie, G., Galmiche, A. and François, C. 2015. The kinase-inhibitor sorafenib inhibits multiple steps of the Hepatitis C Virus infectious cycle in vitro. *Antiviral Research*. **118**, pp.93–102.

Dhingra, V., Li, X., Liu, Y. and Fu, Z.F. 2007. Proteomic profiling reveals that rabies virus infection results in differential expression of host proteins involved in ion homeostasis and synaptic physiology in the central nervous system. *Journal of neurovirology*. **13**(2), pp.107–117.

Dietzschold, B., Li, J., Faber, M. and Schnell, M. 2008. Concepts in the pathogenesis of rabies. *Future Virology*. **3**(5), pp.481–490.

Dietzschold, B., Wunner, W.H., Wiktor, T.J., Lopes, A.D., Lafon, M., Smith, C.L. and KoPROWSKI, H. 1983. Characterization of an antigenic determinant of the glycoprotein that correlates with pathogenicity of rabies virus. *Proceedings of the National Academy of Sciences*. **80**(1), pp.70–74.

Doggrell, S.A. 2005. Rho-kinase inhibitors show promise in pulmonary hypertension. *Expert Opinion on Investigational Drugs*. **14**(9), pp.1157–1159.

Doherty, G.J. and McMahon, H.T. 2008. Mediation, Modulation, and Consequences of Membrane-Cytoskeleton Interactions. *Annual Review of Biophysics*. **37**(1), pp.65–95.

Dutertre, S., Nicke, A. and Tsetlin, V.I. 2017. Nicotinic acetylcholine receptor inhibitors derived from snake and snail venoms. *Neuropharmacology*. **127**, pp.196–223.

Dwane, S., Durack, E. and Kiely, P.A. 2013. Optimising parameters for the differentiation of SH-SY5Y cells to study cell adhesion and cell migration. *BMC Research Notes*. **6**(1), p.366.

Dykes, S.S., Steffan, J.J. and Cardelli, J.A. 2017. Lysosome trafficking is necessary for EGF-driven invasion and is regulated by p38 MAPK and Na+/H+ exchangers. *BMC Cancer*. **17**(1).

Engel, S., Scolari, S., Thaa, B., Krebs, N., Korte, T., Herrmann, A., Veit, M. and Scolari, S. 2010. FLIM-FRET and FRAP reveal association of influenza virus haemagglutinin with membrane rafts. *Biochemical Journal*. **425**(3), pp.567–573.

Essuman, K., Summers, D.W., Sasaki, Y., Mao, X., DiAntonio, A. and Milbrandt, J. 2017. The SARM1 Toll/Interleukin-1 Receptor Domain Possesses Intrinsic NAD+ Cleavage Activity that Promotes Pathological Axonal Degeneration. *Neuron*. **93**(6), pp.1334-1343.e5.

Etessami, R., Conzelmann, K.-K.K., Fadai-Ghotbi, B., Natelson, B., Tsiang, H. and Ceccaldi, P.-E.E. 2000. Spread and pathogenic characteristics of a G-deficient rabies virus recombinant: an in vitro and in vivo study. *Journal of General Virology*. **81**(9), pp.2147–2153.

Faber, M., Faber, M.-L., Papaneri, A., Bette, M., Weihe, E., Dietzschold, B. and Schnell, M.J. 2005. A single amino acid change in rabies virus glycoprotein increases virus spread and enhances virus pathogenicity. *Journal of virology*. **79**(22), pp.14141–8.

Faber, M., Li, J., Kean, R.B., Hooper, D.C., Alugupalli, K.R. and Dietzschold, B. 2009. Effective preexposure and postexposure prophylaxis of rabies with a highly attenuated recombinant rabies virus. *Proceedings of the National Academy of Sciences of the United States of America*. **106**(27), pp.11300–11305.

Faber, M., Pulmanausahakul, R., Hodawadekar, S.S., Spitsin, S., McGettigan, J.P., Schnell, M.J. and Dietzschold, B. 2002. Overexpression of the rabies virus glycoprotein results in enhancement of apoptosis and antiviral immune response. *Journal of virology*. **76**(7), pp.3374–3381.

Faber, M., Pulmanausahakul, R., Nagao, K., Prosniak, M., Rice, A.B., Koprowski, H., Schnell, M.J. and Dietzschold, B. 2004. Identification of viral genomic elements responsible for rabies virus neuroinvasiveness. *Proceedings of the National Academy of Sciences of the United States of America*. **101**(46), pp.16328–16332.

Farzad, R., Gholami, A., Hayati-Roodbari, N. and Shahbazzadeh, D. 2020. The anti-rabies activity of Caspian cobra venom. *Toxicon*.

Favoreel, H.W., Van Minnebruggen, G., Nauwynck, H.J., Enquist, L.W. and Pensaert, M.B. 2002. A Tyrosine-Based Motif in the Cytoplasmic Tail of Pseudorabies Virus Glycoprotein B Is Important for both Antibody-Induced Internalization of Viral Glycoproteins and Efficient Cell-to-Cell Spread. *Journal of Virology*. **76**(13), pp.6845–6851.

Favoreel, H.W., Van Minnebruggen, G., Van De Walle, G.R., Ficinska, J. and Nauwynck, H.J. 2006. Herpesvirus interference with virus-specific antibodies: Bridging antibodies, internalizing antibodies, and hiding from

antibodies *In*: *Veterinary Microbiology*. Elsevier, pp.257–263.

Fertuck, H.C. and Salpeter, M.M. 1974. Localization of acetylcholine receptor by 125I labeled α bungarotoxin binding at mouse motor endplates. *Proceedings of the National Academy of Sciences of the United States of America*. **71**(4), pp.1376–1378.

Ficinska, J., Van Minnebruggen, G., Nauwynck, H.J., Bienkowska-Szewczyk, K. and Favoreel, H.W. 2005. Pseudorabies Virus Glycoprotein gD Contains a Functional Endocytosis Motif That Acts in Concert with an Endocytosis Motif in gB To Drive Internalization of Antibody-Antigen Complexes from the Surface of Infected Monocytes. *Journal of Virology*. **79**(11), pp.7248–7254.

Finke, S., Brzozka, K., Conzelmann, K.-K.K., Brzózka, K. and Conzelmann, K.-K.K. 2004. Tracking fluorescence-labeled rabies virus: enhanced green fluorescent protein-tagged phosphoprotein P supports virus gene expression and formation of infectious particles. *J Virol*. **78**(22), pp.12333–12343.

Finke, S. and Conzelmann, K.-K.K. 2003. Dissociation of rabies virus matrix protein functions in regulation of viral RNA synthesis and virus assembly. *J Virol*. **77**(22), pp.12074–12082.

Finke, S. and Conzelmann, K.K. 2005. Replication strategies of rabies virus. *Virus Res*. **111**(2), pp.120–131.

Finke, S., Cox, J.H. and Conzelmann, K.K. 2000. Differential transcription attenuation of rabies virus genes by intergenic regions: generation of recombinant viruses overexpressing the polymerase gene. *J Virol*. **74**(16), pp.7261–7269.

Finke, S., Mueller-Waldeck, R. and Conzelmann, K.K. 2003. Rabies virus matrix protein regulates the balance of virus transcription and replication. *J Gen Virol*. **84**(Pt 6), pp.1613–1621.

Fisher, C.R., Streicker, D.G. and Schnell, M.J. 2018. The spread and evolution of rabies virus: Conquering new frontiers. *Nature Reviews Microbiology*. **16**(4), pp.241–255.

Fooks, A.R., Banyard, A.C. and Ertl, H.C.J. 2019. New human rabies vaccines in the pipeline. *Vaccine*. **37**, pp.A140–A145.

Fooks, A.R., Banyard, A.C., Horton, D.L., Johnson, N., McElhinney, L.M. and Jackson, A.C. 2014. Current status of rabies and prospects for elimination. *The Lancet*. **384**(9951), pp.1389–1399.

Fox, J.P., Koprowski, H., Conwell, D.P., Black, J. and Gelfand, H.M. 1957. Study of antirabies immunization of man; observations with HEP Flury and other vaccines, with and without hyperimmune serum, in primary and recall immunizations. *Bulletin of the World Health Organization*. **17**(6), pp.869–904.

Fu, Z.F. and Jackson, A.C. 2005. Neuronal dysfunction and death in rabies virus infection. *Journal of NeuroVirology*. **11**(1), pp.101–106.

Fuller, J., Álvarez-Rodríguez, B., Todd, E.J.A.A., Mankouri, J., Hewson, R. and Barr, J.N. 2020. Hazara Nairovirus Requires COPI Components in both Arf1-Dependent and Arf1-Independent Stages of Its Replication Cycle. *Journal of Virology*. **94**(17).

Gadalla, M.R. and Veit, M. 2020. Toward the identification of ZDHHC enzymes required for palmitoylation of viral protein as potential drug targets. *Expert Opinion on Drug Discovery*. **15**(2), pp.159–177.

Gao, J., Wang, X., Zhao, M., Liu, E., Duan, M., Guan, Z., Guo, Y. and Zhang, M. 2019. Entry of Challenge Virus Standard (CVS)-11 into N2a cells via a clathrin-mediated, cholesterol-, dynamin-, pH-dependent endocytic pathway. *Virology Journal*. **16**(1), pp.1–12.

Gao, M., Duan, H., Liu, J., Zhang, H., Wang, X., Zhu, M., Guo, J., Zhao, Z., Meng, L. and Peng, Y. 2014. The multi-targeted kinase inhibitor sorafenib inhibits enterovirus 71 replication by regulating IRES-dependent translation of viral proteins. *Antiviral Research*. **106**(1), pp.80–85.

Gastka, M., Horvath, J. and Lentz, T.L. 1996. Rabies virus binding to the nicotinic acetylcholine receptor α subunit demonstrated by virus overlay protein binding assay. *Journal of General Virology*. **77**(10), pp.2437–2440.

Gaucherand, L., Porter, B.K., Levene, R.E., Price, E.L., Schmaling, S.K., Rycroft, C.H., Kevorkian, Y., McCormick, C., Khaperskyy, D.A. and Gaglia, M.M. 2019. The Influenza A Virus Endoribonuclease PA-X Usurps Host mRNA Processing Machinery to Limit Host Gene Expression. *Cell Reports*. **27**(3), pp.776-792.e7.

Gaudin, Y. 1997. Folding of rabies virus glycoprotein: epitope acquisition and interaction with endoplasmic reticulum chaperones. *Journal of Virology*. **71**(5), pp.3742–3750.

Gaudin, Y. 2000. Rabies virus-induced membrane fusion pathway. *The Journal of Cell Biology*. **150**(3), pp.601–612.

Gaudin, Y., Moreira, S., Benejean, J., Blondel, D., Flamand, A. and Tuffereau, C. 1999. Soluble ectodomain of rabies virus glycoprotein expressed in eukaryotic cells folds in a monomeric conformation that is antigenically distinct from the native state of the complete, membrane-anchored glycoprotein. *Journal of General Virology* **80 (Pt 7)**, pp.1647–1656.

Gaudin, Y., Ruigrok, R.W., Knossow, M. and Flamand, A. 1993. Low-pH conformational changes of rabies virus glycoprotein and their role in membrane fusion. *Journal of Virology*. **67**(3), pp.1365–1372.

Gaudin, Y., Ruigrok, R.W.H., Tuffereau, C., Knossow, M. and Flamand, A. 1992. Rabies virus glycoprotein is a trimer. *Virology*. **187**(2), pp.627–632.

Gaudin, Y., Tuffereau, C., Benmansour, A. and Flamand, A. 1991. Fatty acylation of rabies virus proteins. *Virology*. **184**(1), pp.441–444.

Gaudin, Y., Tuffereau, C., Durrer, P., Flamand, A. and Ruigrok, R.W. 1995. Biological function of the low-pH, fusion-inactive conformation of rabies virus glycoprotein (G): G is transported in a fusion-inactive state-like conformation. *Journal of virology*. **69**(9), pp.5528–5534.

Gaudin, Y. and Whitt, M.A. 2014. Rhabdovirus glycoproteins *In*: *Biology and Pathogenesis of Rhabdo- and Filoviruses*. World Scientific Publishing Co., pp.49–73.

Ge, P., Tsao, J., Schein, S., Green, T.J., Luo, M. and Zhou, Z.H. 2010. Cryo-EM model of the bullet-shaped vesicular stomatitis virus. *Science*. **327**(5966), pp.689–693.

Geue, L., Schares, S., Schnick, C., Kliemt, J., Beckert, A., Freuling, C., Conraths, F.J., Hoffmann, B., Zanoni, R., Marston, D., McElhinney, L., Johnson, N., Fooks, A.R., Tordo, N. and Müller, T. 2008. Genetic characterisation of attenuated SAD rabies virus strains used for oral vaccination of wildlife. *Vaccine*. **26**(26), pp.3227–3235.

Gluska, S., Zahavi, E.E., Chein, M., Gradus, T., Bauer, A., Finke, S. and Perlson, E. 2014. Rabies Virus Hijacks and accelerates the p75NTR retrograde axonal transport machinery. *PLoS Pathog*. **10**(8), p.e1004348.

Goldhill, D.H., Langat, P., Xie, H., Galiano, M., Miah, S., Kellam, P., Zambon, M., Lackenby, A. and Barclay, W.S. 2018. Determining the Mutation Bias of Favipiravir in Influenza Virus Using Next-Generation Sequencing. *Journal of Virology*. **93**(2).

González, S.A., Paladino, M.G. and Affranchino, J.L. 2012. Palmitoylation of the feline immunodeficiency virus envelope glycoprotein and its effect on fusion activity and envelope incorporation into virions. *Virology*. **428**(1), pp.1–10.

Graham, S.C., Assenberg, R., Delmas, O., Verma, A., Gholami, A., Talbi, C., Owens, R.J., Stuart, D.I., Grimes, J.M. and Bourhy, H. 2008. Rhabdovirus Matrix Protein Structures Reveal a Novel Mode of Self-Association D. Lyles, ed. *PLoS Pathogens*. **4**(12), p.e1000251.

Gravotta, D., Bay, A.P., Jonker, C.T.H., Zager, P.J., Benedicto, I., Schreiner, R., Caceres, P.S. and Rodriguez-Boulan, E. 2019. Clathrin and clathrin adaptor AP-1 control apical trafficking of megalin in the biosynthetic and recycling routes. *Molecular Biology of the Cell*. **30**(14), pp.1716–1728.

Griffin, D.E., Lin, W.H. and Pan, C.H. 2012. Measles virus, immune control, and persistence. *FEMS Microbiology Reviews*. **36**(3), pp.649–662.

Guo, Y., Duan, M., Wang, X., Gao, J., Guan, Z. and Zhang, M. 2019. Early events in rabies virus infection—Attachment, entry, and intracellular trafficking. *Virus Research*. **263**(September 2018), pp.217–225.

Hampson, K., Dobson, A., Kaare, M., Dushoff, J., Magoto, M., Sindoya, E. and Cleaveland, S. 2008. Rabies exposures, post-exposure prophylaxis and deaths in a region of endemic canine rabies. *PLoS Neglected Tropical Diseases*. **2**(11), p.e339.

Hanahan, D. 1983. Studies on transformation of Escherichia coli with plasmids. *Journal of Molecular Biology*. **166**(4), pp.557–580.

Harmon, S.A., Robinson, E.N. and Summers, D.F. 1985. Ultrastructural localization of L and NS enzyme subunits on vesicular stomatitis virus RNPs using gold sphere-staphylococcal protein A-monospecific IgG conjugates. *Virology*. **142**(2), pp.406–410.

Hellert, J., Buchrieser, J., Larrous, F., Minola, A., de Melo, G.D., Soriaga, L., England, P., Haouz, A., Telenti, A., Schwartz, O., Corti, D., Bourhy, H. and Rey, F.A. 2020. Structure of the prefusion-locking broadly neutralizing antibody RVC20 bound to the rabies virus glycoprotein. *Nature Communications*. **11**(1), pp.1–8.

Hemachudha, T., Phanuphak, P., Sriwanthana, B., Manutsathit, S., Phanthumchinda, K., Siriprasomsup, W., Ukachoke, C., Rasameechan, S. and Kaoroptham, S. 1988. Immunologic study of human encephalitic and paralytic rabies. Preliminary report of 16 patients. *The American Journal of Medicine*. **84**(4), pp.673–677.

Hemachudha, T., Ugolini, G., Wacharapluesadee, S., Sungkarat, W., Shuangshoti, S. and Laothamatas, J. 2013. Human rabies: neuropathogenesis, diagnosis, and management. *The Lancet Neurology*. **12**(5), pp.498–513.

Hemachudha, T., Wacharapluesadee, S., Lumlertdaecha, B., Orciari, L.A., Rupprecht, C.E., La-ongpant, M., Juntrakul, S. and Denduangboripant, J. 2003. Sequence Analysis of Rabies Virus in Humans Exhibiting Encephalitic or Paralytic Rabies. *The Journal of Infectious Diseases*. **188**(7), pp.960–966.

Hicks, D.J., Fooks, A.R. and Johnson, N. 2012. Developments in rabies vaccines. *Clinical and Experimental Immunology*. **169**(3), pp.199–204.

Hoffmann, E., Krauss, S., Perez, D., Webby, R. and Webster, R.G. 2002. Eight-plasmid system for rapid generation of influenza virus vaccines. *Vaccine*. **20**(25–26), pp.3165–3170.

Holthusen, K., Talaty, P. and Everly, D.N. 2015. Regulation of Latent Membrane Protein 1 Signaling through Interaction with Cytoskeletal Proteins. *Journal of Virology*. **89**(14), pp.7277–7290.

Hotta, K., Bazartseren, B., Kaku, Y., Noguchi, A., Okutani, A., Inoue, S. and Yamada, A. 2009. Effect of cellular cholesterol depletion on rabies virus infection. *Virus Research*. **139**(1), pp.85–90.

Huang, C.S., Zhou, J., Feng, A.K., Lynch, C.C., Klumperman, J., DeArmond, S.J. and Mobley, W.C. 1999. Nerve growth factor signaling in caveolae-like domains at the plasma membrane. *Journal of Biological Chemistry*. **274**(51), pp.36707–36714.

Hueffer, K., Khatri, S., Rideout, S., Harris, M.B., Papke, R.L., Stokes, C. and

Schulte, M.K. 2017. Rabies virus modifies host behaviour through a snake-toxin like region of its glycoprotein that inhibits neurotransmitter receptors in the CNS. *Scientific Reports*. **7**(1).

Hummeler, K., Koprowski, H. and Wiktor, T.J. 1967. Structure and Development of Rabies Virus in Tissue Culture. *Journal of Virology*. **1**(1), pp.152–170.

Ilinskaya, A., Heidecker, G. and Derse, D. 2010. Opposing Effects of a Tyrosine-Based Sorting Motif and a PDZ-Binding Motif Regulate Human T-Lymphotropic Virus Type 1 Envelope Trafficking. *Journal of Virology*. **84**(14), pp.6995–7004.

Ito, N., Kakemizu, M., Ito, K.A., Yamamoto, A., Yoshida, Y., Sugiyama, M. and Minamoto, N. 2001. A Comparison of Complete Genome Sequences of the Attenuated RC-HL Strain of Rabies Virus Used for Production of Animal Vaccine in Japan, and the Parental Nishigahara Strain. *Microbiology and Immunology*. **45**(1), pp.51–58.

Ito, N., Takayama, M., Yamada, K., Sugiyama, M. and Minamoto, N. 2001. Rescue of Rabies Virus from Cloned cDNA and Identification of the Pathogenicity-Related Gene: Glycoprotein Gene Is Associated with Virulence for Adult Mice. *Journal of Virology*. **75**(19), pp.9121–9128.

Jaarsma, D. and Hoogenraad, C.C. 2015. Cytoplasmic dynein and its regulatory proteins in Golgi pathology in nervous system disorders. *Frontiers in Neuroscience*. **9**(OCT), p.397.

Jovic, M., Sharma, M., Rahajeng, J. and Caplan, S. 2010. The early endosome: A busy sorting station for proteins at the crossroads. *Histology and Histopathology*. **25**(1), pp.99–112.

Kim, D., Jensen, S., Noble, K., Kc, B., Roux, K.H., Motamedchaboki, K. and Roux, K.J. 2016. An improved smaller biotin ligase for BioID proximity labeling Y. Zheng, ed. *Molecular biology of the cell*. **27**(8), pp.1188–1196.

Kim, M.D., Kolodziej, P. and Chiba, A. 2002. Growth cone pathfinding and filopodial dynamics are mediated separately by Cdc42 activation. *Journal of Neuroscience*. **22**(5), pp.1794–1806.

Knobel, D.L., Cleaveland, S., Coleman, P.G., Fevre, E.M., Meltzer, M.I., Miranda, M.E., Shaw, A., Zinsstag, J. and Meslin, F.X. 2005. Re-evaluating the burden of rabies in Africa and Asia. *Bullutin of the World*

*Health Organi*zation **83**(5), pp.360–368.

Kolesnikova, L., Bohil, A.B., Cheney, R.E. and Becker, S. 2007. Budding of Marburgvirus is associated with filopodia. *Cellular Microbiology*. **9**(4), pp.939–951.

Kopczynski, C.C. and Heah, T. 2018. Netarsudil ophthalmic solution 002% for the treatment of patients with open-angle glaucoma or ocular hypertension. *Drugs of Today*. **54**(8), pp.467–478.

Koprowski, H., Fayaz, A., Nour Salehi, S. and Mohammadi, M. 1976. Successful Protection of Humans Exposed to Rabies Infection: Postexposure Treatment With the New Human Diploid Cell Rabies Vaccine and Antirabies Serum. *JAMA: The Journal of the American Medical Association*. **236**(24), pp.2751–2754.

Kueck, T., Foster, T.L., Weinelt, J., Sumner, J.C., Pickering, S. and Neil, S.J.D. 2015. Serine Phosphorylation of HIV-1 Vpu and Its Binding to Tetherin Regulates Interaction with Clathrin Adaptors D. T. Evans, ed. *PLOS Pathogens*. **11**(8), p.e1005141.

Kumari, S., Mg, S. and Mayor, S. 2010. Endocytosis unplugged: Multiple ways to enter the cell. *Cell Research*. **20**(3), pp.256–275.

Kuzmin, I. V, Rupprecht, C.E. and Nagarajan, T. 2014. Basic facts about Lyssaviruses. *Current Laboratory Techniques in Rabies Diagnosis, Research, and Prevention*. **1**(3).

Lafon, M. 2008. Rabies *In*: C. Reiss, ed. *Neurotropic viral infections*. Cambridge University Press, pp.35–49.

Lafon, M. 2005. Rabies virus receptors. *Journal of Neurovirology*. **11**(1), pp.82–87.

Lafon, M., Wiktor, T.J. and Macfarlan, R.I. 1983. Antigenic sites on the CVS rabies virus glycoprotein: Analysis with monoclonal antibodies. *Journal of General Virology*. **64**(4), pp.843–851.

Lahaye, X., Vidy, A., Pomier, C., Obiang, L., Harper, F., Gaudin, Y. and Blondel, D. 2009. Functional characterization of Negri bodies (NBs) in rabies virus-infected cells: Evidence that NBs are sites of viral transcription and replication. *Journal of Virology*. **83**(16), pp.7948–7958.

Langevin, C. and Tuffereau, C. 2002. Mutations conferring resistance to neutralization by a soluble form of the neurotrophin receptor (p75NTR) map outside of the known antigenic sites of the rabies virus glycoprotein. *Journal of Virology*. **76**(21), pp.10756–10765.

Lankester, F.J., Wouters, P.A.W.M., Czupryna, A., Palmer, G.H., Mzimbiri, I., Cleaveland, S., Francis, M.J., Sutton, D.J. and Sonnemans, D.G.P. 2016. Thermotolerance of an inactivated rabies vaccine for dogs. *Vaccine*. **34**(46), pp.5504–5511.

Laurent, E.M., Sofianatos, Y., Komarova, A., Gimeno, J.-P., Samavarchi Tehrani, P., Kim, D.-K., Abdouni, H., Duhamel, M., Cassonnet, P., Knapp, J.J., Kuang, D., Chawla, A., Sheykhkarimli, D., Rayhan, A., Li, R., Pogoutse, O., Hill, D.E., Calderwood, M.A., Falter-Braun, P., Aloy, P., Stelzl, U., Vidal, M., Gingras, A.-C., Pavlopoulos, G.A., Van Der Werf, S., Fournier, I., Roth, F.P., Salzet, M., Demeret, C., Jacob, Y. and Coyaud, E. 2020. Global BioID-based SARS-CoV-2 proteins proximal interactome unveils novel ties between viral polypeptides and host factors involved in multiple COVID19-associated mechanisms. *bioRxiv*., 2020.08.28.272955.

Lazarovits, J. and Roth, M. 1988. A single amino acid change in the cytoplasmic domain allows the influenza virus hemagglutinin to be endocytosed through coated pits. *Cell*. **53**(5), pp.743–752.

Ledeen, R. and Wu, G. 2018. Gangliosides of the nervous system *In*: *Gangliosides*. Humana Press Inc., pp.19–55.

Lee, K.-F., Li, E., Huber, L.J., Landis, S.C., Sharpe, A.H., Chao, M. V and Jaenisch, R. 1992. Targeted mutation of the gene encoding the low affinity NGF receptor p75 leads to deficits in the peripheral sensory nervous system. *Cell*. **69**(5), pp.737–749.

Leemans, A., De Schryver, M., Van der Gucht, W., Heykers, A., Pintelon, I., Hotard, A.L., Moore, M.L., Melero, J.A., McLellan, J.S., Graham, B.S., Broadbent, L., Power, U.F., Caljon, G., Cos, P., Maes, L. and Delputte, P. 2017. Antibody-Induced Internalization of the Human Respiratory Syncytial Virus Fusion Protein. *Journal of Virology*. **91**(14).

Lehmann, M.J., Sherer, N.M., Marks, C.B., Pypaert, M. and Mothes, W. 2005. Actin- and myosin-driven movement of viruses along filopodia precedes their entry into cells. *Journal of Cell Biology*. **170**(2), pp.317–325.

Lentz, T.L. 1990. Rabies virus binding to an acetylcholine receptor alpha-

subunit peptide. *J Mol Recognit*. **3**(2), pp.82–88.

Lentz, T.L., Burrage, T.G., Smith, A.L., Crick, J. and Tignor, G.H. 1982. Is the acetylcholine receptor a rabies virus receptor? *Science*. **215**(4529), pp.182–184.

Lentz, T.L., Hawrot, E. and Wilson, P.T. 1987. Synthetic peptides corresponding to sequences of snake venom neurotoxins and rabies virus glycoprotein bind to the nicotinic acetylcholine receptor. *Proteins: Structure, Function, and Bioinformatics*. **2**(4), pp.298–307.

Leslie, M.J., Messenger, S., Rohde, R.E., Smith, J., Cheshier, R., Hanlon, C. and Rupprecht, C.E. 2006. Bat-associated rabies virus in skunks. *Emerging Infectious Diseases*. **12**(8), pp.1274–1277.

Leung, A.K.C., Davies, H.D. and Hon, K.L.E. 2007. Rabies: Epidemiology, pathogenesis, and prophylaxis. *Advances in Therapy*. **24**(6), pp.1340–1347.

Levental, I., Lingwood, D., Grzybek, M., Coskun, Ü. and Simons, K. 2010. Palmitoylation regulates raft affinity for the majority of integral raft proteins. *Proceedings of the National Academy of Sciences of the United States of America*. **107**(51), pp.22050–22054.

Lewis, P., Fu, Y. and Lentz, T.L. 2000. Rabies virus entry at the neuromuscular junction in nerve–muscle cocultures. *Muscle & Nerve*. **23**(5), pp.720–730.

Lewis, P. and Lentz, T.L. 1998. Rabies virus entry into cultured rat hippocampal neurons. *Journal of Neurocytology*. **27**(8), pp.559–573.

Li, C., Zhang, H., Ji, L., Wang, X., Wen, Y., Li, G., Fu, Z. and Yang, Y. 2019. Deficient Incorporation of Rabies Virus Glycoprotein into Virions Enhances Virus-Induced Immune Evasion and Viral Pathogenicity. *Viruses*. **11**(3), p.218.

Li, J., Ertel, A., Portocarrero, C., Barkhouse, D.A., Dietzschold, B., Hooper, D.C. and Faber, M. 2012. Postexposure Treatment with the Live-Attenuated Rabies Virus (RV) Vaccine TriGAS Triggers the Clearance of Wild-Type RV from the Central Nervous System (CNS) through the Rapid Induction of Genes Relevant to Adaptive Immunity in CNS Tissues. *Journal of Virology*. **86**(6), pp.3200–3210.

Li, M., Yang, C., Tong, S., Weidmann, A. and Compans, R.W. 2002. Palmitoylation of the Murine Leukemia Virus Envelope Protein Is Critical for Lipid Raft Association and Surface Expression. *Journal of Virology*. **76**(23), pp.11845–11852.

Li, X.-Q., Sarmento, L. and Fu, Z.F. 2005. Degeneration of Neuronal Processes after Infection with Pathogenic, but Not Attenuated, Rabies Viruses. *Journal of Virology*. **79**(15), pp.10063–10068.

Liu, P., Yang, J., Wu, X. and Fu, Z.F. 2004. Interactions amongst rabies virus nucleoprotein, phosphoprotein and genomic RNA in virus-infected and transfected cells. *Journal of General Virology*. **85**(12), pp.3725–3734.

Low, M.G. 1989. The glycosyl-phosphatidylinositol anchor of membrane proteins. *BBA - Reviews on Biomembranes*. **988**(3), pp.427–454.

Lundberg, L., Brahms, A., Hooper, I., Carey, B., Lin, S.C., Dahal, B., Narayanan, A. and Kehn-Hall, K. 2018. Repurposed FDA-Approved drug sorafenib reduces replication of Venezuelan equine encephalitis virus and other alphaviruses. *Antiviral Research*. **157**, pp.57–67.

Luo, J., Zhang, B., Lyu, Z., Wu, Y., Zhang, Y. and Guo, X. 2020. Single amino acid change at position 255 in rabies virus glycoprotein decreases viral pathogenicity. *FASEB Journal*.

Luo, J., Zhang, B., Wu, Y. and Guo, X. 2020. Amino Acid Mutation in Position 349 of Glycoprotein Affect the Pathogenicity of Rabies Virus. *Frontiers in Microbiology*. **11**.

MacGibeny, M.A., Koyuncu, O.O., Wirblich, C., Schnell, M.J. and Enquist, L.W. 2018. Retrograde axonal transport of rabies virus is unaffected by interferon treatment but blocked by emetine locally in axons A. L. Cunningham, ed. *PLOS Pathogens*. **14**(7), p.e1007188.

Maillard, A.P. and Gaudin, Y. 2002. Rabies virus glycoprotein can fold in two alternative, antigenically distinct conformations depending on membrane-anchor type. *Journal of General Virology*. **83**(6), pp.1465–1476.

Majer, M., Herrmann, A., Hilfenhaus, J., Mauler, R., Lehmann, H.G., Hennessen, W. and Kuwert, E.K. 1977. A comparison of the Pasteur and Pitman-Moore strains of rabies virus for the production of rabies vaccine in human diploid cells. *Journal of Biological Standardization*.

5(3), pp.249–256.

Mallik, R., Rai, A.K., Barak, P., Rai, A. and Kunwar, A. 2013. Teamwork in microtubule motors. *Trends in Cell Biology*. **23**(11), pp.575–582.

Malumbres, M. and Barbacid, M. 2007. Cell cycle kinases in cancer. *Current Opinion in Genetics and Development*. **17**(1), pp.60–65.

Maness, P.F. 2003. Cellular signalling mechanisms of neural cell adhesion molecules Anitha K Panicker Mona Buhusi. *Frontiers in Bioscience*. **8**(4), p.1014.

Marcus, P.I. and Sekellick, M.J. 1975. Cell killing by viruses. II. Cell killing by vesicular stomatitis virus: a requirement for virion-derived transcription. *Virology*. **63**(1), pp.176–190.

Marissen, W.E., Kramer, R.A., Rice, A., Weldon, W.C., Niezgoda, M., Faber, M., Slootstra, J.W., Meloen, R.H., Clijsters-van der Horst, M., Visser, T.J., Jongeneelen, M., Thijsse, S., Throsby, M., de Kruif, J., Rupprecht, C.E., Dietzschold, B., Goudsmit, J. and Bakker, A.B.H. 2005. Novel Rabies Virus-Neutralizing Epitope Recognized by Human Monoclonal Antibody: Fine Mapping and Escape Mutant Analysis. *Journal of Virology*. **79**(8), pp.4672–4678.

Marosi, A., Dufkova, L., Forró, B., Felde, O., Erdélyi, K., Širmarová, J., Palus, M., Hönig, V., Salát, J., Tikos, R., Gyuranecz, M., Růžek, D., Martina, B., Koraka, P., Osterhaus, A.D.M.E. and Bakonyi, T. 2019. Combination therapy of rabies-infected mice with inhibitors of pro-inflammatory host response, antiviral compounds and human rabies immunoglobulin. *Vaccine*. **37**(33), pp.4724–4735.

Marosi, A., Forgách, P., Gyuranecz, M., Sulyok, K.M. and Bakonyi, T. 2019. Evaluation of in vitro inhibitory potential of type-I interferons and different antiviral compounds on rabies virus replication. *Vaccine*. **37**(33), pp.4663–4672.

Marsh, M. and Pelchen-Matthews, A. 2000. Endocytosis in viral replication. *Traffic*. **1**(7), pp.525–532.

Matsumoto, S. 1974. Morphology of rabies virion and cytopathology of virus infected cells. *Seminars of Immunobiology Standard* **Vol. 21**, pp.25–34.

De Mattos, C.A., Favi, M., Yung, V., Pavletic, C. and De Mattos, C.C. 2000.

Bat rabies in urban centers in Chile. *Journal of Wildlife Diseases*. **36**(2), pp.231–240.

Mayle, K.M., Le, A.M. and Kamei, D.T. 2012. The intracellular trafficking pathway of transferrin. *Biochimica et Biophysica Acta - General Subjects*. **1820**(3), pp.264–281.

Mazarakis, N.D., Azzouz, M., Rohll, J.B., Ellard, F.M., Wilkes, F.J., Olsen, A.L., Carter, E.E., Barber, R.D., Baban, D.F., Kingsman, S.M., Kingsman, A.J., O'Malley, K. and Mitrophanous, K.A. 2001. Rabies virus glycoprotein pseudotyping of lentiviral vectors enables retrograde axonal transport and access to the nervous system after peripheral delivery. *Human Molecular Genetics*. **10**(19), pp.2109–2121.

McElhinney, L.M., Marston, D.A., Brookes, S.M. and Fooks, A.R. 2014. Effects of carcase decomposition on rabies virus infectivity and detection. *Journal of Virological Methods*. **207**, pp.110–113.

McGarvey, P.B., Hammond, J., Dienelt, M.M., Hooper, D.C., Fang Fu, Z., Dietzschold, B., Koprowski, H. and Michaels, F.H. 1995. Expression of the rabies virus glycoprotein in transgenic tomatoes. *Bio/Technology*. **13**(12), pp.1484–1487.

McGettigan, J.P., Naper, K., Orenstein, J., Koser, M., McKenna, P.M. and Schnell, M.J. 2003. Functional Human Immunodeficiency Virus Type 1 (HIV-1) Gag-Pol or HIV-1 Gag-Pol and Env Expressed from a Single Rhabdovirus-Based Vaccine Vector Genome. *Journal of Virology*. **77**(20), pp.10889–10899.

McKenna, P., McGettigan, J., Pomerantz, R., Dietzschold, B. and Schnell, M. 2003. Recombinant Rhabdoviruses as Potential Vaccines for HIV-1 and Other Diseases. *Current HIV Research*. **1**(2), pp.229–237.

McLane, K.E., Wu, X., Schoepfer, R., Lindstrom, J.M. and Conti-Tronconi, B.M. 1991. Identification of sequence segments forming the α-bungarotoxin binding sites on two nicotinic acetylcholine receptor α subunits from the avian brain. *Journal of Biological Chemistry*. **266**(23), pp.15230–15239.

Mebatsion, T., Konig, M., Conzelmann, K.-K.K., König, M. and Conzelmann, K.-K.K. 1996. Budding of rabies virus particles in the absence of the spike glycoprotein. *Cell*. **84**(6), pp.941–951.

Mebatsion, T., Weiland, F. and Conzelmann, K.-K. 1999. Matrix protein of

rabies virus is responsible for the assembly and budding of bullet-shaped particles and interacts with the transmembrane spike glycoprotein G. *Journal of Virology*. **73**(1), pp.242–250.

Meiring, J.C.M., Shneyer, B.I. and Akhmanova, A. 2020. Generation and regulation of microtubule network asymmetry to drive cell polarity. *Current Opinion in Cell Biology*. **62**, pp.86–95.

Ménager, P., Roux, P., Mégret, F., Bourgeois, J.P., Le Sourd, A.M., Danckaert, A., Lafage, M., Préhaud, C. and Lafon, M. 2009. Toll-like receptor 3 (TLR3) plays a major role in the formation of rabies virus negri bodies. *PLoS Pathogens*. **5**(2).

Meslin, F.-X. 2008. Rabies as a Traveler-s Risk, Especially in High-endemicity Areas. *Journal of Travel Medicine*. **12**(suppl_1), pp.S30–S40.

Minghui, R., Stone, M., Semedo, M.H. and Nel, L. 2018. New global strategic plan to eliminate dog-mediated rabies by 2030. *The Lancet Global Health*. **6**(8), pp.e828–e829.

Mitrabhakdi, E., Shuangshoti, S., Wannakrairot, P., Lewis, R.A., Susuki, K., Laothamatas, J. and Hemachudha, T. 2005. Difference in neuropathogenetic mechanisms in human furious and paralytic rabies. *Journal of the Neurological Sciences*. **238**(1–2), pp.3–10.

Morimoto, K., Foley, H.D., McGettigan, J.P., Schnell, M.J. and Dietzschold, B. 2000. Reinvestigation of the role of the rabies virus glycoprotein in viral pathogenesis using a reverse genetics approach. *Journal of Neurovirology*. **6**(5), pp.373–381.

Morimoto, K., Ni, Y.J. and Kawai, A. 1992. Syncytium formation is induced in the murine neuroblastoma cell cultures which produce pathogenic type G proteins of the rabies virus. *Virology*. **189**(1), pp.203–216.

Müller-Taubenberger, A., Lupas, A.N., Li, H., Ecke, M., Simmeth, E. and Gerisch, G. 2001. Calreticulin and calnexin in the endoplasmic reticulum are important for phagocytosis. *EMBO Journal*. **20**(23), pp.6772–6782.

Müller, T.F., Schröder, R., Wysocki, P., Mettenleiter, T.C. and Freuling, C.M. 2015. Spatio-temporal Use of Oral Rabies Vaccines in Fox Rabies Elimination Programmes in Europe B. Bird, ed. *PLOS Neglected Tropical Diseases*. **9**(8), p.e0003953.

Murphy, F.A. 1977. Rabies pathogenesis. *Archives of Virology*. **54**(4), pp.279–297.

Nakagawa, K., Kobayashi, Y., Ito, N., Suzuki, Y., Okada, K., Makino, M., Goto, H., Takahashi, T. and Sugiyama, M. 2017. Molecular Function Analysis of Rabies Virus RNA Polymerase L Protein by Using an L Gene-Deficient Virus. *Journal of Virology*. **91**(20).

Negri, A. 1903. Contributo allo studio dell eziologia della rabia. *Bullutin of the Society of Medical Surgary* **2**, pp.88–114.

Nel, L. 2001. *Sixth Southern and Eastern African Rabies Group Meeting*. Lilongwe, Malawi.

Nihalani, D., Solanki, A.K., Arif, E., Srivastava, P., Rahman, B., Zuo, X., Dang, Y., Fogelgren, B., Fermin, D., Gillies, C.E., Sampson, M.G. and Lipschutz, J.H. 2019. Disruption of the exocyst induces podocyte loss and dysfunction. *Journal of Biological Chemistry*. **294**(26), pp.10104–10119.

Nikolic, D.S., Lehmann, M., Felts, R., Garcia, E., Blanchet, F.P., Subramaniam, S. and Piguet, V. 2011. HIV-1 activates Cdc42 and induces membrane extensions in immature dendritic cells to facilitate cell-to-cell virus propagation. *Blood*. **118**(18), pp.4841–4852.

Nobile, C., Rudnicka, D., Hasan, M., Aulner, N., Porrot, F., Machu, C., Renaud, O., Prévost, M.-C., Hivroz, C., Schwartz, O. and Sol-Foulon, N. 2010. HIV-1 Nef Inhibits Ruffles, Induces Filopodia, and Modulates Migration of Infected Lymphocytes. *Journal of Virology*. **84**(5), pp.2282–2293.

Ochsenbauer, C., Dubay, S.R. and Hunter, E. 2000. The Rous Sarcoma Virus Env Glycoprotein Contains a Highly Conserved Motif Homologous to Tyrosine-Based Endocytosis Signals and Displays an Unusual Internalization Phenotype. *Molecular and Cellular Biology*. **20**(1), pp.249–260.

Oh, M.J., Akhtar, J., Desai, P. and Shukla, D. 2010. A role for heparan sulfate in viral surfing. *Biochemical and Biophysical Research Communications*. **391**(1), pp.176–181.

Ohno, Y., Kihara, A., Sano, T. and Igarashi, Y. 2006. Intracellular localization and tissue-specific distribution of human and yeast DHHC cysteine-rich domain-containing proteins. *Biochimica et Biophysica Acta - Molecular*

and Cell Biology of Lipids. **1761**(4), pp.474–483.

Ortiz, D.A., Glassbrook, J.E. and Pellett, P.E. 2016. Protein-Protein Interactions Suggest Novel Activities of Human Cytomegalovirus Tegument Protein pUL103. *Journal of Virology*. **90**(17), pp.7798–7810.

Paratcha, G., Ledda, F. and Ibáñez, C.F. 2003. The neural cell adhesion molecule NCAM is an alternative signaling receptor for GDNF family ligands. *Cell*. **113**(7), pp.867–879.

Pasteur, L., Chamberland, C. and Roux, E. 1884. New communication on rabies. *Acad Sci*. **98**, pp.457–463.

Perrin, P., Thibodeau, L. and Sureau, P. 1985. Rabies immunosome (subunit vaccine) structure and immunogenicity. Pre- and post-exposure protection studies. *Vaccine*. **3**(4), pp.325–332.

Piccinotti, S., Kirchhausen, T. and Whelan, S.P.J. 2013. Uptake of rabies virus into epithelial cells by clathrin-mediated endocytosis depends upon actin. *Journal of Virology*. **87**(21), pp.11637–11647.

Piccinotti, S. and Whelan, S.P.J. 2016. Rabies Internalizes into Primary Peripheral Neurons via Clathrin Coated Pits and Requires Fusion at the Cell Body. *PLoS Pathogens*. **12**(7).

St. Pierre, C.A., Leonard, D., Corvera, S., Kurt-Jones, E.A. and Finberg, R.W. 2011. Antibodies to cell surface proteins redirect intracellular trafficking pathways. *Experimental and Molecular Pathology*. **91**(3), pp.723–732.

Du Pont, V., Plemper, R.K. and Schnell, M.J. 2019. Status of antiviral therapeutics against rabies virus and related emerging lyssaviruses. *Current Opinion in Virology*. **35**, pp.1–13.

Potratz, M., Zaeck, L., Christen, M., te Kamp, V., Klein, A., Nolden, T., Freuling, C.M., Müller, T. and Finke, S. 2020. Astrocyte Infection during Rabies Encephalitis Depends on the Virus Strain and Infection Route as Demonstrated by Novel Quantitative 3D Analysis of Cell Tropism. *Cells*. **9**(2), p.412.

Préhaud, C., Wolff, N., Terrien, E., Lafage, M., Mégret, F., Babault, N., Cordier, F., Tan, G.S., Maitrepierre, E. and Ménager, P. 2010. Attenuation of rabies virulence: takeover by the cytoplasmic domain of

its envelope protein. *Sci. Signal.* **3**(105), pp.ra5–ra5.

Pringle, C.R. 1991. The order Mononegavirales. *Archives of Virology*. **117**(1–2), pp.137–140.

Pronobis, M.I., Deuitch, N. and Peifer, M. 2016. The Miraprep: A Protocol that Uses a Miniprep Kit and Provides Maxiprep Yields F. Hayes, ed. *PLOS ONE*. **11**(8), p.e0160509.

Pulmanausahakul, R., Li, J., Schnell, M.J. and Dietzschold, B. 2008. The Glycoprotein and the Matrix Protein of Rabies Virus Affect Pathogenicity by Regulating Viral Replication and Facilitating Cell-to-Cell Spread. *Journal of Virology*. **82**(5), pp.2330–2338.

Ramsey, J., Renzi, E.C., Arnold, R.J., Trinidad, J.C. and Mukhopadhyay, S. 2017. Palmitoylation of Sindbis Virus TF Protein Regulates Its Plasma Membrane Localization and Subsequent Incorporation into Virions. *Journal of Virology*. **91**(3).

Raux, H., Flamand, A. and Blondel, D. 2000. Interaction of the rabies virus P protein with the LC8 dynein light chain. *Journal of Virology*. **74**(21), pp.10212–10216.

Ravkov, E. V., Smith, J.S. and Nichol, S.T. 1995. Rabies virus glycoprotein gene contains a long 3' noncoding region which lacks pseudogene properties. *Virology*. **206**(1), pp.718–723.

Reardon, T.R., Murray, A.J., Turi, G.F., Wirblich, C., Croce, K.R., Schnell, M.J., Jessell, T.M. and Losonczy, A. 2016. Rabies Virus CVS-N2cδG Strain Enhances Retrograde Synaptic Transfer and Neuronal Viability. *Neuron*. **89**(4), pp.711–724.

Reck-Peterson, S.L., Redwine, W.B., Vale, R.D. and Carter, A.P. 2018. The cytoplasmic dynein transport machinery and its many cargoes. *Nature Reviews Molecular Cell Biology*. **19**(6), pp.382–398.

Resh, M.D. 2004. Membrane targeting of lipid modified signal transduction proteins. *Sub-cellular biochemistry*. **37**, pp.217–232.

Rider, M.A., Cheerathodi, M.R., Hurwitz, S.N., Nkosi, D., Howell, L.A., Tremblay, D.C., Liu, X., Zhu, F. and Meckes, D.G. 2018. The interactome of EBV LMP1 evaluated by proximity-based BioID approach. *Virology*. **516**, pp.55–70.

Riedel, C., Vasishtan, D., Pražák, V., Ghanem, A., Conzelmann, K.K. and Rümenapf, T. 2019. Cryo EM structure of the rabies virus ribonucleoprotein complex. *Scientific Reports*. **9**(1), pp.1–6.

Rimola, J., Díaz-González, Á., Darnell, A., Varela, M., Pons, F., Hernandez-Guerra, M., Delgado, M., Castroagudin, J., Matilla, A., Sangro, B., Rodriguez de Lope, C., Sala, M., Gonzalez, C., Huertas, C., Minguez, B., Ayuso, C., Bruix, J. and Reig, M. 2018. Complete response under sorafenib in patients with hepatocellular carcinoma: Relationship with dermatologic adverse events. *Hepatology*. **67**(2), pp.612–622.

Ritchie, C., Cylinder, I., Platt, E.J. and Barklis, E. 2015. Analysis of HIV-1 Gag Protein Interactions via Biotin Ligase Tagging. *Journal of Virology*. **89**(7), pp.3988–4001.

Robach, J.G. and Lamb, R.A. 2010. Analysis of parainfluenza virus-5 hemagglutinin-neuraminidase protein mutants that are blocked in internalization and degradation. *Virology*. **406**(2), pp.189–201.

Roche, S. and Gaudin, Y. 2002. Characterization of the equilibrium between the native and fusion-inactive conformation of rabies virus glycoprotein indicates that the fusion complex is made of several trimers. *Virology*. **297**(1), pp.128–135.

Roche, S. and Gaudin, Y. 2004. Evidence that Rabies Virus Forms Different Kinds of Fusion Machines with Different pH Thresholds for Fusion. *Journal of Virology*. **78**(16), pp.8746–8752.

Roth, A.F., Feng, Y., Chen, L. and Davis, N.G. 2002. The yeast DHHC cysteine-rich domain protein Akr1p is a palmitoyl transferase. *Journal of Cell Biology*. **159**(1), pp.23–28.

Roth, G.A., ..., Naghavi, M. and Murray, C.J.L. 2018. Global, regional, and national age-sex-specific mortality for 282 causes of death in 195 countries and territories, 1980–2017: a systematic analysis for the Global Burden of Disease Study 2017. *The Lancet*. **392**(10159), pp.1736–1788.

Rousso, I., Mixon, M.B., Chen, B.K. and Kim, P.S. 2000. Palmitoylation of the HIV-1 envelope glycoprotein is critical for viral infectivity. *Proceedings of the National Academy of Sciences of the United States of America*. **97**(25), pp.13523–13525.

Roux, K.J., Kim, D.I., Raida, M. and Burke, B. 2012. A promiscuous biotin

ligase fusion protein identifies proximal and interacting proteins in mammalian cells. *J Cell Biol*. **196**(6), pp.801–810.

Royle, S.J., Bobanović, L.K. and Murrell-Lagnado, R.D. 2002. Identification of a non-canonical tyrosine-based endocytic motif in an ionotropic receptor. *Journal of Biological Chemistry*. **277**(38), pp.35378–35385.

Royle, S.J. and Murrell-Lagnado, R.D. 2003. Constitutive cycling: A general mechanism to regulate cell surface proteins. *BioEssays*. **25**(1), pp.39–46.

Rupprecht, C., Kuzmin, I. and Meslin, F. 2017. Lyssaviruses and rabies: Current conundrums, concerns, contradictions and controversies. *F1000Research*. **6**.

Rupprecht, C.E., Hanlon, C.A. and Slate, D. 2005. Oral vaccination of wildlife against rabies: Opportunities and challenges in prevention and control *In*: *Developments in Biologicals*., pp.173–184.

Sacramento, D., Badrane, T.H., Bourhy, H. and Tordo, N. 1992. Molecular epidemiology of rabies virus in France: Comparison with vaccine strains. *Journal of General Virology*. **73**(5), pp.1149–1158.

Sanders, S.S., Martin, D.D.O., Butland, S.L., Lavallée-Adam, M., Calzolari, D., Kay, C., Yates, J.R. and Hayden, M.R. 2015. Curation of the Mammalian Palmitoylome Indicates a Pivotal Role for Palmitoylation in Diseases and Disorders of the Nervous System and Cancers. *PLoS Computational Biology*. **11**(8), p.1004405.

Schelhaas, M., Ewers, H., Rajamäki, M.-L., Day, P.M., Schiller, J.T. and Helenius, A. 2008. Human Papillomavirus Type 16 Entry: Retrograde Cell Surface Transport along Actin-Rich Protrusions T. J. Hope, ed. *PLoS Pathogens*. **4**(9), p.e1000148.

Schmidt, M.F.G. and Schlesinger, M.J. 1979. Fatty acid binding to vesicular stomatitis virus glycoprotein: a new type of post-translational modification of the viral glycoprotein. *Cell*. **17**(4), pp.813–819.

Schnell, M.J., Buonocore, L., Boritz, E., Ghosh, H.P., Chernish, R. and Rose, J.K. 1998. *Requirement for a non-specific glycoprotein cytoplasmic domain sequence to drive efficient budding of vesicular stomatitis virus*.

Schnell, M.J., McGettigan, J.P., Wirblich, C. and Papaneri, A. 2010. The cell biology of rabies virus: using stealth to reach the brain. *Nature Review Microbiol*ogy **8**(1), pp.51–61.

Schnell, M.J., Mebatsion, T. and Conzelmann, K.-K. 1994. Infectious rabies viruses from cloned cDNA. *The EMBO journal*. **13**(18), p.4195.

Schubert, O.T., Röst, H.L., Collins, B.C., Rosenberger, G. and Aebersold, R. 2017. Quantitative proteomics: Challenges and opportunities in basic and applied research. *Nature Protocols*. **12**(7), pp.1289–1294.

Schudt, G., Kolesnikova, L., Dolnik, O., Sodeik, B. and Becker, S. 2013. Live-cell imaging of Marburg virus-infected cells uncovers actin-dependent transport of nucleocapsids over long distances. *Proceedings of the National Academy of Sciences of the United States of America*. **110**(35), pp.14402–14407.

Scolari, S., Imkeller, K., Jolmes, F., Veit, M., Herrmann, A. and Schwarzer, R. 2016. Modulation of cell surface transport and lipid raft localization by the cytoplasmic tail of the influenza virus hemagglutinin. *Cellular Microbiology*. **18**(1), pp.125–136.

Seif, I., Coulon, P., Rollin, P.E. and Flamand, A. 1985. Rabies virulence: effect on pathogenicity and sequence characterization of rabies virus mutations affecting antigenic site III of the glycoprotein. *Journal of Virology*. **53**(3), pp.926–934.

Semerdjieva, S., Shortt, B., Maxwell, E., Singh, S., Fonarev, P., Hansen, J., Schiavo, G., Grant, B.D. and Smythe, E. 2008. Coordinated regulation of AP2 uncoating from clathrin-coated vesicles by rab5 and hRME-6. *Journal of Cell Biology*. **183**(3), pp.499–511.

Seo, W., Prehaud, C., Khan, Z., Sabeta, C. and Lafon, M. 2017. Investigation of rabies virus glycoprotein carboxyl terminus as an in vitro predictive tool of neurovirulence. A 3R approach. *Microbes and Infection*. **19**(9–10), pp.476–484.

Servat, A., Cliquet, F. and Wasniewski, M. 2020. Assessing the Potency of Inactivated Veterinary Vaccines and Oral Live Vaccines Against Rabies *In*: *Rabies and Rabies Vaccines*. Springer International Publishing, pp.181–193.

Shakin-Eshleman, S., Remaley, A., Eshleman, J., Wunner, W. and Spitalnik, S. 1992. N-linked glycosylation of rabies virus glycoprotein. Individual

sequons differ in their glycosylation efficiencies and influence on cell surface expression. *Journal of Biological Chemistry*. **267**, pp.10690–10698.

Shiraki, K., Daikoku, T., Takemoto, M., Yoshida, Y., Suzuki, K., Akahori, Y., Okuno, T., Kurosawa, Y. and Asano, Y. 2011. Neutralizing Anti-gH Antibody of Varicella-Zoster Virus Modulates Distribution of gH and Induces Gene Regulation, Mimicking Latency. *Journal of Virology*. **85**(16), pp.8172–8180.

Shneyer, B.I., Ušaj, M., Wiesel-Motiuk, N., Regev, R. and Henn, A. 2017. ROS induced distribution of mitochondria to filopodia by Myo19 depends on a class specific tryptophan in the motor domain. *Scientific Reports*. **7**(1).

Shuai, L., Wang, J., Zhao, D., Wen, Z., Ge, J., He, X., Wang, X. and Bu, Z. 2019. Integrin β1 Promotes Peripheral Entry by Rabies Virus. *Journal of Virology*. **94**(2).

Smith, T.G., Jackson, F.R., Morgan, C.N., Carson, W.C., Martin, B.E., Gallardo-Romero, N., Ellison, J.A., Greenberg, L., Hodge, T., Squiquera, L., Sulley, J., Olson, V.A. and Hutson, C.L. 2020. Antiviral ranpirnase TMR-001 inhibits rabies virus release and cell-to-cell infection in vitro. *Viruses*. **12**(2).

Sobocinska, J., Roszczenko-Jasinska, P., Ciesielska, A. and Kwiatkowska, K. 2018. Protein palmitoylation and its role in bacterial and viral infections. *Frontiers in Immunology*. **8**(JAN).

Song, Y., Hou, J., Qiao, B., Li, Y., Xu, Y., Duan, M., Guan, Z., Zhang, M. and Sun, L. 2013. Street rabies virus causes dendritic injury and F-actin depolymerization in the hippocampus. *Journal of General Virology*. **94**(PART2), pp.276–283.

De Souza, A. and Madhusudana, S.N. 2014. Survival from rabies encephalitis. *Journal of the Neurological Sciences*. **339**(1–2), pp.8–14.

St-Germain, J.R., Astori, A., Samavarchi-Tehrani, P., Abdouni, H., Macwan, V., Kim, D.-K., Knapp, J.J., Roth, F.P., Gingras, A.-C. and Raught, B. 2020. A SARS-CoV-2 BioID-based virus-host membrane protein interactome and virus peptide compendium: new proteomics resources for COVID-19 research. *bioRxiv*., 2020.08.28.269175.

Stakaitytė, G., Nwogu, N., Dobson, S.J., Knight, L.M., Wasson, C.W.,

Salguero, F.J., Blackbourn, D.J., Blair, G.E., Mankouri, J., Macdonald, A. and Whitehouse, A. 2017. Merkel Cell Polyomavirus Small T Antigen Drives Cell Motility via Rho-GTPase-Induced Filopodium Formation. *Journal of Virology*. **92**(2), p.2020.

Starodubova, E.S., Kuzmenko, Y. V., Latanova, A.A., Preobrazhenskaya, O. V. and Karpov, V.L. 2017. C-terminal lysosome targeting domain of CD63 modifies cellular localization of rabies virus glycoprotein. *Molecular Biology*. **51**(3), pp.404–407.

Staubus, A.O., Alfadhli, A., Barklis, R.L. and Barklis, E. 2019. Replication of HIV-1 envelope protein cytoplasmic domain variants in permissive and restrictive cells. *Virology*. **538**, pp.1–10.

Steck, F., Haefliger, U., Stocker, C. and Wandeler, A. 1978. Oral immunization of foxes against rabies. *Experientia*. **34**, p.1662.

Sun, X., Yau, V.K., Briggs, B.J. and Whittaker, G.R. 2005. Role of clathrin-mediated endocytosis during vesicular stomatitis virus entry into host cells. *Virology*. **338**(1), pp.53–60.

Sundaramoorthy, V., Green, D., Locke, K., O'Brien, C.M., Dearnley, M. and Bingham, J. 2020. Novel role of SARM1 mediated axonal degeneration in the pathogenesis of rabies M. J. Schnell, ed. *PLOS Pathogens*. **16**(2), p.e1008343.

Superti, F., Derer, M. and Tsiang, H. 1984. Mechanism of Rabies virus entry into CER cells. *Journal of General Virology*. **65**(4), pp.781–789.

Superti, F., Hauttecoeur, B., Morelec, M.-J.J., Goldoni, P., Bizzini, B. and Tsiang, H. 1986. Involvement of gangliosides in rabies virus infection. *Journal of general virology*. **67**(1), pp.47–56.

Tao, L., Ge, J., Wang, X., Wen, Z., Zhai, H., Hua, T., Zhao, B., Kong, D., Yang, C. and Bu, Z. 2011. Generation of a recombinant rabies Flury LEP virus carrying an additional G gene creates an improved seed virus for inactivated vaccine production. *Virology Journal*. **8**(1), pp.1–7.

Tao, L., Ge, J., Wang, X., Zhai, H., Hua, T., Zhao, B., Kong, D., Yang, C., Chen, H. and Bu, Z. 2010. Molecular Basis of Neurovirulence of Flury Rabies Virus Vaccine Strains: Importance of the Polymerase and the Glycoprotein R333Q Mutation. *Journal of Virology*. **84**(17), pp.8926–8936.

Tarantola, A. 2017. Four thousand years of concepts relating to rabies in animals and humans, its prevention and its cure. *Tropical Medicine and Infectious Disease*. **2**(2).

Thanomsridetchai, N., Singhto, N., Tepsumethanon, V., Shuangshoti, S., Wacharapluesadee, S., Sinchaikul, S., Chen, S.T., Hemachudha, T. and Thongboonkerd, V. 2011. Comprehensive proteome analysis of hippocampus, brainstem, and spinal cord from paralytic and furious dogs naturally infected with rabies. *Journal of Proteome Research*. **10**(11), pp.4911–4924.

Thoulouze, M.-I., Lafage, M., Schachner, M., Hartmann, U., Cremer, H. and Lafon, M. 1998. The neural cell adhesion molecule is a receptor for rabies virus. *Journal of virology*. **72**(9), pp.7181–7190.

Tsiang, H. 1979. Evidence for an intraaxonal transport of fixed and street rabies virus. *Journal of Neuropathology and Experimental Neurology*. **38**(3), pp.286–296.

Tu, Z., Gong, W., Zhang, Y., Feng, Y., Li, N. and Tu, C. 2015. Proteomic Analyses of Purified Particles of the Rabies Virus. *Bing du xue bao = Chinese journal of virology / [bian ji, Bing du xue bao bian ji wei yuan hui]*. **31**(3), pp.209–216.

Tuffereau, C., Bénéjean, J., Blondel, D., Kieffer, B. and Flamand, A. 1998. Low-affinity nerve-growth factor receptor (P75NTR) can serve as a receptor for rabies virus. *The EMBO journal*. **17**(24), pp.7250–7259.

Tuffereau, C., Leblois, H., Bénéjean, J., Coulon, P., Lafay, F. and Flamand, A. 1989. Arginine or lysine in position 333 of ERA and CVS glycoprotein is necessary for rabies virulence in adult mice. *Virology*. **172**(1), pp.206–212.

Tuffereau, C., Schmidt, K., Langevin, C., Lafay, F., Dechant, G. and Koltzenburg, M. 2007. The Rabies Virus Glycoprotein Receptor p75NTR Is Not Essential for Rabies Virus Infection. *Journal of Virology*. **81**(24), pp.13622–13630.

Tytgat, H.L.P., Schoofs, G., Driesen, M., Proost, P., Van Damme, E.J.M., Vanderleyden, J. and Lebeer, S. 2015. Endogenous biotin-binding proteins: An overlooked factor causing false positives in streptavidin-based protein detection. *Microbial Biotechnology*. **8**(1), pp.164–168.

Ujike, M., Huang, C., Shirato, K., Matsuyama, S., Makino, S. and Taguchi, F.

2012. Two palmitylated cysteine residues of the severe acute respiratory syndrome coronavirus spike (S) protein are critical for S incorporation into virus-like particles, but not for M-S co-localization. *Journal of General Virology*. **93**(4), pp.823–828.

V'kovski, P., Gerber, M., Kelly, J., Pfaender, S., Ebert, N., Braga Lagache, S., Simillion, C., Portmann, J., Stalder, H., Gaschen, V., Bruggmann, R., Stoffel, M.H., Heller, M., Dijkman, R. and Thiel, V. 2019. Determination of host proteins composing the microenvironment of coronavirus replicase complexes by proximity-labeling. *eLife*. **8**.

Valiya Veettil, M., Sadagopan, S., Kerur, N., Chakraborty, S. and Chandran, B. 2010. Interaction of c-Cbl with Myosin IIA Regulates Bleb Associated Macropinocytosis of Kaposi's Sarcoma-Associated Herpesvirus K. Früh, ed. *PLoS Pathogens*. **6**(12), p.e1001238.

Veit, M. 2012. Palmitoylation of virus proteins. *Biology of the Cell*. **104**(9), pp.493–515.

Viets, H.R. 1926. A case of hydrophobia with negri bodies in the brain. *Archives of Neurology And Psychiatry*. **15**(6), pp.735–737.

Vigerust, D.J. and Shepherd, V.L. 2007. Virus glycosylation: role in virulence and immune interactions. *Trends in Microbiology*. **15**(5), pp.211–218.

Vogt, C., Eickmann, M., Diederich, S., Moll, M. and Maisner, A. 2005. Endocytosis of the Nipah Virus Glycoproteins. *Journal of Virology*. **79**(6), pp.3865–3872.

Vzorov, A.N., Weidmann, A., Kozyr, N.L., Khaoustov, V., Yoffe, B. and Compans, R.W. 2007. Role of the long cytoplasmic domain of the SIV Env glycoprotein in early and late stages of infection. *Retrovirology*. **4**, p.94.

Walker, P.J., Dietzgen, R.G., Joubert, D.A. and Blasdell, K.R. 2011. Rhabdovirus accessory genes. *Virus Research*. **162**(1–2), pp.110–125.

Van de Walle, G.R., Favoreel, H.W., Nauwynck, H.J. and Pensaert, M.B. 2003. Antibody-induced internalization of viral glycoproteins and gE-gI Fc receptor activity protect pseudorabies virus-infected monocytes from efficient complement-mediated lysis. *Journal of General Virology*. **84**(4), pp.939–948.

Wang, C., Wang, J., Shuai, L., Ma, X., Zhang, H., Liu, R., Chen, W., Wang, X., Ge, J., Wen, Z. and Bu, Z. 2019. The Serine/Threonine Kinase AP2-Associated Kinase 1 Plays an Important Role in Rabies Virus Entry. *Viruses*. **12**(1), p.45.

Wang, J., Wang, Z., Liu, R., Shuai, L., Wang, X.X., Luo, J., Wang, C., Chen, W., Wang, X.X., Ge, J., He, X., Wen, Z. and Bu, Z. 2018. Metabotropic glutamate receptor subtype 2 is a cellular receptor for rabies virus M. J. Schnell, ed. . **14**(7), p.e1007189.

Wang, X., Zhang, S., Sun, C., Yuan, Z.G., Wu, X., Wang, D., Ding, Z. and Hu, R. 2011. Proteomic profiles of mouse neuro N2a cells infected with variant virulence of rabies viruses. *Journal of Microbiology and Biotechnology*. **21**(4), pp.366–373.

Wang, Z.W., Sarmento, L., Wang, Y., Li, X., Dhingra, V., Tseggai, T., Jiang, B. and Fu, Z.F. 2005. Attenuated rabies virus activates, while pathogenic rabies virus evades, the host innate immune responses in the central nervous system. *Journal of virology*. **79**(19), pp.12554–12565.

Warrell, D.A. 1976. The clinical picture of rabies in man. *Transactions of the Royal Society of Tropical Medicine and Hygiene*. **70**(3), pp.188–195.

Warrell, D.A. and Warrell, M.J. 1995. Human rabies: a continuing challenge in the tropical world. *Schweizerische medizinische Wochenschrift*. **125**(18), pp.879–85.

Warrell, M.J. and Warrell, D.A. 2004. Rabies and other lyssavirus diseases *In*: *Lancet*. Elsevier, pp.959–969.

Weir, D.L., Laing, E.D., Smith, I.L., Wang, L.F. and Broder, C.C. 2014. Host cell virus entry mediated by Australian bat lyssavirus G envelope glycoprotein occurs through a clathrin-mediated endocytic pathway that requires actin and Rab5. *Virology Journal*. **11**(1), pp.1–10.

Wen, X., Ding, L., Wang, J.-J., Qi, M., Hammonds, J., Chu, H., Chen, X., Hunter, E. and Spearman, P. 2014. ROCK1 and LIM Kinase Modulate Retrovirus Particle Release and Cell-Cell Transmission Events. *Journal of Virology*. **88**(12), pp.6906–6921.

Whitt, M.A., Buonocor, L., Prehaud, C. and Rose, J.K. 1991. Membrane fusion activity, oligomerization, and assembly of the rabies virus glycoprotein. *Virology*. **185**(2), pp.681–688.

Whitt, M.A. and Rose, J.K. 1991. Fatty acid acylation is not required for membrane fusion activity or glycoprotein assembly into VSV virions. *Virology*. **185**(2), pp.875–878.

Wickersham, I.R., Lyon, D.C., Barnard, R.J., Mori, T., Finke, S., Conzelmann, K.K., Young, J.A. and Callaway, E.M. 2007. Monosynaptic restriction of transsynaptic tracing from single, genetically targeted neurons. *Neuron*. **53**(5), pp.639–647.

Wickersham, I.R., Sullivan, H.A. and Seung, H.S. 2010. Production of glycoprotein-deleted rabies viruses for monosynaptic tracing and high-level gene expression in neurons. *Nature Protocols*. **5**(3), pp.595–606.

Wiktor, T.J., Fernandes, M. V. and Koprowski, H. 1964. Cultivation of Rabies Virus in Human Diploid Cell Strain WI-38. *The Journal of Immunology*. **93**(3).

Wilde, H. 2007. Failures of post-exposure rabies prophylaxis. *Vaccine*. **25**(44), pp.7605–7609.

Wilde, H. and Hemachudha, T. 2015. The “Milwaukee Protocol” for Treatment of Human Rabies Is No Longer Valid. *The Pediatric Infectious Disease Journal*. **34**(6), pp.678–679.

Willoughby, R.E., Tieves, K.S., Hoffman, G.M., Ghanayem, N.S., Amlie-Lefond, C.M., Schwabe, M.J., Chusid, M.J. and Rupprecht, C.E. 2005. Survival after Treatment of Rabies with Induction of Coma. *New England Journal of Medicine*. **352**(24), pp.2508–2514.

Winkler, W.G., Fashinell, T.R., Leffingwell, L., Howard, P. and Conomy, J.P. 1973. Airborne Rabies Transmission in a Laboratory Worker. *JAMA: The Journal of the American Medical Association*. **226**(10), pp.1219–1221.

Wirblich, C. and Schnell, M.J. 2011. Rabies virus (RV) glycoprotein expression levels are not critical for pathogenicity of RV. *Journal of virology*. **85**(2), pp.697–704.

World Health Organization 2018. *WHO expert consultation on rabies: third report* [Online]. World Health Organization. [Accessed 16 February 2020]. Available from: https://apps.who.int/iris/handle/10665/272364.

Wu, X., Smith, T.G. and Rupprecht, C.E. 2011. From brain passage to cell

adaptation: The road of human rabies vaccine development. *Expert Review of Vaccines*. **10**(11), pp.1597–1608.

Wu, Y., Pons, V., Goudet, A., Panigai, L., Fischer, A., Herweg, J.A., Kali, S., Davey, R.A., Laporte, J., Bouclier, C., Yousfi, R., Aubenque, C., Merer, G., Gobbo, E., Lopez, R., Gillet, C., Cojean, S., Popoff, M.R., Clayette, P., Le Grand, R., Boulogne, C., Tordo, N., Lemichez, E., Loiseau, P.M., Rudel, T., Sauvaire, D., Cintrat, J.C., Gillet, D. and Barbier, J. 2017. ABMA, a small molecule that inhibits intracellular toxins and pathogens by interfering with late endosomal compartments. *Scientific Reports*. **7**(1), pp.1–13.

Wunner, W.H., Reagan, K.J. and Koprowski, H. 1984. Characterization of saturable binding sites for rabies virus. *Journal of virology*. **50**(3), pp.691–697.

Xu, H., Hao, X., Wang, S., Wang, Z., Cai, M., Jiang, J., Qin, Q., Zhang, M. and Wang, H. 2015. Real-time imaging of rabies virus entry into living vero cells. *Scientific Reports*. **5**(1), pp.1–12.

Xue, X.H., Zheng, X.X., Wang, H.L., Ma, J.Z., Li, L., Gai, W.W., Wang, T.C., Yang, S.T. and Xia, X.Z. 2014. An inactivated recombinant rabies CVS-11 virus expressing two copies of the glycoprotein elicits a higher level of neutralizing antibodies and provides better protection in mice. *Virus Genes*. **48**(3), pp.411–420.

Yamada, K., Noguchi, K., Komeno, T., Furuta, Y. and Nishizono, A. 2016. Efficacy of Favipiravir (T-705) in Rabies Postexposure Prophylaxis. *Journal of Infectious Diseases*. **213**(8), pp.1253–1261.

Yamada, K., Noguchi, K. and Nishizono, A. 2014. Efficient N-glycosylation at position 37, but not at position 146, in the street rabies virus glycoprotein reduces pathogenicity. *Virus Research*. **179**(1), pp.169–176.

Yamada, K., Noguchi, K., Nonaka, D., Morita, M., Yasuda, A., Kawazato, H. and Nishizono, A. 2013. Addition of a single N-glycan to street rabies virus glycoprotein enhances virus production. *Journal of General Virology*. **94**(PART2), pp.270–275.

Yamada, K., Park, C.H., Noguchi, K., Kojima, D., Kubo, T., Komiya, N., Matsumoto, T., Mitui, M.T., Ahmed, K., Morimoto, K., Inoue, S. and Nishizono, A. 2012. Serial passage of a street rabies virus in mouse neuroblastoma cells resulted in attenuation: Potential role of the additional N-glycosylation of a viral glycoprotein in the reduced

pathogenicity of street rabies virus. *Virus Research*. **165**(1), pp.34–45.

Yan, X., Mohankumar, P.S., Dietzschold, B., Schnell, M.J. and Fu, Z.F. 2002. The rabies virus glycoprotein determines the distribution of different rabies virus strains in the brain. *Journal of Neurovirol*ogy **8**(4), pp.345–352.

Yang, F., Lin, S., Ye, F., Yang, J., Qi, J., Chen, Zhujun, Lin, X., Wang, J., Yue, D., Cheng, Y., Chen, Zimin, Chen, H., You, Y., Zhang, Z., Yang, Y., Yang, M., Sun, H., Li, Y., Cao, Y., Yang, S., Wei, Y., Gao, G.F. and Lu, G. 2020. Structural Analysis of Rabies Virus Glycoprotein Reveals pH-Dependent Conformational Changes and Interactions with a Neutralizing Antibody. *Cell Host and Microbe*. **27**(3), pp.441-453.e7.

Yang, J., Koprowski, H., Dietzschold, B. and Fu, Z.F. 1999. Phosphorylation of Rabies Virus Nucleoprotein Regulates Viral RNA Transcription and Replication by Modulating Leader RNA Encapsidation. *Journal of Virology*. **73**(2), pp.1661–1664.

Yang, Y., Huang, Y., Gnanadurai, C.W., Cao, S., Liu, X., Cui, M. and Fu, Z.F. 2015. The Inability of Wild-Type Rabies Virus To Activate Dendritic Cells Is Dependent on the Glycoprotein and Correlates with Its Low Level of the De Novo -Synthesized Leader RNA. *Journal of Virology*. **89**(4), pp.2157–2169.

Yelverton, E., Norton, S., Obijeski, J.F. and Goeddel, D. V. 1983. Rabies virus glycoprotein analogs: Biosynthesis in Escherichia coli. *Science*. **219**(4585), pp.614–620.

Yin, K., Li, Y., Ma, Z., Yang, Y., Zhao, H., Liu, C., Jin, M., Wudong, G., Sun, Y., Hang, T., Zhang, H., Wang, F. and Wen, Y. 2020. SNAP25 regulates the release of the Rabies virus in nerve cells via SNARE complex-mediated membrane fusion. *Veterinary Microbiology*. **245**, p.108699.

Zan, J., An, S.T., Mo, K.K., Zhou, J.W., Liu, J., Wang, H.L., Yan, Y., Liao, M. and Zhou, J.Y. 2016. Rabies virus inactivates cofilin to facilitate viral budding and release. *Biochemical and Biophysical Research Communications*. **477**(4), pp.1045–1050.

Zandi, F., Eslami, N., Torkashvand, F., Fayaz, A., Khalaj, V. and Vaziri, B. 2013. Expression changes of cytoskeletal associated proteins in proteomic profiling of neuroblastoma cells infected with different strains of rabies virus. *Journal of medical virology*. **85**(2), pp.336–347.

Zeiler, F.A. and Jackson, A.C. 2015. Critical Appraisal of the Milwaukee Protocol for Rabies: This Failed Approach Should Be Abandoned. *Canadian Journal of Neurological Sciences*. **43**(1), pp.44–51.

Zhang, S., Teng, X., Toyama, Y. and Saunders, T.E. 2020. Periodic Oscillations of Myosin-II Mechanically Proofread Cell-Cell Connections to Ensure Robust Formation of the Cardiac Vessel. *Current Biology*. **30**(17), pp.3364-3377.e4.

Zhang, Y., Wang, Y., Feng, Y., Tu, Z., Lou, Z. and Tu, C. 2020. Proteomic Profiling of Purified Rabies Virus Particles. *Virologica Sinica*. **35**(2), pp.143–155.